

**Electron quantization and localization
in metal films and nanostructures**

Habilitationsschrift

**vorgelegt der
Mathematisch-Naturwissenschaftlichen
Fakultät der Universität Potsdam**

**von
Dr. rer. nat. Oliver Rader**

Juli 2004

Abstract

It has been known for several years that under certain conditions electrons can be confined within thin layers even if these layers consist of metal and are supported by a metal substrate. In photoelectron spectra, these layers show characteristic discrete energy levels and it has turned out that these lead to large effects like the oscillatory magnetic coupling technically exploited in modern hard disk reading heads.

The current work asks in how far the concepts underlying quantization in two-dimensional films can be transferred to lower dimensionality. This problem is approached by a stepwise transition from two-dimensional layers to one-dimensional nanostructures. On the one hand, these nanostructures are represented by terraces on atomically stepped surfaces, on the other hand by atom chains which are deposited onto these terraces up to complete coverage by atomically thin nanostripes. Furthermore, self organization effects are used in order to arrive at perfectly one-dimensional atomic arrangements at surfaces.

Angle-resolved photoemission is particularly suited as method of investigation because it reveals the behavior of the electrons in these nanostructures in dependence of the spacial direction which distinguishes it from, e. g., scanning tunneling microscopy. With this method intense and at times surprisingly large effects of one-dimensional quantization are observed for various exemplary systems, partly for the first time. The essential role of bandgaps in the substrate known from two-dimensional systems is confirmed for nanostructures. In addition, we reveal an ambiguity without precedent in two-dimensional layers between spacial confinement of electrons on the one side and superlattice effects on the other side as well as between effects caused by the sample and by the measurement process. The latter effects are huge and can dominate the photoelectron spectra.

Finally, the effects of reduced dimensionality are studied in particular for the d electrons of manganese which are additionally affected by strong correlation effects. Surprising results are also obtained here.

Zusammenfassung

"Quantisierung und Lokalisierung von Elektronen in metallischen Filmen und Nanostrukturen"

Es ist seit einigen Jahren bekannt, dass Elektronen unter bestimmten Bedingungen in dünne Filme eingeschlossen werden können, selbst wenn diese Filme aus Metall bestehen und auf Metall-Substrat aufgebracht werden. In Photoelektronenspektren zeigen diese Filme charakteristische diskrete Energieniveaus, und es hat sich herausgestellt, dass sie zu großen, technisch nutzbaren Effekten führen können, wie der oszillatorischen magnetischen Kopplung in modernen Festplatten-Leseköpfen.

In dieser Arbeit wird untersucht, inwieweit die der Quantisierung in zweidimensionalen Filmen zu Grunde liegenden Konzepte auf niedrigere Dimensionalität übertragbar sind. Das bedeutet, dass schrittweise von zweidimensionalen Filmen auf eindimensionale Nanostrukturen übergegangen wird. Diese Nanostrukturen sind zum einen die Terrassen auf atomar gestuften Oberflächen, aber auch Atomketten, die auf diese Terrassen aufgebracht werden, bis hin zu einer vollständigen Bedeckung mit atomar dünnen Nanostreifen. Daneben werden Selbstorganisationseffekte ausgenutzt, um zu perfekt eindimensionalen Atomanordnungen auf Oberflächen zu gelangen.

Die winkelaufgelöste Photoemission ist als Untersuchungsmethode deshalb so geeignet, weil sie das Verhalten der Elektronen in diesen Nanostrukturen in Abhängigkeit von der Raumrichtung zeigt, und unterscheidet sich darin beispielsweise von der Rastertunnelmikroskopie. Damit ist es möglich, deutliche und manchmal überraschend große Effekte der eindimensionalen Quantisierung bei verschiedenen exemplarischen Systemen zum Teil erstmals nachzuweisen. Die für zweidimensionale Filme wesentliche Rolle von Bandlücken im Substrat wird für Nanostrukturen bestätigt. Hinzu kommt jedoch eine bei zweidimensionalen Filmen nicht vorhandene Ambivalenz zwischen räumlicher Einschränkung der Elektronen in den Nanostrukturen und dem Effekt eines Übergitters aus Nanostrukturen sowie zwischen Effekten des Elektronenverhaltens in der Probe und solchen des Messprozesses. Letztere sind sehr groß und können die Photoemissionsspektren dominieren.

Abschließend wird der Effekt der verminderten Dimensionalität speziell für die d-Elektronen von Mangan untersucht, die zusätzlich starken Wechselwirkungseffekten unterliegen. Auch hierbei treten überraschende Ergebnisse zu Tage.

Abbreviations used

bcc	body-centered cubic
fcc	face-centered cubic
GMR	giant magnetoresistance
hcp	hexagonal close packed
IMFP	inelastic mean free path
L	langmuir ($1 \text{ L} = 10^{-6} \text{ Torr s}$)
LEED	low-energy electron diffraction
MCXD	magnetic circular x-ray dichroism
ML	monolayer
PEAD	photoelectron angle distribution
RKKY	Ruderman-Kittel-Kasuya-Yoshida
STM	scanning tunneling microscopy

Contents

1	Introduction	5
2	Methodical aspects	15
2.1	Basic principles of photoemission	15
2.2	Surface sensitivity	16
2.3	Single-particle model of photoemission	17
2.4	Angle-resolved photoemission	18
2.5	Bulk and surface states	20
2.6	Symmetry and selection rules	21
2.7	Deviations from the single particle picture	23
2.8	Spin-resolved photoemission	24
2.9	Magnetic x-ray circular dichroism	25
3	Quantization in ultrathin films	29
3.1	Evolution of the 3d electronic structure	29
3.2	Ni/Cu/Ni spin valve structures	33
3.3	Rare-earth metal: Gd/W(110)	35
4	Quantization at stepped surfaces	39
4.1	W(331): Initial- or final-state effects?	39
4.2	Monoatomic Co and Cu wires	44
4.3	Carbon nanostripes	47
5	Quantization in self-organized nanostructures	51
5.1	Spin-polarized quantum-wire states	51
5.2	An elastic "sieve" in k-space: Gd/W(110)	54
6	Localization in Mn films and nanostructures	59
6.1	From zero to two dimensions	59
6.2	Spin-polarized states in two and three dimensions	63
6.3	Strong electron correlation in bcc Mn films	65
7	Summary	71
8	Acknowledgement	75

4

CONTENTS

9 References

77

10 Twelve papers presented

83

Chapter 1

Introduction

The term "electron quantization" is often readily identified with semiconductor research and application. This is probably because in the semiconductor field, the exploitation of quantum-size effects has been pursued early on with the result that corresponding devices, like the quantum-well laser, have meanwhile become part of daily life. Semiconductors have band gaps which support electron quantization. For layered systems of metals, conditions for quantization are not as obvious. It is remarkable that their most important application, namely oscillatory long-range magnetic coupling and giant magnetoresistance (GMR) [89B1,88B1], were linked to electron quantization after their exploitation in ultrasensitive sensors for reading heads of hard disks had already been in progress [92O1,93G1,93C2,98H1]. Metals do not possess an absolute band gap around the Fermi energy. However, they have relative band gaps, i.e., forbidden zones that exist for a certain direction of the electron wave vector \mathbf{k} and/or one spin orientation. These band gaps are often much larger than in semiconductors and together with the benign conditions for epitaxial growth with atomically sharp interfaces, metal nanostructures promise electron confinement to atomic dimensions [99P1,2000C1,2001L2]. We will first look at the oscillatory magnetic coupling because of its importance for the field of metal quantum-well systems. After this, we will progressively reduce the dimensionality of metal-on-metal structures and explore which of the concepts from two-dimensional structures can be kept and what becomes entirely new in metal nanostructures.

Fig. 1.1 shows the principle of oscillatory magnetic coupling. Depending on the thickness of the nonmagnetic spacer layer, the magnetic coupling between ferromagnetic layers oscillates between parallel and antiparallel. Electron quantization occurs in the nonmagnetic spacer layer that separates two ferromagnetic layers (fig. 1.2a). At both interfaces, electrons are reflected and form standing waves. In an angle-resolved photoemission experiment, the quantized states in the nonmagnetic spacer layer can be probed. Fig. 1.3 shows quantum-well states in Cu/Co(100). A characteristic feature is that with increasing Cu coverage (in monoatomic layers, ML), the energetic spacing between quantum-well peaks decreases. This is exactly what is expected from the behavior of electrons

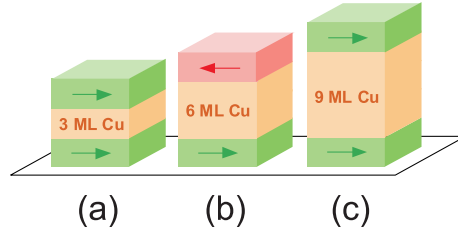


Figure 1.1: Schematic of long-range oscillatory magnetic interlayer coupling.

in a one-dimensional potential well as seen from fig. 1.2b.

When a film or multilayer with antiparallel coupling like in fig. 1.1b is produced, parallel coupling can be brought about by the influence of external magnetic fields such as from the bits on a magnetic hard disk. At zero field, the coupling will switch back to antiparallel. This situation is depicted in fig. 1.4 for Cr as nonferromagnetic spacer material. (Cr is used for historical reasons as the oscillatory coupling was erroneously ascribed to the antiferromagnetism of Cr. In technical applications Co/Cu/Co or permalloy/Cu/permalloy structures are favored.) The principle of the giant magnetoresistance effect is readily understood if the current is viewed upon as the sum of two spin currents (fig. 1.4). For antiparallel coupling, each spin current undergoes strong scattering in the ferromagnetic layer with magnetization opposite to the spin moment of the electron and a high resistance results. For parallel coupling, one spin current is scattered very little and this one leads to a low resistance.

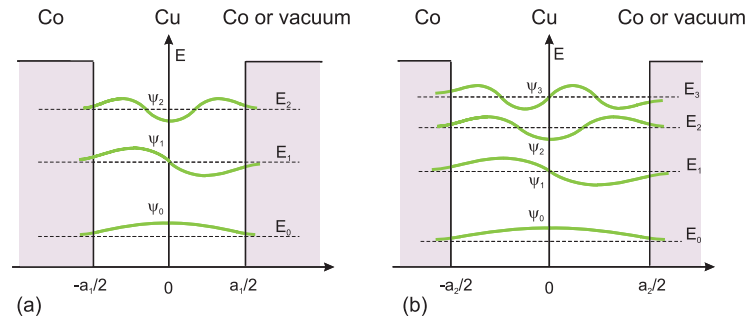


Figure 1.2: One-dimensional potential well as model for quantization in a two-dimensional film (a). The interfaces to the substrate and to vacuum act as boundaries of the well. With increasing width, more quantum-well states can be accommodated in the well (b).

The reason for the oscillatory magnetic coupling is the spin dependence of the band gaps in the ferromagnets. If quantum-well states are able to transmit the magnetic coupling, they must themselves be spin polarized regardless of the fact that they occur in a nonmagnetic material. The proof of this is the

spin-resolved measurement shown in fig. 1.5: The quantum-well peaks occur predominantly in the spectra for minority-spin electrons (downward triangles).

The above is a textbook example for the strong effects that quantized electronic states can have in metals. Although the quantum-well model of magnetic interlayer coupling is generally accepted by now, there is still a number of open questions concerning the electronic structure of magnetic and nonmagnetic two-dimensional films.

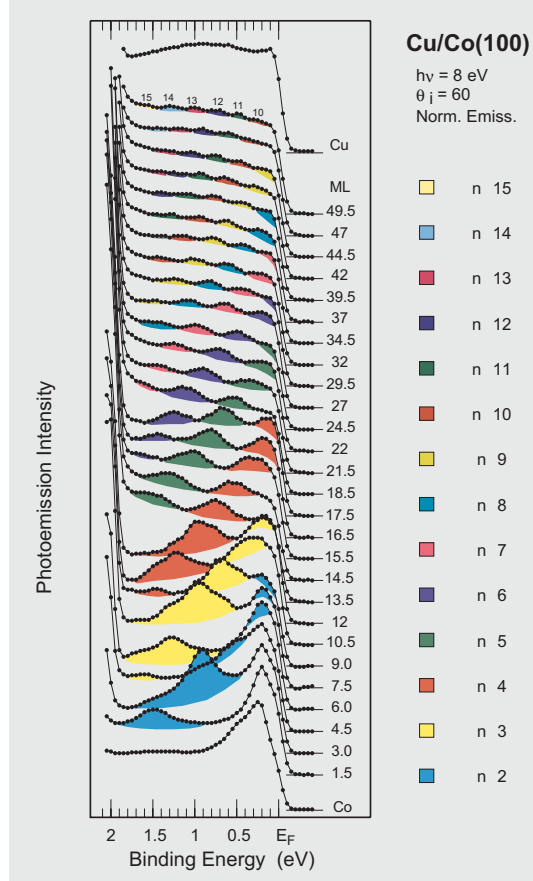


Figure 1.3: Angle-resolved photoemission spectra showing quantum-well states of Cu/Co(100). Each spectrum corresponds to a different Cu coverage in monoatomic layers (ML). Quantum-well peaks cross the Fermi energy with the same period of 5.6 ML that is characteristic of the oscillatory magnetic coupling. n denotes the quantum number. From ref. [86C1].

After introducing the experimental methods in chap. 2, we will touch upon some of these questions in chap. 3 starting out in sect. 3.1 with the simplest example of a two-dimensional quantum-well system. This is the one formed by

a transition-metal monolayer on a noble-metal substrate. We give arguments why the Ni film on Cu(100) should be a good representative of two-dimensional behavior. Given the simplicity of the system, the recent observation of three-dimensional behavior in the literature [97M1] has been a surprise. The system Ni/Cu(100) along with some others are therefore a good starting point to demonstrate the experimental method and the power of angle-resolved photoemission to distinguish and clarify two-dimensional behavior of electrons. The key to this is the momentum-resolving property of angle-resolved photoemission (sect. 2.4).

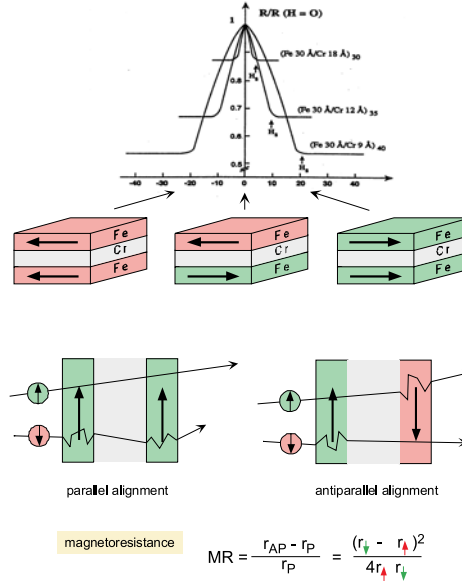


Figure 1.4: Giant magnetoresistance effect in Fe/Cr multilayers. The magnetic structure in zero field is antiparallel due to the oscillatory magnetic coupling effect. When the Fe magnetizations are aligned parallel by an external magnetic field, the electrical resistance drops. Experimental data from ref. [88B1].

The extreme surface sensitivity of the method (sect. 2.2) is naturally well suited for studying thin films and nanostructures at surfaces. However, for buried films like the nonmagnetic interlayer of giant magnetoresistive systems like Co/Cu/Co(100) or Ni/Cu/Ni(100), this can be a disadvantage. For this reason, usually Cu/Co(100) without a Co capping layer is chosen to study quantum-well state formation in angle-resolved photoemission or inverse photoemission. As each reflection of electrons at an interface leads to a certain phase shift and phase shifts at Cu-vacuum and Cu-Co interfaces differ, the direct connection of quantum-well data with data on the magnetic coupling is problematic. This leads for example to the question whether the appearance of a quantum-well peak at the Fermi energy in the spacer layer causes parallel or antiparallel cou-

pling of the magnetic layers. For this reason, the system Ni/Cu/Ni(100) has been studied and compared to Cu/Ni(100) in sect. 3.2. It will be seen that the influence of the magnetic cap layer goes much beyond that of a constant phase shift.

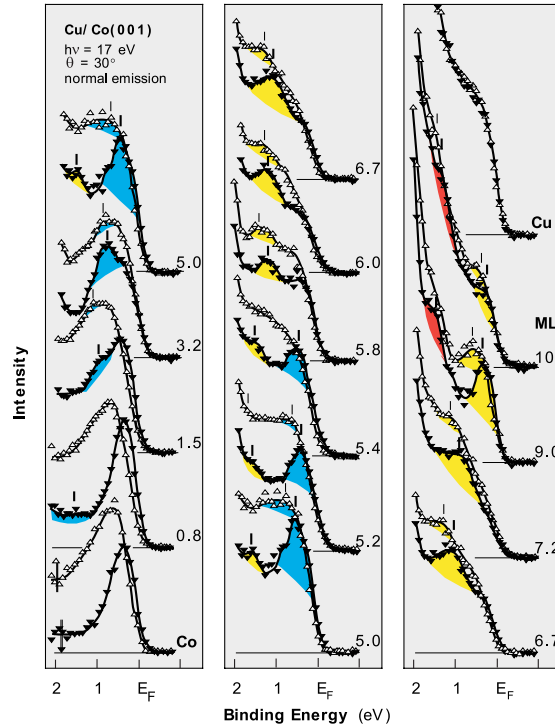


Figure 1.5: Spin- and angle-resolved photoemission spectra of quantum-well states of Cu/Co(100). Upward triangles are for majority spin and downward triangles for minority spin. Quantum-well states are primarily of minority spin leading to an oscillation of the spin polarization at the Fermi energy with Cu coverage. Original data from ref. [92C2].

The last section of chap. 3, sect. 3.3, is devoted to an entirely different quantum-well material: the rare earth gadolinium. As a ferromagnetic metal, the electronic structure of Gd comprises localized magnetic 4f and itinerant 5d electrons. In the framework of the RKKY model of magnetic coupling, the 5d electrons mediate the magnetic coupling between the partially occupied 4f orbitals. They are in this way responsible for the magnetic structure of the elemental rare earths which strongly varies within this material class. In the description of the oscillatory magnetic coupling of trilayers like Co/Cu/Co, there is an apparent similarity between the RKKY model of magnetic coupling and the quantum-well model. Therefore, the observation of quantum-well states of rare earth 5d electrons would be highly interesting. It will be shown that confinement

and quantization of Gd states succeeds when the film is grown on the standard substrate for epitaxial growth of rare earths, namely W(110). In particular, its favourite band gap properties and their importance for confinement will be discussed. The standard model for quantum-well state description, the phase accumulation model, will be applied. In the particular case of Gd, the model is used to determine the dispersion of Gd 5d electrons, and this clarifies a dispute raised in the literature as to whether or not rare earth 5d electrons show strong electron correlation.

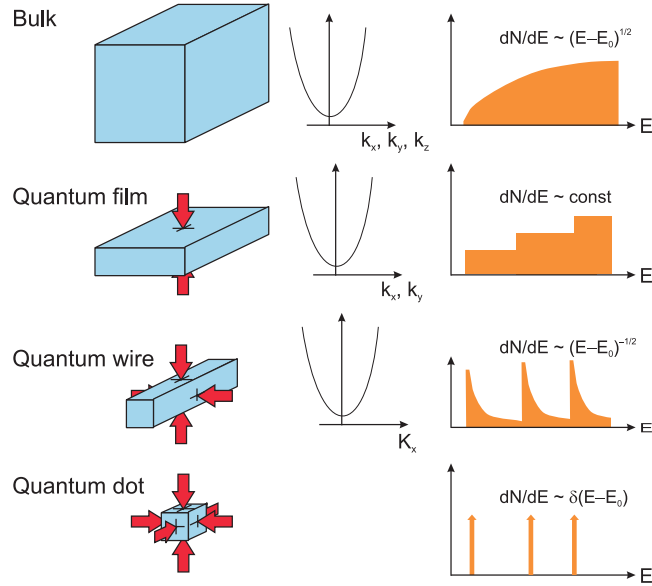


Figure 1.6: Comparison of $E(\mathbf{k})$ dispersions and electronic state densities for confinement in zero, one, two, and three dimensions.

Quantum-well state formation in two-dimensional metal films has meanwhile been observed on a regular basis [2000C1], and research needs to move on towards qualitatively new challenges which are to be discovered in lower dimensionality than two. Fig. 1.6 shows the effect of progressive confinement on the electronic structure starting out from the volume: The quantum film leads for \mathbf{k} -vectors along the z -direction to discrete states appropriately described by the one-dimensional potential well of fig. 1.2 and the phase accumulation model (sect. 3.3). In both perpendicular directions, x and y , electrons disperse like in the volume, and this leads to a step-like density of states. We will explore the transition from the quantum film to the quantum wire, where ultimately electrons propagate only along one direction. In the framework of the present thesis, this task will be achieved in two steps:

At first, we will treat vicinal surfaces in chap. 4, i. e., surfaces that deviate from a low-Miller-index surface by a slight miscut. These stepped surfaces form

a lateral superlattice with fixed period. In sect. 4.1 we look at clean stepped W(110) because we consider it, by analogy to flat W(110), a promising substrate for the growth of a large variety of metal nanostructures. The unusual behavior of a certain feature of the clean W is described. This feature shows a repeated $E(\mathbf{k})$ band dispersion. After the standard tests in angle-resolved photoemission, described already in sect. 3.1, this feature evolves as surface localized, i. e., of dimensionality two or lower. It will be seen that angle-dependent photoemission can further distinguish between two- and one-dimensional behavior where for stepped surfaces two-dimensional behavior is understood as electron itinerance across the superlattice of steps. Such behavior requires the respective wave function to be macrosurface oriented. One-dimensional behavior, on the other hand, means a localization of the wave function at the microsurface (terrace). The experiment unequivocally determines one-dimensional behavior. This has interesting consequences in so far as the abovementioned repetition of $E(\mathbf{k})$ must be a diffraction effect, i. e., it occurs in the final state of the photoemission transition. Moreover, it appears that the well-known umklapp formalism for final state scattering at superlattices gives the correct period but not the correct emission angle and, therefore, a different description will be put forward.

The next step is to use stepped surfaces as template for the growth of metallic nanowires. The repulsive step-step interaction on vicinal Pt(111) leads to a narrow distribution of step widths, and the growth of nanowires of monoatomic width of Cu and Co/Pt(997) has been described in the literature. Below monolayer coverage, the surface sensitivity of angle-resolved photoemission does no longer favor nanostructures over their substrate. Therefore, as additional way to enhance the nanostructure signal, photoemission for photon energies around the Cooper minimum of the substrate valence-band orbitals, i. e., Pt 5d, has been conducted in sect. 4.2. Magnetism is very sensitive to the number of nearest neighbors or, in other words, to the dimensionality. Therefore, in sect. 4.2, the one-dimensionality of Co is demonstrated indirectly via an enhancement of the magnetic exchange splitting between majority- and minority-spin electrons. It should be mentioned that the work described in sect. 4.2 has later been confirmed by collaborators showing directly by magnetic circular x-ray dichroism (MCXD) that the system Co/Pt(997) is the first example of a one-dimensional ferromagnetic chain [2002G1].

Chap. 4 is concluded by increasing the nanostructure coverage on the stepped substrate to a full monolayer equivalent. This step is undertaken in 4.3, and it is that precisely possible employing a graphitization method which principally can produce mono- but not double layers. The result of graphitization of Ni(771) is a full coverage by carbon nanostripes of graphene (i. e., monolayer graphite) structure. The band dispersion of graphite is known to be two-dimensional and leads to very large dispersions. In contrast to the clean vicinal W(110) surfaces of sect. 4.1, it is expected that all of the graphene $E(\mathbf{k})$ bands are affected by the superlattice of steps. Therefore, the anisotropy of the electronic structure with respect to directions parallel and perpendicular to the steps and stripes is most clearly seen from the angle-resolved photoemission. All of the band dispersions experience a doubling in the perpendicular direction.

In analogy to the experiment on vicinal W(110), the electrons are found to be localized at the individual stripes, and the repetition of $E(\mathbf{k})$ is assigned to a diffraction effect in the final state.

There are two reasons for leaving stepped surfaces aside again in chap. 5. First of all, the coherence of the step arrangement and/or of nanostructure growth may not be sufficient to arrive at the first observation of the expected one-dimensional dispersion for monoatomic metal chains. And secondly, the repetition effects of $E(\mathbf{k})$ discovered in chap. 4 depend on the periodicity of the step lattice. To vary the period means to prepare a different crystal surface because angle resolved photoemission requires a laterally uniform surface. Several vicinal W and Ni surfaces have been compared, however, such studies are limited by experimental resources. Chap. 5, therefore, deals with chains of high coherence which have been observed in self-organized growth on flat substrates with rectangular surface lattice like (110) and the superlattice constant of which can be adjusted. Interestingly, this marks also a change away from the lattice-matched growth conditions of two-dimensional quantum-well states towards lattice-mismatched growth of nanostructures.

Au/Ni(110) is such a system which around 0.6 ML undergoes a structural transition which leads to a coherent array of Au chains. These chains are monoatomic but with a zigzag shape. In sect. 5.1, the corresponding change from one- to three-dimensionality in the electronic structure can be witnessed in Au-coverage-dependent photoemission spectra. A perfect one-dimensional dispersion of Au sp states is measured, i. e., parabolic along the chains and flat in the perpendicular direction. Paper VII was the first publication of a one-dimensional dispersion for a metal chain together with the work by Segovia et al. of Au on stepped Si [99S1]. The result is surprising and not immediately justified based on the respective state densities of Au and Ni. Instead, strong hybridization of Au and Ni sp states and vanishing dimensionality effects could be expected as well. The solution to this problem is the presence of bulk band gaps in the Ni substrate. It appears that they are as important for electron confinement in one-dimensional nanowires as they are in two-dimensional quantum-well structures. For the GMR system Cu/Co(100), electron confinement depends on the spin, and consequently quantum-well states are spin polarized (fig. 1.5). It is shown that exactly the same happens in one-dimensional quantum wires of Au/Ni(110) emphasizing once again the role of the band gap in the substrate electronic structure for confinement and quantization.

In sect. 5.2, we will return to the system Gd/W(110) because it enables us to test the variation of lateral superlattice effects with the lattice constant. This occurs, if one limits the Gd coverage to submonolayer amounts. They grow on W(110) in a series of superstructures which can be characterized as chains. The reason for this arrangement is the strong dipole that the Gd atom forms due to charge transfer when Gd adsorbs on W. The repulsive dipole-dipole interaction between Gd atoms keeps them apart. Due to the anisotropy of the W(110) surface, the lattice constant along the chains remains constant whereas the interchain distance shrinks in small steps as the Gd submonolayer coverage is increased. Angle-resolved photoemission spectra change very strongly during

this process and present a wealth of features. As yet another method to enhance the nanostructure signal in photoemission, resonant excitation via the Gd 4d core level is applied. The result is that the strongly varying peaks are not due to Gd. They are instead explained as a diffraction effect of W-derived electrons at the Gd superlattice following the simple description by the umklapp picture. Unlike the results of Au/Ni(110) in sect. 5.1, this is a final-state effect. And just like on W(331) and W(551) (sect. 4.1), the presence of the band gap avoids the contribution from direct transitions to the spectra which facilitates the observation of the umklapp effects. The increasing Gd coverage translates into a quasicontinuous series of \mathbf{k} -vectors which probe the W(110) band structure along the surface. This hypothesis is proven through an elegant test involving the clean W(110).

Up to this point, all of the electronic states discussed can be characterized as delocalized in three dimensions and the wide band width of noble-metal sp and d electrons, transition-metal and rare-earth d electrons, and graphite sp electrons ideally complemented the expectations based on the simple models of quantization visualized in figs. 1.2 and 1.6. Can we expect a similar dependence on the dimensionality when the electron orbital is more strongly localized? In chap. 6, we study how electrons in the half-filled 3d orbital of Mn behave for various environments, and we repeat the course in reverse order, i. e., from dimensionality zero to three. In sect. 6.1 we prepare one-dimensional Mn arrangements by deposition of a 0.5 ML film on Ni(110). The surface arrangement is such that next Mn neighbors are avoided through a repulsive Mn-Mn interaction and this leads to a $c(2 \times 2)$ structure. Increasing the coverage from 0.5 to 1 ML and beyond corresponds to a transition from a zero- to a two- and three-dimensional arrangement of Mn atoms. Photoemission spectra of the Mn 2p core level show indeed a very sensitive reaction to changes in the dimensionality: A strong extra peak due to electron correlation which is only present for the zero-dimensional structure around 0.5 ML coverage. The results are compared with those from 0.5 ML Mn/Cu(100) which is well characterized as ordered surface alloy. There is some similarity to the case of diluted magnetic alloys or so-called 'spin glasses' like Mn in Cu which can also be termed 'zero dimensional'. Photoemission shows, however, that correlation effects are much larger for the zero-dimensional surface arrangement of Mn as for Mn diluted in the bulk. In addition, only in the surface alloy, Mn atoms come so close to each other that long-range structural as well as magnetic order can occur.

Such $c(2 \times 2)$ structure is not observed for Mn on Fe(110). Fe is of bcc structure and on the close-packed (110)-surface, epitaxial $p(1 \times 1)$ growth is found. Some contradictory reports about the magnetic coupling of Mn to the Fe(100) surface were the motivation for a careful coverage-dependent study by MCXD. The MCXD spectra in absorption showed not only a characteristic dependence of the magnetic coupling on the coverage ranging from zero to parallel to antiparallel and again to zero but also of the electronic structure which becomes progressively less localized between 0.3 and 2 ML. The branching ratio of absorption spectra served as a helpful indicator of the dimensionality.

The strong localization of Mn electrons is based on half filling or a d^5 electron

configuration of the d and with a 100% spin polarization of Mn d states. This calls for a spin-resolved photoemission study of the valence band, however, the method requires besides the local spin polarization also long-range ferromagnetic order. This can in principle be achieved for Mn on Fe(110) but requires very low coverages (< 2 ML) the magnetic coupling of which is extremely sensitive to vacuum quality. In the volume, Mn prefers antiferromagnetic order. The way out is to study a ferromagnetic Mn compound. The challenging sample preparation for spin resolved studies was achieved for epitaxial films of Mn pnictides, in particular MnSb(0001). In sect. 6.2, spin resolved photoemission is used to probe two high-symmetry points of the bulk band structure of MnSb and determine the magnetic exchange splittings between majority- and minority-spin states of Mn. The results are in agreement with spin-polarized band structure calculations without strong electron correlations but the splitting of nonbonding Mn states is slightly larger in the experiment. The experiment revealed the presence of a large spin-polarized band gap in MnSb when projected onto the (0001) surface. It will be seen that a spin-polarized surface state is supported by this band gap.

Mn has a complicated atomic structure with four allotropes, of which the one stable at room temperature, α -Mn ($T < 727^\circ\text{C}$), is most complicated with 58 atoms in the unit cell. This may be the reason why angle-resolved photoemission has produced bulk band structures of all magnetic transition metals but Mn [99R1]. This shall be achieved in sect. 6.3. There is a way to produce bulk-like epitaxial films of fcc Mn on $\text{Cu}_3\text{Au}(100)$, and during the experiment on Fe(110) mentioned above we developed a way to grow epitaxial films of bcc Mn on W(110). Extensive experiments to determine band dispersions for epitaxial Mn give surprising results entirely different from those for Cr, Fe, Co, and Ni and in clear contrast to theoretical band structures for Mn.

Chapter 2

Methodical aspects

2.1 Basic principles of photoemission

The photoelectric effect was discovered by Hertz when experimenting with sparks. Spark formation across a gap was part of an electronic oscillator which later enabled his most noted achievement, the production of electromagnetic waves. In 1887 Hertz found that ultraviolet light from a spark leads to electron emission. This finding was quantitatively explained by Einstein in 1905 introducing the photon as quantum of light [05E1]. Einstein's equation

$$E_{\text{kin,max}} = h\nu - \Phi \quad (2.1.1)$$

relates the maximum kinetic energy of an electron emitted in the photoelectric effect to a quantized photon energy minus the energy necessary to release the electron from the solid, the so-called work function. The use of photoelectron emission to study the electronic structure of solids was developed later — one of the cornerstones of this development being the nobel price for Kai Siegbahn in 1981 for the development of electron spectroscopy for chemical analysis (ESCA). Fig. 2.1a shows the sketch of a photoelectron spectrum. The electrons on the right hand side are the most loosely bound ones and their distribution extends up to the Fermi energy in the case of a metallic sample. This means, the spectrum measures electrons from the occupied part of the density of states. In order to extend eq. 2.1.1 to the other electrons in the spectrum, the binding energy is defined by

$$E_B = h\nu - E_{\text{kin}} - \Phi. \quad (2.1.2)$$

Electrons deriving from the valence band can be found at binding energies of several electron volts while those from core levels contribute between several ten eV and several ten thousand electron volts. Other features in the spectrum may stem from Auger transitions and photoemission satellites. With increasing E_B up to the edge formed by electrons of zero kinetic energy, a background of inelastically scattered electrons contributes to the spectrum.

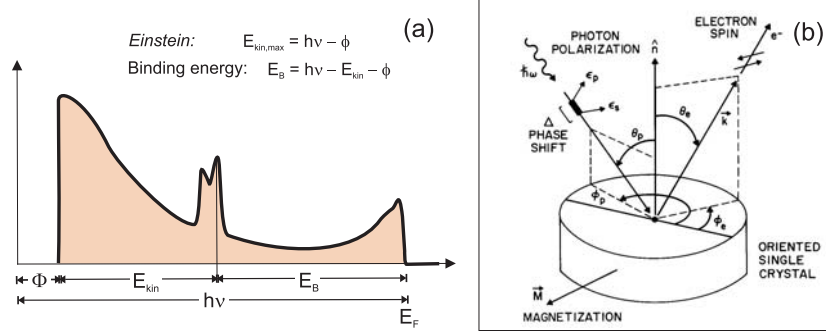


Figure 2.1: Schematics of a photoelectron spectrum (a) and of the experimental geometry (b).

Fig. 2.1.1b shows the geometry of a photoemission experiment which is complete in the sense that it can deliver all quantum numbers of the electron (constraints for the solid will be treated in sect. 2.4): The momentum is derived from the measurement of the angle of the emitted electron and of its kinetic energy and the spin can be detected as well. In addition, the polarization of the incoming light is marked as well as the magnetization axis in the case of a ferromagnetic sample.

2.2 Surface sensitivity

Photoelectron spectroscopy is a very surface sensitive technique since the escape depth of electrons is limited by inelastic scattering. The number of photoelectrons that leave the crystal depends exponentially on the thickness of the traversed film:

$$I = I_0 e^{-d/\lambda} \quad (2.2.1)$$

The parameter λ in eq. 2.2.1 is the inelastic mean free path (IMFP) of the electrons. The prime loss processes are excitation of electron-hole pairs and of plasmons. The dependence of the IMFP on the material and the kinetic energy of the electrons is described by a formula given by Seah and Dench [79S1]:

$$\lambda[\text{nm}] = 0.41 (a[\text{nm}])^{3/2} \sqrt{E[\text{eV}]} \quad (2.2.2)$$

where the material constant a denotes the size of the atoms in the traversed region and is defined independently of the crystal structure in ref. [79S1]. The dependence of λ on the energy leads to the so-called universal curve with reaches a minimum of about 2 ML around 50 eV above E_F .

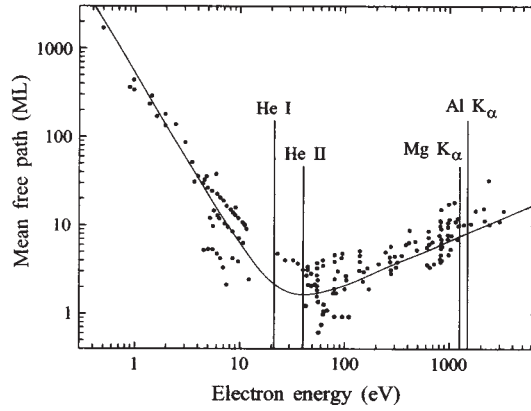


Figure 2.2: Inelastic mean free path of electrons as function of kinetic energy. Data points stem from different materials [79S1]. In addition, excitation lines from laboratory light sources are given.

2.3 Single-particle model of photoemission

Photoemission of an electron is a quantum mechanical transition from an occupied eigenstate (the initial state $|\psi_i\rangle$) to the final state $\langle\psi_f|$ of a quantum mechanical system. The transition rate between two eigenfunctions of the Hamiltonian H' is given by Fermi's golden rule

$$P_{fi} = \frac{2\pi}{\hbar} |\langle\psi_f|H'|\psi_i\rangle|^2 \delta(E_f - E_i - h\nu) \quad (2.3.1)$$

where the δ distribution guarantees conservation of energy and H' denotes the Hamiltonian for the interaction between electron with momentum operator $\mathbf{p} = -i\hbar\frac{\partial}{\partial\mathbf{r}}$ and vector potential of the electromagnetic radiation field \mathbf{A} neglecting higher order contributions (dipole approximation):

$$H' = \frac{e}{2mc} (\mathbf{A} \cdot \mathbf{p} + \mathbf{p} \cdot \mathbf{A}).$$

Considering the commutation relationship $[\mathbf{A}, \mathbf{p}] = -i\hbar\nabla\mathbf{A}$ and $\nabla\mathbf{A} = 0$ for a transversal field, this simplifies as

$$H' = \frac{e}{mc} \mathbf{A} \cdot \mathbf{p}.$$

Here, \mathbf{A} is assumed to be constant and fixed in space (for exceptions, see [79L1]), so that

$$P_{fi} \propto |\langle\psi_f|\mathbf{p}|\psi_i\rangle \cdot \mathbf{A}|^2 \delta(E_f - E_i - h\nu). \quad (2.3.2)$$

Applying the commutation relationship of $H = p^2/2m + V(\mathbf{r})$ with \mathbf{p} and \mathbf{r}

$$\langle \psi_f | [\mathbf{p}, H] | \psi_i \rangle = (E_i - E_f) \langle \psi_f | \mathbf{p} | \psi_i \rangle = -i\hbar \langle \psi_f | \nabla V | \psi_i \rangle$$

and with the equation $h\nu = E_f - E_i$ one gets a different form of the matrix element in eq. 2.3.2:

$$\langle \psi_f | \mathbf{p} | \psi_i \rangle = \frac{i}{\nu} \langle \psi_f | \nabla V | \psi_i \rangle$$

This shows that photoemission cannot take place in a potential $V(\mathbf{r}) = \text{const.}$ like the free electron gas. The solid provides for momentum conservation.

The simplest case in which photoemission occurs is a free-electron system bound by a potential barrier located at the site of the two-dimensional interface between the semi-infinite solid and vacuum. With \mathbf{e}_z as the unit vector normal to the surface one gets

$$\nabla V = \frac{\partial V}{\partial z} \mathbf{e}_z$$

and eq. 2.3.2 simplifies yielding

$$P_{fi} \propto \left| \langle \psi_f | \frac{\partial V}{\partial z} | \psi_i \rangle A_z \right|^2 \delta(E_f - E_i - h\nu). \quad (2.3.3)$$

This general-purpose approximation emphasizes the transition between the eigenstates $|\psi_i\rangle$ and $\langle\psi_f|$ of the solid. Besides the energy conservation, eq. 2.3.3 provides important symmetry conditions which will be described in sect. 2.6.

2.4 Angle-resolved photoemission

If we attribute single-crystal properties to the solid, then V becomes a periodic potential and the states ψ_i and ψ_f satisfy the Bloch condition. At the surface, the Bloch condition reads

$$\psi(\mathbf{r} + \mathbf{q}) = e^{i\mathbf{k}_{\parallel} \cdot \mathbf{q}} \psi(\mathbf{r}) \quad (2.4.1)$$

because strict translational symmetry holds only parallel to the surface (\mathbf{q} denotes a lattice vector in that surface). For the photoelectron, eq. 2.4.1 results in the conservation of the component of \mathbf{k} parallel to the surface \mathbf{k}_{\parallel} when passing through the two-dimensional surface barrier, however, plus or minus a reciprocal surface lattice vector \mathbf{G} [64K1]:

$$\begin{aligned} \mathbf{k} &= \mathbf{k}_{\parallel} + \mathbf{k}_{\perp} \\ \mathbf{k}_{i\parallel} &= \mathbf{k}_{f\parallel} \pm \mathbf{G} \end{aligned} \quad (2.4.2)$$

Therefore, $\mathbf{k}_{i\parallel}$ is known only in the reduced Brillouin zone if the wave vector outside of the solid \mathbf{k}^{ext} which we identify with \mathbf{k}_f can be determined. As the electron is free outside of the solid, its wave vector satisfies

$$|\mathbf{k}^{\text{ext}}| = \sqrt{\frac{2m}{\hbar^2} E_{\text{kin}}}$$

and we get its parallel component from

$$\mathbf{k}_{\parallel}^{\text{int}} = \sqrt{\frac{2m}{\hbar^2} E_{\text{kin}}} \sin \theta \quad (2.4.3)$$

$$\mathbf{k}_{\perp}^{\text{ext}} = \sqrt{\frac{2m}{\hbar^2} E_{\text{kin}}} \cos \theta. \quad (2.4.4)$$

Eq. 2.4.2 holds also for superlattices of steps or nanostructures and will become important in Chaps. 4 and 5. Note also that \mathbf{k}_{\perp} is not conserved due to lack of periodicity.

In the three-step model [64B1], the photoemission process is depicted in the band structure by a direct transition from an occupied initial state below E_F to an unoccupied final state above E_F with the energy difference between both determined by the photon energy as

$$E_f(\mathbf{k}^{\text{int}}) - E_i(\mathbf{k}^{\text{int}}) = h\nu. \quad (2.4.5)$$

Characterizing the transition as 'direct' or 'optical' implies that \mathbf{k}_{\parallel} as well as \mathbf{k}_{\perp} are conserved during the first step. The second step is the transport to the surface and allows for scattering effects through an IMFP λ . A consequence not considered in the model is the influence of λ on the conservation of \mathbf{k}_{\perp} on the way of the electron to the surface. If λ is much greater than the interplanar spacing, the coherence of excitations from different layers conserves \mathbf{k}_{\perp} . If, on the other hand, λ is of the same order of magnitude or less than the interplanar distance, a broadening of $\mathbf{k}_{f\perp}$ sets in. This will become important in sect. 3.3.

The one-step model treats the whole excitation starting from the initial state within the solid until the final state, which is located in the detector, on equal footing. The electron is, apart from inelastic scattering which determines the IMFP, also affected by elastic scattering which changes its angular distribution and this is considered identifying the photoemission final state $\langle \psi_f |$ with a time reversed low-energy electron diffraction (LEED) state [70M1]. On this basis, the one-step model of photoemission is especially suitable for the treatment of overlayers and layered compounds [74L1]. The effect of the IMFP is included by means of an optical potential and a complex \mathbf{k}_{\perp} .

However, the simplest and often sufficient approach to the final state is to assume a free electron final state and describing the ionic potential of the solid by an average V_0 providing

$$E_f = \frac{\hbar^2}{2m} \left(\mathbf{k}_{f\parallel}^2 + (\mathbf{k}_{f\perp}^{\text{ext}})^2 \right)$$

$$E_f + V_0 = \frac{\hbar^2}{2m} \left(\mathbf{k}_{f\parallel}^2 + (\mathbf{k}_{f\perp}^{\text{int}})^2 \right)$$

and thus

$$\mathbf{k}_{f\perp}^{\text{int}} = \sqrt{(\mathbf{k}_{f\perp}^{\text{ext}})^2 + \frac{2mV_0}{\hbar^2}}. \quad (2.4.6)$$

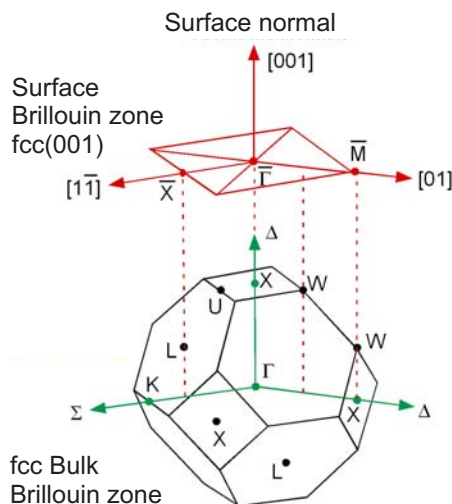


Figure 2.3: Bulk and surface Brillouin zones for the fcc lattice and its (001) surface.

V_0 can either be regarded as an adjustable parameter in a band mapping experiment or it can be taken as a value provided by theory, approximately as the zero of the muffin tin potential in an augmented plane wave band structure calculation.

How angle-resolved photoemission is applied for band mapping is seen from the following figures: Fig. 2.3 shows the Brillouin zone for the fcc lattice structure together with the projection onto the (001) surface. Photoelectrons from the bulk detected along the [001] surface normal will originate from the Γ X-direction of the bulk Brillouin zone. The band structure along this direction is displayed in fig. 2.4a for fcc Cu. Vertical arrows indicate possible direct transitions between an occupied initial-state band and an unoccupied final-state band with the arrow length corresponding to the energy of the incident photons. Varying the photon energy, a series of initial-state \mathbf{k} -vectors can be accessed as shown in the stack of angle-resolved photoemission spectra in fig. 2.4b. A large collection of experimental band structures has been measured in this way for various crystalline solids and can be accessed in the literature [89G1].

2.5 Bulk and surface states

Fig. 2.3 has already indicated the relationship between the volume Brillouin zone and the two-dimensional Brillouin zone of one of its possible surfaces. This picture shall be supplemented by the electronic states. Fig. 2.5 displays therefore a combination of bulk and surface band structures. At the left-hand side, the bulk band structure $E(\mathbf{k}_\perp)$ of Cu is displayed featuring two band gaps.

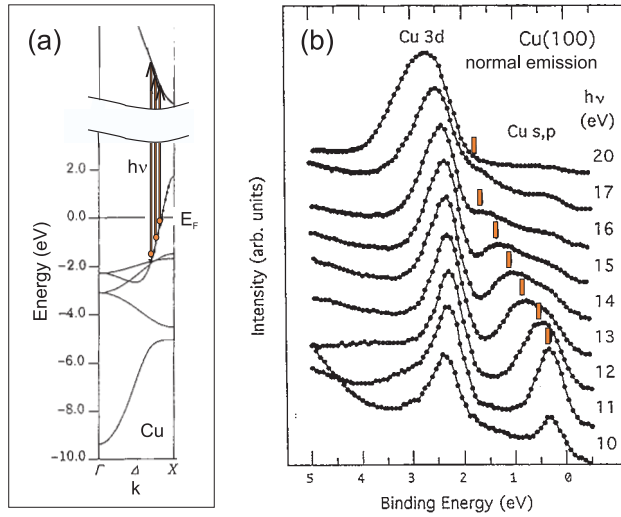


Figure 2.4: a: Band structure for fcc Cu. Vertical arrows indicate possible direct transitions. The bands are taken from ref. [93B1]. b: Angle-resolved photoemission spectra of Cu(100) in normal-emission geometry for various photon energies. The dispersion of an sp bulk band of Cu is sampled along the ΓX -direction.

The right hand surface shows a projection of the bulk bands along \mathbf{k}_\perp leading to a division of the two-dimensional surface Brillouin zone into regions degenerate with bulk states ("hatched" by narrow dispersions) and those where states are symmetry forbidden in three dimensions (white). Due to the broken symmetry at the crystal surface, this condition is relaxed and states may instead exist in two dimensions as surface states in the band gaps (squares). Outside of the gaps such state enters the bulk continuum for a certain value of \mathbf{k}_\parallel . The state mixes with degenerate bulk states and will still lead to an enhanced probability for electrons at the surface atoms. Such state is called a surface resonance, and the different decay of wave functions is depicted in fig. 2.6.

2.6 Symmetry and selection rules

In addition to energy and momentum, the symmetry of the electron wave function can be determined in a photoemission experiment. A crystalline surface is required and the detector must be situated in a mirror plane perpendicular to the surface. Both the final state and the total dipole matrix element in eq. 2.3.3 must be symmetric with respect to this mirror plane since an odd symmetry final state ψ_f as a continuous function has to have a point of zero in the mir-

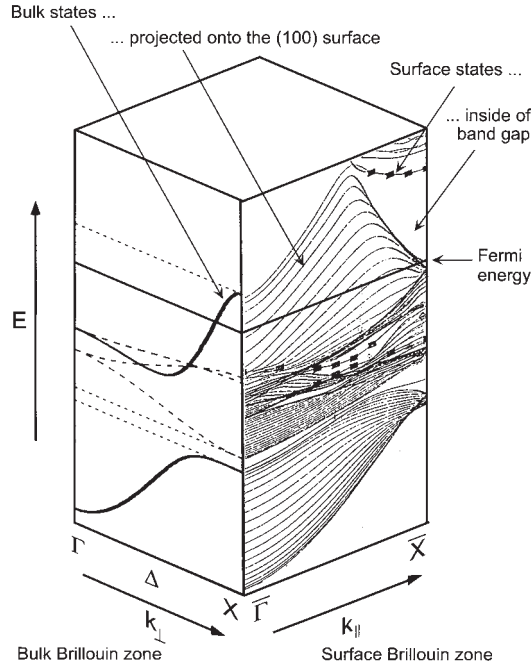


Figure 2.5: Cu bulk band structure projected onto the (100) surface. Two-dimensional surface states may form in the surface-projected forbidden bulk band gaps.

ror plane. This property of the final-state together with the polarization of the light enables the determination of the initial-state symmetry. If the polarization vector is in the mirror plane, the dipole operator $\mathbf{A} \cdot \mathbf{p}$ is even with respect to this mirror plane and the initial state must be even. If the polarization vector is perpendicular to the mirror plane, the dipole operator $\mathbf{A} \cdot \mathbf{p}$ is odd as is the initial state. The usual convention is s-polarization when \mathbf{A} lies perpendicular to the mirror plane which can be achieved by normal incidence; p-polarized light requires a polarization vector \mathbf{A} in the mirror plane.

For normal emission from cubic surfaces, tab. 2.6.1 from ref. [77H1] shows the dipole-allowed initial states. Similar tables for the more general case of off-normal emission can be found in ref. [80E1]. For hcp crystals see ref. [80B1]. For the (100) surface and purely s-polarized light only states of odd (Δ_5) symmetry are excited, a p-polarization component will excite even (Δ_1) symmetry states.

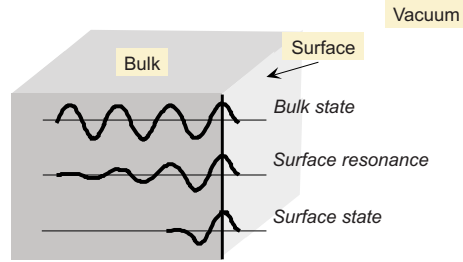


Figure 2.6: Sketch of the decay of wave functions into the bulk.

Crystal Face	Coordinate Axes			Irreducible Representations	Initial State Symmetry		
	x	y	z		$\mathbf{A} \parallel x$	$\mathbf{A} \parallel y$	$\mathbf{A} \parallel z$
(001)	[100]	[010]	[001]	$\Delta_1 \Delta'_1 \Delta_2 \Delta'_2 \Delta_5$	Δ_5	Δ_5	Δ_1
(110)	[001]	[1 $\bar{1}$ 0]	[110]	$\Sigma_1 \Sigma_2 \Sigma_3 \Sigma_4$	Σ_3	Σ_4	Σ_1
(111)	[$\bar{1}$ 10]	[$\bar{1}$ $\bar{1}$ 2]	[111]	$\Lambda_1 \Lambda_2 \Lambda_3$	Λ_3	Λ_3	Λ_1

Tab. 2.6.1. Dipole-allowed initial state symmetries for normal emission from cubic faces. With the z -axis in the direction of the surface normal the cases $\mathbf{A} \parallel x$ and $\mathbf{A} \parallel y$ correspond to s -polarized light, $\mathbf{A} \parallel z$ corresponds to p -polarization. From ref. [77H1].

2.7 Deviations from the single particle picture

Photoelectrons interact with other electrons of the system. It was mentioned in sect. 2.2 that inelastic scattering limits the IMFP of the photoelectron through excitation of electron-hole pairs and plasmons. This holds also for the hole created in the excitation process. When this hole is filled by another electron, a third electron can be excited to states above the Fermi level. This excitation leads to a line broadening of the initial state which can be accounted for by replacing the δ -function in eq. 2.3.3 by a Lorentzian.

In addition, the charge of the hole is screened by the remaining electrons. This leads to a lowering of the energy of the ionized system, and the measured binding energy shifts towards the Fermi level. Broadenings and shifts due to the coupling of the hole to the rest of the system can be described by a complex self energy $\Sigma_i(\mathbf{k}, E)$. The effects included in $\Sigma_i(\mathbf{k}, E)$ comprise, e. g., electron-electron and electron-phonon coupling.

The δ -function in eq. 2.3.3 is then replaced by the spectral function of the hole state $A_i(\mathbf{k}, E_f - h\nu)$. $A_i(\mathbf{k}, E_f - h\nu)$ is a function of quasimomentum \mathbf{k} and energy E like

$$A_i(\mathbf{k}, E) = \frac{1}{\pi} \frac{\text{Im}\Sigma_i(\mathbf{k}, E)}{(E - E_i(\mathbf{k}) - \text{Re}\Sigma_i(\mathbf{k}, E))^2 + (\text{Im}\Sigma_i(\mathbf{k}, E))^2}. \quad 2.7.1$$

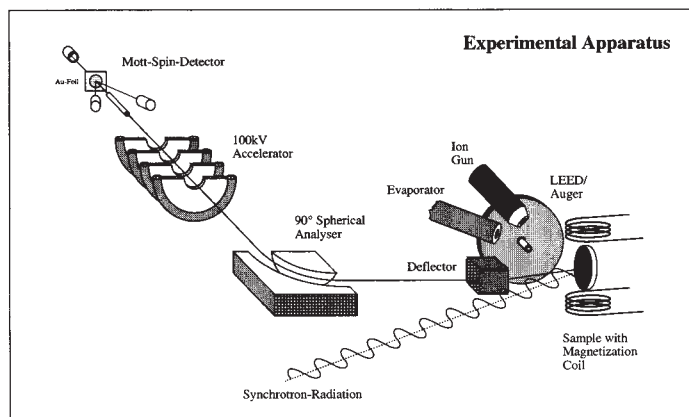


Figure 2.7: Apparatus for spin-resolved photoemission with cross-sectional view through analyzer and electron accelerator.

This function attains a maximum for

$$E(\mathbf{k}) = E_i(\mathbf{k}) + \text{Re}\Sigma_i(\mathbf{k}, E). \quad 2.7.2$$

The real part of the self-energy leads to a shift of the photoemission peak with respect to the single-particle energy, and the imaginary part causes a broadening. If eq. 2.7.2 has more than one solution, the solutions are divided up into main lines and satellite lines or the coherent and incoherent part of the spectrum, respectively. Increasing the electron correlation will transfer spectral weight from the coherent to the incoherent part.

2.8 Spin-resolved photoemission

The observable in a spin-resolved photoemission experiment is the electron spin polarization P which is defined as the expectation value of the Pauli spin operator σ :

$$P = \langle \sigma \rangle = \text{Trace}(\sigma \rho)$$

The spin polarization with respect to a certain direction, the quantization axis which is provided by the experimental setup, becomes

$$P = \frac{N^\uparrow - N^\downarrow}{N^\uparrow + N^\downarrow} \quad (2.8.1)$$

where N^\uparrow and N^\downarrow are the numbers of electrons with magnetic moments parallel to the given quantization axis and antiparallel, respectively.

P is typically measured by means of Mott scattering [85K1]. Mott discovered in 1929 that the spin dependent terms in the Coulomb scattering from

heavy atoms arise from relativistic L - S coupling and cause a left-right intensity asymmetry A [29M1]. In the apparatuses used in this work the photoelectrons are accelerated after having left the energy analyzer to about 100 keV and scattered off a thin Au foil target. Fig. 2.7 shows the apparatus. Two Si surface barrier detectors placed symmetrically at scattering angles of $\pm 120^\circ$ measure the intensities N_1 and N_2 respectively. The asymmetry A is defined as

$$A = \frac{N_1 - N_2}{N_1 + N_2}.$$

A is related to the polarization P in the axis perpendicular to that defined by both detectors. In our case the former is the vertical, so that in normal emission geometry the in-plane magnetization is probed. A depends on P like

$$A(P) = \frac{A_a + PS}{1 + A_a PS}$$

where S denotes the Sherman function which measures the efficiency of the spin analyzer and has a maximum for 100 keV electrons at a scattering angle of 120° . Multiple scattering effects decrease S , so that the finite thickness of the Au foil leads to $S \sim 0.2$ in the present apparatus. A_a is the apparatus asymmetry which is canceled out to a large extent by reversing the magnetization of the sample and taking for P the average of the measured asymmetries of both magnetization directions \bar{A} divided by the Sherman function:

$$P = \bar{A}/S$$

With the known (spin-integrated) spectrum $I_0(E_B)$ and the known polarization curve $P(E_B)$ one gets the spin-resolved spectra $I^\uparrow(E_B)$ and $I^\downarrow(E_B)$ from

$$I^\uparrow(E_B) = \frac{1}{2} I_0(E_B) (1 + P(E_B))$$

$$I^\downarrow(E_B) = \frac{1}{2} I_0(E_B) (1 - P(E_B)).$$

As for ferromagnets the number of photoelectrons with their magnetic moments aligned parallel to the magnetization direction predominates, $I^\uparrow(E_B)$ is called *majority spin* spectrum and $I^\downarrow(E_B)$ *minority spin* spectrum.

2.9 Magnetic x-ray circular dichroism

Faraday discovered in 1846 the change of the light polarization vector when the light is transmitted through a magnetic material [1846F1]. This is principally understood as the effect of dipole selection rules in interband transitions. Right and left circularly polarized light allows for transitions involving changes of the magnetic quantum number $\Delta m_j = +1$ and $\Delta m_j = -1$, respectively. In 1975, Erskine and Stern predicted for Ni a magneto-optical effect in the soft x-ray regime [75E1]. This effect leads to different absorption spectra depending

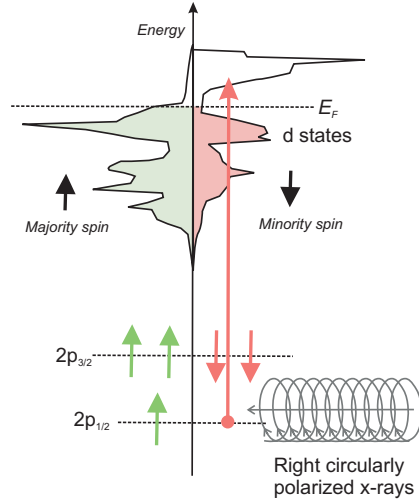


Figure 2.8: Principle of magnetic circular x-ray dichroism with schematic density of electronic states of Fe.

on whether the sample is magnetized parallel or antiparallel to the propagation direction of the circularly polarized light. The principle is depicted in fig. 2.8 for the L-edge of Fe. The density of d states is energetically split by the exchange interaction leading to a larger number of occupied majority spin states (left) than minority spin states (right). The process involves two steps: In the first step, the incoming right circularly polarized x-rays selectively excite an electron from the 2p level ($2p_{1/2}$ in fig. 2.8) into an unoccupied d level of the same spin. The spin-split d density of states acts like an 'analyzer' for these electrons based on the fact that more unoccupied states are available for minority spin electrons than for majority spin electrons.

Experimentally, this effect was at first proven for the K-edge of Fe [87S1] and later for the L-edge of Ni [90C1]. The method is based on absorption and is thus described by the sum over all transition probabilities given by eq. 2.3.1 and becomes therefore

$$\sigma(h\nu) \propto \sum_{\psi_f} |\langle \psi_f | \mathbf{A} \cdot \mathbf{p} | \psi_i \rangle|^2 \delta(E_f - E_i - h\nu). \quad (2.9.1)$$

The reason for the sensitivity to the electron spin is the following: Although the electric field does not interact with the spin (selection rule $\Delta m_s = 0$), the spin is coupled to the orbital moment through the large spin-orbit coupling in the 2p orbitals of the 3d transition metals. Fig. 2.9a shows the simple model given by Erskine and Stern, for the example of transitions from the $2p_{1/2}$ level. The widths of the connecting lines between initial and final states represent the transition probabilities. They require evaluation of the Clebsch-Gordan coefficients for the addition of angular momenta responsible, e. g., for

the relative strength of transitions $m_l = 1 \rightarrow m_l = 2$. The above model is simplified in so far as it considers spin-orbit splitting for the core levels only. This simplification leads, e. g., to an absorption cross section ratio of L_3 to L_2 edges of 2 : 1 and an MCXD cross section ratio of $-1 : 1$ both underestimating the experimental findings.

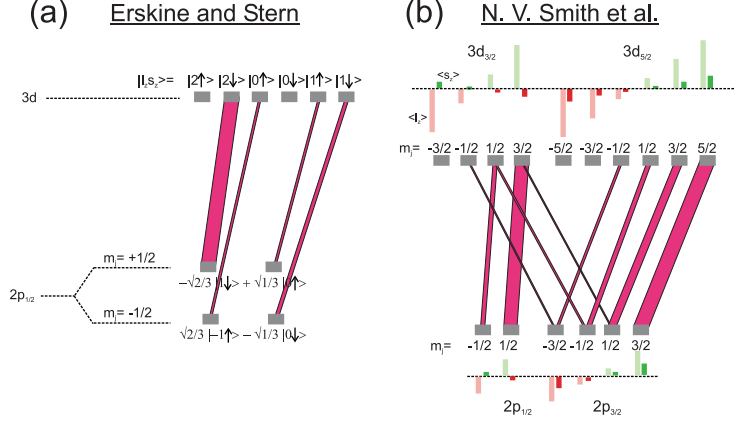


Figure 2.9: Model according to Erskine and Stern [75E1] (a) and model by N. V. Smith et al. [92S1] (b).

Smith et al. [92S1] have therefore derived a fully relativistic model which is shown in fig. 2.9b and gives more realistic ratios of the cross section between L_3 and L_2 edges.

The inherent element specificity has made MCXD a very successful method for magnetometry. This is due, in particular, to the derivation of sum rules to extract spin and orbital moments from MCXD spectra of the 3d metals [92T1,93C1]. Based on the notation used in fig. 2.10, the sum rules are

$$m_{\text{orb}} = -\frac{4 \int_{L_3+L_2} (\mu_+ - \mu_-) d\omega}{3 \int_{L_3+L_2} (\mu_+ + \mu_-) d\omega} (10 - n_{3d}) \quad (2.9.1)$$

for the orbital moment and

$$m_{\text{spin}} = \frac{6 \int_{L_3} (\mu_+ - \mu_-) d\omega - 4 \int_{L_3+L_2} (\mu_+ - \mu_-) d\omega}{\int_{L_3+L_2} (\mu_+ + \mu_-) d\omega} \times (10 - n_{3d}) \left(1 + \frac{7 \langle T_z \rangle}{2 \langle S_z \rangle}\right)^{-1}. \quad (2.9.2)$$

The operator $\langle T_z \rangle$ containing multipole contributions to the spin density can become important in systems of non-cubic symmetry. Ignoring this term, the sum rules become on the basis of the integrals in fig. 2.10

$$m_{\text{orb}} = -4q(10 - n_{3d})/3r \quad (2.9.3)$$

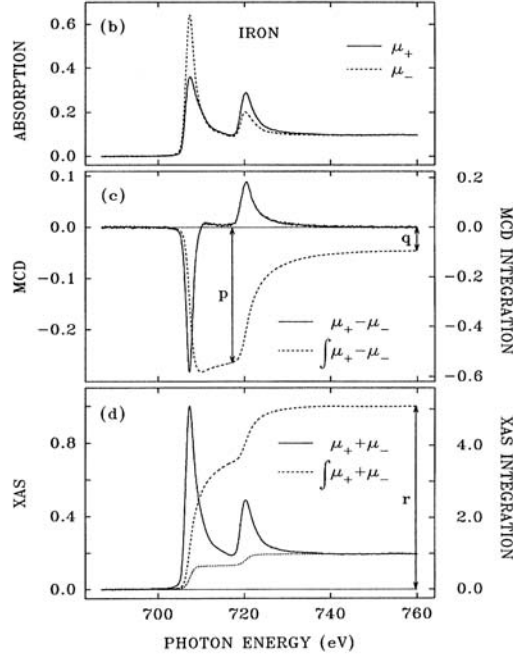


Figure 2.10: Application of the sum rules for the example of Fe. From ref. [95C1].

and

$$m_{\text{spin}} = -(6p - 4q)(10 - n_{3d})/r \quad (2.9.4)$$

and the ratio of orbital and spin moment can be calculated with

$$\frac{m_{\text{orb}}}{m_{\text{spin}}} = \frac{2q}{9p - 6q}. \quad (2.9.5)$$

For elements for which the 2p spin-orbit splitting is so small that L_3 and L_2 edges overlap in such a way that the evaluation of the integral $\int_{L_3+L_2} (\mu_+ - \mu_-)$ becomes ambiguous, the spin sum rule cannot be applied. This is the case with Mn [96T1].

Chapter 3

Quantization in ultrathin films

3.1 Evolution of the 3d electronic structure

This work treats a fundamental problem of low dimensional systems in an instructive way and for this reason is positioned at the beginning of the current compilation. It is generally accepted that for a two-dimensional film, the electron wave vector perpendicular to the film \mathbf{k}_\perp is not a good quantum number. Such two-dimensional film is ideally represented by an unsupported monoatomic layer. In reality, it needs to be placed on the flat surface of a single crystalline substrate.

Preparation with sufficient purity, in particular absence of residual gas contaminants, and calibration of the monoatomic layer thickness are experimental problems that for many systems have in recent years been overcome. A more fundamental problem is to preserve as far as possible the two-dimensionality of the electronic structure of the overlayer by the appropriate choice of a substrate that minimizes the electronic interaction across the interface. The first choice would be insulators or semiconductors because they reduce the interaction to a minimum for electrons near the Fermi energy, however, they tend to react strongly with transition metals leading to intermixing of atomic sites and ultimately to a destruction of the electronic as well as the geometrical two-dimensionality.

The use of noble metals as substrate materials can mean a way out of this problem since growth conditions are often fine with sharp interfaces and electronic interactions are limited to a low density of sp states from the Fermi energy to several eV below. Early experiments have shown, though, that the low surface energies of Ag and Au as compared to those of transition metals lead to surface segregation of these elements. This means, the monoatomic overlayer is covered by a considerable fraction of a monolayer of the substrate material producing at least partially a sandwich structure. Comparing the situation for

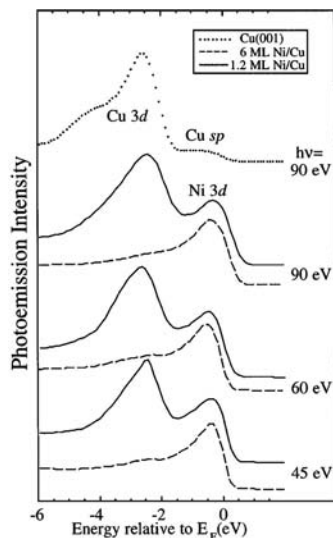


Figure 3.1: Angle-integrated photoemission spectra comparing 1.2 ML Ni/Cu(100) (dashes) to bulklike 6 ML Ni/Cu(100) (solid line) for various photon energies. It is concluded in ref. [97M1] that the d bandwidth is not narrowed for the monolayer as compared to bulk. From ref. [97M1].

room temperature, this effect is less pronounced for Cu than for Ag and Au. Cu has, therefore, often served as substrate for epitaxial growth. On Cu(100), monolayers and bulklike films of Co, Ni, and the peculiar fcc structure of Fe have been stabilized.

As these systems are rather well established model systems, it was more than surprising that for 1.2 ML Ni/Cu(100) a bulklike electronic structure was observed [97M1]. More precisely, two findings were reported in ref. [97M1]: (i) The bandwidth of Ni d states was found to be the same as in bulk Ni. This can be seen in fig. 3.1 where the Ni d contribution to the spectra is marked. (ii) The photoelectron angle distribution (PEAD) pattern showed a strong dependence on the photon energy. The apparatus used in ref. [97M1] is one of a few electron spectrometers worldwide that deliver not only one angle resolved photoemission spectrum at a time but a whole distribution of angles at a given kinetic energy, translated, as usual, into a certain binding energy. The energy chosen in ref. [97M1] is the Fermi energy. The observed changes with photon energy took the authors to the conclusion that the electrons at E_F in 1.2 ML Ni, which for all practical purposes can be identified with the Ni monolayer, show a dispersion with \mathbf{k}_\perp in analogy to the well-established method to obtain bulk band structures introduced in fig. 2.4. The effect in the PEAD is indeed impressive. Fig. 3.2a shows the variation of the PEAD for the three-dimensional Cu(100) substrate with completely different patterns appearing at 45, 60, and

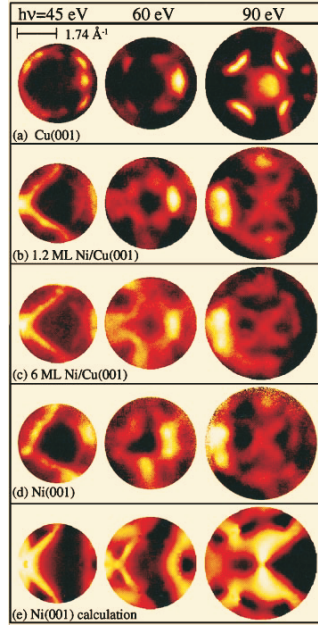


Figure 3.2: Angle distribution of photoelectrons from the Fermi energy. The variations of the monolayer pattern (b) with the photon energy is interpreted as a three-dimensional behavior of electrons at E_F . From ref. [97M1].

90 eV photon energy. In part b of the figure, the pattern for 1.2 ML Ni does also change with photon energy. In part c, the third remarkable observation is made in so far as the PEAD pattern of 1.2 ML Ni and its photon-energy dependence equal the ones of a bulklike 6 ML Ni film. (A thickness of 6 ML is usually considered a good approximation to the three-dimensional bulk when d states of 3d transition metals are referred to.)

We have at first attacked the problem by Ni-thickness dependent measurements, i. e., we produced different thicknesses by successively increasing the Ni coverage. We assume that a bandwidth extracted from angle-*integrated* photoemission is ill defined because the weight of different emission angles is unclear and the spectra undergo strong broadening. The occupied d bandwidth is therefore better defined as the lowest energy of d states. In order to ensure that photoemission transitions from this band are symmetry allowed and therefore appear in the spectra, the transition and critical point should be defined. As we compare a Ni monolayer to Ni bulk, we have to chose appropriate conditions valid for both. These conditions are firstly the center of the surface Brillouin zone, $\bar{\Gamma}$, defined by normal electron emission, and secondly the center of the bulk Brillouin zone, Γ , selected through the proper \mathbf{k}_\perp at $h\nu = 43$ eV. These conditions are realized in fig. 1 of Paper I where one can in fact distinguish very different critical point energies for 1.2 ML and for bulklike 6 ML. (In addi-

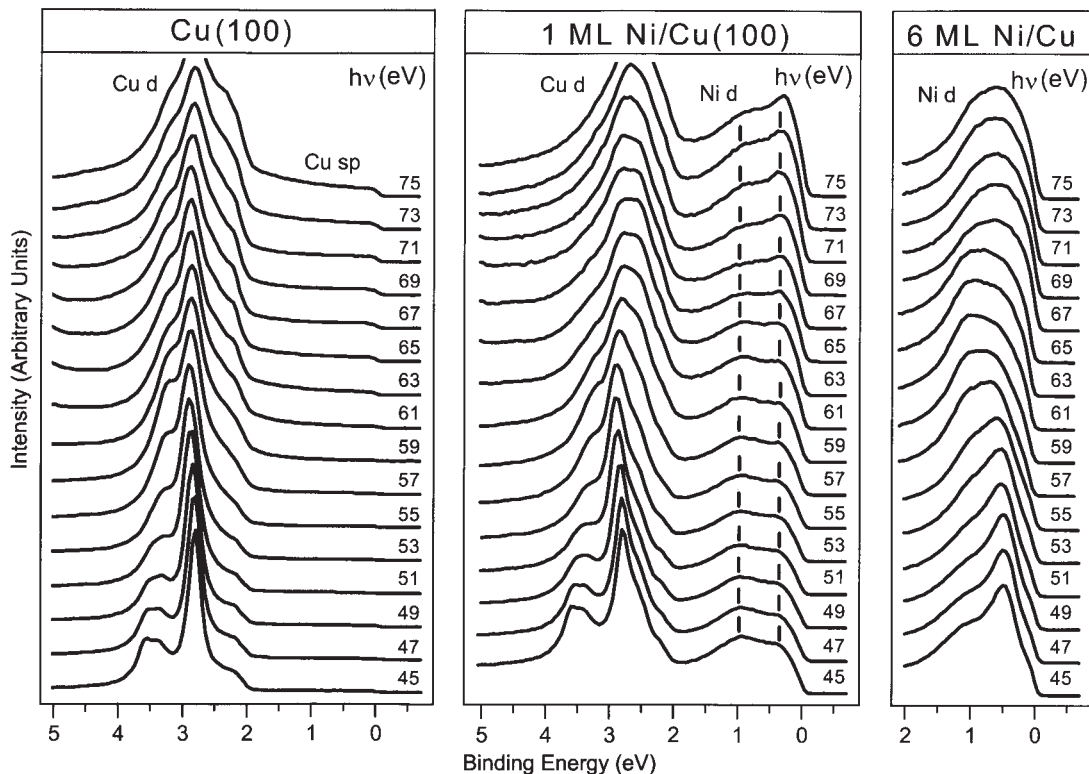


Figure 3.3: Photoelectron spectra in normal emission for 45 to 75 eV photon energy. The d states of bulk Cu and bulklike Ni strongly disperse with \mathbf{k}_\perp whereas d states of the Ni monolayer stay at fixed binding energies. The electronic structure of the Ni monolayer is therefore not three-dimensional.

tion, there appears even another submonolayer coverage, 0.4 ML, with distinct spectrum.)

This is direct proof that the occupied d bandwidth is very different for the monolayer and for bulk. This is no unexpected outcome since the absence of next neighbor atoms generally leads to a band narrowing. For the Ni atom in the monolayer there are no neighbors towards vacuum and no transition-metal neighbors towards the substrate. In the main part of Paper I, comparisons to calculated band structures for bulk Ni and 1 ML Ni/Cu(100), which fortunately are available in the literature, are conducted to ensure that the measured transitions are indeed representative of the d bandwidth. This comparison becomes more complicated because d electrons in Ni are strongly correlated (sect. 2.7). In photoemission, the correlation in Ni reduces measured binding energies by about 30% as has been tested for various critical points in bulk Ni. It is assumed

that the value 30% is valid for the monolayer as well and has been used in the present comparison.

In fig. 2 of Paper I, the evolution of the d states with thickness is compared for different systems, and qualitatively the same behavior is found for overlayers of Ni, Co, and Cu. An additional narrowing occurring just between 1 and 2 ML was interpreted as due to even and odd symmetry states reversing their energetic order. This was, to our knowledge, never noted before.

Now we turn to the second problem, the three-dimensionality claimed in ref. [97M1]. The dependence of photoemission spectra on the bulk wave vector \mathbf{k}_\perp is shown in fig. 3.3 from unpublished data. The photon-energy dependence in normal emission is compared for Cu(100), 1 ML Ni/Cu(100), and bulklike 6 ML Ni/Cu(100). Both the d states of Cu (left) and the bulklike Ni film (right) show a substantial dispersion with photon energy. The monolayer spectra (center) show the Cu 3d dispersion from the underlying substrate together with two nondispersing peaks of the Ni monolayer between 1 eV binding energy and the Fermi level. This shows that \mathbf{k}_\perp is not a good quantum number and that the electronic structure of the Ni monolayer on Cu(100) is not three-dimensional.

In spite of these clear data, it is not yet established how the authors of ref. [97M1] arrive at their very different conclusions. During the review process of Paper I, we were urged to make a commitment concerning this question, and we suggested a slight overestimation of the thickness by 1 ML in ref. [97M1]. It is, however, also possible that other effects play a role. In a new paper [2003G1], the authors of ref. [97M1] claim that final states effects dominate the PEAD. While data and model calculations appear not very convincing in ref. [2003G1], it is generally likely that such effects play a role in the case of 1.2 ML Ni/Cu(100). Ref. [2003G1] tries to illustrate this, however, solely for a bulklike film of Co/Cu(100) and without any comment concerning the dimensionality of the Ni monolayer.

3.2 Ni/Cu/Ni spin valve structures

While remaining with the Ni/Cu(100) system, the present paragraph leads us to an example for explicit quantization of electronic states and their changes for various film thicknesses. In other words, the increase of the width of the potential well is directly visualized by different energy eigenvalues for each new quantization condition, i. e., each additional monolayer like in fig. 1.2.

In the following we introduce the context and the motivation of Paper II: According to most definitions, a spin valve means a GMR element like a trilayer or multilayer as shown in fig. 1.4. At the time of Paper II, quantum-well state formation was already observed in photoemission and inverse photoemission from other combinations of transition metals and noble metals such as Cu/Co(100), Co/Cu(100), and Fe/Cu(100) [92O1,93O1]. Therefore, quantum-well detection in Cu/Ni(100) or Ni/Cu(100) (fig. 2a and b, respectively, of Paper II) would by itself not have been a surprise. The point of Paper II is instead the exploration of double layers, and the study was motivated by two observations:

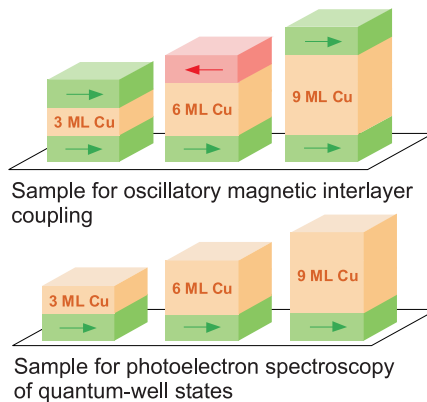


Figure 3.4: Comparison of the samples for the analysis of the magnetic coupling and of quantum-well state formation.

The first one is connected to the magnetic interlayer coupling, e. g., the coupling between Co or Ni layers separated by a Cu spacer. The oscillation of the coupling with increasing spacer was generally accepted, and it was shown that it is connected to quantum-well states [9201,93O1,93G1,93C2]. The spin polarization of quantum-well states at E_F had been measured [93C2,93G1], however, the argumentation had one problem: To detect the sp states in photoemission, one cannot afford to cover the surface by a transition-metal overlayer several monolayers thick because this would suppress the emission from underneath and contribute a high spectral weight of d states from the cap layer. This is seen in sect. 3.1. An additional reason why a magnetic cap layer was avoided in spin resolved measurements [93C2,93G1] was that the measured spin polarization should unambiguously be assigned to electrons of the Cu and induced polarization should be excluded. (A very small polarization [$< 0.05\mu_B$] has indeed been measured by MCXD for Cu 3d states at the ferromagnetic interfaces of a Co/Cu multilayer [94S2].)

For these two reasons, the comparison between quantum-well states (their period, phase, spin polarization) and the magnetic interlayer coupling had always been one between a bilayer (mainly Cu/Co) and a trilayer (Co/Cu/Co) system (fig. 3.4). It was clear from the description by the phase accumulation model [94S1] that the phase shift upon electron reflection at the film-substrate interface follows a complicated energy-dependent behavior and, moreover, is different from the one at the film-vacuum interface. This knowledge is prerequisite for relating the measured spin polarization (majority or minority) to the measured coupling (parallel or antiparallel) in the trilayers.

The second question was whether quantum-well states would not only form in the nonmagnetic spacer layer but also in the ferromagnetic cap layer. At the

time of Paper II, an additional modulation of the magnetic interlayer coupling as a function of the thickness of the ferromagnetic layer had just been found experimentally [92C1,93B1], and theoretically [94B1] the question was posed whether this new observation would stay consistent with the quantum-well model.

For this study it was crucial that the spectra do not become dominated from d emission of the transition metal. It is essential to use inverse photoemission to probe the unoccupied states because the d shell of the ferromagnetic transition metals is more than half filled. Ni has the highest filling, consequently it contributes the least d emission to the unoccupied states, more precisely: it contributes only minority spin states ('strong ferromagnet').

Paper II answers the first question in the following way: Very large phase shifts are observed. When looking at fig. 3c of Paper II and comparing 5.9 ML Ni/9 ML Cu/Ni(100) to 9 ML Cu/Ni(100), we can see that at a given binding energy of, e. g., 1 eV the spectral shape changes from a peak to a valley and back to a peak. This means that the phase shift induced by the extra magnetic layer on top can easily reach 2π .

The second problem has a surprising result. The extra Ni layer changes the spectra in a similar way as an equivalent coverage of Cu would do. This means that quantum-well states form throughout the double layer and that they consequently possess both Ni and Cu character. This explains the influence of the *ferromagnetic* layer thickness on the magnetic coupling and supports the quantum-well model.

3.3 Rare-earth metal: Gd/W(110)

Quantum-well state formation has been observed in a large number of metallic layer systems combining noble metals, transition metals, alkali metals, sp-metals, and rare-gas layers. Some of these transition metals are magnetic and some serve as interlayers where quantum-well state formation can profoundly affect the magnetic structure in a multilayer as explained in chap. 1.

The simplest interlayer-coupling system Co/Cu/Co is described on the basis of quantization of sp-electrons of Cu as mediators of the magnetic coupling between 3d electrons in the Co. In this sense, the description is analogous to the RKKY model of magnetic transition-metal impurities in noble metals. The oscillatory character of the RKKY interaction extends, however, in three dimensions from a given impurity and leads to magnetic frustration. Loosely speaking, a so-called 'frustrated' magnetic moment receives contradictory information from various nearest moments concerning its energetically preferred direction. This energetical degeneracy typically results in a wealth of effects of 'frozen' magnetic configurations termed 'spin-glass behavior'. In a simplified picture (which is inferior to the quantum-well picture when it comes to quantitative statements), the interlayer coupling is indeed the one-dimensional case of the RKKY interaction along the film normal [95B1].

Based on this analogy, the question for quantum-well states in rare earths is straightforward. The magnetic structure of rare earths is based on the same

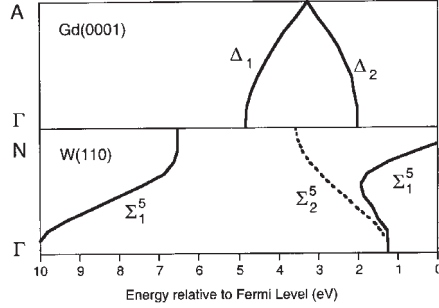


Figure 3.5: Bulk band structures along the growth direction [110] for W and [0001] for Gd after refs. [87G1] and [94N1], respectively. The Gd states appear inside of a bulk band gap of the W.

RKKY physics, however, unlike magnetic 3d impurities in noble metals, the RKKY model describes in rare earths the interaction of magnetic moments in localized but open 4f orbitals. The interaction is mediated by delocalized 5d6s electrons in the valence band. Thus, the difference is that in diluted magnetic alloys the conduction electrons are part of the noble-metal host whereas the magnetic 3d orbitals are localized at the impurity sites. The rare-earth metals consist of only one element with 4f magnetic moments and 5d6s delocalized conduction electrons on each atomic site and consequently there is no structural disorder and frustration effects are not expected.

The magnetic structure of elemental rare earths is very rich with ferromagnetism, antiferromagnetism, helical structures and phase transitions between them while the valence band structure is qualitatively very similar among the rare earths distinguishing basically only between divalent and trivalent rare earths. As the electronic structure of the valence band determines the magnetic structure, the analysis of quantized valence-band states can possibly clarify the electronic origin of the magnetic structure of the rare earths. This task, however, cannot be achieved immediately. The reason is that the RKKY interaction depends on the oscillation period at the Fermi energy. Epitaxial growth of rare earth films has to date only been reached along the hcp [0001]-direction. The Gd quantum-well films were grown with this orientation along which the Gd bulk bands do not cross E_F as band structure calculations show.

Fig. 1 of Paper III shows the first quantum-well states observed for a rare earth. The W(110) has a large band gap extending from -6.3 to -2.0 eV (3.5) (the shoulder seen at -3.3 eV does not count since it is not due to a direct transition but assigned to a high density of states). The adsorption of Gd is first seen from emission from Gd 4f states at -8.3 eV. The Gd 4f are half filled in the ground state ($4f^7$), and the peak at -8.3 eV is an unresolved multiplet of the $4f^6$ final state (7F). The binding energy shift from -8.3 to -8.05 eV indicates roughly the completion of the first adsorbed Gd monolayer. We will

return to this point further below.

In the present context, the prime aspect of the valence band structures of Gd and W is that fact that the band gap of the W enables confinement of electrons in the Gd overlayer because at these energies they do not find states to occupy in the W substrate. For the method of photoelectron spectroscopy, this has the additional advantage that no intensity from direct transitions will contribute to the spectrum which facilitates the observation of new, overlayer-induced states. Inside of this gap characteristic sharp peaks are seen. In fig. 1 of Paper III this is best seen between 2 and 3 ML and between 3 and 4 ML coverage. It was not possible to form distinct peaks above 3.7 ML nominal coverage. This difficulty can be understood considering that the quantum-well peaks in fig. 1 appear only after annealing to 650 K, and it is known that above this temperature the Gd film breaks up into clusters on top of a Gd monolayer. This means that Gd grows on W(110) in the Stranski-Krastanov growth mode and layer-by-layer growth is only metastable [96T2].

The energy positions of quantum-well peaks in fig. 1 of Paper III stem from a model calculation. The 'phase accumulation model', originally developed to describe surface states [85S1] gives a good description of the energies of quantum-well states [94S1]. It is based on the Bohr-Sommerfeld quantization rule

$$\Phi_B + \Phi_C + 2ka_0N = 2\pi n \quad (3.3.1)$$

which describes the phase shifts accumulated when an electron is reflected at the surface (Φ_B), the interface between film and substrate (Φ_C), and during propagation through the film ($2ka_0N$, where a_0 is the thickness of one monolayer and N the number of monolayers). For formation of standing waves, the total phase accumulated must be an integral multiple of 2π . Besides k , also Φ_B and Φ_C are energy dependent and eq. 3.3.1 allows for an instructive graphical solution displayed in fig. 2 of Paper III and used in fig. 1.

As the energies of the quantum-well states asymptotically approach critical-point energies of the bulk band structure, they can be used to determine the Gd bulk band dispersions. This is particularly useful for Gd for which the band structure was controversial: From measurements on bulk Gd following the classical method of fig. 2.4 it was concluded that the bandwidth of Gd is only about half of the one predicted from local density theory [92K1]. This would mean that the Gd 5d states are strongly correlated — a very unusual result with serious consequences for the magnetism of the rare earths. At the time of Paper III, it had just been shown by spin-resolved photoemission [2001M1] that the peak assignment in ref. [92K1] is incorrect. The reason is the small IMFP of electrons in rare earth. This leads to a reduced probing depth which affects \mathbf{k}_\perp as quantum number. A strong \mathbf{k}_\perp -broadening is the result and complicated lineshapes in the spectra [2001M1] which can lead to erroneous assignments. The electronic structure of the quantum-well system, instead, is two dimensional and does not depend on \mathbf{k}_\perp . Therefore, the reduced probing depth is unimportant resulting in relatively sharp peaks in fig. 1 of Paper III. This gives us also the opportunity to determine the Gd band width for the first time: The 5d band

of Gd extends from -1.8 to -4.6 eV according to the quantum-well experiment which compares favorably to the calculated dispersion from -2.0 to -4.9 eV in local density theory [94N1]. The 5d states in Gd are therefore not strongly correlated.

After the appearance of Paper III, some corrections have been made based on the more accurate work presented in sect. 5.2. The spectrum assigned to 1 ML has been reassigned based on several repetitions of the thickness-dependent measurements. In this first work, the thickness calibration was only based on the evaporation rate as measured with an oscillating quartz microbalance. The shift of the W 4f peak to lower binding energy was found to be in agreement with the transition from the first to the second monolayer. However, the thickness differs depending on whether substrate or adsorbate units are used [86K1] and the shift of W 4f is more precisely related to a transition from the 5×2 to the 5×3 structure with accompanying compression of the Gd layer. This compression starts at 0.7 ML and is already completed for 1 ML. This recalibration does not change the integral number of layers and the assignment of the quantum-well peaks since this it depends only on the integral number of layers. The states near E_F assigned to W in fig. 3 of Paper III had tentatively been called 'interface states' because they could neither be explained by Gd states nor by direct transitions of the W substrate. They are now considered to be nondirect transitions of the umklapp type like most other peaks discussed in chap. 5.2. This assignment remains consistent with the observation made in fig. 3 of Paper III that similar peaks appear for 1.2 ML Ag/W(110) as well.

Chapter 4

Quantization at stepped surfaces

4.1 W(331): Initial- or final-state effects?

It is a natural wish to use the experience gained with quantization in two-dimensional films to explore the one-dimensional case and find out whether the concepts for electron scattering, confinement, and quantization will hold for nanostructures at surfaces as well.

Scanning tunneling microscopy (STM) has taken the lead showing that manipulation by an STM tip is a possible way to arrange atoms into nanostructures. Secondly, the electronic quantization effects resulting from the nanostructuring could also be picked up by the same instrument. Fig. 4.1 shows the fascinating 'quantum corrals' from refs. [93C3,2000M1]. The STM is spectroscopically tuned to a surface state in a bulk band gap of Cu(111) the identification of which on pure Cu by photoemission is shown in fig. 4.2. The electrons occupying this surface state undergo scattering at the adsorbed Fe atoms, and build up an interference pattern of standing electron waves.

By angle-resolved photoemission, no similarly exciting achievements related to nanostructures have been published to date. The method of angle-resolved photoemission can resolve the electron wave vector \mathbf{k} and as such requires a periodic repetition of the respective nanostructure at the surface. This means angle-resolved photoemission studies the behavior of the electron whereas STM yields a density of states or a topography. By means of angle-resolved photoemission, it is possible to distinguish electrons with momentum parallel to a given obstruction at the surface from those with a 'head-on' trajectory. Secondly and more trivial, photoemission as a nonlocal probe requires a certain area density of nanostructures in order to obtain a sufficient signal-to-background ratio.

The simplest surface to fulfill this requirement is a pure stepped surface, and vicinal W(110) surfaces have been studied in Paper IV. Fig. 4.3 shows one of the samples used in Paper IV. Historically, stepped metal surfaces were stud-

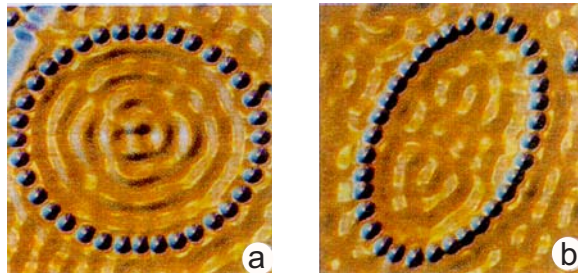


Figure 4.1: 'Quantum corrals' from ref. [2000M1]. STM probes surface-state electrons of Cu confined within a nanostructure of adsorbed Fe atoms.

ied because of their catalytic properties and angle-resolved photoemission was applied early on. It was shown that stepped Au(112) with (111)-terraces gave similar spectra for emission along the terrace-normal direction as from a flat Au(111) crystal [79H1]. Ref. [79H1] did not consider the behavior of possible surface-localized states. The first time that a behavior different from the terrace-orientation of ref. [79H1] was reported, was when electrons were found extended across the macrosurface of vicinal Cu(111) [88S1]. The basis for the conclusion of ref. [88S1] was the \mathbf{k} -vector dependence of inverse photoemission perpendicular to the steps which showed an orientation of $E(\mathbf{k})$ dispersions relative to the macrosurface. The next remarkable results were the finding of a switchover from terrace-localized to macrosurface-extended behavior for a certain step width for vicinal Cu(111) surfaces [2000O1] and lateral quantization on vicinal Au(111) [2001M2]. The remarkable result of lateral quantization in angle-resolved photoemission, manifested as two discrete energies [2001M2], was an awaited result since STM spectroscopy had already been able to demonstrate confinement and quantization of surface state electrons on vicinal Ag(111) [98B1].

All of the above photoemission and STM papers sampled the same surface state which exists on fcc noble metals along the [111] surface normal. It is sometimes referred to as the 'L-gap surface state'. This state extends energetically only down to 0.4 eV which limits the band structure effects one can possibly observe and/or requires high energy resolution.

The motivation for the present experiment is twofold: Firstly, we want to understand under which condition one-dimensional behavior occurs and under which condition two-dimensional behavior. Two suggestions have been made in connection with the data from the L-gap surface state on vicinal Cu and Au: In ref. [2000O1] the step width for which the transition from step-localized to macrosurface-localized behavior occurs, 1.7 nm, was compared to typical scattering lengths but a conclusion could not be presented. In ref. [2001O1], a more precise reasoning was given based on the projection of the confining bulk band gap onto the macrosurface and its location in the \mathbf{k}_\perp -direction.

The generality of these assumptions can only be tested on a broader basis including different systems. With vicinal W(110) surfaces, we chose such sys-

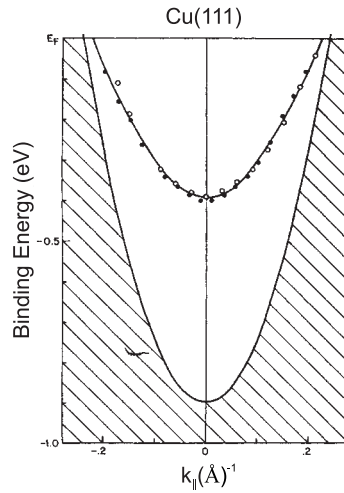


Figure 4.2: E vs. \mathbf{k} dispersion from a Cu(111) surface state based on photoemission data [83K1]. This state is probed in fig. 4.1.

tems that hold the potential of serving as practical templates for nanostructure growth since W(110) is a versatile substrate for epitaxial growth of metals. For the time being, electrons occupying surface states at stepped surfaces can be considered a representation of electrons in nanostructures. Gap properties of W(110) and their role for quantum-well states have been discussed in sect. 4.1, and this gap is potentially important for the observation of electronic states at the steps. Assuming that electron quantization in nanostructures on stepped substrates will rely on the confinement conditions provided by the substrate, surface-state confinement will be decisive for the tailoring of the electronic properties of nanostructures.

The experiment comprises angle scans in the directions parallel and perpendicular to the steps. The paper begins with a comparison of normal emission spectra of flat W(110) [fig. 2a of Paper IV, bottom] with W(331) [fig. 2a of Paper IV, red spectrum] with the result that a new peak 'S' appears at 0.8 eV too low binding energy on W(331) where 'too low' means that 'S' appears inside of the forbidden gap.

Comparison of a large number of data shows that this is the result of a doubling of one band between 4 and 6 eV. This band is probably a surface state or resonance split off from the W(110) bulk band gap of approximately the same shape. [This is the typical case of a Tamm-type surface state not yet identified on W(110).] Its identification may have been hindered in the past by the energetic vicinity of typical contamination peaks of W around 5 to 6 eV.) In \mathbf{k} -space, the two bands are shifted by a value corresponding to $\frac{1}{6}\overline{\Gamma\Gamma'}$ which is equal to the periodicity of the superlattice of steps (fig. 4 of Paper IV). This

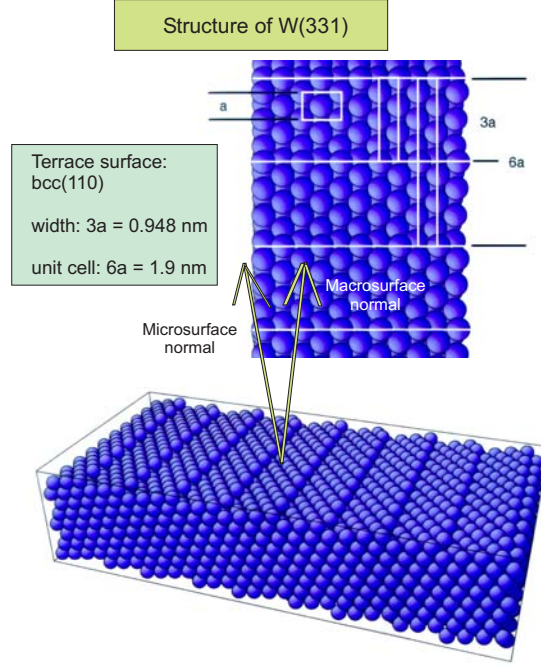


Figure 4.3: Geometry of W(331) with (110)-oriented terraces.

is confirmed by experiments on W(551) with a 10-fold periodicity in the LEED (implying a shift by $\frac{1}{10}\overline{\Gamma\Gamma'}$). From the appearance of more than two branches for W(551) ($\mathbf{G}_{551} = 0.40\text{\AA}^{-1}$) in fig. 4 of Paper IV it is concluded that the effect is rather a periodicity than a splitting: The periodicity \mathbf{G} relates to the one of the step lattice through

$$\mathbf{G} = 2\pi/L \quad 4.1.1.$$

where L is the step width. This is obtained from a construction of the reciprocal surface lattice, and another simple reasoning is taking the separation in \mathbf{k} -space between the centers of the first and second Brillouin zone for flat W(110), $\overline{\Gamma\Gamma'} = 4.0\text{\AA}^{-1}$, and relating it to the measured periodicity in the LEED:

$$\mathbf{G}_{331} = \frac{1}{6}\overline{\Gamma\Gamma'} = 0.66\text{\AA}^{-1}$$

$$\mathbf{G}_{551} = \frac{1}{10}\overline{\Gamma\Gamma'} = 0.40\text{\AA}^{-1}$$

This is the same periodicity regardless whether the effect is an *initial state* effect in the repeated zone scheme or a *final state* effect in the umklapp picture of eq. 2.4.2. The difference between the two is obvious. In the three-step model

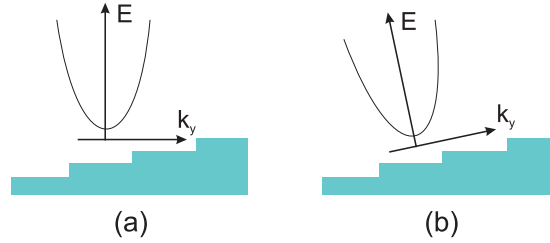


Figure 4.4: Comparison of $E(\mathbf{k})$ dispersions for microsurface (a) and macrosurface (b) orientation of the electronic wave function.

of photoemission (sect. 2.4), \mathbf{G} enters already in the first step in case an initial-state superlattice effect is present whereas it is only part of the third step in case scattering at the superlattice occurs during the photoemission process. This is the second question to be clarified in Paper IV.

Thanks to emission from the bulk bands, the terrace-normal direction is known with good accuracy, given by the lowest band in fig. 3c ($h\nu = 125$ eV) and fig. 4 ($h\nu = 105, 110,$ and 125 eV) of Paper IV. It is seen that the features 'S' and 'S*' are split symmetrically around the $[110]$ microsurface normal. In figs. 3 and 4 of Paper IV, \mathbf{k}_{\parallel} is already related to the microsurface through eq. 2.3.3. Therefore, the position of the macrosurface normal depends on the photon energy, and for selected photon energies of 50, 62.5, and 105 eV, the $[331]$ macrosurface normal is given in fig. 4b. It is obvious that neither 'S' nor 'S*' are related to the macrosurface. This means that condition 'a' rather than condition 'b' of fig. 4.4 applies.

The consequence is that the electron wave function is not two-dimensionally extended across the step superlattice. This means the repetition of the band 'S' can only be a final state effect. Assignment to a final-state scattering effect is indeed supported by the pronounced intensity behavior when the energy is changed. The data, shown in fig. 3 of Paper IV, reveals that this behavior is similar for the photoemission experiment and for LEED. When only one parabolic dispersion can be observed in photoemission ($h\nu = 62.5$ eV), there is practically also only one in the LEED.

It should be mentioned that in the description of the final-state effect, there is a problem with the position of the split bands. To realize this problem, we take again advantage of the deep bulk band which marks the microsurface normal for 105, 110, and 125 eV photon energy. It is seen that no emission of the new features occurs along the microsurface normal, for none of the photon energies studied. This means the branches are shifted by $\pm \frac{1}{2}\mathbf{G}$ which is not identical to the umklapp condition eq. 2.4.2. To realize this, one may consider band 'S' on flat $W(110)$ (fig. 4a of Paper IV) as initial state and try to describe its disappearance by eq. 2.4.2.

Therefore, a new model will be required to understand photoemission data from stepped $W(110)$. Such description must also explain why band 'S' is af-

fects by final-state effects and others are not. The proper description is the one given by Henzler for LEED of stepped surfaces [76M1]. Splitting in the LEED occurs for the antiphase condition of scattering from neighboring microspheres. This is the N-point of the bulk Brillouin zone of W from which band 'S' is split off. The deep bulk band, instead, stems from the Γ -point and is not split.

Last but not least, the reasoning of ref. [2002M1] should be tested. Ref. [2002M1] defines as condition for one-dimensional behavior of the L-gap surface state on vicinal Cu(111) that the cutoff angle of the surface is small enough that the macrosurface projected band gap does not close in on the surface state. Ref. [2002M1] relates the size of the band gap parallel to the surface, k_{gap} , to the location of the gap in the k_{\perp} -direction, which in the present case is the N-point, $k_{\text{N}} = 1.4 \text{ \AA}^{-1}$. It is practically a rotation of the gap given by k_{gap} around the center of the bulk Brillouin zone, Γ , with the aim to find the angle θ where the projected gap vanishes. For Cu(111), this happens already for the small angle of 7° . For the present case holds

$$\theta = \tan^{-1}(k_{\text{gap}}/k_{\text{N}}). \quad 4.1.2$$

If we evaluate k_{gap} near the energetic middle of the gap, e. g., at 5 eV below E_{F} , we obtain $k_{\text{gap}} = 0.42 \text{ \AA}^{-1}$ and $\theta = 16^\circ$. This means that for crystals cut by less than 16° , the wave function for surface state electrons in the gap would remain microsphere localized or one-dimensional.

This means vicinal W(110) and the surface state 'S' identified are very well suited for future studies of lateral quantization effects. Moreover, electrons in nanostructures to be grown on top will benefit from the same one-dimensional confinement conditions. Support for the notion that one-dimensional confinement is rather the rule than the exception comes recently also from STM. Ref. [2003H1] analyzed the electronic structure of individual wide terraces on vicinal Cu(111) and investigated the likelihood of two-dimensional superlattice effects. The authors observe that singularities which formerly had been interpreted as due to gap formation caused by the step superlattice are instead a local property of the microsphere [2003H1].

4.2 Monoatomic Co and Cu wires

In Paper V, we move on from a clean stepped surface to so-called step decoration. The basic principle of step decoration is the step-flow growth mode for metal adsorbates on metal substrates. This growth mode has been demonstrated, e. g., for Cu/Mo(110) [89M1] and one can hope to create a complete atomic wire of an adsorbate at the step edges. A strong effect on the electronic structure must occur for the monoatomic wire due to lacking neighbor atoms, and it should be possible to distinguish the monoatomic wire from the complete monolayer. The complete monolayer shall be represented by 1 ML stripes which can be prepared on the same stepped substrate.

The first demonstration of a different electronic structure for a monoatomic wire and a complete monolayer was performed by inverse photoemission in ref.

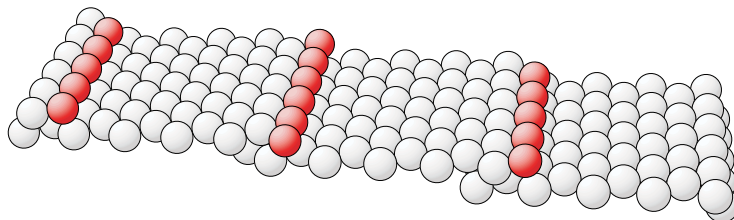


Figure 4.5: Geometry of 0.12 ML Co/Pt(997).

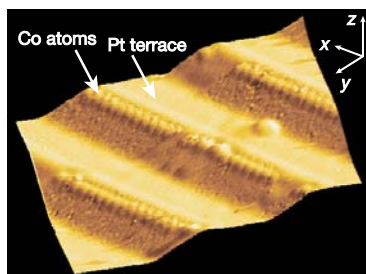


Figure 4.6: STM topograph of Pt(997). The surface has a 6.45° miscut angle relative to the (111) surface. Monoatomic chains of Co decorate the Pt step edges. The coverage is 0.13 ML. The step width and interchain spacing is 20.2 Å. From ref. [2000G1].

[94H1] for Cu on W(331). An energy shift by 0.3 eV between an adsorbed Cu chain corresponding to $\frac{1}{6}$ ML Cu and the full monolayer coverage was found [94H1]. To identify the chain contribution, difference spectra had to be used. While the results appear credible, the identification relied largely on difference spectra, and the comparison to $\frac{1}{6}$ ML Cu on flat W(110) suffered from negative contributions in difference spectra.

The idea of Paper V is to use a substrate for which the chain growth is characterized at atomic resolution. Secondly, magnetic and nonmagnetic chains shall be compared.

At the EPF Lausanne, growth of atomic chains of Cu, Ag, and Co on Pt(997) had been characterized with He atom scattering and STM [2000G1,2000G2]. A collaboration with the EPF enabled an experiment on the same Pt(997) substrate characterized in refs. [2000G1,2000G2] with its highly regular step superlattice with a miscut angle of 6.45° and 20.2 Å terrace width (fig. 1 of Paper V, figs. 4.5 and 4.6). Spectroscopically, the Pt substrate offers perfect conditions for determining the electronic properties of adsorbates and nanostructures. The reason is the behavior of the photoionization cross section with the photon energy, depicted for the atomic case in fig. 4.7b. The valence band of Pt is formed by 5d electrons the cross section of which assumes a Cooper minimum around 200 eV photon energy. Taking into account the cross section for Cu 3d and Co

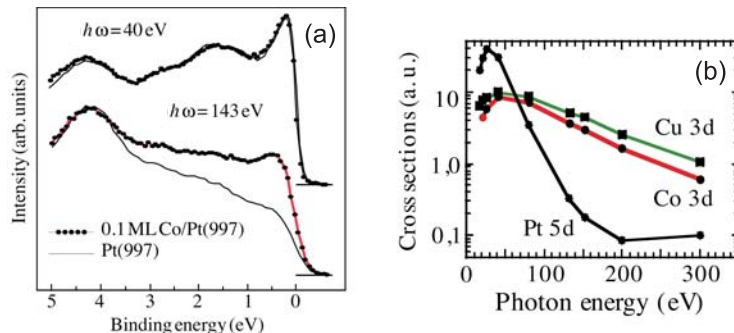


Figure 4.7: Angle-resolved photoemission spectra of 0.12 ML Co/Pt(997) at photon energies of 40 eV and 147 eV (a). The calculated atomic photoionization cross section for Pt 5d [85Y1] varies strongly between these energies (b).

3d orbitals, it is seen that Cu and Co are favored above 100 eV. The effect is impressive.

Fig. 4.7 displays the same low Co coverage, 0.12 ML (fig. 4.5) at 40 eV and 147 eV photon energy. While at 40 eV, spectra with and without the Co atoms are identical, at 147 eV intense emission from Co can be distinguished. For intensity reasons at the W/U undulator beamline at BESSY I, fig. 3 of Paper V shows spectra at $h\nu = 122$ eV which offers inferior 5d suppression but better statistics than 147 eV. It is known from the characterization that 0.12 ML corresponds to an atomic chain of Co or Cu at each step edge of the Pt(997). Below 0.1 ML Cu, it can be observed that a single Cu 3d state develops at 2.3 eV binding energy. As a noble metal, Cu does not contribute any d states near E_F . Above 0.17 ML, the Cu 3d states shift to higher binding energy. This shift reflects the change in dimensionality due to extra Cu neighbors.

The behavior is somewhat different for Co. Fig. 3b of Paper V shows that below 0.4 ML, spectral intensity grows at two energy positions: ~ 2.4 eV and ~ 0.3 eV. This is identified as the magnetic exchange splitting between majority- and minority-spin states of the Co and is strong indication for the presence of at least a local magnetic moment of the Co chain on Pt(997).

With increasing coverage it is observed that the energy separation between these two features decreases slightly. This is better seen from the spectrum in fig. 4 of Paper V where the clean Pt spectrum has been subtracted. The exchange splitting of the Co chains is with ~ 2.1 eV larger than the one measured for monolayer Co which is between 1.4 and 1.9 eV [92C2,90S1] and for bulklike Co films (1.4 eV [94A1]). This behavior reflects, in a band picture, the narrowing of electronic bands for reduced dimensionality followed by an increase in the exchange splitting. Starting out from the atom, it means that the magnetic moment of Co ($3d^7$ configuration) of $3 \mu_B$ is consecutively reduced by adding Co neighbors down to the Co bulk value of $1.7 \mu_B$.

The confirmation of the assignment to a pair of exchange split states would

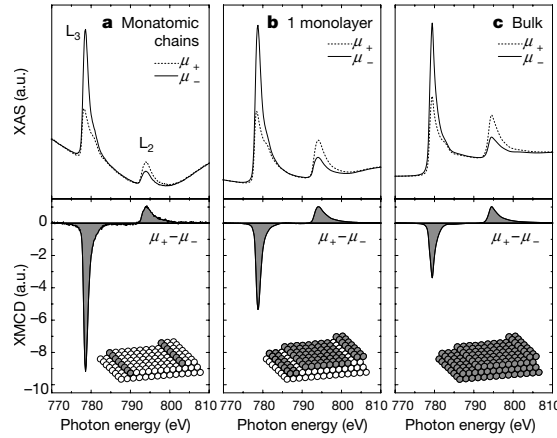


Figure 4.8: Magnetic circular x-ray dichroism measurement from ref. [2000G1]. One-dimensional ferromagnetism is proven for the first time. The orbital moment of the single atomic chain is strongly enhanced with respect to the one of the monolayer and of bulk Co.

require spin-resolved photoemission. We have cooled the sample to ~ 100 K but did not observe any spin polarization indicating that the ferromagnetic ordering temperature T_C is below 100 K. This statement is limited to magnetization axes in plane, parallel and perpendicular to the step direction. For geometrical reasons, an out-of plane magnetization could not be tested.

After these studies, Gambardella et al. have verified ferromagnetic order below $T = 15$ K using magnetic circular x-ray dichroism at the ESRF [2002G1]. Fig. 4.8 shows the result for the single atomic chain, the monolayer and thick Co/Pt(997). The enhancement of the magnetic moment was found to be much stronger for the orbital moment which was with $m_L = (0.68 \pm 0.05) \mu_B$ five times larger than for bulk Co. The magnetization follows a strong uniaxial anisotropy with a cosine-type behavior in the plane perpendicular to the wire axis with a maximum at 43° . The anisotropy provided by the Pt(997) substrate is obviously sufficient to create one-dimensional ferromagnetism which, on the other hand, is not possible in one- or two-dimensional isotropic Heisenberg models, according to Mermin and Wagner [66M1].

4.3 Carbon nanostripes

In Paper VI, we conclude the transition to the full monolayer coverage on top of a regular step lattice. In sect. 4.1 the regime for which electron states show one-dimensional localization was already increased in \mathbf{k} -space and in energy with respect to the studies of fcc noble metal (111) vicinals in the literature

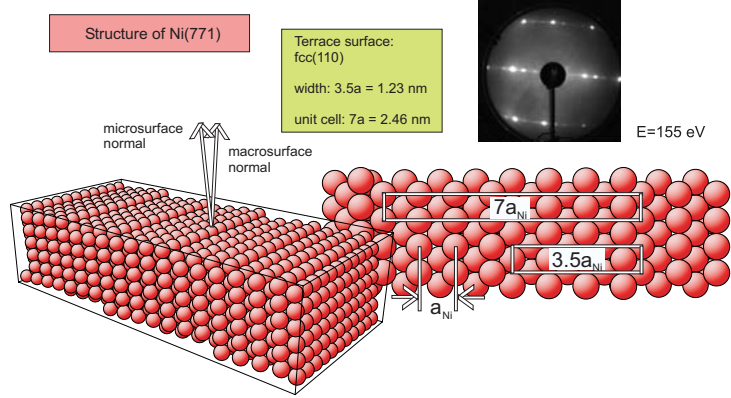


Figure 4.9: Geometry and LEED of Ni(771).

which are limited from E_F to 0.4 eV — the bottom of the surface state band. Energetically, about 2 eV were reached through the gap conditions on vicinal W(110) in Paper IV, and in the present chapter it shall be attempted to impose the step character onto the complete occupied valence band of a monoatomic overlayer.

As overlayer, graphene (monolayer graphite) was chosen because interlayer bonding in graphite is so weak that the electronic structure is considered two-dimensional even in the bulk. Graphitization of Ni can be achieved by a catalytic reaction involving the heating of Ni under a partial pressure of 1×10^{-6} mbar of carbon-containing gases like propylene. The electronic structure of graphene on flat Ni has already been studied by angle-resolved photoemission and serves as reference for the current experiment. The occupied width of the valence band is ~ 20 eV.

The experiment consists, like the one in sect. 4.1, of the emission-angle dependence of photoemission spectra for \mathbf{k} -vectors parallel and perpendicular to the steps or stripes. A photon energy of 50 eV was chosen for which the Ni(771) substrate displays featureless spectra (apart from the vicinity of E_F) across the whole range of angles presented here. For this reason, it is not needed to produce any difference spectra. The electron analyzer (Scienta SES200 type) enables parallel detection and readout of a range of emission angles $\sim 7^\circ$ wide. Therefore, manual rotation of the angle between analyzer and sample is limited to choosing appropriate ranges with sufficient overlap for verification purposes. The benefit can be seen in fig. 4.10 which shows the upper range of the valence band comprising the graphene π -states. For \mathbf{k} -vectors parallel to the stripes, a single sinusoidal dispersion of π -states is seen. In the perpendicular direction, in contrast, there are two π -bands of similar intensity shifted against each other in \mathbf{k} -space. This data from Paper VI constitutes the first observation of a split

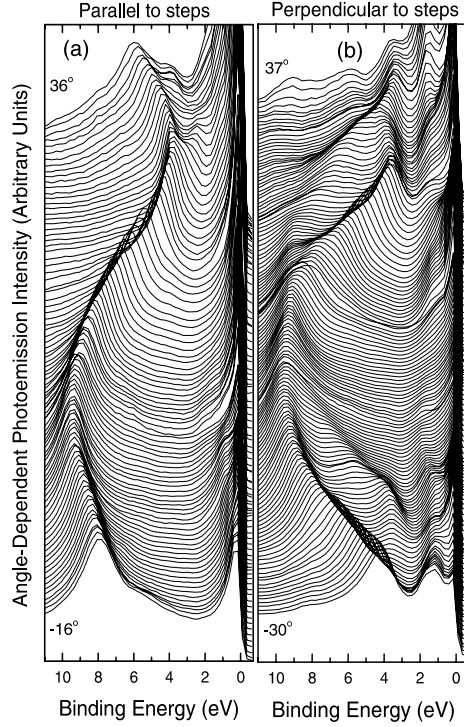


Figure 4.10: Angle-resolved photoemission spectra for carbon nanostripes on Ni(771). A doubling of the band dispersion occurs for \mathbf{k} -vectors perpendicular to the stripes. The step superlattice is imposed onto the entire graphene band structure.

dispersion due to a step superlattice together with the independently published splitting of the L-gap surface state near E_F on vicinal Cu(111) [2002M1] which is, due to the limited energy range of 0–0.4 eV, of minor clarity.

The results obtained can further be analyzed with the help of the $E(\mathbf{k})$ dispersions plotted in figs. 3 and 4 of Paper VI. It is seen that $\mathbf{G} = 2\pi/L$ is fulfilled with $L = 12.3$ Å being the step width of Ni(771). Like in sect. 4.1, this raises the question for an initial- or a final-state effect as origin.

The argumentation in favor of an umklapp-like final-state effect is based on two observations: Firstly, one of the two dispersions is centered around the terrace normal, i. e., the [110]-direction, as seen in fig. 4 of Paper VI. This means a behavior like in fig. 4.4a. An initial-state superlattice effect requires itinerance of the electrons across the steps, and the wave function must therefore be a Bloch wave of the macrosurface. No indication for such behavior, ideally depicted in fig. 4.4b, can be found. Secondly, there appear gaps in one of the dispersions, most clearly seen at $2\mathbf{G} = +1.0$ Å⁻¹ in fig. 4 of Paper VI. This gap could be due to Bragg reflection at the step superlattice. However,

testing the dispersion for various photon energies produces a different result. The background is that for an electronic system which is of dimensionality two (or lower), $E(\mathbf{k})$ dispersions measured for different photon energies must be identical according to eq. 2.4.3. While the bands perfectly match between 40 and 90 eV photon energy (fig. 5b of Paper VI), the gap displays a shift with photon energy (see arrows in fig. 5b). This is indication for a final-state effect bearing some similarity to the vanishing of branch S^* in sect. 4.1.

Chapter 5

Quantization in self-organized nanostructures

5.1 Spin-polarized quantum-wire states

When repulsive forces act between adsorbate atoms, this may lead to the formation of a superstructure. If the substrate possesses a rectangular surface unit cell like (110), ordering into chains appears possible. Such a system has been characterized for Au/Ni(110) using STM [95P1]. At low Au coverages, the formation of a Au/Ni surface alloy is observed, even though Au is immiscible with bulk Ni at room temperature. At a critical Au coverage of 0.4 ML, a 'dealloying' phase separation is observed during which 0.16 ML Au 'pop' out of the alloyed surface layer and form Au chains along the [001]-direction. These chains have a characteristic longitudinal superstructure of alternating Au dimers and trimers which is arranged in a zigzag shape. This is seen in fig. 5.1.

The motivation for the work was the fact that a one dimensional dispersion for an atomic wire had never been measured before. The only references were a clean stepped Cu(100) surface (10° miscut and ~ 10 Å terrace width) where \mathbf{k} -resolved inverse photoemission had shown the dispersion of an image-potential induced surface state [94O1]. This dispersion was flat perpendicular to the steps and parabolic in the parallel direction.

A measurement of the one-dimensional dispersion of a metallic wire had, on the other hand, been reported neither for the unoccupied nor for the occupied states and it was possible that the coherence of available stepped substrates was insufficient. The self-organized growth of Au/Ni(110) promises a complicated but very coherent geometrical structure. As in sect. 4.3, the Ni gives a relatively featureless photoemission spectrum at appropriate photon energies and is therefore spectroscopically well suited as substrate for quantum wires.

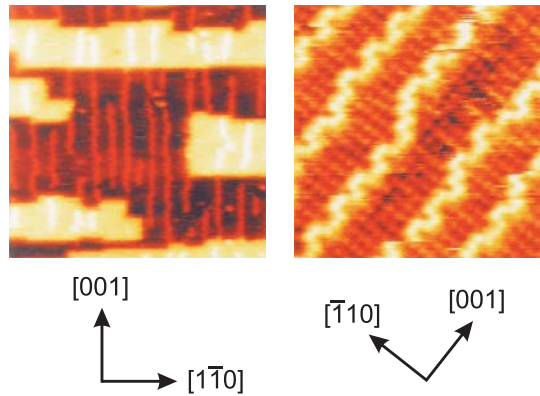


Figure 5.1: STM characterization of Au chains on Ni(110) after ref. [95P1]. The chains possess a zigzag structure and are formed by dealloying. The different islands on the left-hand side consist of a Au-Ni surface alloy and the Ni atoms replaced by the alloying, respectively.

Au as chain material offers the possibility to study both dispersions of weakly dispersive but intense 5d states and of strongly dispersive but weak 6sp states and both can be used to cross check the results.

Fig. 2 of Paper VII shows the thickness dependence of photoemission spectra in normal emission. One can distinguish three stages which agree very well with the STM characterization of ref. [95P1]: Stage I is the surface alloying and shows two characteristic Au 5d peaks. It is known that a certain amount of Au atoms stays alloyed at all stages, therefore we must expect these peaks to contribute to the spectra also for higher Au coverages. Stage II is the 'dealloying' occurring above 0.4 ML. An additional Au 5d feature grows at lower binding energy and becomes sharp and intense at 0.6 ML. At this coverage, there appears also a new peak in the range of sp states as marked in fig. 2. The behavior of this peak will be studied to greater detail. Stage III is the coalescence of the Au adsorbates leading finally to three-dimensional growth.

Figs. 5.2 and 5.3 show the measurement principle and the result, respectively, for Au chains formed at 0.6 ML. It is seen that for \mathbf{k} -vectors perpendicular to the chains the sp-derived peak stays at constant binding energy whereas it shows a parabolic dispersion in the parallel direction. This is the behavior expected for a one-dimensional quantum wire.

It was not immediately clear why such pronounced one-dimensional dispersion occurs for sp states which can easily mix with those of the Ni substrate. To this end, a first-principles band structure calculation has been conducted by our collaborators from Jülich. The result is that a bulk band gap in the energy range of the sp band of the chains enables the electron confinement perpendicular to the surface.

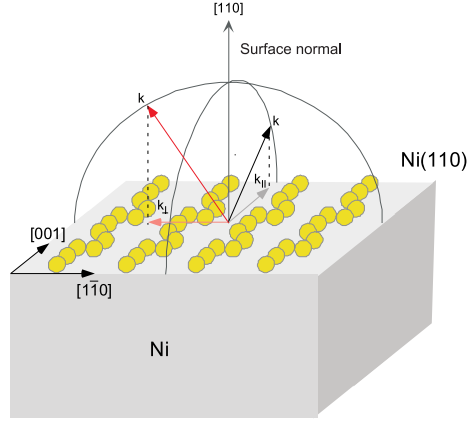


Figure 5.2: Measurement of one-dimensional dispersion by angle-resolved photoemission.

An interesting consequence exists due to the fact that bulk band gaps in Ni are spin polarized: By analogy to magnetic quantum-well systems in two-dimensions, one could expect a spin polarization also for the electrons in the Au chains on Ni(110).

Spin-resolved photoemission at -8° off-normal emission, where the quantum-wire peak is strong, reveals indeed a minority spin polarization (fig. 4 of Paper VII). This polarization, the sign of which agrees with the calculation, does not mean that the Au chain is magnetic but that the confinement of sp electrons in the Au chain depends on their spin. Accordingly, majority-spin electrons can easier scatter into the Ni substrate while minority-spin electrons are stronger confined to the one-dimensional chains. This is to be seen in full analogy to the magnetic quantum-well systems in two-dimensions like Co/Cu/Co(100) (fig. 1.5).

The last observation concerns the broadening seen in the spectra around -8° , and $+8^\circ$. This broadening resembles a splitting into two peaks. The simplest explanation is a connection to the zigzag structure of dimers and trimers along the chains. The periodicity is 3 Ni lattice constants which means an extra critical point is expected for $\pm 8.3^\circ$ for measurements at 22 eV photon energy. The agreement with this estimation makes it very likely that the broadening or splitting is indeed caused by Bragg reflection at this longitudinal superlattice.

Parallel to the publication of our work, a second observation of a one-dimensional dispersion of quantum wires has been published [99S1]. In ref. [99S1], Au chains were deposited on stepped Si. The authors of ref. [99S1] observe a one-dimensional dispersion and a splitting into two peaks as well. In contrast to us, they assign the split peaks to the dispersions of spinon and holon quasiparticles, respectively. The separation into spin and charge excitations is expected for strictly one-dimensional metals in the framework of Tomonaga-Luttinger theory. In later studies of Au/Si, the splitting has been traced back to

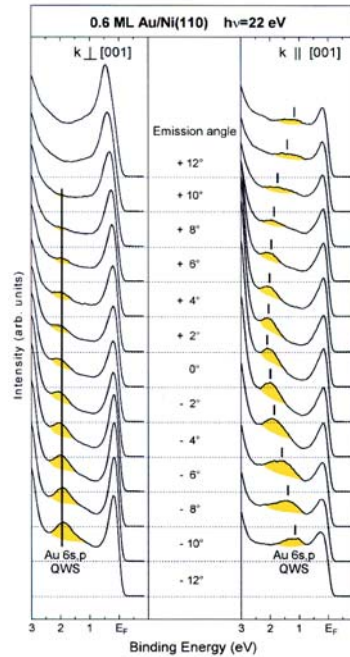


Figure 5.3: One-dimensional dispersion of Au chains on Ni(110).

conventional origin of a pair of bonding and antibonding states [2001L1,2003A1].

5.2 An elastic "sieve" in k-space: Gd/W(110)

There is one parameter which has not been explored yet in the band structure measurements of one-dimensional systems, namely the superlattice constant. In analogy to the thickness dependence of two-dimensional films, varying the spacing between chains should lead to observable effects on the electronic structure. While separated chains should display one-dimensional behavior, the dispersion may become increasingly more two-dimensional when the chains are moved together increasing the overlap of wave functions.

If confinement of electrons between chains can be achieved, changing the chain-chain separation will modify quantization conditions. The spectrum must show characteristic quantum-well peaks as a function of submonolayer coverage.

While the spacing of Au chains on Ni(110) can to a certain extent be varied by the coverage, a system with a stronger repulsive interaction was chosen for the present experiment. When rare earths like Gd are adsorbed on W(110), charge transfer from the Gd to the W occurs. This charge transfer leads to the formation of a strong dipole oriented perpendicular to the surface. This dipole is, e. g., responsible for the substantial lowering of the work function of W upon

Gd adsorption by 2 eV.

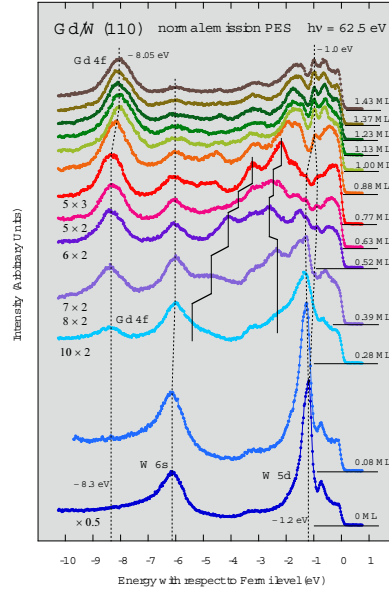


Figure 5.4: Angle-resolved photoemission spectra in normal emission of Gd/W(110). The spectral shape changes strongly in the submonolayer range of Gd coverage.

In the lateral direction, the strongly repulsive dipole-dipole interaction causes a series of superstructures of submonolayer rare earths. These structures have been characterized by LEED and Auger electron spectroscopy in ref. [86K1]. Although ref. [86K1] is very detailed, not all of the structures identified could be presented as original LEED pictures, possibly due to the simultaneous presence of more than one superstructure. Therefore, the confirmation of the structural models by STM was very important [97P1]. As predicted, up to a coverage of 0.7 ML, the Gd atoms form chains along $[1\bar{1}0]$ which approach each other with increasing Gd deposition. The interatomic spacing along the chains, i. e., their lattice constant, remains thereby constant. This is shown in fig. 1 of Paper VIII.

For the photoemission experiment, the band gap properties of the W(110)

substrate are exemplified in fig. 3.5: Between 2 and 6.3 eV binding energy an even-symmetry bulk band gap extends which is responsible for confinement and quantization in thicker films of Gd (Paper III), Au [93K1,2002S1], and Ag [2002S2].

In fig. 5.4 the Gd thickness dependence is shown up to 1.43 ML. At the bottom, the clean W(110) spectrum at 62.5 eV photon energy is shown, known from sect. 4.1. For the same coverage when the first Gd deposition is witnessed from the growth of the Gd 4f peak at 8.3 eV, shoulders appear at 5.4 and 2.3 eV. The shoulder at 5.4 eV moves towards E_F with increasing coverage. Practically every deposition step in fig. 5.4 creates a completely new spectrum. Such behavior has previously only been seen for monolayer coverage increments in two-dimensional quantum-well systems. The associated superstructures are labeled in fig. 5.4 up to 5×2 for which the interatomic spacing along the chains still remains constant. For coverages above 0.7 ML, the Gd lattice becomes close packed, and the Gd 4f peak successively shifts. We conclude that its final position at 8.05 eV marks the completion of the monolayer.

Similar as in sect. 4.2, we try to enhance the relative contribution from the adatoms to the spectra in order to assign the new features. Rare earths open up a particular pathway due to the localization of the (unoccupied) 4f orbital. The method is resonant excitation of a Gd 4d core electron into an unoccupied Gd 4f state. The decay of the 4d core hole leads to enhanced emission from occupied Gd 4f and 5d states. The enhancement of the Gd 4f emission is by a factor of 20. We have chosen two photon energies, 145 and 147 eV, below the maximum of the resonance (~ 149 eV). These photon energies are reasonably close to each other in order not to change the conditions for direct transitions of the W too much and still reach to an enhancement of the Gd 4f by a factor of 3.7.

Fig. 3 of Paper VIII shows the result. For each deposition step, spectra at 62.5, 145, and 147 eV are presented. The area between the spectra at 145 and 147 eV corresponds to the Gd 5d partial density of states. It is seen that none of the new features marked by ticks in fig. 5.4 is due to Gd.

If the structures are due to the W substrate, they may still be either initial- or final-state effects. It cannot be denied that the appearance of the spectra in fig. 5.4 bears a reminiscence of $E(\mathbf{k})$ band dispersions. How important final-state scattering effects at one-dimensional superlattices are, has already been shown in sect. 4.3 for graphene/Ni(771) and in sect. 4.1 for W(331) and W(551) where the \mathbf{k} -dependence in the direction perpendicular to the steps was studied.

The possibility for superlattice umklapp effects to contribute to the spectra in normal emission is shown in fig. 4 of Paper VIII. A cross section through the crystal is shown. The $\bar{\Gamma}$ -point is the center of the surface Brillouin zone of W(110). The $\bar{\Gamma}\bar{\Gamma}'$ directions are inequivalent on a rectangular (110) surface lattice, so we define the direction as [001] which is perpendicular to the Gd chains, i. e., the direction along which the interchain spacing decreases with coverage. For a fictitious $4 \times n$ structure, fig. 4a shows reciprocal lattice rods. For a point on the reciprocal superlattice, separated by \mathbf{G}_1 from $\bar{\Gamma}$, the Ewald

sphere is drawn. It intersects the rod through $\bar{\Gamma}$ and therefore the selected point can contribute to the normal-emission spectrum. This is equivalent to eq. 2.4.2. For increasing Gd coverage, here e. g., a $2 \times n$ structure, fig. 4b shows that now points from a larger vector \mathbf{G}_2 can contribute. In this way, the band structure of the W is systematically sampled by superlattice umklapp vectors \mathbf{G} .

There is an interesting test for the validity of this interpretation: Usually, the band structure along an in-plane direction is measured in angle-dependent photoemission by tilting either the sample or the electron analyzer in a way that the emission angle θ is changed and the wave vector component parallel to the surface is obtained according to eq. 2.4.3. If the Gd-coverage dependence samples the band structure of the W(110) substrate along the in-plane [001]-direction (the direction perpendicular to the chains), the clean W(110) must show a similar angle dependence along [001].

The result is shown in fig. 5 of Paper VIII. The Gd coverage dependence follows the angle dependence very closely in the energy range of the gap (2 to 6.3 eV binding energy). Extra structures in the Gd coverage dependence are only the gap boundary (N-point of the bulk Brillouin zone) at 6.3 eV, which is a direct transition and emission from Gd 4f at 8.3 eV. Beyond the 5×3 structure at 0.7 ML, other umklapp processes play a role including other directions than [001], therefore deviations occur there like extra peaks for 0.77 and 0.88 ML which were not assigned.

All in all, fig. 5 of Paper VIII can be considered a textbook example of the umklapp processes in angle-resolved photoemission [64K1,83W1]. Such effects will always be present when trying to determine the electronic structure and functionality of repeated nanostructures at surfaces.

Chapter 6

Localization in Mn films and nanostructures

6.1 From zero to two dimensions

In sects. 3.3 and 5.2 we had the opportunity to witness the behavior of both delocalized 5d6s electrons and localized 4f electrons of Gd when the dimensionality is increased from zero to two. Figure 5.4 showed that for 4f electrons only a binding-energy shift occurs. This is nothing more than a rigid movement of the Gd energy levels as a result of a redistribution of the 5d6s valence band and is in this respect similar to a core-level shift. This is fully in agreement with the well-known atomiclike multiplet character of the Gd 4f level which can be resolved in photoemission at low temperature [94F1].

The 3d level of Mn instead is an intermediate case in principle described by band theory. However, we discovered already a strong deviation in the magnetic exchange splitting by a factor of two between experiment and theory for 0.5 ML $c(2 \times 2)$ Mn/Cu(100) [97R1] and even the appearance of a photoemission satellite in the valence band of this system [97R2]. This is indicative of strong electron correlation. Because the substrates which support the zero-dimensional Mn arrangements, i. e., Cu(100) and Ni(100), have filled and almost filled d orbitals, respectively, correlation effects among d electrons are also enhanced in these substrates. One consequence is that Cu [79I1] and Ni [80E2] display correlation satellites in their valence bands as well. The satellites of Mn and Cu appear at similar binding energies [97R1] which makes an assignment difficult in view of the low concentration of 0.5 ML Mn for which this effect occurs and the correspondingly small contribution to the photoemission signal.

Photoemission from core levels is element specific and is used in Paper IX as a probe of extra electron localization due to the low-dimensional arrangement of Mn. First of all, the geometrical structure is characterized. By analogy to the $c(2 \times 2)$ surface alloy structures identified for 0.5 ML Mn on Cu(100) [93W1], Ni(100) [93W2], and Cu(110) [98R1], we deposited Mn on Ni(110) and observed

the formation of a clear $c(2 \times 2)$ superstructure by LEED as displayed in fig. 1b of Paper IX. (Our assignment of the $c(2 \times 2)$ structure to an ordered surface alloy has been fully confirmed by a recent x-ray diffraction study of Mn/Ni(110) [2004D1].) The structure observed at 1.1 ML likely corresponds to a corrugated Mn monolayer on the Ni because such corrugated monolayers have been found for Mn/Ni(100) as well [93W2].

This qualitative structural characterization by LEED enables us to tune the dimensionality from zero to two and to three by subsequent deposition of Mn on Ni(110). This is done in fig. 2 of Paper IX. The Mn 2p core level with a spin-orbit splitting of 11 eV enables the observation of satellite structures and to cross check their appearance for the $2p_{1/2}$ and $2p_{3/2}$ peaks. Fig. 2 of Paper IX shows for the $c(2 \times 2)$ structure intense satellites that accompany the $2p_{1/2}$ and $2p_{3/2}$ peaks at 5 eV higher binding energies. The effect is already much weaker for the Mn monolayer, and for thicker layers core-level spectra typical of 3d transition metals without satellites are measured.

An analysis method untypical for metal systems is applied. As the data strongly indicates that the enhanced localization of Mn d electrons in the zero-dimensional geometrical arrangement causes the satellite, a localized model is applied. This model is found in the configuration-interaction scheme on a local cluster of atoms. It has been very successful in the description of 3d transition metal compounds like oxides [98I1]. The cluster model is very flexible and can describe three-dimensional or lower dimensional interaction provided, however, that the local structure of the 3d transition-metal ion and the interaction with its ligand atoms determines the electronic structure rather than the long-range periodicity of the solid.

An analysis of the spectra based on the configuration-interaction model allows us to determine model parameters which can quantify the enhanced electron localization. These are the Coulomb interaction energy U_{dd} among 3d electrons in the Mn, which does not vary very much for Mn in solids (~ 3 eV as compared to ~ 20 eV in the gas phase), and the parameters for the hybridization between Mn 3d and Ni 3d, the charge-transfer energy Δ (1 eV) and the transfer integral T (1.2 eV) describing the hopping between Ni 3d and Mn 3d orbitals. An important result is that $\Delta < U_{dd}$ which means, as the core level reflects the order of energy levels in the valence band, that the main peak at lower binding energy corresponds to a Mn $d^6 \underline{L}$ ground-state configuration, i. e., the transfer of one electron from a neighboring Ni d orbital (\underline{L} usually denotes a ligand hole) to the Mn d orbital, and the satellite peak at higher binding energy to a pure Mn d^5 configuration. The result of the simple model can also be interpreted as a separation into a coherent and an incoherent part of the spectrum in the sense of sect. 2.7.

Moreover, two things can be learned from a comparison to Cu as substrate: Fig. 4 of Paper IX compares 0.5 ML $c(2 \times 2)$ Mn on Ni(110) and Cu(100) substrates: The satellite peak is more intense on Cu. This reflects the reduced interaction of a 3d transition metal overlayer with the substrate if the substrate is a noble metal as discussed in sect. 3.1. The fact that the dimensionality can be tuned for Mn/Cu(100) in a similar way as for Mn/Ni(110) is seen from the

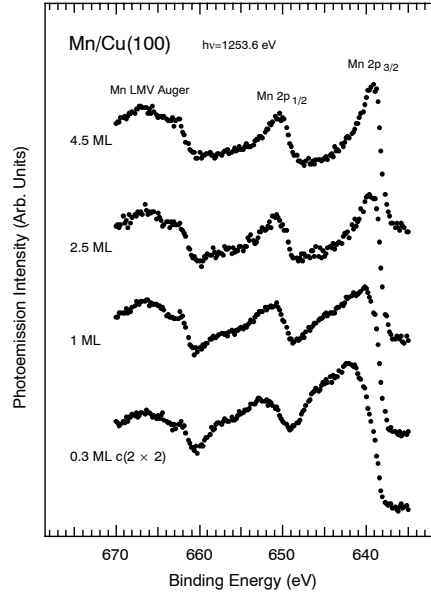


Figure 6.1: Photoelectron spectra of the Mn 2p core level for various coverages of Mn on Cu(100). The dimensionality changes from zero for the $c(2 \times 2)$ structure around half-monolayer coverage to two for the monolayer and three for thicker films. A photoemission satellite at ~ 5 eV higher binding energy due to enhanced localization appears for the $c(2 \times 2)$ structure.

unpublished fig. 6.1.

Secondly, one can ask in how far these results for Mn at the surface differ from those of diluted alloys. Mn in Cu is a famous spin-glass system [80M1], and it can be used to compare one-dimensional Mn at the Cu surface and in the Cu bulk. Several Mn-Cu alloys have been prepared in situ by co-deposition and fig. 6.2 shows that for smallest concentrations (2.5%) there is no similarly strong correlation satellite as in fig. 6.1. This shows that the preparation of Mn as zero-dimensional nanostructure arrangement at the surface leads indeed to correlation effects not reached by dilution in the volume. It is instructive to see that the position and shape of the main peak remains approximately the same for 0.3 ML $c(2 \times 2)$ Mn/Cu(100) and $\underline{\text{CuMn}}_{2.5\%}$. This is in line with its assignment to a $d^6\bar{L}$ configuration which reflects the presence of Cu neighbors. The d^5 configuration assigned to the satellite must, instead, be connected to the surface site.

Another system should briefly be mentioned because it presents another way of detecting the influence of reduced dimensionality on the Mn d states. The study was motivated by our experiments on the non-epitaxial system Mn/Fe(100) where we found a ferromagnetic Mn layer coupled antiparallel to the Fe [97R3].

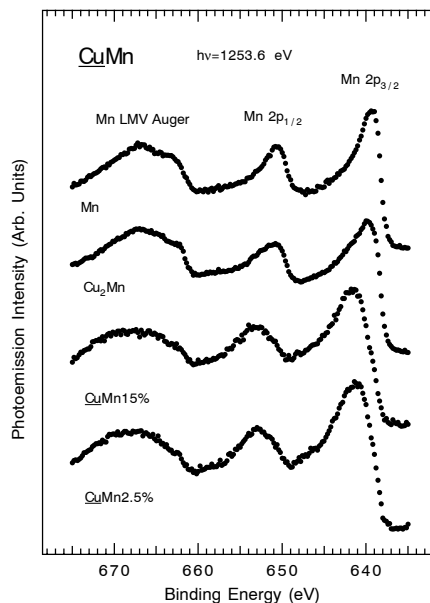


Figure 6.2: Same as fig. 6.1 but for Mn in the bulk of Cu. Zero-dimensional Mn diluted in Cu (2.5%) does not lead to a similarly strong satellite as at the surface (fig. 6.1).

This sign of the coupling was in agreement with the literature [95R1,97D1,-97D2,98I2] but a parallel coupling had also been reported [97A1,97A2]. The parallel coupling has been related to the superior surface structure of Fe(100) grown as thin film on MgO(100) [97A1,97A2]. It is in fact likely that an inferior order of the substrate surface leads to interdiffusion which in turn causes an antiparallel coupling since Mn diluted in Fe is known to couple antiparallel. In Paper X we found that Mn grows epitaxially in a $p(1 \times 1)$ structure on Fe(110) which is the close-packed surface of the bcc structure. The coupling seen for Mn on Fe(110) (figs. 1 and 2 of Paper X) is absent up to 0.3 ML, then parallel with small net magnetic moment and vanishing above 2 ML.

In the same coverage range, the branching ratio, i. e., with the nomenclature of sect. 2.9, the ratio $\int_{L_3}(\mu_+ + \mu_-) : \int_{L_2}(\mu_+ + \mu_-)$, successively decreases with coverage. A similar behavior has already been observed for Mn/Co(100) [94O2]. It has been shown in ref. [88T1] that high-spin states have a larger spin-orbit branching ratio than low-spin states if spin-orbit splitting in the valence band can be neglected. This means that the behavior seen in fig. 2 of Paper X reflects a successive decrease of the local magnetic moment of Mn with increasing coverage due to hybridization with neighboring Mn d states. The effect is so large because the Mn d^5 configuration has the highest spin moment of $5\mu_B$ in the atom and an average of only $0.65\mu_B$ per atom in the bulk structure of α -

Mn. For other 3d elements the effect is naturally not that large but comparing monoatomic Co chains to the monolayer and bulk in fig. 4.8 [2000G1] a similar effect can be seen.

A surprising effect was found in Paper X. Exposition to small amounts of oxygen (0.5 L) reverses the Mn-Fe coupling from parallel to antiparallel. In two publications that simultaneously appeared with Paper X a reversal of the magnetic coupling of Mn was observed as well, namely for oxygen adsorption on Mn/Co(100) [98O1] and for residual gas adsorption on Mn/Fe(100) [98A1]. The evaluation of the branching ratio helps to understand this effect. Fig. 4 of Paper X shows that the branching ratio increases strongly with oxygen adsorption indicating that oxidized submonolayer Mn is of d^5 configuration. The reversal of the Mn-Fe coupling from parallel to antiparallel occurs, however, for lower oxygen doses (0.5 L) than the oxidation does (~ 2 L). This points towards a possibly minor rearrangement of the Mn adsorption geometry induced by oxygen. Nevertheless, the problem of oxygen-induced reversal of the Mn-Fe and Mn-Co coupling has in spite of extensive theoretical efforts not been solved to date [2004P1].

6.2 Spin-polarized states in two and three dimensions

The low average magnetic moment of $0.65\mu_B$ per atom in bulk α -Mn shows that the five electron spins of Mn are not aligned parallel in the solid. If the enhanced localization of Mn d states in the zero-dimensional arrangements of sect. 6.1 is due to the half filling, it requires local alignment, i. e., full spin polarization of Mn d states or $5\mu_B$.

This can directly be probed by spin-resolved photoemission provided long-range ferromagnetic order exists. This, in turn, requires a remanent magnetization since the method does not tolerate external magnetic fields. Apart from submonolayers on surfaces and their unstable magnetic structure (sect. 6.1) this is only achievable in compounds where direct Mn-Mn neighbors are avoided.

The Mn mononictide MnSb is ferromagnetic below 585 K, has a theoretical magnetic moment of $3.5\mu_B$ [85C1], and epitaxial growth on GaAs(111) has been developed [95A1]. Fig. 2 of Paper XI shows spin-resolved valence band spectra in normal emission for two photon energies corresponding to the A-point ($h\nu = 25.8$ eV) and the Γ -point ($h\nu = 38.2$ eV) of the NiAs-type crystal structure (inset in fig. 1b). The spectrum at the A-point shows higher spin polarization than at the Γ -point possibly due to somewhat larger probing depth around 20 eV kinetic energy which gives surface imperfections smaller spectral weight. The main peak at -2.8 eV is of majority spin. This is also the lower boundary for the exchange splitting since only occupied states can be probed. Theory predicts a splitting of 2.6 eV and an energy position of -2.3 eV. It is not possible to conclude on the dispersion with \mathbf{k}_\perp between A and Γ , i. e., with the photon energy, because the predicted dispersion is small (the real space unit cell of the

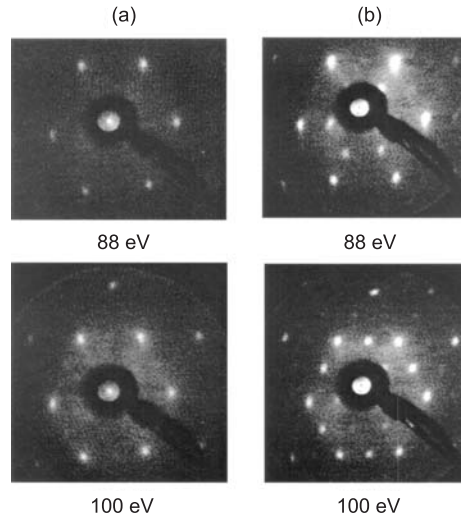


Figure 6.3: Structure of MnSb(0001) after annealing to 180°C (a) and 250°C (b) where a 2×2 structure appears.

NiAs-lattice is large along [0001]). The minority-spin band should cross E_F between A and Γ and the changes in intensity at E_F seen in fig. 1 of Paper XI could be due to the dispersion. All in all, there is no large deviation between the occupied part of the local-spin-density calculations (Paper XI and ref. [85C1]) and the spin-resolved experiment.

The band structure in fig. 3 of Paper XI indicates an interesting feature. Instead of a rigid splitting between majority and minority spin there is a band gap for majority spin which does not exist for minority spin. This is because the Mn-Sb bonding states (dashes) are deep in energy, and lead to a small exchange splitting but cannot be fully occupied for minority spin. Therefore the minority-spin band extends all the way up to cross E_F near Γ and closes in this way the band gap for minority spin. For spintronic applications such spin-polarized band gaps are very interesting when they appear at E_F . In this case the solid becomes a half metal which is defined as a metal for one spin and a semiconductor or insulator for the other spin [83D1]. This exotic property has so far only been shown for the Mn perovskite $\text{La}_{0.7}\text{Sr}_{0.3}\text{MnO}_3$ by spin resolved photoemission [98P1]. The observation made above makes MnSb an interesting model system last but not least because of its structural compatibility with GaAs and the relation to the Heusler compound NiMnSb predicted to be half metallic [83D1] but not confirmed in spin-resolved experiments [2001Z1].

When preparing the surface of MnSb(0001), we observe that the 1×1 structure in LEED turns into a 2×2 structure for annealing around 250°C (fig. 6.3). Fig. 6.4a shows the spin-resolved spectrum from the 1×1 surface interpreted on the basis of bulk transitions. Fig. 6.4b shows the spectrum after annealing

to $\approx 250^\circ\text{C}$ and (2×2) -formation. An apparent change is the appearance of an intensive extra peak 1.6 eV below E_F , which has been labeled SS. The hatched lines give the theoretical bulk band gap which appears along Γ -A and is thus effective at $\bar{\Gamma}$, the center of the surface Brillouin zone. The gap exists only for majority spin and extends from -0.69 eV (Λ_4 at $3/4 \Gamma A$) to -1.61 eV (Γ_{6+}) (see fig. 3 of Paper XI). The peak labeled SS at -1.6 eV appears inside but close to the border of this gap. This border is, however, defined by Γ_{6+} , which is far away in k-space, so that the nearest majority-spin emission expected on the basis of the bulk band structure is the one marked in fig. 6.4b at -3.0 eV. From this argument it becomes obvious that the peak SS cannot be explained from the band structure of bulk MnSb.

We have tested the dependence of the spectra on gas adsorption. A freshly prepared sample has been exposed to a small amount of oxygen (0.15 L) at lower temperature (≈ 130 K). The changes due to oxygen adsorption (Fig. 3c) are the following: (i) O-2*p*-derived emission appears between -5 and -6 eV in the spectra. (ii) The features assigned to bulk MnSb become broadened. (iii) The peak SS at -1.6 eV is reduced in intensity. This attenuation of SS is stronger than the one of the majority-spin peak at -3.0 eV which we have assigned to a bulk initial state. This high surface sensitivity is interpreted in favor of an assignment of SS as surface state. In addition, an *ab initio* calculation of the band structure has been performed by our collaborators [2004L1]. Results for the case of termination by a Mn monolayer show surface state with exactly the same energy and spin as in experiment. (See $\bar{\Gamma}$ in Fig. 6.5.) This is a remarkable result. Termination by an Sb monolayer does not give the surface state.

In conclusion, the spin-dependent electronic structure of MnSb(0001) is substantially modified by annealing. This shows that even if a spin gap is predicted by the bulk band structure, two-dimensional states in these gaps can disturb this property. This holds for interfaces in the same way as for the surface and will be important for gaps at the Fermi energy where it may affect half metallicity.

6.3 Strong electron correlation in bcc Mn films

In the present section we complete our excursion on Mn arriving at three dimensions. Generally, $E(\mathbf{k})$ dispersions of the magnetic transition metals measured by angle-resolved photoemission have been interpreted in the literature as showing good overall agreement with the energy eigenvalues calculated for the ground state on the basis of density functional theory and the local (spin) density approximation [99R1]. Nevertheless, some deviations are apparent. For Cr and Fe, energy positions with respect to the Fermi level have been found to be about 10% smaller in experiment than in theory. Results from Co may indicate larger deviations but the amount of data is yet insufficient to conclude this question. For Ni the band narrowing in photoemission is substantial. Ratios of theoretical over experimental energy positions between 1.3 and 1.5 have been obtained. For Ni, the exchange splittings at high-symmetry points of the Brillouin zone are smaller than calculated by a factor of two [99R1]. The 6 eV satellite seen in

photoemission spectra of core levels [75H1] and in the valence band [77G1] is a clear indication of strong correlation effects in Ni. On the other hand, the 6 eV correlation satellite initially reported for Mn [82S1] has turned out to be an unwanted contamination effect [87R1] and the spectra shown in ref. [87R1] are a reference for clean polycrystalline Mn films.

There are no angle-resolved photoemission studies of Mn [99R1]. The reason is probably that Mn has a very complicated structure in the bulk. The room-temperature phase is the α -Mn phase ($T < 727^\circ\text{C}$) with 58 atoms in the unit cell and a lattice constant of 8.9 Å. Among the high-temperature phases, the β -phase has 20 atoms per unit cell, and the γ - and δ -phases form fcc and bcc lattices, respectively. The β - and γ -phases have been obtained at room temperature after alloying and quenching [99R1].

We have undertaken two angle-resolved photoemission studies on bulklike epitaxial Mn films. The first one was on fcc Mn(100) grown on Cu₃Au(100) according to the characterization in ref. [99S2] and is still unpublished [2004B1]. The second one followed the observation of epitaxial growth of a few monolayers of Mn on Fe(110) in sect. 6.1. As the bulklike Fe(110) film of Paper X has been grown on W(110), we developed a method to grow 15–30 ML Mn epitaxially on W(110) by postannealing which yields a clear $p(1 \times 1)$ pattern of 15 ML bcc Mn(110) in fig. 1a of Paper XII. The single crystalline property enables \mathbf{k} -dependent studies varying \mathbf{k}_\perp by changing the photon energy as shown for Cu in fig. 2.4 for normal electron emission and \mathbf{k}_\parallel by changing the emission angle at fixed photon energy according to eq. 2.4.3. The results are shown in figs. 1c and 1b of Paper XII, respectively. In fig. 1c there appears a broad nondispersive peak at -2.7 eV and a peak with a small but clear dispersion near E_F . The situation in fig. 1b is the same but the dispersion near E_F appears even more clearly. This behavior is compared to a local density calculation [88F1] the results of which have been compiled in fig. 2. In the calculation the lattice constant of bcc Mn is varied on a large scale so that even atomic-like magnetic moments of up to $4.9\mu_B$ are reached. The comparison shows that the energy position of the main peak in the experiment (-2.7 eV) is strongly underestimated by the calculation for the experimental lattice constants [$a_W = 3.15$ Å according to the arrow in fig. 2]. When conducting the comparison between experiment and theory, we have to note the following: The energy eigenvalue N_2^\uparrow at the N-point is slightly deeper than at Γ but it cannot be observed by the experiment in normal emission (see Σ_2 in tab. 2.6.1). The results of ref. [88F1] for extreme lattice constants, on the other hand, can also not explain the experimental data since at $4.9\mu_B$ the minority-spin states are fully unoccupied and there are no states predicted to explain the peak at E_F seen in the experiment.

An alternative explanation based on local density theory could invoke surface effects. There is a band structure calculation which predicts large moments at the top surface atomic layer of bcc Mn(110) [94A2]. The large moments correspond to a large exchange splitting which could explain the peak at -2.7 eV. Two arguments contradict this idea: firstly, for photon energies from 6 eV to 160 eV as surface-layer derived peak must show an intensity variation in the

spectra due to the changing IMPF (fig. 2.2) which is not observed. Secondly, it must be sensitive to adsorbates like oxygen. No oxygen effect on the -2.7 eV peak is however seen in fig. 6.6.

This shows that electron correlation is so strong in the bulk of Mn that even in three dimensions the transfer of spectral weight from the coherent to the incoherent part of the spectrum is so large that the incoherent part dominates over the dispersing quasiparticle peaks in the spectra.

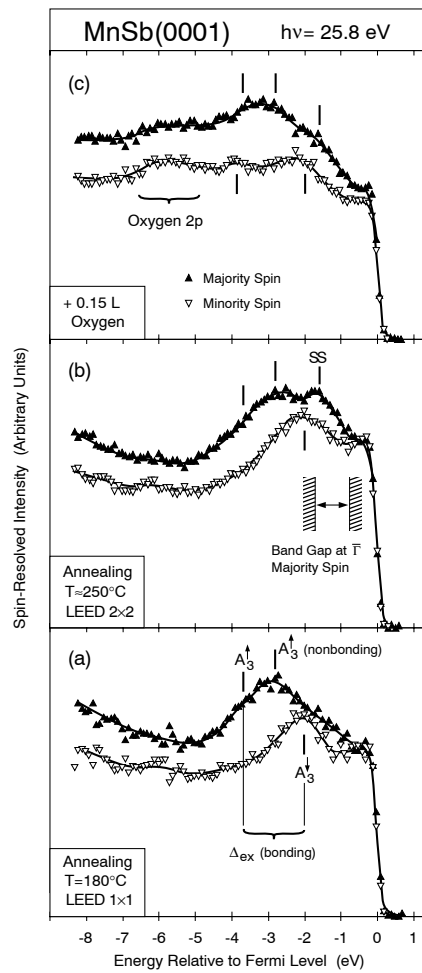


Figure 6.4: Spin-resolved photoemission of MnSb(0001). The spectrum at the A-point of the bulk Brillouin zone (a) shows the magnetic exchange splitting of bulk Mn states: $\Delta_{ex}(\text{Mn nonbonding}) > 2.8$ eV; $\Delta_{ex}(\text{Mn-Sb bonding}) = 1.7 \pm 0.3$ eV. After annealing a majority-spin surface state (SS) appears inside of a bulk band gap of the same spin (b). The surface state is sensitive to oxygen adsorption (c).

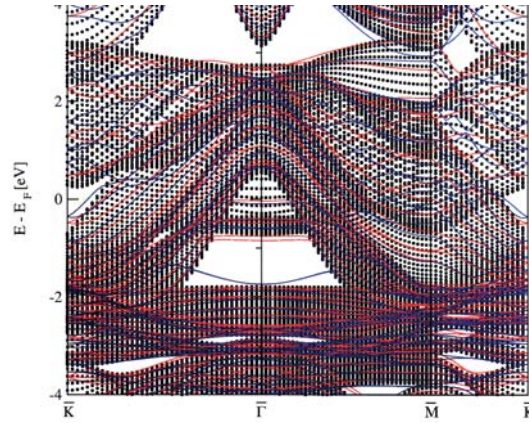


Figure 6.5: $E(\mathbf{k})$ band dispersion for majority spin calculated from first principles for a 1×1 Mn-terminated MnSb(0001) surface [2004L1]. A surface state of majority spin is predicted at -1.7 eV inside of a bulk band gap of the same spin in perfect agreement with the experiment.

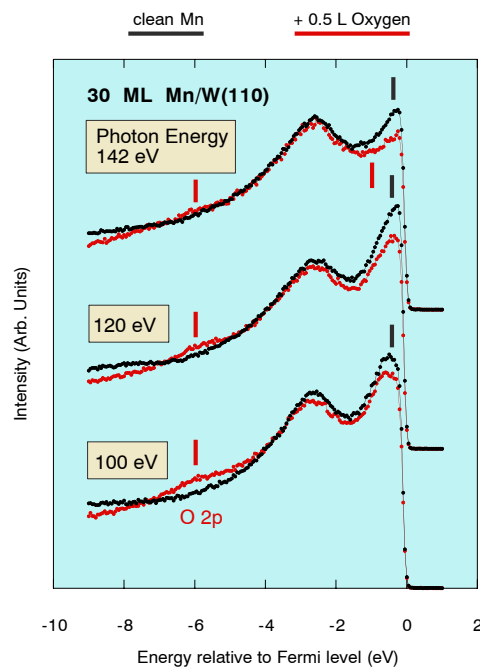


Figure 6.6: Oxygen dependence of bcc Mn(110) at various photon energies. The peak at -2.7 eV is not due to a surface state.

Chapter 7

Summary

In a series of publications we have shown how the dimensionality of the condensed matter affects the electronic states. This is demonstrated for metal-on-metal nanostructures which are much less investigated than corresponding semiconductor structures. The methods we have applied in our experimental studies were angle-resolved photoemission, inverse photoemission, spin-resolved photoemission, core-level photoemission, x-ray absorption, and magnetic circular x-ray dichroism in absorption. The samples were thin film layered structures which must be prepared *in situ*. In fact, considerable effort has gone into the *in situ* preparation and characterization of these nanostructured materials.

For itinerant electronic states, the evolution from the two-dimensional monolayer to a film with three-dimensional electronic structure was demonstrated. Quantum-well states in two-dimensional films and the influence of a cap layer on them were studied. The quantization of valence-band states in a rare earth and possible applications were demonstrated.

The transition from dimensionality two to one was undertaken on stepped W, Pt, and Ni surfaces and interesting effects were found for the clean steps, those decorated by monoatomic chains and by a full-monolayer coverage of nanostripes. Self-organized monoatomic Au chains on Ni(110) produce a truly one-dimensional dispersion and behave analogously to the states in two-dimensional GMR systems including a spin-polarization of the nonmagnetic quantum-wire states. The preparation of monoatomic Gd chains on W(110) mainly leads to strong umklapp effects which depend on the chain separation in a characteristic way.

The influence of the dimensionality on Mn 3d states is seen for various systems. In self-organized zero-dimensional Mn arrangements on metal substrates, the electron correlation is enhanced in such a way that photoemission satellites appear. The separation into main peak and satellite is not an atomic property of the Mn but depends on the atomic environment. Consequently, the high electron correlation discovered in three dimensional Mn manifests itself in a different way. The photoemission spectrum shows a strong incoherent contribution. It shows no wave-vector dependence in contrast to a narrow quasiparticle band

observed at the Fermi energy.

The main results from the present work can be summarized in the following form:

- The electronic structure of 3d-transition-metal films on noble-metal substrates is sufficiently decoupled from the substrate to be determined mainly by its dimensionality.
- Quantum-well states in GMR trilayer structures are strongly influenced by a magnetic cap layer. Phase shifts of 180° are possible and quantum-well states can extend across the interface between a magnetic and nonmagnetic layer. This explains why the long-range oscillatory magnetic coupling does not only depend on the thickness of the nonmagnetic but also of the magnetic layer.
- Valence-band states of rare earths can be confined and quantized in two dimensions which offers a unique way to determine the bulk band structure bypassing momentum broadening effects. Itinerant Gd 5d states behave as predicted by local-density theory and are not strongly correlated.
- Stepped tungsten crystals lead to one-dimensional anisotropy effects in $E(\mathbf{k})$ dispersions as observed in photoemission. One-dimensional confinement of surface-state electrons at terraces is the rule when band gaps are present. Superlattice effects on the band dispersion are due to final-state electron diffraction. They are present or absent depending on the phase of the wave function in the initial state.
- The density of states of monoatomic chains can efficiently be measured by photoemission at excitation energies near the Cooper minimum of the valence orbitals of the substrate. The density of states of monoatomic chains of magnetic transition metals shows metallicity and magnetism. The one-dimensionality can be observed through an enhanced magnetic exchange splitting.
- For nanostripes of monolayer graphite on stepped substrates electrons are localized in the stripes. The superlattice periodicity leads to a doubling of the band dispersion. The effects are due to the photoexcited final state like for surface states on clean stepped tungsten but occur over the whole valence band width.
- Au on Ni(110) was the first example of a one-dimensional electronic structure for a metal-on-metal system. One-dimensionality is supported by band gaps in Ni. The band gaps impose a spin polarization on the Au quantum-wire states in an analogous way as in two-dimensional quantum-well structures. Longitudinal one-dimensional superlattice effects can be observed as well.
- Gd/W(110) forms an elastic superlattice of chains which can effectively be used to probe the W band structure. Therefore, the Gd coverage

dependence of normal emission spectra is equivalent to the emission angle dependence for clean W(110).

- The correlation among 3d electrons in Mn can be enhanced in self-organized zero-dimensional nanostructures such that satellites appear in core-level photoemission spectra. Their disappearance in three-dimensional Mn films indicates the different chemical surrounding of Mn atoms but not that correlation effects are weak in the Mn bulk. Only the stabilization of single-crystalline Mn films allows the following observations: Binding energies and dispersions do not agree with local density calculations. The absence of a band dispersion at higher binding energies indicates a strong incoherent contribution to the spectra. This identifies bulk Mn as the second strongly correlated transition metal besides Ni.

We do not want to close without mentioning again that truly one dimensional metals display exotic phenomena like separation of spin and charge excitations of the electron [63L1,74L2,81H1]. These effects are not yet established for nanostructures as they are currently prepared [99S1,2001L1,2003A1] and it is likely that in order to observe them, semiconductor substrates with large band gaps must be used. The method of angle-resolved photoemission has the potential to discover these effects, and it is hoped that the awareness of the phenomena reported in the current work will help to attack this and many other interesting problems of one-dimensional physics successfully in the future.

Chapter 8

Acknowledgement

The current work is based on a large variety of systems the extensive *in situ* preparation of which had to be learned, developed, or at least discovered. To present meaningful and large experimental effects, a big quantity of data had to be measured, analyzed, and discussed. I am deeply indebted to my supervisor Prof. W. Gudat and my other collaborators from experiment and theory V. K. Adamchuk, H. Akinaga, K. S. An, G. Bihlmayer, S. Blügel, C. Carbone, A. Dallmeyer, W. Eberhardt, A. Fujimori, P. Gambardella, S. A. Gorovikov, F. J. Himpsel, T. Kachel, A. Kakizaki, N. Kamakura, A. Kimura, R. Kläsges, S. Miyanishi, T. Mizokawa, C. Pampuch, G. V. Prudnikova, A. M. Shikin, K. Shimada, M. Shirai, and A. Varykhalov.

Among my colleagues at BESSY whom I thank for their strong and uncomplicated engagement of which I have been profiting over many years, I want to mention in particular C. Hellwig, Ch. Jung, R. Follath, and G. Reichardt. During the course of the past decade I enjoyed the hospitality of University of Tokyo, Photon Factory, NAIST Nara, Ritsumeikan University, Hiroshima University, IBM T. J. Watson Research Center, Elettra, and MAXlab. The experimental work there was supported by an even larger number of people which are impossible to list here.

Support by BMBF (05KS1IPA/0) and DFG (RA1041/1-1 and 436RUS113/735/0-1) is gratefully acknowledged.

Chapter 9

References

- [1846F1] M. Faraday, Phil. Trans. Roy. Soc. **136**, 1 (1846)
- [1887H1] H. Hertz, Ann. Phys. **31**, 983 (1887)
- [05E1] A. Einstein, Ann. Phys. **17**, 132 (1905)
- [29M1] N. F. Mott, Proc. Roc. Soc. A **124**, 425 (1929)
- [63L1] J.M. Luttinger, J. Math. Phys. **4**, 1154 (1963)
- [64B1] C. N. Berglund, W. E. Spicer, Phys. Rev. **136**, 1030 (1964)
- [64K1] E. O. Kane, Phys. Rev. Lett. **12**, 97 (1964)
- [66M1] N. D. Mermin, H. Wagner, Phys. Rev. Lett. **17**, 1133 (1966)
- [70M1] G. D. Mahan, Phys. Rev. B **2**, 4334 (1970)
- [74L1] A. Liebsch, Phys. Rev. Lett. **32**, 1203 (1974)
- [74L2] A. Luther and V. J. Emery, Phys. Rev. Lett. **33**, 589 (1974)
- [75E1] J. L. Erskine, E. A. Stern, Phys. Rev. B **12**, 5016 (1975)
- [75H1] S. Hüfner, G. K. Wertheim, Phys. Lett. A **51**, 301 (1975)
- [76M1] M. Henzler, Appl. Phys. **9**, 11 (1976)
- [77G1] C. Guillot, Y. Ballu, J. Paigné, J. Lecante, K. P. Jain, P. Thiry, R. Pinchaux, Y. Pétroff, L. M. Falicov, Phys. Rev. Lett. **39**, 1632 (1977)
- [77H1] J. Hermanson, Solid State Commun. **22**, 9 (1977)
- [79H1] P. Heimann, H. Miosga, H. Neddermeyer, Solid State Commun. **29**, 463 (1979)
- [79I1] M. Iwan, F. J. Himpsel, D. E. Eastman, Phys. Rev. Lett. **43**, 1829 (1979)
- [79L1] H. L. Levinson, P. J. Feibelman, E. W. Plummer, Phys. Rev. Lett. **43**, 952 (1979)
- [79S1] M. P. Seah, W. A. Dench, Surf. Interface Anal. **1**, 2 (1979)
- [80B1] R. L. Benbow, Phys. Rev. B **22**, 3775 (1980)
- [80E1] W. Eberhardt, F. J. Himpsel, Phys. Rev. B **21**, 5572 (1980). Erratum: Phys. Rev. B **23**, 5650 (1981)
- [80E2] W. Eberhardt, E. W. Plummer, Phys. Rev. B **21**, 3245 (1980)
- [80M1] J. A. Mydosh, G. J. Nieuwenhuys in E. P. Wohlfarth (ed.), Ferromagnetic Materials, Vol. 1 (North-Holland, Amsterdam, 1980)
- [81H1] F. D. Haldane, J. Phys. C **14**, 2585 (1981)

- [82S1] H. Sugawara, A. Kakizaki, I. Nagakura, T. Ishii, *J. Phys. F* **12**, 2929 (1982)
- [83D1] R. A. de Groot, F. M. Mueller, P. G. van Engen, K. H. J. Buschow, *Phys. Rev. Lett.* **50**, 2024 (1983)
- [83K1] S. D. Kevan, *Phys. Rev. Lett.* **50**, 526 (1983)
- [83W1] D. Westphal, A. Goldmann, *Surf. Sci.* **126**, 253 (1983)
- [85C1] R. Coehoorn, C. Haas, R. A. de Groot, *Phys. Rev. B* **31**, 1990 (1985)
- [85K1] J. Kessler, *Polarized Electrons* (Springer, Heidelberg, 1985)
- [85S1] N. V. Smith, *Phys. Rev. B* **32**, 3549 (1985)
- [85Y1] J. J. Yeh, I. Lindau, *At. Data Nuc. Data Tab.* **31**, 1 (1985)
- [86C1] C. Carbone, E. Vescovo, R. Kläsger, D. D. Sarma, W. Eberhardt, *Solid State Commun.* **100**, 749 (1996).
- [86K1] J. Kolaczkiwicz, E. Bauer, *Surf. Sci.* **175**, 487 (1986)
- [87G1] R. H. Gaylord and S. D. Kevan, *Phys. Rev. B* **36**, 9337 (1987)
- [87R1] S. Raaen, V. Murgai, *Phys. Rev. B* **36**, 887 (1987)
- [87S1] G. Schütz, W. Wagner, W. Wilhelm, P. Kienle, R. Zeller, R. Frahm, G. Materlik, *Phys. Rev. Lett.* **58**, 737 (1987)
- [88B1] M. N. Baibich, J. M. Broto, A. Fert, F. Nguyen Van Dau, F. Petroff, P. Eitenne, G. Creuzet, A. Friederich, J. Chazelas, *Phys. Rev. Lett.* **61**, 2472 (1988)
- [88F1] G. Fuster, N. E. Brener, J. Callaway, J. L. Fry, Y. Z. Zhao, D. A. Papaconstantopoulos, *Phys. Rev. B* **38**, 423 (1988)
- [88S1] A. P. Shapiro, T. Miller, T.-C. Chiang, *Phys. Rev. B* **38**, 1779 (1988)
- [89B1] G. Binasch, P. Grünberg, F. Saurenbach, W. Zinn, *Phys. Rev. B* **39**, 482 (1989)
- [89G1] A. Goldmann, E. E. Koch (eds.), *Electronic Structure of Solids: Photoemission Spectra and Related Data*, Landolt-Börnstein, New Series, Group III, Vol. 23 (Springer, Berlin, 1989)
- [89M1] M. Mundschau, E. Bauer, W. Swiech, *J. Appl. Phys.* **65**, 581 (1989)
- [90C1] C. T. Chen, F. Sette, Y. Ma, S. Modesti, *Phys. Rev. B* **42**, 7262 (1990)
- [90S1] C. M. Schneider, J. J. de Miguel, P. Bressler, P. Schuster, R. Miranda, J. Kirschner, *J. Electron Spectr. Relat. Phenom.* **51**, 263 (1990)
- [92C1] Q. Chen, M. Onellion, A. Wall, P. Dowben, *J. Phys.: Condens Mat.* **4**, 7985 (1992)
- [92C2] W. Clemens, T. Kachel, O. Rader, E. Vescovo, S. Blügel, C. Carbone, W. Eberhardt, *Solid State Commun.* **81**, 739 (1992)
- [92K1] B. Kim, A. B. Andrews, J. L. Erskine, K. J. Kim, B. N. Harmon, *Phys. Rev. Lett.* **68**, 1931 (1992)
- [92O1] J. E. Ortega, F. J. Himpsel, *Phys. Rev. Lett.* **69**, 844 (1992)
- [92S1] N. V. Smith, C. T. Chen, F. Sette, L. F. Mattheis, *Phys. Rev. B* **46**, 1023 (1992)
- [92T1] B. T. Thole, P. Carra, F. Sette, G. van der Laan, *Phys. Rev. Lett.* **68**, 1943 (1992)
- [93B1] P. Bruno, *Europhys. Lett.* **23**, 615 (1993)

- [93C1] P. Carra, B. T. Thole, M. Altarelli, X. Wang, *Phys. Rev. Lett.* **70**, 694 (1993)
- [93C2] C. Carbone, E. Vescovo, O. Rader, W. Gudat, W. Eberhardt, *Phys. Rev. Lett.* **71**, 2805 (1993)
- [93C3] M. F. Crommie, C. P. Lutz, D. M. Eigler, *Science* **262**, 218 (1993)
- [93G1] K. Garrison, Y. Chang, P. D. Johnson, *Phys. Rev. Lett.* **71** 2801 (1993)
- [93K1] H. Knoppe and E. Bauer, *Phys. Rev. B* **48**, 5621 (1993)
- [93O1] J. E. Ortega, F. J. Himpsel, G. J. Mankey, R. F. Willis, *Phys. Rev. B* **47**, 1540 (1993)
- [93W1] M. Wuttig, Y. Gauthier, S. Blügel, *Phys. Rev. Lett.* **70**, 3619 (1993)
- [93W2] M. Wuttig, T. Flores, C. C. Knight, *Phys. Rev. B* **48**, 12082 (1993)
- [94A1] U. Alkemper, C. Carbone, E. Vescovo, W. Eberhardt, O. Rader, W. Gudat, *Phys. Rev. B* **50**, 17496 (1994)
- [94A2] M. Aldén, H. L. Skriver, S. Mirbt, B. Johansson, *Surf. Sci.* **315**, 157 (1994)
- [94B1] P. J. H. Bloemen, M. T. Johnson, M. T. H. van de Vorst, R. Coehoorn, J. J. de Vries, R. Jungblut, J. aan de Stegge, A. Reinders, W. J. M. de Jonge, *Phys. Rev. Lett.* **72**, 764 (1994)
- [94F1] A. V. Fedorov, E. Arenholz, K. Starke, E. Navas, L. Baumgarten, C. Laubschat, G. Kaindl, *Phys. Rev. Lett.* **73**, 601 (1994)
- [94H1] F. J. Himpsel, J. E. Ortega, *Phys. Rev. B* **50**, 4992 (1994)
- [94N1] W. Nolting, T. Dambeck, G. Borstel, *Z. Phys. B: Condens. Mat.* **94**, 409 (1994)
- [94O1] J. E. Ortega, F. J. Himpsel, R. Haight, D. R. Peale, *Phys. Rev. B* **49**, 13859 (1994)
- [94O2] W. L. O'Brien, B. P. Tonner, *Phys. Rev. B* **50**, 2963 (1994)
- [94S1] N. V. Smith, N. B. Brookes, Y. Chang, P. D. Johnson, *Phys. Rev. B* **49**, 332 (1994)
- [94S2] M. G. Samant, J. Stöhr, S. S. P. Parkin, G. A. Held, B. D. Hermsmeier, F. Herman, M. Van Schilfgaarde, L.C. Duda, D. C. Mancini, N. Wassdahl, R. Nakajima, *Phys. Rev. Lett.* **72**, 1112 (1994)
- [95A1] H. Akinaga, Y. Suzuki, K. Tanaka, K. Ando, T. Katayama, *Appl. Phys. Lett.* **67**, 141 (1995)
- [95B1] P. Bruno, *Phys. Rev. B* **52**, 411 (1995)
- [95C1] C. T. Chen, Y. U. Idzerda, H.-J. Lin, N. V. Smith, G. Meigs, E. Chaban, G. H. Ho, E. Pellegrin, F. Sette, *Phys. Rev. Lett.* **75**, 152 (1995)
- [95P1] L. Pleth Nielsen, F. Besenbacher, I. Stensgaard, E. Laegsgaard, C. Engdahl, P. Stoltze, J. K. Nørskov, *Phys. Rev. Lett.* **74**, 1159 (1995)
- [95R1] Ch. Roth, Th. Kleemann, F. U. Hillebrecht, E. Kisker, *Phys. Rev. B* **52** R15691 (1995)
- [96T1] Y. Teramura, A. Tanaka, T. Jo, *J. Phys. Soc. Jpn.* **65**, 1053 (1996)
- [96T2] E. D. Tober, R. X. Ynzunza, C. Westphal, C. S. Fadley, *Phys. Rev. B* **53**, 5444 (1996)
- [97A2] S. Andrieu, M. Finazzi, F. Yubero, H. Fischer, P. Arcade, F. Chevrier, L. Hennet, H. Hricovini, G. Krill, M. Piecuch, J. Magn. Magn. Mat.

- 165**, 191 (1997)
- [97A2] S. Andrieu, M. Finazzi, F. Yubero, H. Fischer, P. Arcade, F. Chevrier, L. Hennet, H. Hricovini, G. Krill, M. Piecuch, *Europhys. Lett.* **38**, 459 (1997)
- [97D1] J. Dresselhaus, D. Spanke, F. U. Hillebrecht, E. Kisker, G. van der Laan, J. B. Goedkoop, N. B. Brookes, *Phys. Rev. B* **56**, 5461 (1997)
- [97D2] H. A. Dürr, G. van der Laan, D. Spanke, F. U. Hillebrecht, N. B. Brookes, *Europhys. Lett.* **40**, 171 (1997)
- [97M1] G. J. Mankey, K. Subramanian, R. L. Stockbauer, R. L. Kurtz, *Phys. Rev. Lett.* **78**, 1146 (1997)
- [97P1] R. Pascal, Ch. Zarnitz, M. Bode, R. Wiesendanger, *Phys. Rev. B* **56**, 3636 (1997)
- [97R1] O. Rader, W. Gudat, C. Carbone, E. Vescovo, S. Blügel, R. Kläsges, W. Eberhardt, M. Wuttig, J. Redinger, F. J. Himpsel, *Phys. Rev. B* **55**, 5405 (1997)
- [97R2] O. Rader, E. Vescovo, M. Wuttig, D. D. Sarma, S. Blügel, F. J. Himpsel, A. Kimura, K. S. An, T. Mizokawa, A. Fujimori, C. Carbone, *Europhys. Lett.* **39**, 429 (1997)
- [97R3] O. Rader, W. Gudat, D. Schmitz, C. Carbone, W. Eberhardt, *Phys. Rev. B* **56**, 5053 (1997)
- [98A1] S. Andrieu, E. Foy, H. Fischer, M. Alnot, F. Chevrier, G. Krill, M. Piecuch, *Phys. Rev. B* **58**, 8210 (1998)
- [98B1] L. Burgi, O. Jeandupeux, A. Hirstein, H. Brune, K. Kern, *Phys. Rev. Lett.* **81** 5370 (1998)
- [98H1] F. J. Himpsel, J. E. Ortega, G. J. Mankey, R. F. Willis, *Adv. Phys.* **47**, 511 (1998)
- [98I1] M. Imada, A. Fujimori, Y. Tokura, *Rev. Mod. Phys.* **70**, 1039 (1998)
- [98I2] T. Igel, R. Pfandzelter, H. Winter, *Phys. Rev. B* **58**, 2430 (1998)
- [98O1] W. L. O'Brien, B. P. Tonner, *Phys. Rev. B* **58**, 3191 (1998)
- [98P1] J. H. Park, E. Vescovo, H. J. Kim, C. Kwon, R. Ramesh, T. Venkatesan, *Nature* **392**, 794 (1998)
- [98R1] Ch. Ross, B. Schirmer, M. Wuttig, Y. Gauthier, G. Bihlmayer, S. Blügel, *Phys. Rev. B* **57**, 2607 (1998)
- [99P1] J. J. Paggel, T. Miller, T. C. Chiang, *Science* **283**, 1709 (1999)
- [99R1] O. Rader, W. Gudat, *Landolt-Börnstein, New Series, Group III, Vol. 23C2* (ed. A. Goldmann) (Springer, Berlin, 1999)
- [99S1] P. Segovia, D. Purdie, M. Hengsberger, Y. Baer, *Nature* **402**, 504 (1999)
- [99S2] B. Schirmer, B. Feldmann, A. Sokoll, Y. Gauthier, M. Wuttig, *Phys. Rev. B* **60**, 5895 (1999)
- [2000C1] T. C. Chiang, *Surf. Sci. Rep.* **39**, 181 (2000)
- [2000M1] H. C. Manoharan, C. P. Lutz, D. M. Eigler, *Nature* **403**, 512 (2000)
- [2000O1] J. E. Ortega, S. Speller, A. R. Bachmann, A. Mascaraque, E. G. Michel, A. Närmann, A. Mugarza, A. Rubio, F. J. Himpsel, *Phys. Rev. Lett.* **84**, 6110 (2000)
- [2000G1] P. Gambardella, M. Blanc, H. Brune, K. Kuhnke, K. Kern, *Phys.*

- Rev. B **61**, 2254 (2000)
- [2000G2] P. Gambardella, M. Blanc, L. Burgi, K. Kuhnke, K. Kern, Surf. Sci. **449**, 93 (2000)
- [2001L1] R. Losio, K. N. Altmann, A. Kirakosian, J.-L. Lin, D. Y. Petrovykh, F. J. Himpsel, Phys. Rev. Lett. **86**, 4632 (2001)
- [2001L2] D. A. Luh, T. Miller, J. J. Paggel, M. Y. Chou, T. C. Chiang, Science **292**, 1131 (2001)
- [2001M1] K. Maiti, M. C. Malagoli, E. Magnano, A. Dallmeyer, C. Carbone, Phys. Rev. Lett. **86**, 2846 (2001)
- [2001M2] A. Mugarza, A. Mascaraque, V. Perez-Dieste, V. Repain, S. Rousset, F. J. Garcia de Abajo, J. E. Ortega, Phys. Rev. Lett. **87**, 107601 (2001)
- [2001O1] J. E. Ortega, A. Mugarza, A. Narmann, A. Rubio, S. Speller, A. R. Bachmann, J. Lobo, E. G. Michel, F. J. Himpsel, Surf. Sci. **482**, 764 (2001)
- [2001Z1] W. Zhu, B. Sinkovic, E. Vescovo, C. Tanaka, J. S. Moodera, Phys. Rev. B **64**, 060403 (2001)
- [2002G1] P. Gambardella, A. Dallmeyer, K. Maiti, M. C. Malagoli, W. Eberhardt, K. Kern, C. Carbone, Nature **416**, 301 (2002)
- [2002M1] A. Mugarza, A. Mascaraque, V. Repain, S. Rousset, K. N. Altmann, F. J. Himpsel, Yu. M. Koroteev, E. V. Chulkov, F. J. Garcia de Abajo, J. E. Ortega, Phys. Rev. B **66**, 245419 (2002)
- [2002S1] A. M. Shikin, O. Rader, G. V. Prudnikova, V. K. Adamchuk, W. Gudat, Phys. Rev. B **65**, 075403 (2002)
- [2002S2] A. M. Shikin, O. Rader, W. Gudat, G. V. Prudnikova, V. K. Adamchuk, Surf. Rev. Lett. **9**, 1375 (2002)
- [2003A1] J. R. Ahn, H. W. Yeom, H. S. Yoon, I.-W. Lyo, Phys. Rev. Lett. **91**, 196403 (2003)
- [2003G1] X. Gao, A. N. Kveshnikov, R. H. Madjoe, R. L. Stockbauer, R. L. Kurtz, Phys. Rev. Lett. **90**, 037603 (2003)
- [2003H1] M. Hansmann, J. I. Pascual, G. Ceballos, H.-P. Rust, K. Horn, Phys. Rev. B **67**, 121409 (2003)
- [2004B1] S. Biermann, A. Dallmeyer, C. Carbone, W. Eberhardt, C. Pampuch, O. Rader, M. I. Katsnelson, A. I. Lichtenstein, unpublished
- [2004D1] M. De Santis, V. Abad-Langlais, Y. Gauthier, P. Dolle, Phys. Rev. B **69**, 115430 (2004)
- [2004L1] M. Lezaic, S. Blügel, unpublished
- [2004P1] S. Pick, C. Demangeat, Catalysis Today **89**, 369 (2004)

Chapter 10

Twelve papers presented

- Paper I C. Pampuch, O. Rader, R. Kläsger, C. Carbone, "Evolution of the electronic structure in ultrathin Co, Ni, and Cu films", *Phys. Rev. B* **63**, 153409 (2001)
- Paper II F. J. Himpsel, O. Rader, "Quantum well states in Ni/Cu/Ni spin valve structures", *Appl. Phys. Lett.* **67**, 1151 (1995)
- Paper III O. Rader, A. M. Shikin, "Quantization of electronic states in a rare-earth film: Gd/W(110)", *Phys. Rev. B* **64**, 201406(R) (2001)
- Paper IV A. M. Shikin, A. Varykhalov, G. V. Prudnikova, V. K. Adamchuk, W. Gudat, O. Rader, "Photoemission from stepped W(110): Initial- or final-state effect?", *Phys. Rev. Lett.* **93**, 146802 (2004)
- Paper V A. Dallmeyer, C. Carbone, W. Eberhardt, C. Pampuch, O. Rader, W. Gudat, P. Gambardella, K. Kern, "Electronic states and magnetism of monatomic Co and Cu wires", *Phys. Rev. B* **61**, R5133 (2000)
- Paper VI A. M. Shikin, S. A. Gorovikov, V. K. Adamchuk, W. Gudat, O. Rader, "Electronic structure of carbon nanostripes", *Phys. Rev. Lett.* **90**, 256803 (2003)
- Paper VII C. Pampuch, O. Rader, T. Kachel, W. Gudat, C. Carbone, R. Kläsger, G. Bihlmayer, S. Blügel, W. Eberhardt, "One-dimensional spin-polarized quantum-wire states in Au on Ni(110)", *Phys. Rev. Lett.* **85**, 2561 (2000)
- Paper VIII O. Rader, A. M. Shikin, "An elastic "sieve" to probe momentum space: Gd chains on W(110)", *Phys. Rev. Lett.* **93**, 256802 (2004)
- Paper IX O. Rader, T. Mizokawa, A. Fujimori, A. Kimura, "Structure and electron correlation of Mn on Ni(110)", *Phys. Rev. B* **64**, 165414 (2001)
- Paper X O. Rader, C. Pampuch, W. Gudat, A. Dallmeyer, C. Carbone, W. Eberhardt, "Parallel, antiparallel and no magnetic coupling in sub-monolayer Mn on Fe(110)", *Europhys. Lett.* **46**, 231 (1999)
- Paper XI O. Rader, A. Kimura, N. Kamakura, K.-S. An, A. Kakizaki, S. Miyanishi, H. Akinaga, M. Shirai, K. Shimada, A. Fujimori, "Ex-

change splittings of Mn- and Sb-derived states by spin-resolved valence-band photoemission of MnSb”, *Phys. Rev. B* **57**, R689 (1998)

Paper XII O. Rader, C. Pampuch, W. Gudat, A. Dallmeyer, C. Carbone, W. Eberhardt, ”Epitaxy and strong electron correlation of bcc Mn(110)”, unpublished

Evolution of the electronic structure in epitaxial Co, Ni, and Cu films

C. Pampuch and O. Rader

BESSY, Albert-Einstein-Strasse 15, D-12489 Berlin, Germany

R. Kläsches and C. Carbone

Institut für Festkörperforschung, Forschungszentrum Jülich, D-52425 Jülich, Germany

(Received 31 May 2000; published 30 March 2001)

Recently, electronic structure and band width of the system 1.2 monolayers Ni/Cu(100) have been found to be Ni-bulk-like [Mankey *et al.*, Phys. Rev. Lett. **78**, 1146 (1997)]. Therefore, we have traced the development of the electronic structure with thickness for various 3*d* transition metals using angle-resolved photoemission. All studied systems show similar behavior. We find, in contrast to the previous report, a very different electronic structure for the monolayer and for bulk. Moreover, our measured binding energies support the results of local-density calculations which obtain strong narrowing of the 3*d* band width of 1 monolayer Ni/Cu(100) as compared to bulk Ni.

DOI: 10.1103/PhysRevB.63.153409

PACS number(s): 73.21.-b, 79.60.Dp

Low-dimensional materials have been attracting both experimental and theoretical interest due their peculiar physical properties which can differ significantly from those of materials with higher dimensionality. So-called finite-size effects occur when a structure is restricted in one dimension, this is, e.g., the case when the thickness of a film decreases down to atomic dimensions corresponding to a transition from three-dimensional to two-dimensional behavior. In this case the electronic band width becomes narrower due to an atomic coordination reduced with respect to the one of the bulk. This can be quantified as $W \propto \sqrt{n}$ in the tight-binding model, where W is the valence band width and n the number of nearest neighbors, and has been confirmed in countless calculations of the electronic structure of crystal surfaces, free-standing monolayers, and monolayers on weakly interacting substrates such as noble metals.

A well-established method to experimentally investigate the electronic structure of bulk systems, surfaces, and thin films is angle-resolved photoemission.¹ Mankey *et al.*² have recently employed angle-resolved photoemission to study the electronic structure of Ni/Cu(100) films. Reference 2 reports that electronic structure and band width of atomically thin Ni films [1.2 monolayer (ML) on Cu(100)] do not differ from those of bulk Ni.² This finding is based on angle-integrated photoemission spectra and on photoelectron angular distribution patterns for a narrow energy window around the Fermi energy obtained with a display-type analyzer.³ It has been interpreted as a hybridization and charge-transfer effect between Ni and Cu through which the Ni monolayer develops the characteristics of a bulk electronic structure.² Similar behavior has also been observed in atomically thin Cu/Ni(100) and Co/Cu(100) films.²

We are not aware of any corroboration or rejection of this surprising finding, with the exception of an x-ray-absorption study which notes that from absorption spectra 1 ML and 5 ML Ni/Cu(100) can be well distinguished as the density of unoccupied 3*d* states is by 20% larger for 1 ML than for 5 ML.⁴ Band theory has early on predicted for 1 ML Ni/Cu(100) a reduced magnetic moment⁵⁻⁷ ($0.37\mu_B$ in Ref. 5; $0.24\mu_B$ in Ref. 7; the bulk Ni value is $0.59\mu_B$ in Ref. 8),

which can be explained by band narrowing.⁷ The development of the band structure of Ni/Cu(100) with thickness has been studied and quantized states have been identified up to at least 15-ML Ni by inverse photoemission,⁹ but no systematic study has been reported for occupied states. We have therefore reinvestigated the development of the electronic structure in epitaxial Co, Ni, and Cu films by angle-resolved photoemission. In this paper we show that the electronic structure of atomically thin films is not bulklike, in contrast to the result of Ref. 2. In addition, the angle-resolved spectra allow us to trace the evolution of the electronic structure with thickness.

Angle-resolved photoemission experiments have been performed at the TGM 5 undulator beamline at the BESSY I storage ring in Berlin. The synchrotron light was incident at an angle of about 30° for normal-electron-emission geometry. This leads to a mixed (*s* and *p*) light-polarization geometry. A 90° spherical analyzer with an energy resolution of about 200 meV at an angular acceptance of 1° has been used. The spectra for different thicknesses were taken at normal emission with a photon energy of 43 eV because this corresponds for the present fcc materials to the Γ point along [100] for binding energies near E_F .

The Cu(100) crystal has been prepared by sputtering and annealing (600 °C) cycles. The base pressure of the vacuum system was 1×10^{-10} mbar. The various overlayers have been produced *in situ* by e^- -beam evaporation onto Cu(100) at room temperature. The pressure rose to a maximum of 5×10^{-10} mbar during the Co, Ni, and Cu evaporations. Evaporation rates have been measured with a quartz-crystal microbalance, and the quartz reading was used for thickness calibration. The materials were deposited at a typical rate of 0.5–1 Å/min. All systems show epitaxial growth at room temperature, but the growth modes of the various systems differ in detail: Between fcc Co and Cu there is only a small lattice mismatch. Reflection high-energy electron diffraction oscillations have been observed up to 40 ML for Co/Cu(100).¹⁰ Scanning tunneling microscopy (STM) (Refs. 11–13) shows that the growth occurs in a layer-by-layer mode of high quality above 2 ML up to at least 15 ML.

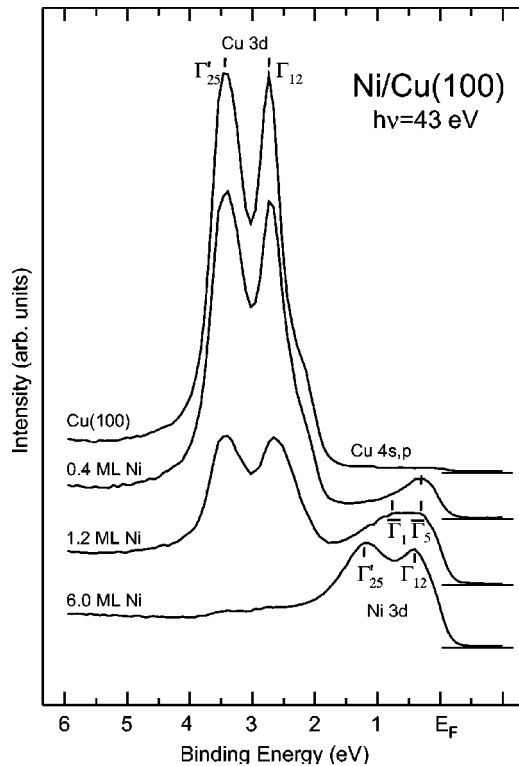


FIG. 1. Angle-resolved photoemission spectra of the valence band. Normal-emission spectra in the vicinity of the Brillouin-zone center of Cu(100) and selected coverages of Ni/Cu(100).

Below 2 ML nominal coverage, a substantial amount of simultaneous bilayer growth has been reported,^{12,14} but its extent is still under discussion.¹³ In an STM study of Ni/Cu(100),¹⁵ nearly perfect submonolayer growth and very good layer-by-layer growth up to 3.4 ML has been reported. There are indications for subsurface growth of the first Ni monolayer on Cu(100) at room temperature from x-ray photoemission and CO adsorption behavior¹⁶ and from low-energy electron diffraction (LEED) (Ref. 17) supported by recent first-principles total-energy calculations.¹⁸ Cu grows on Co/Cu(100) (Ref. 10) and on Ni/Cu(100) (Ref. 19) in an epitaxial layer-by-layer mode. Therefore, we have used 8 ML Ni/Cu(100) and 10 ML Co/Cu(100) as Ni(100) and Co(100) substrates, respectively. In the present work, the surface order has been checked by LEED. A sharp $p(1 \times 1)$ LEED pattern and low background intensity have been observed in all preparation stages for all systems [0–8 ML Ni/Cu(100), 0–2.8 ML Cu/Ni(100), 0–10 ML Co/Cu(100), and 0–2.6 ML Cu/Co(100)] confirming good structural order in the topmost surface layer.

The spectra in Fig. 1 reveal the dependence of the Ni electronic structure on the overlayer thickness. We show complete valence-band spectra of Cu(100) and of 0.4, 1.2, and 6 ML Ni/Cu(100) at arbitrary normalization. Regions of Ni 3*d* and Cu 3*d* emission can easily be distinguished as the pure Cu spectrum shows at 43-eV photon energy no feature between 2 eV and the Fermi level. Cu 3*d* emission occurs between 2 and 4 eV. The peak at 2.7-eV binding energy originates from the Δ_1 band (Γ_{12}), and the second peak at 3.4-eV binding energy from the Δ_5 band (Γ'_{25}). The shoulder

at 2-eV binding energy is due to Cu 4*s,p* emission.

In the spectrum of 0.4 ML Ni, a single peak is observed at 0.3-eV binding energy. At larger thickness of 1.2 ML, a second peak appears at 0.8-eV binding energy. For the 6-ML Ni film, two peaks derived from Ni 3*d* states are observed at 0.4 and 1.2-eV binding energy. Only a very weak feature due to emission from the Cu 3*d* band is seen between 2 and 4-eV binding energy. This is a clear indication that the Cu substrate is covered almost completely by 6-ML Ni.

For a more detailed discussion we turn to Fig. 2, which displays the energy region of the 3*d* photoemission of Co, Ni, and Cu films for smaller thickness intervals. The peaks marked in Fig. 1 and Fig. 2(a) contain contributions from both spin directions. They are not resolved since the exchange splitting in Ni is small (experimentally 0.15 eV for bulk Δ_1 , near the Γ point²⁰). Energy positions obtained for 1 ML are 0.3 and 0.75 eV. The energy positions agree with published photoemission measurements on 1 and 2 ML Ni/Cu(100) at normal emission.²¹ The present work goes beyond Ref. 21 in the sense that larger thicknesses are reached in Fig. 2(a) and that the spectra have been measured near the Γ point. Therefore, we can observe that energy positions close to those of bulk states are already reached at 3 ML. The Ni bulk band structure has an extremum in binding energy at a photon energy of 44 eV corresponding to the Γ point for 3*d*-derived states. The peak at 0.4-eV binding energy for 3–10 ML originates from the Δ_1 band (Γ_{12}) and the feature at 1.2-eV binding energy originates from the Δ_5 band (Γ'_{25}).

Figure 2(b) shows the case of fcc Co/Cu(100). The bulk exchange splitting of fcc Co is large—experimentally 1.55 eV at Γ'_{25} (Ref. 22). Still, we observe one peak less than in Fig. 2(a). This is due to the following reasons: (i) Co has a lower number of 3*d* electrons than Ni which shifts energy positions upwards and (ii) the majority-spin peak of Δ_5 (Γ'_{25}) is broad, and it is difficult to determine its energy position even in spin-resolved spectroscopy. Therefore, the peak marked in Fig. 2(b) is of minority spin and develops into Γ'_{25} [experimentally at 0.9 eV (Ref. 22)]. For 1 ML, more than one peak at 0.45 eV cannot be assigned with certainty. In case of substantial bilayer growth^{12–14} it can indeed be expected that distinction of 1 from 2 ML in the spectra becomes difficult.

In Fig. 2(c), we show Cu/Ni(100) and take advantage of the comparatively narrow width of 3*d* peaks in Cu and of the absence of exchange splitting. Below 1 ML, one peak is seen at 2.75 eV. Around 1 ML, peaks appear at 2.8 and 3.2 eV. Based on calculations of Cu monolayers, e.g., Ref. 23, the higher-binding-energy peak is assigned to $\bar{\Gamma}_1$ and the lower-binding-energy peak to $\bar{\Gamma}_5$. Towards larger thicknesses the peaks move closer together until around 1.5 ML they cannot be separated from each other at the present resolution. At 2 ML, peak positions (3.35 and 2.95 eV) are not too far from the ones of bulk Cu [3.6 and 2.9 eV from pure Cu(100) at the top of Fig. 2(c)]. Note that the order of odd- and even-symmetry states is reversed for monolayer and for bulk, thus the mutual approach of peaks around 1.5 ML likely marks a crossing over of states. It is possible that for Ni/Cu(100) and Co/Cu(100) this is not observed very well due to a tendency

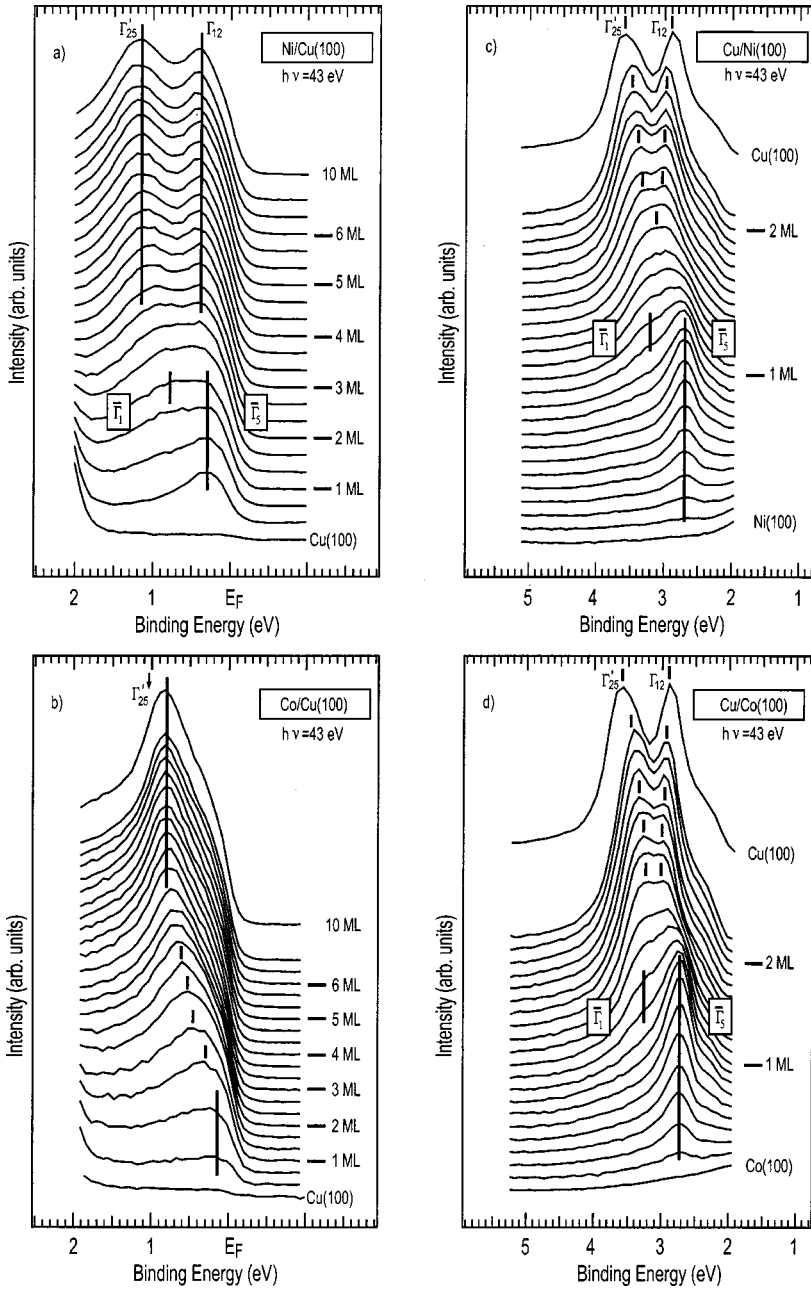


FIG. 2. Spectra showing the energy range of $3d$ emission in detail. All systems show similar behavior with film thickness.

for bilayer growth below 2 ML thickness as observed for Co/Cu(100) and a possible tendency for subsurface growth of Ni/Cu(100).

The situation in Fig. 2(d) for Cu/Co(100) is similar. Spectra resemble the ones of Ref. 24, Fig. 4, measured at 50-eV photon energy. Binding energies in Fig. 2(d) are 2.75 eV for thicknesses below 1 ML and 2.8 and 3.25 eV at 1 ML. The merging of peaks between 1 and 2 ML is somewhat less

pronounced than for Cu/Ni(100) in Fig. 2(c). Measured energy positions have been summarized in Table I.

We want to discuss the relevance of the present data for assessing the band width of Ni/Cu(100). All calculations find a substantial narrowing of the $3d$ band width for the Ni monolayer. It has been quantified as being by 30% narrower for the free Ni(100) monolayer.²⁶ Also on Cu(100), 1 ML Ni has with a FWHM of just 1.6 eV⁵ a very narrow $3d$ band,⁶

TABLE I. Peak positions determined in the experiment (binding energies in eV).

Thickness	Ni/Cu(100)	Co/Cu(100)	Cu/Ni(100)	Cu/Co(100)
1 ML	0.75 ($\bar{\Gamma}_1$), 0.3 ($\bar{\Gamma}_5$)	0.3 ($\bar{\Gamma}_1$)	3.2 ($\bar{\Gamma}_1$), 2.8 ($\bar{\Gamma}_5$)	3.25 ($\bar{\Gamma}_1$), 2.8 ($\bar{\Gamma}_5$)
Bulk	1.2 (Γ'_{25}), 0.4 (Γ_{12})	0.8 (Γ'_{25})	3.6 (Γ'_{25}), 2.9 (Γ_{12})	3.6 (Γ'_{25}), 2.9 (Γ_{12})

which is also narrower than the density of states of the interior Cu planes.⁷ We can compare our measured peak positions to the energy eigenvalues given in Refs. 5 and 7. The lowest measureable states in normal emission are $\bar{\Gamma}_1$ at 0.75 eV for 1 ML and Γ'_{25} at 1.15 eV for 6 ML. Experimental literature values for Γ'_{25} range from 1.1 to 1.2 eV.²⁵ Due to the particularly strong electron correlation in Ni, these values are much closer to the Fermi energy than energy eigenvalues from local-density theory, which range for Γ'_{25} from 1.97 to 2.15 eV (Ref. 25). This correlation effect has to be considered in addition to the finite-size effect we are discussing here. Local-density theory gives for $\bar{\Gamma}_1$ of 1 ML Ni/Cu(100) 1.13 eV (Ref. 7) and 1.16 eV (Ref. 5) (minority-spin values are not given in Ref. 7). If we assume the same effect on $\bar{\Gamma}_1$ as on Γ'_{25} , we expect from photoemission a value around 0.65 eV for $\bar{\Gamma}_1$. This is very near to our experimental value of 0.75 eV. Thus, the behavior of the deepest measureable state at $\bar{\Gamma}$ and Γ with thickness, which changes from 0.75 to 1.15 eV from 1 to 6 ML in our experiment, is obviously well described by the theoretical change from 1.1 to 2 eV when electron correlation is taken into account. In this way, the experimental data corroborate local-density theory, which

obtains strong narrowing of the 3d band width in 1 ML Ni/Cu(100) with respect to bulk Ni.

We conclude that the electronic structure of all films studied reveals a strong dependence on thickness, including Ni/Cu(100). All systems show similar behavior with respect to the evolution of the electronic structure with thickness. States are probed simultaneously at $\bar{\Gamma}$ for monolayers and Γ for thicker layers, and by comparison to local-density theory, it is concluded that the band width increases substantially in going from monolayer to bulk. This corroborates the view that the dimensionality of transition-metal noble-metal overlayer systems mainly determines the character of the electronic states. Compared to this, the effect of hybridization should be negligible.

The results presented for the occupied electronic structure indicate that the electronic structure at the Fermi energy must also be different for the monolayer and thicker layers. This holds even more as the strong changes that the unoccupied electronic structure of Ni/Cu(100) undergoes with thickness have already been observed.⁹ The difference in conclusion between Ref. 2 and the present work might be connected to differences in thickness calibration. We see from Fig. 2(a) (e.g., the spectrum of 2.3 ML) that this difference does not need to be large. An underestimation of the thickness by one monolayer in Ref. 2 might be sufficient to explain the differences in conclusion.

-
- ¹Angle Resolved Photoemission, edited by S. D. Kevan (Elsevier, Amsterdam, 1992).
- ²G.J. Mankey, K. Subramanian, R.L. Stockbauer, and R.L. Kurtz, Phys. Rev. Lett. **78**, 1146 (1997).
- ³Z. Qu, A. Goonewardene, K. Subramanian, J. Karunamuni, N. Mainkar, L. Ye, R.L. Stockbauer, and R.L. Kurtz, Surf. Sci. **324**, 133 (1995).
- ⁴P. Srivastava, N. Haack, H. Wende, R. Chauvistré, and K. Baberschke, Phys. Rev. B **56**, R4398 (1997).
- ⁵Ding-sheng Wang, A.J. Freeman, and H. Krakauer, Phys. Rev. B **24**, 1126 (1981).
- ⁶J. Tersoff and L.M. Falicov, Phys. Rev. B **26**, 2270 (1982).
- ⁷H. Huang, X. Zhu, and J. Hermanson, Phys. Rev. B **29**, 6186 (1984).
- ⁸V. L. Moruzzi, J. F. Janak, and A. R. Williams, *Calculated Electronic Properties of Metals* (Pergamon, New York, 1978).
- ⁹F.J. Himpsel and O. Rader, Appl. Phys. Lett. **67**, 1151 (1995).
- ¹⁰Z.Q. Qiu, J. Pearson, and S.D. Bader, Phys. Rev. B **46**, 8659 (1992).
- ¹¹A. Clark, G. Jennings, R.F. Willis, P.J. Rous, and J.B. Pendry, Surf. Sci. **187**, 327 (1987).
- ¹²A.K. Schmid and J. Kirschner, Ultramicroscopy **42-44**, 483 (1992).
- ¹³U. Ramsperger, A. Vaterlaus, P. Pfäffli, U. Maier, and D. Pescia, Phys. Rev. B **53**, 8001 (1996).
- ¹⁴Hong Li and B.P. Tonner, Surf. Sci. **237**, 141 (1990).
- ¹⁵J. Shen, J. Giergiel, and J. Kirschner, Phys. Rev. B **52**, 8454 (1995).
- ¹⁶B. Hernnäs, M. Karolewski, H. Tillborg, A. Nilsson, and A. Mårtensson, Surf. Sci. **302**, 64 (1994).
- ¹⁷S.H. Kim, K.S. Lee, H.G. Min, J. Seo, S.C. Hong, T.H. Rho, and J.-S. Kim, Phys. Rev. B **55**, 7904 (1997).
- ¹⁸L.V. Pourovskii, N.V. Skorodumova, Yu.Kh. Vekilov, B. Johansson, and I.A. Abrikosov, Surf. Sci. **439**, 111 (1999).
- ¹⁹B. Müller, B. Fischer, L. Nedelmann, A. Fricke, and K. Kern, Phys. Rev. Lett. **76**, 2358 (1996).
- ²⁰R. Kläsches, Ph. D. thesis, Universität zu Köln, 1998.
- ²¹M.A. Thompson and J.L. Erskine, Phys. Rev. B **31**, 6832 (1985).
- ²²W. Clemens, T. Kachel, O. Rader, E. Vescovo, S. Blügel, C. Carbone, and W. Eberhardt, Solid State Commun. **81**, 739 (1992); W. Clemens, E. Vescovo, T. Kachel, C. Carbone, and W. Eberhardt, Phys. Rev. B **46**, 4198 (1992).
- ²³J. Noffke, W. Brunn, and K. Hermann, Z. Phys. B: Condens. Matter **29**, 353 (1978).
- ²⁴C. Carbone, E. Vescovo, R. Kläsches, W. Eberhardt, O. Rader, and W. Gudat, J. Appl. Phys. **76**, 6966 (1994).
- ²⁵O. Rader, W. Gudat, in Landolt-Börnstein, New Series III, Vol. 23C2, edited by A. Goldmann (Springer, Berlin, 1999).
- ²⁶Xue-yuan Zhu and J. Hermanson, Phys. Rev. B **27**, 2092 (1983).

Quantum well states in Ni/Cu/Ni spin valve structures

F. J. Himpsel^{a)}

IBM T. J. Watson Research Center, P. O. B. 218, Yorktown Heights, New York, 10598

O. Rader

BESSY, Lentzeallee 100, D-14195 Berlin, Germany

(Received 6 April 1995; accepted for publication 19 June 1995)

Quantized states are mapped in Ni/Cu/Ni(100) trilayer structures, which are taken as a more accurate rendering of spin valve devices than the bilayers studied previously. We find that an extra Ni overlayer affects the energy of quantized states in the Cu layer, explaining why the magnetic coupling is affected by the thickness of the magnetic layer, and how a phase difference may occur between magnetic coupling oscillations in trilayers and density of states oscillations in bilayers. The potential step that confines electrons to the Cu spacer is determined to be 0.9 eV. © 1995 American Institute of Physics.

Spin valve structures have attracted considerable attention as magnetic field sensors in reading heads for magnetically stored data.^{1,2} Their active element consists of two ferromagnetic layers, coupled by a nonmagnetic spacer. When an external magnetic field switches the orientation of the magnetic layers from antiparallel to parallel, the electrical resistance drops dramatically. This giant magnetoresistance effect can be an order of magnitude larger³ than the 2% magnetoresistance of bulk permalloy ($\text{Ni}_{0.8}\text{Fe}_{0.2}$) which represents the state of the art in magnetic reading heads. In the absence of an external field, the relative orientation of the ferromagnetic layers oscillates with the spacer thickness.⁴⁻⁶ The underpinnings of these effects can be found in the electronic structure of magnetic multilayers. Quantum well states have been observed in noble metal overlayers on ferromagnets.⁷ These states are spin polarized and thus able to transmit magnetic information across a noble metal.^{8,9} The periodic appearance of these states at the Fermi level E_F coincides with the periodic switching of the magnetic coupling in spin valves. A mechanism for generating spin polarized, quantized states has been proposed,^{7,9} where minority spin electrons are confined by reflection at the interfaces (see Fig. 1), whereas majority spin electrons are transmitted. Such a spin-dependent interface reflectivity plays an important role in many models of magnetoresistance.¹⁰

While there is strong circumstantial evidence that magnetic phenomena in spin valves are connected to quantum well states, it is desirable to close some gaps in the arguments. For instance, quantum well states near E_F have only been observed in "bilayer" structures which contain a single ferromagnetic layer and a nonmagnetic overlayer. These states are confined by a ferromagnet on one side and by vacuum on the other. In order to obtain the active element of a spin valve one needs to add a second ferromagnetic layer and produce a trilayer structure where the metal/vacuum interface is replaced by a metal/ferromagnet interface. The change in the boundary conditions will affect the real and imaginary part of the electron reflectivity, i.e., their confinement and their phase.⁹ For example, the schematic picture in Fig. 1 shows that a trilayer cannot support confined states in the antiparallel configuration. One interface reflects a par-

ticular spin, but the other does not. In the bilayer, the vacuum interface is always reflective. The phase shift is important for answering the simple question whether a quantized state at E_F corresponds to antiparallel or parallel coupling, or in between. Empirically, one finds a correlation with antiparallel coupling,^{5,7} comparing quantum well states in bilayers and the coupling in trilayers. Figure 1 implies for this case that the density-of-states maxima either disappear or exhibit a phase shift when going from bilayers to trilayers. We find that a magnetic overlayer causes phase shifts as large as 2π .

Another question associated with trilayers concerns the confinement of quantized states. Do they exist exclusively in the nonmagnetic spacer, or can they also form in the magnetic overlayer? Are there two sets of quantized states, one in the spacer, the other in the ferromagnet, or do they interact to form a common wave function? Experimental results on the coupling in trilayers indicate that the spacer layer thickness dominates their magnetic behavior, suggesting that quantized states primarily reside in the spacer. However, an influence of the magnetic layer thickness on the coupling has been found as well, and this effect exhibits a period expected from quantum well states in the ferromagnet.¹¹ Such states are clearly visible in our trilayer data.

The particular materials selected for our work, i.e., Cu/Ni, are motivated by applications in spin valves, where the

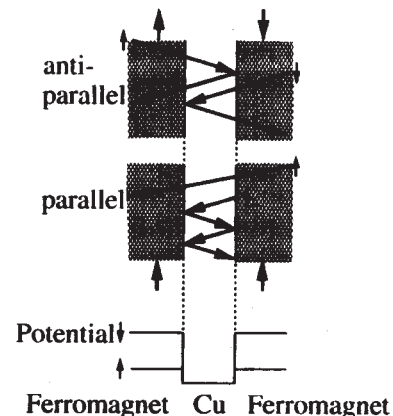


FIG. 1. Reflection of electrons at the interfaces of a spin valve for various magnetic configurations. The potential step confining electrons at E_F to the Cu layer is 0.9, 0.7, and 1.3 eV for fcc Ni, Co, Fe, resp. (spin-averaged) (Ref. 14). The exchange splitting between the majority and the minority spin potentials in the ferromagnets is 0.3, 1.0, 1.2, and 2 eV for Ni, Co, fcc Fe, and bcc Fe (Ref. 14).

^{a)}Electronic mail: himpsel@watson.ibm.com

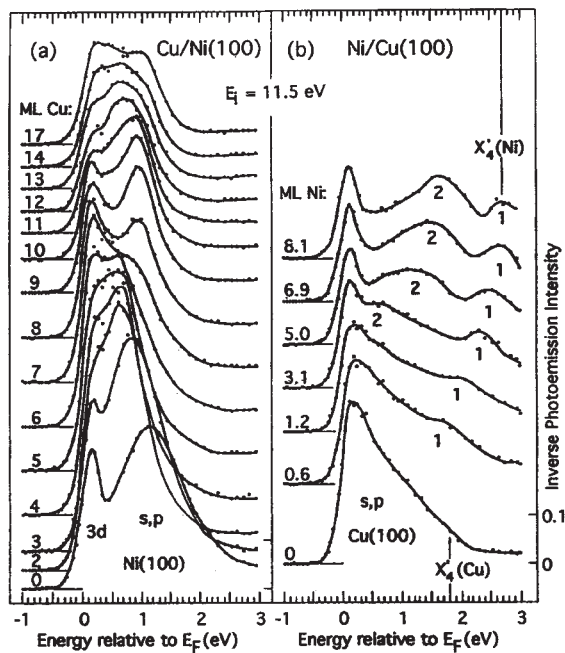


FIG. 2. Inverse photoemission spectra showing the density of unoccupied states for Cu layers on Ni(100) and vice versa. The bulk continuum (bottom curves) is discretized into quantum well states for thin overlayers. The thickness is given in monolayers (1 ML=1.8 Å).

magnetically soft $\text{Cu/Ni}_{0.8}\text{Fe}_{0.2}$ combination allows for low switching fields.¹ There exists early work¹² on quantized states in Ni/Cu/Ni(100) sandwich structures via low-energy electron transmission. The states observed with this technique lie above the vacuum level and are too far away from E_F to contribute to transport and magnetic phenomena. The previous analysis methods of electronic states in multilayer structures though are still applicable.

For optimally probing quantum well states in Ni/Cu/Ni structures we have chosen inverse photoemission at low incident electron energies (11.5 eV above E_F in normal incidence).¹³ Thereby, we minimize the main difficulty of this experiment, i.e., to avoid being swamped by the high density of Ni 3d states, which exceeds that of the *s,p*-like quantum well states by more than an order of magnitude. This has hampered spectroscopic studies of quantized states in trilayers up to now. Since most of the Ni 3d states are occupied, we look at unoccupied states with inverse photoemission and only have to deal with a narrow band of Ni 3d states within 0.25 eV of E_F .^{13,14} In addition, by playing the low cross section of Ni 3d states at low energies in our favor, we are able to suppress the Ni 3d peak at the Fermi level to a fraction of the *s,p*-band peak area [see the Ni(100) spectrum in Fig. 2]. The substrate crystals were prepared by mechanical and electrochemical polishing in order to obtain the smoothest possible surfaces. Overlayers were evaporated at room temperature in the low 10^{-10} Torr pressure range.

Figure 2 displays results for the Cu/Ni(100) and Ni/Cu(100) bilayer systems, which will serve as a reference for the Ni/Cu/Ni(100) trilayer data in Fig. 3. Ni on Cu(100) exhibits quantized states (numbered) that shift upwards with increasing energy and converge towards the upper edge of

the *s,p*-band at the X'_4 point of the Ni band structure.^{7,14} Similar behavior has been found for Co on Cu(100) and Cu on fcc Co(100) and Fe(100).⁷ From the asymptotic energy of the highest quantum well state for Ni on Cu(100) we obtain an energy of 2.7 eV above E_F for the X'_4 point in Ni. Together with the value of 1.8 eV for the X'_4 of Cu obtained from quantum well states in Cu overlayers⁷ we obtain a (spin-averaged) band offset of 0.9 eV between Cu and Ni. Such a band offset tends to confine electron states to the Cu layer (see Fig. 1). Cu on Ni(100) exhibits quantized states, also, but their energies exhibit an anomalous downwards shift with increasing thickness. Nevertheless, the first maximum in the density of states at E_F occurs for 5–6 monolayers Cu, the same as in Cu on fcc Co(100) and Fe(100). It also coincides with the first peak in the antiparallel coupling for Co/Cu/Co(100)⁵ and permalloy/Cu/permalloy(100)⁶ trilayers.

For Ni/Cu/Ni(100) trilayers we separate the two thickness variables by displaying spectra versus Ni thickness (at fixed Cu thickness) in Figs. 3(a)–3(c) and the reverse in Fig. 3(d). Three different Cu spacers of 3, 7, 9 monolayers are chosen in Figs. 3(a)–3(c) to represent the first maxima and minima in the oscillations of the density-of-states, the magnetic coupling, and the magnetoresistance. They have a 6 monolayer period for a Cu(100) spacer.^{5–7} The Ni overlayer has a strong effect on the phase of these oscillations. For example, the intensity at 1 eV in Fig. 3(c) goes through a full cycle as state 1 moves up and state 2 appears, implying a Ni-induced phase shift as large as 2π .

To characterize the quantized states in trilayers (numbered in Fig. 3) let us consider the following scenarios: Depositing Ni on a Cu layer could (1) quench all quantum states, (2) quench the Cu quantum states and create a new set of Ni quantum states, (3) preserve the Cu quantum states without creating Ni quantum states, (4) create two sets of quantum states, one in the Cu layer, the other in the Ni layer, or (5) form a single set of quantized states that extend throughout Cu and Ni with mixed Ni+Cu character. The data favor the last option, at least in the limit of thin Ni layers. The number of discrete states does not change after adding a 2 Å Ni layer as shown in Fig. 3(d). This rules out options (1) and (4). The Ni overlayer is thin enough that we should be able to see through it¹⁵ and detect any state remaining at the position of the Cu quantum state. For distinguishing between the remaining options (2), (3), and (5) we have to assess the Cu or Ni character of the states. Figure 3 shows that they cannot be purely Cu-like, since they shift up in energy with increasing Ni overlayer thickness. In fact, the uppermost state moves past the upper edge of the Cu *s,p* band at 1.8 eV (Fig. 3). The trilayer states cannot be purely Ni-like, either, since their energy does depend on the thickness of the Cu underlayer, as demonstrated in Fig. 3(d). These arguments leave only option 5, i.e., states extending throughout the Cu and Ni layers. The band structure¹⁴ of Cu(100) and Ni(100) allows electrons near E_F to propagate from Cu to Ni at zero parallel momentum, thus forming resonances instead of truly-confined states. A systematic analysis of the structures in Figs. 2 and 3 reveals that the trilayer states can be approximated by a set of Ni quantum well states on bulk Cu(100)

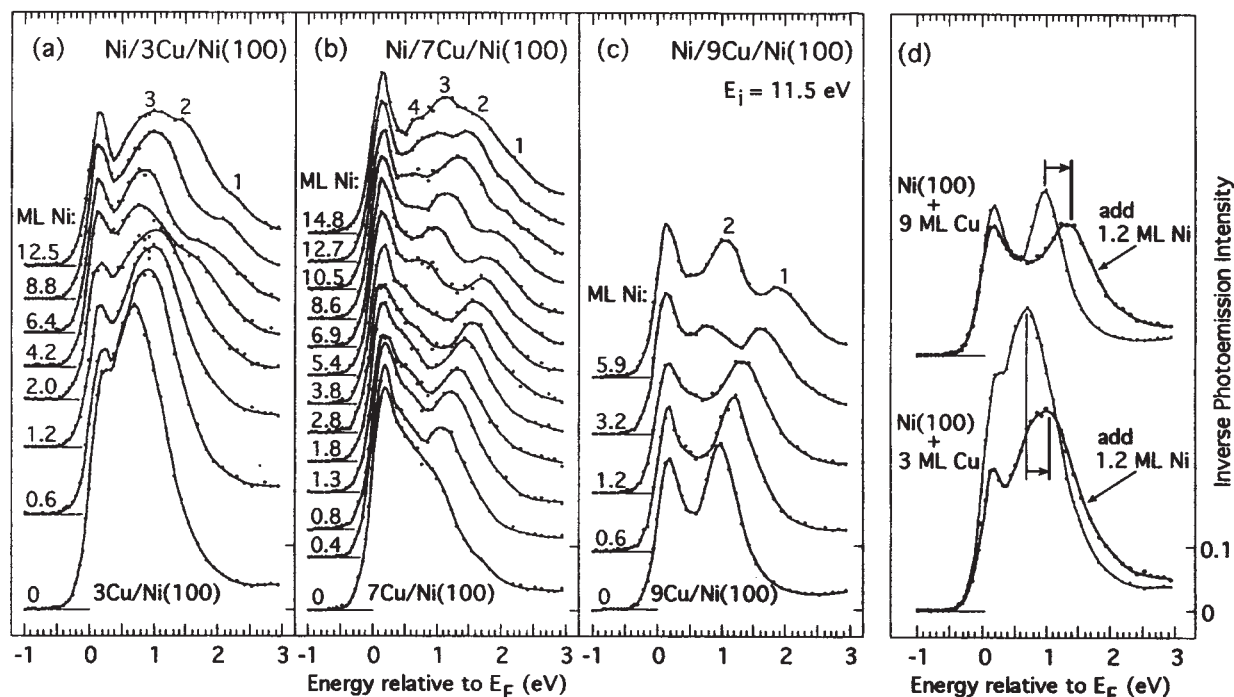


FIG. 3. Density-of-states spectra similar to Fig. 2 for Ni/Cu/Ni(100) structures that are representative of the active element of a spin valve. The three panels [(a)–(c)] are for Cu spacer layers with a thickness of 3, 7, and 9 monolayers and variable Ni thickness. Cu quantum well states are shifted by the Ni overlayer, demonstrating the influence of a second ferromagnetic layer. Panel (d) shows spectra with a fixed Ni overlayer thickness of 2 Å and variable Cu spacer thickness. The energy position of the states depends on the Cu spacer thickness, as well as on the Ni overlayer thickness showing that the states have both Cu and Ni character.

that is shifted down in energy as the thickness of either the Cu underlayer or the Ni overlayer decreases. Such behavior is characteristic of a well consisting of the combined Cu and Ni layers.

For thick Ni overlayers one would expect an asymptotic wave function in the Cu spacer that carries the magnetic coupling in spin valves. Truly-confined quantum well states below E_F reach the asymptotic limit after a few monolayers.¹⁶ We have resonances that can propagate as far as the mean free path for electrons near E_F , which is much longer than that of our probe electrons at 11.5 eV above E_F .¹⁵ Therefore, we cannot determine the full phase shift induced by a thick Ni overlayer in the Cu density of states.

In summary, we have determined the electronic structure of Ni/Cu/Ni(100) trilayers, which approximate spin valve devices better than the bilayers studied so far. The additional magnetic layer shifts the energy of quantum well states in the Cu spacer. This interaction between states in the spacer and the magnetic layer explains why the thickness of the magnetic layer can affect the magnetic coupling, and why magnetic oscillations in trilayers can be phase shifted with respect to density-of-states oscillations in bilayers.

O.R. acknowledges financial support from VdFFB.

¹ D. E. Heim, R. E. Fontana, C. Tsang, V. S. Speriosu, B. A. Gurney, and M. L. Williams, *IEEE Trans. Mag.* **30**, 316 (1994); T. L. Hylton, K. R. Coffey, M. A. Parker, and J. K. Howard, *Science* **261**, 1021 (1993).

² S. S. P. Parkin, *Appl. Phys. Lett.* **61**, 1358 (1992).

³ S. S. P. Parkin, Z. G. Li, and D. J. Smith, *Appl. Phys. Lett.* **58**, 2710 (1991); E. E. Fullerton, M. J. Conover, J. E. Mattson, C. H. Sowers, and S. D. Bader, *Appl. Phys. Lett.* **63**, 1699 (1993).

⁴ S. S. P. Parkin, R. Bhadra, and K. P. Roche, *Phys. Rev. Lett.* **66**, 2152 (1991).

⁵ J. J. de Miguel, A. Cebollada, J. M. Gallego, R. Miranda, C. M. Schneider, P. Schuster, and J. Kirschner, *J. Magn. Magn. Mater.* **93**, 1 (1991); Z. Q. Qiu, J. Pearson, and S. D. Bader, *Phys. Rev. B* **46**, 8659 (1992).

⁶ S. S. P. Parkin (unpublished).

⁷ J. E. Ortega and F. J. Himpsel, *Phys. Rev. Lett.* **69**, 844 (1992); J. E. Ortega, F. J. Himpsel, G. J. Mankey, and R. F. Willis, *Phys. Rev. B* **47**, 1540 (1993); *J. Appl. Phys.* **73**, 5771 (1993).

⁸ K. Garrison, Y. Chang, and P. D. Johnson, *Phys. Rev. Lett.* **71**, 2801 (1993); C. Carbone, E. Vescovo, O. Rader, W. Gudat, and W. Eberhardt, *Phys. Rev. Lett.* **71**, 2805 (1993).

⁹ P. Bruno, *Phys. Rev. B* **52**, 411 (1995); L. Nordström, P. Lang, R. Zeller, and P. H. Dederichs, *Europhys. Lett.* **29**, 395 (1995); J. Mathon *et al.*, *Phys. Rev. Lett.* **74**, 3696 (1995).

¹⁰ P. M. Levy, S. Zhang, and A. Fert, *Phys. Rev. Lett.* **65**, 1643 (1990); A. Barthélémy and A. Fert, *Phys. Rev. B* **43**, 13124 (1991); R. Q. Hood and L. M. Falicov, *Phys. Rev. B* **46**, 8287 (1992); A. C. Ehrlich, *Phys. Rev. Lett.* **71**, 2300 (1993).

¹¹ Q. Chen, M. Onellion, A. Wall, and P. A. Dowben, *J. Phys. Condens. Matter* **4**, 7985 (1992); P. J. H. Bloemen, M. T. Johnson, M. T. H. van Vorst, R. Coehoorn, J. J. de Vries, R. Jungblut, J. aan de Stegge, A. Reinders, and W. J. M. de Jonge, *Phys. Rev. Lett.* **72**, 764 (1994); P. Bruno, *Europhys. Lett.* **23**, 615 (1993).

¹² Q. G. Zhu, Y. Yang, E. D. Williams, and R. L. Park, *Phys. Rev. Lett.* **59**, 835 (1987); H. Iwasaki, B. T. Jonker, and R. L. Park, *Phys. Rev. B* **32**, 643 (1985).

¹³ F. J. Himpsel and Th. Fauster, *Phys. Rev. B* **26**, 2679 (1982); M. Donath, *Appl. Phys. A* **49**, 351 (1989).

¹⁴ For the bands of fcc, Cu, Co, Ni, Fe, see, G. J. Mankey, R. F. Willis, and F. J. Himpsel, *Phys. Rev. B* **48**, 10284 (1993); our value for X_4' in Ni is more precise than the previous result. For magnetic splittings see, F. J. Himpsel, *Phys. Rev. Lett.* **67**, 2363 (1991).

¹⁵ From the attenuation of the Cu signal by Ni overlayers we obtain a probing depth of about 7 Å at an electron energy 11.5 eV above E_F .

¹⁶ D. Li, J. Pearson, J. E. Mattson, S. D. Bader, and P. D. Johnson, *Phys. Rev. B* **51**, 7195 (1995).

Quantization of electronic states in a rare-earth film: Gd/W(110)

O. Rader¹ and A. M. Shikin^{1,2}

¹BESSY, Albert-Einstein-Str. 15, D-12489 Berlin, Germany

²Institute of Physics, St. Petersburg State University, St. Petersburg 198904, Russia

(Received 14 August 2001; published 6 November 2001)

A variety of distinct peaks occurs in photoemission spectra of ultrathin Gd on W(110) depending on the overlayer thickness, in particular a series of sharp peaks inside of a symmetry gap of the W band structure. Our phase-accumulation analysis assigns these structures to quantum-well states hitherto undetected in rare earths. This is of considerable importance since valence electrons mediate the magnetic coupling and determine the magnetic structure of rare-earth metals. As a first example of its impact, we demonstrate how the new quantum-well data help to resolve a current controversy concerning the nature of the Gd electronic structure.

DOI: 10.1103/PhysRevB.64.201406

PACS number(s): 73.21.Fg, 71.20.Eh, 79.60.-i

There are several examples for the interplay of localized magnetic moments with delocalized conduction electrons. In a spin-glass material, typically a solution of a magnetic $3d$ transition metal in a noble-metal host, the magnetic coupling between the localized magnetic moments is being mediated by s,p conduction electrons of the host metal. This Ruderman-Kittel-Kasuya-Yosida (RKKY) interaction is long-ranging and oscillatory with respect to the sign of the magnetic interaction. The one-dimensional rendering of such a system consists of two ferromagnetic layers separated by a noble metal spacer, and indeed these systems display long-range oscillations of their magnetizations.¹ In the course of studies of magnetic coupling phenomena in trilayers and multilayers the behavior of the s,p electrons in question could for the first time be observed directly as peaks with thickness-dependent energies and Fermi level crossings in direct and inverse photoemission spectra.²⁻⁴ It is possible to observe these states because they are the result of electron confinement in a two-dimensional overlayer between a ferromagnet-noble-metal interface and a noble-metal-vacuum interface and can be described as two-dimensional quantum-well states. Due to the large s,p band width they can be observed for thick noble-metal overlayers and represent an impressive visualization of the RKKY interaction.²⁻⁷ Meanwhile, quantum-well-state formation has been incorporated into interlayer-coupling theory⁸ and photoemission spectra are now being used to measure fractions of monolayer thicknesses, oscillation periods, interface phase shifts, lifetimes, and Fermi surface dimensions with extreme precision.⁷

A role analogous to the one of s,p electrons in a spin glass is being played by s,d electrons in rare-earth metals. The localized $4f$ orbitals and magnetic moments interact via the itinerant $5d6s$ electrons. Although there is no atomic disorder like in the spin-glasses, this interaction gives rise to a variety of complicated magnetic structures. Among rare-earth metals, Gd is the only simple bulk ferromagnet ($T_C = 293$ K), it has a half-filled $4f$ shell and is trivalent ($5d^16s^2$). Photoemission studies of the Gd band structure led to different conclusions.⁹⁻¹¹ Strong deviations between measurements and calculated bands have been attributed to lifetime broadening^{9,11} and to strong electron correlation.¹⁰ Interestingly, the first systems for which oscillatory magnetic interlayer coupling has been observed are Gd/Y and Dy/Y

multilayers, and many more rare-earth systems have been established in the meantime like Gd/Dy and Dy/Lu.¹² In view of the large number of photoemission studies on thin and ultrathin rare-earth films, it is remarkable that quantum-well-state formation has to date remained undetected in rare-earth materials. The only systematic thickness dependent study published suggests no interesting structure in valence-band photoemission from 2 to 10 Å Gd/W(110).¹³ The identification of quantum-well states of the s,d electrons in rare-earth films could represent an important step in the description of the interlayer coupling and of the magnetic structure of superlattices, alloys and of the pure rare-earth metals in general. Through the analogy of RKKY interaction in three dimensions and quantum-well state formation in two dimensions it is possible to introduce *via* the quantum-well thickness the distance as parameter and study the RKKY interaction with spin-resolved or magnetic dichroism spectroscopy. As a first application we show how the reduced momentum broadening enables us to determine critical point energies which are important for the question of strong correlation effects of Gd valence electrons.

We have studied ultrathin epitaxial films of Gd on W(110). The W(110) substrate has been heated in oxygen and flashed *in situ* for cleaning. The presence of a sharp $p(1 \times 1)$ low-energy electron diffraction (LEED) pattern and absence of C1s and O1s photoemission intensity have been verified before overlayer deposition. Gd has been evaporated by electron-beam heating and deposited onto the substrate at room temperature. An oscillating quartz has been used for calibration of the deposited thickness. The growth of Gd on W(110) at $T=300$ K occurs layer by layer up to 3 monolayers (ML) at room temperature¹⁴ (for recent scanning tunneling microscopy images see Ref. 15). The spectra in the present work have been measured at 300 K after annealing to 650 K in order to improve crystallinity while keeping island formation at a limited level. Linearly polarized synchrotron radiation from the U125/1-PGM undulator beamline¹⁶ at BESSY II has been used for excitation of photoelectrons. The surface-projected light-polarization vector was along $[110]$ leading to mixed ($s+p$) polarization. A VG Escalab MK2 photoemission analyzer has been used at 1° angle resolution in normal emission.

Figure 1 shows photoemission spectra taken at 62.5 eV photon energy and 300 K. The bottom displays a spectrum of

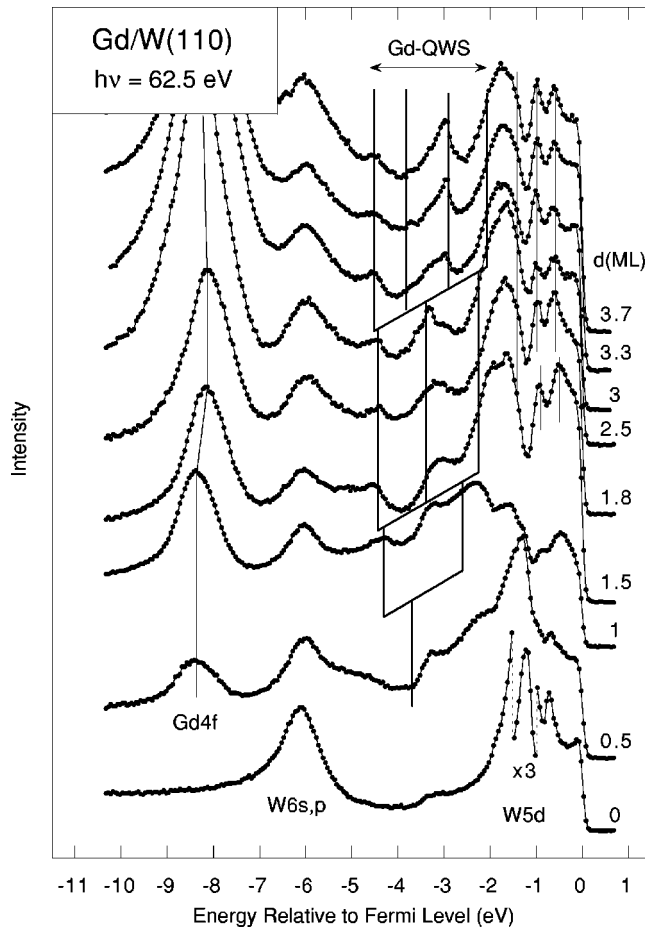


FIG. 1. Photoemission spectra of Gd/W(110) for various Gd coverages. Quantum-well states appear below -2 eV. Apart from Gd4f all vertical lines are theoretical energy positions taken from Fig. 2 for 1, 2, 3, and 4 ML.

the W(110) substrate. No C1s photoemission could be detected, therefore the peak at -6 eV, which is also characterized by corresponding dispersion with photon energy, is assigned to W 6s,p states (Σ_5^1). Intensive emission from a W5d surface resonance is seen around -1.3 eV.¹⁷ Growth of the Gd overlayer is at first seen from Gd4f emission centered around -8.4 eV. This binding energy stays constant up to 1.0 ML and moves to -8.2 eV at 2 ML. This behavior is typical of shallow core levels of electropositive adsorbates like alkali metals.¹⁸ In the present context, the Gd4f shift indicates completion of 1 ML and in this way serves for confirmation of the coverage given to the right-hand side of Fig. 1 on the basis of the quartz calibration of the evaporator.

The 1-ML spectrum is dominated by a new peak in the region -2.2 to -2.5 eV. In addition, a smaller peak at -4.3 eV is only present for this coverage. These two peaks disappear at 1.5-ML deposition in favor of new peaks at -4.5 and -3 eV. At 2.5 ML, a sharp peak appears at -3.35 eV. (The strong changes of the spectral shape occurring in the range between -2 eV and E_F will be the subject of a separate publication.¹⁹) At 3 ML, a new sharp peak appears at -2.95 eV and simultaneously the peak at lower energy shifts from -4.5 to -4.6 eV. While the peak at -2.95 eV grows

(3.3-ML nominal thickness), a small peak appears at -3.7 eV, and the rest of the spectrum remains unchanged for 3.3 and 3.7 ML.

The W band structure displays an even-symmetry bulk band gap from -6.3 to -2.0 eV at the center of the (110) surface Brillouin zone.¹⁷ As a result, the interaction of the overlayer electronic structure with the substrate is reduced, and electron confinement and formation of quantized states can be expected. For details see Refs. 20–22 where this has been demonstrated for Ag and Au overlayers on W(110). Gd is well suited for quantum-well formation on W(110) since, according to local-density calculations of the band structure,²³ in the energy range of the W gap, the $\Delta_{1,2}$ bulk bands of Gd 5d6s electrons appear between ≈ -2 and -4.9 eV.

However, attempts to measure this dispersion in photoemission experiments on in bulk and bulklike films of Gd met difficulties leading to a controversy as for the nature of the Gd electronic structure. In a pioneering work, Himpsel and Reihl⁹ concluded that strong momentum broadening due to reduced electron-mean-free paths in Gd leads to an absence of bulk band dispersion in photoemission spectra. Critical point energies delivered by Ref. 9 were very different from calculated ones. Kim *et al.*¹⁰ studied the temperature-dependent exchange splitting of the Δ_2 band and determine a dispersion of 0.4 to 0.5 eV, smaller by a factor of 2 than predicted by local-density calculations. The discrepancy has been attributed to strong electron correlation.¹⁰ Most recently, Maiti *et al.*¹¹ assigned on the basis of spin-resolved photoemission at 120 K a broad structure around -2.5 eV to the A_1^+ -point of the bulk Brillouin zone reaching good agreement with the dispersion of local-density theory for the Δ_2^+ band. The broad line shape of this peak and the appearance of a second strong peak around -1.4 eV at 120 K (-1.8 eV at 300 K) present at all photon energies have been explained using simulations on the basis of momentum broadening.¹¹ According to Ref. 11, photoemission measurements are affected via a broadening of \mathbf{k}_\perp , the electron wave vector perpendicular to the sample surface, leading to a distribution of direct photoemission transitions. These appear as peak shapes smeared out plus extra peaks caused by high densities of states, in particular around -1.5 eV. Ref. 11 demonstrates this effect but falls short of determining critical point energies for the Gd valence band.

For a system quantized along the surface normal in such a way that the ground-state band is rendered discrete, broadening of \mathbf{k}_\perp does not affect the accuracy of photoemission measurements of the electronic structure as long as quantum-well peaks are sufficiently separated in energy. In fact, the peaks observed in the present work are well distinguishable and very sharp. Although the background shape is not known precisely enough for a peak fitting procedure, Fig. 1 shows already that peak widths will be of the order of only 0.2 eV FWHM.

The standard method to derive the bulk band structure from quantum-well data has been described in Ref. 7. This method, however, requires larger film thicknesses, a fact that does not reconcile with the limited range^{14,15} of layer growth of Gd/W(110). The way we pursued in the present work is to

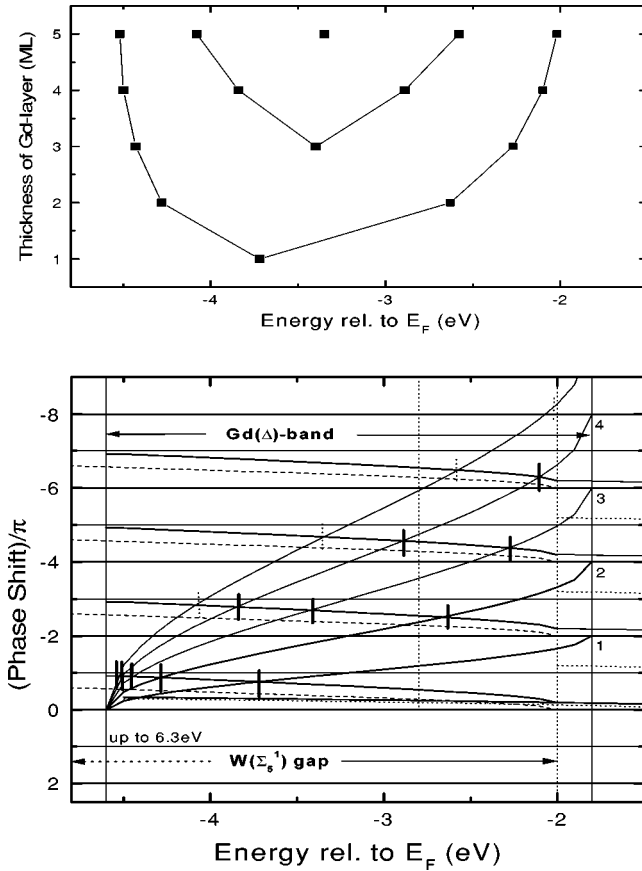


FIG. 2. Phase accumulation approximation for Gd/W(110). Predicted energy positions (top) and graphical solutions (bottom) of the quantum-well model for thicknesses of 1, 2, 3, 4, and 5 ML Gd/W(110).

analyze measured peak positions also based on the phase accumulation model which has been very successful in describing quantum-well states.²⁴ We used a certain simplification of the model introduced in Ref. 20, where as the only parameters the upper and lower edges of the valence band are demanded for determining quantum-well-state energies. These parameters can therefore be determined from comparison to the experiment to high accuracy.

In brief, the phase accumulation analysis is based on the Bohr–Sommerfeld quantization rule for the phases accumulated under reflection (i) at the surface potential barrier (Φ_B), (ii) at the energy gap in the substrate projected onto the interface (Φ_C), and (iii) during propagation of the electron through the overlayer, where quantum-well states are formed as a result of electron confinement due to this reflection:

$$\Phi_B + \Phi_C + 2ka_0N = 2\pi n, \quad (1)$$

where k is the wave vector of an electron propagating in an overlayer of thickness a_0N (a_0 is the interlayer spacing and N the number of adsorbed layers). The total phase accumulation must be an integral multiple of 2π . For the Gd/W(110) system we have the following situation: Below -2 eV is the region of the Gd states of $\Delta_{1,2}$ symmetry.²³ We use one Δ band unfolded according to Ref. 9. As for the W band structure, the region between -6.3 and -2.0 eV is characterized

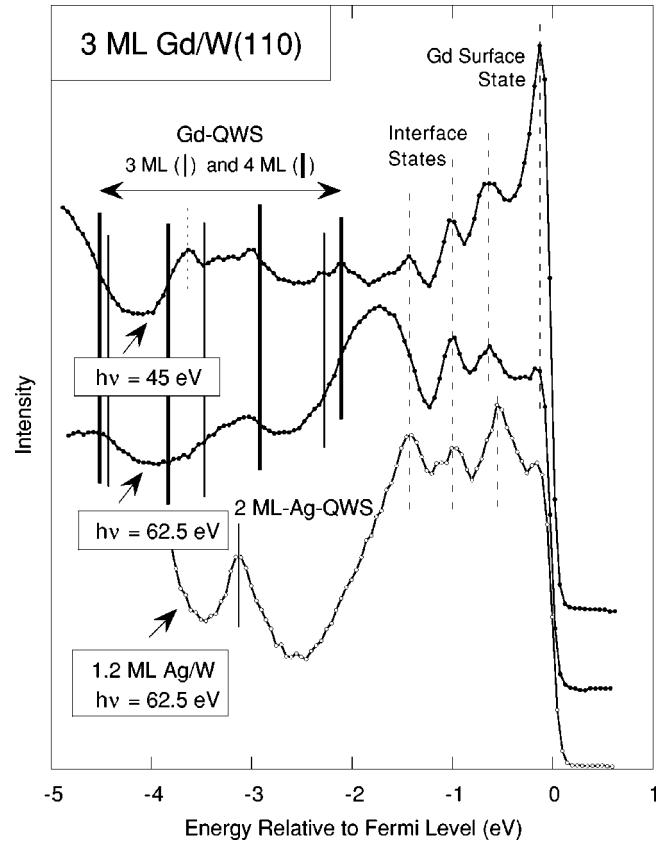


FIG. 3. Comparison for different photon energies for 3 ML nominal Gd coverage. Determination of the quantum-well peak at -2.1 eV is possible from the $h\nu=45$ eV data. Comparison to 1.2 ML Ag/W(110) shows that other sharp peaks (i. e., between -1.4 eV and E_F) are not derived from the Gd band structure and must not be included in the quantum-well analysis.

by an energy gap for Σ_5^1 states.¹⁷ This is the classical situation for formation of quantum-well states in the overlayer due to practically total reflection of electron waves at the Gd surface and Gd/W-interface.

For Φ_B and Φ_C we use the formulas given in Ref. 24, but for the term $2ka_0N$ we take, like in Ref. 20, the expression used in the linear chain approximation²⁵ and obtain

$$2ka_0N = 2 \arccos\left(1 - \frac{2E}{E_U - E_L}\right) \cdot N, \quad (2)$$

where E_U and E_L are the upper and lower band edges in the Gd. Equation (2) has already proven appropriate during analysis of Ag and Au quantum-well states on W(110).²⁰ In Fig. 2, these dependencies are shown for 1, 2, 3, 4, and 5-ML Gd: Intersections of $\Phi_B + \Phi_C - 2\pi n$ (thick solid curves) with $-2ka_0N$ (solid curves) give the graphical solutions of Eq. (1), which are marked by ticks in Fig. 2 (bottom) and by squares in Fig. 2 (top). These are the same energies as those used in Fig. 1. The good agreement with experiment corroborates the quantum-well-derived nature of the features observed in this energy region. We determine the Γ_{4-} point as -1.8 eV and the bottom of the band, Γ_{1+} ,

which has never been determined, as -4.6 eV. These room-temperature values are in good agreement with those from local density calculations.²³

This indicates that momentum broadening is indeed the prime factor obstructing measurements of the band structure in rare earths. Besides broad peak shapes, the appearance of an extra peak around -1.8 eV at 300 K (-1.4 eV at 120 K) at all photon energies from 34 to 50 eV has been noted as a consequence in Ref. 11. Figure 1 is not well suited for demonstrating that this can also be overcome in our quantum-well system because 62.5 eV corresponds to transitions near the hcp Γ point. It is crucial for our analysis to extract the upper quantum-well energy from the data. (Towards the middle of the band, agreement is certainly expected to worsen since the exact shape of the band is not included in our model.) To this end, Fig. 3 displays a spectrum measured at 45 eV for comparison. The broad peak around -1.5 to -2 eV that appears for $h\nu=62.5$ eV is absent for 45 eV. Instead, the upper quantum-well peak can be located at precisely -2.1 eV. Note that the vertical lines in Fig. 3 mark the same theoretical energies for 3 and 4 ML as in Figs. 1 and 2. (Inclusion of results for 2 ML was not considered in view of the broad spectral shape seen in Fig. 1.) The peak at -3.7 eV could be assigned to a small amount of hydrogen contamination on the basis of the energy position (-3.8 eV in Ref. 26).

Figure 3 also shows why -2.1 eV is the uppermost quantum-well energy and the peaks at -1.4 , -1.0 , and -0.65 eV are not included in the quantum-well analysis. Local density bands suggest already that they are not due to Gd bulk bands.²³ The clean W(110) spectrum (see bottom of Fig. 1) gives no clue as to the origin of these states possibly due to dominating intensity from the surface resonance at -1.3 eV. Therefore, we compare to data of 1.2 ML Ag/W(110), $h\nu=62.5$ eV, displaying the -1.4 and -1.0 eV peaks as well, which, therefore, cannot be assigned to Gd.¹⁹

We conclude that quantum-well state formation has for the first time been observed in a rare-earth system. We show that constraints caused by strong momentum broadening in photoemission studies of the band structure of rare earths are lifted in the present quantum-well system. Correlation effects on the valence band are negligible. Under these conditions, direct observation of the states that cause the RKKY interaction as a function of the interaction distance will in the future be extremely useful to understand how the electronic structure determines the magnetic structure of rare earths.

We thank R. Follath for expert support with the U125 beamline. We are grateful to C. Pampuch and G. Prudnikova for collaboration in part of this work. Part of this work has been performed in the framework of the RFFI project No. 01-02-17287.

-
- ¹See, e. g., the review by P.J.H. Bloemen, *Act. Phys. Pol. A* **89**, 277 (1996).
- ²J.E. Ortega and F.J. Himpsel, *Phys. Rev. Lett.* **69**, 844 (1992); F.J. Himpsel *et al.*, *Adv. Phys.* **47**, 511 (1998).
- ³K. Garrison, Y. Chang, and P.D. Johnson, *Phys. Rev. Lett.* **71**, 2801 (1993).
- ⁴C. Carbone *et al.*, *Phys. Rev. Lett.* **71**, 2805 (1993).
- ⁵C. Carbone *et al.*, *Solid State Commun.* **100**, 749 (1996).
- ⁶J.J. Paggel, T. Miller, and T.C. Chiang, *Science* **283**, 1709 (1999).
- ⁷T.C. Chiang, *Surf. Sci. Rep.* **39**, 183 (2000).
- ⁸P. Bruno, *Phys. Rev. B* **52**, 411 (1995).
- ⁹F.J. Himpsel and B. Reihl, *Phys. Rev. B* **28**, 574 (1983).
- ¹⁰B. Kim, A.B. Andrews, J.L. Erskine, K.J. Kim, and B.N. Harmon, *Phys. Rev. Lett.* **68**, 1931 (1992).
- ¹¹K. Maiti, M.C. Malagoli, E. Magnano, A. Dallmeyer, and C. Carbone, *Phys. Rev. Lett.* **86**, 2846 (2001).
- ¹²J. Kwo *et al.*, *Phys. Rev. Lett.* **55**, 1402 (1985); M.B. Salamon *et al.*, *ibid.* **56**, 259 (1986); R.E. Camley *et al.*, *ibid.* **64**, 2703 (1990); R.S. Beach *et al.*, *ibid.* **70**, 3502 (1993).
- ¹³Dongqi Li *et al.*, *J. Magn. Magn. Mat.* **99**, 85 (1991).
- ¹⁴J. Kołaczkiwicz and E. Bauer, *Surf. Sci.* **175**, 487 (1986).
- ¹⁵E.D. Tober *et al.*, *Phys. Rev. B* **53**, 5444 (1996); R. Pascal *et al.*, *ibid.* **56**, 3636 (1997).
- ¹⁶R. Follath, F. Senf, and W. Gudat, *J. Synchr. Rad.* **5**, 769 (1998); R. Follath, *Nucl. Meth. Instr. A* **467-468**, 418 (2001).
- ¹⁷R.H. Gaylor and S.D. Kevan, *Phys. Rev. B* **36**, 9337 (1987); J. Feydt *et al.*, *ibid.* **58**, 14 007 (1998).
- ¹⁸G.K. Wertheim, D.M. Riffe, and P.H. Citrin, *Phys. Rev. B* **49**, 4834 (1994).
- ¹⁹O. Rader, C. Pampuch, G. V. Prudnikova, and A. M. Shikin (unpublished).
- ²⁰A.M. Shikin *et al.*, *Phys. Rev. B* **62**, R2303 (2000); A.M. Shikin, D.V. Vyalikh, G.V. Prudnikova, and V.K. Adamchuk, *Surf. Sci.* **487**, 135 (2001); A.M. Shikin, O. Rader, G.V. Prudnikova, V.K. Adamchuk, and W. Gudat (unpublished).
- ²¹H. Knoppe and E. Bauer, *Phys. Rev. B* **48**, 5621 (1993).
- ²²J. Feydt *et al.*, *Surf. Sci.* **452**, 33 (2000).
- ²³Note that exchange splitting and energy positions have a pronounced temperature dependence (Ref. 10). We used, therefore, the average of the spin-resolved ASW bands from W. Nolting, T. Dambeck, and G. Borstel, *Z. Phys. B: Condens. Matter* **94**, 409 (1994), -2.0 eV for Γ_{4-} and -4.9 eV for Γ_{1+} , to compare to our room-temperature data.
- ²⁴N.V. Smith, *Phys. Rev. B* **32**, 3549 (1985); N.V. Smith *et al.*, *ibid.* **49**, 332 (1994).
- ²⁵M. Grüne *et al.*, *J. Electron Spectrosc. Relat. Phenom.* **98-99**, 121 (1999).
- ²⁶D. Li, J. Zhang, P.A. Dowben, and M. Onellion, *Phys. Rev. B* **48**, 5612 (1993).

Paper IV

Photoemission from Stepped W(110): Initial or Final State Effect?

A. M. Shikin,^{1,2} A. Varykhalov,¹ G. V. Prudnikova,² V. K. Adamchuk,² W. Gudat,^{1,3} and O. Rader^{1,*}

¹BESSY, Albert-Einstein-Str. 15, D-12489 Berlin, Germany

²Institute of Physics, St. Petersburg State University, St. Petersburg, 198504 Russia

³Institut für Physik, Universität Potsdam, P. O. Box 601553, D-14415 Potsdam, Germany

(Received 9 March 2004; published 29 September 2004)

The electronic structure of the (110)-oriented terraces of stepped W(331) and W(551) is compared to the one of flat W(110) using angle-resolved photoemission. We identify a surface-localized state which develops perpendicular to the steps into a repeated band structure with the periodicity of the step superlattices. It is shown that a final-state diffraction process rather than an initial-state superlattice effect is the origin of the observed behavior and why it does not affect the entire band structure.

DOI: 10.1103/PhysRevLett.93.146802

PACS numbers: 73.20.At, 79.60.Bm

Single-crystal surfaces that bear, due to a controlled surface miscut, a regular superlattice of steps are envisaged as adequate templates for the growth of a large number of identical nanostructures like quantum wires and quantum stripes [1]. In this context, vicinal W(110) has developed into an important stepped substrate and controlled growth of nanostructures like stripes formed of Fe has led to novel magnetic anisotropy and coupling phenomena like perpendicular magnetization and dipolar antiferromagnetism [2,3]. These new accomplishments in nanomagnetism occur on a relatively large length scale (e.g., 8 nm) and make use of magnetic dipole interactions. They have not, so far, utilized size quantization of electronic states as were found essential for the magnetic interlayer coupling in two-dimensional films [4]. Whether or not such effects will in the future be used depends on the ability of the stepped substrate to support quantization effects in the electronic structure. The method of choice to test this is angle-resolved photoemission since it provides the electronic structure including band dispersions [5]. The stepped surfaces most extensively studied to date are the (111) vicinals of fcc Cu and Au where surface state electrons in a narrow bulk band gap at the L point are probed [6–11]. Different types of behavior have been obtained: the wave functions were either spread out over the macrosurface [6,10,11] or localized at the microsurface [9], and a switch over from two-dimensional to one-dimensional behavior was observed at a step width of ~ 17 Å [8]. Most recently, we have analyzed data from carbon nanostripes on stepped Ni(771) and observed intense final-state effects due to so-called umklapp scattering at the superlattice of steps and stripes [12] and similar effects occur also in the data from vicinal Au(111) [13]. In the umklapp picture, the photoelectron can undergo scattering at the surface lattice when leaving the crystal and acquire an extra reciprocal surface lattice vector \mathbf{G}_{\parallel} according to $\mathbf{k}_{\parallel,\text{vac}} = \mathbf{k}_{\parallel,\text{crystal}} + \mathbf{G}$ which leads to observable effects especially when the surface periodicity differs from the one of the bulk [14].

The aim of the present work is to clarify the presence of one- or two-dimensional behavior and initial- or final-state effects on stepped W(110). W is in principle well suited since theory predicts a substantial portion of the W density of states surface-localized [15] although the identification of surface states in an experiment is often complicated and has on W been achieved only for a small number of cases. While experimental data are still outstanding, theory went ahead predicting, e. g., that W surface states will be responsible for the observed oscillatory stability conditions of W steps [16].

In this Letter, we will demonstrate strong superlattice effects fulfilling the periodicity of the step superlattice. By angle- and energy-dependent measurements in photoemission and in low-energy electron diffraction (LEED), we show that the observed behavior is due to a final-state diffraction effect at the step superlattice instead of a superlattice bandstructure effect on the initial states. We have chosen the (331) and (551) surfaces characterized by terrace widths of three and five W lattice constants, respectively, or 0.948 and 1.58 nm. Figure 1 shows the surface atom arrangement for these surfaces and a comparison of the surface Brillouin zones of flat and stepped W(110). The miscut angle amounts to 13° for W(331) and 8° for W(551) along the [001] direction leading to step edges oriented along $[1\bar{1}0]$. Our samples have been prepared as usual [17] until LEED showed sharp 6×1 and 10×1 superstructures for W(331) and W(551), respectively. Photoelectrons were excited with linearly polarized synchrotron light at the U125/1 and UE56/1 PGM beamlines [18] at BESSY. A spherical electron analyzer has been used at 1° angle resolution and 50–150 meV combined (photon and electron) energy resolution in a vacuum of 2×10^{-10} mbar.

Figure 2 displays angle-resolved photoemission spectra of W(331) for \mathbf{k}_{\parallel} vectors parallel (a) and perpendicular (b) to the step direction at 62.5 eV photon energy for different polar angles. (We relate all polar angles θ to the [110] microsurface normal.) At the bottom, Fig. 2 shows for the sake of comparison normal-emission spectra from

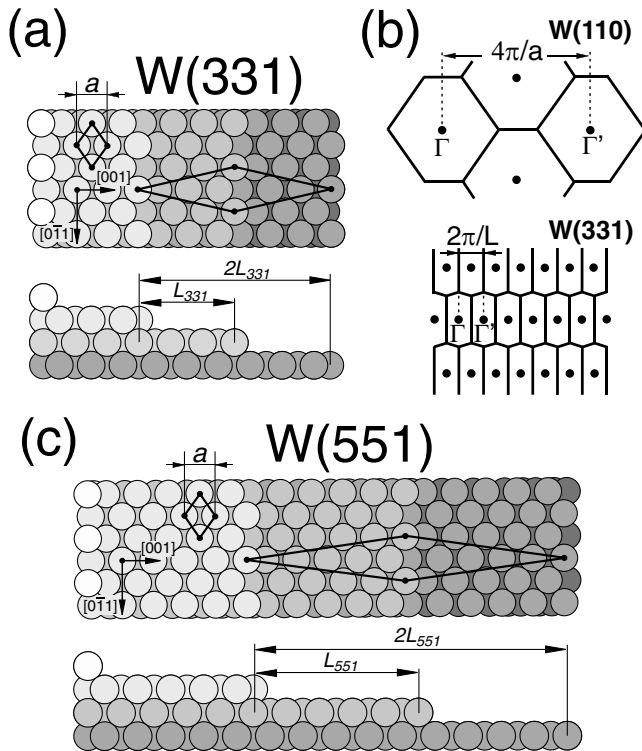


FIG. 1. Geometry of W(331) (a) and relation of its surface Brillouin zone to the one of flat W(110) (b). The steps run perpendicular to the [001] or Γ -H direction and are by a factor of 5/3 wider on W(551) (c).

flat W(110) measured in such a way as to ensure the same measurement conditions as for the vicinals [i. e., the \mathbf{E} -vector of the light points along $[0\bar{1}1]$ in Fig. 2(a) and along [001] in Fig. 2(b)]. Prominent features identified earlier on W(110) are an intense surface-resonance (SR) at 1.2 eV for $\bar{\Gamma}$ [17,19] and bulk emission from the top of the Σ_1 band which is sampled near the N_1 point of the bulk Brillouin zone when excited around 63 eV photon energy. The comparable spectrum in the emission-angle series from W(331) in Fig. 2, i. e., the one for emission along the microsurface normal [110], is colored red. For \mathbf{k}_{\parallel} parallel to the steps [Fig. 2(a)], peak S is seen to disperse symmetrically about the red spectrum. Surface-resonance emission at 1.2 eV can in principle be assigned by comparison to W(110) [19], but the small intensity on the stepped surface suggests that bulk emission may actually dominate the peak.

The [110]-normal-emission spectra display strong differences: For W(331), the Σ_1 band does not appear at 6 eV as for W(110) but at 5.2 eV where states are *forbidden in bulk W* due to the large gap (6.2 to 3.3 eV) for emission along [110] [17,19].

The top panel of Fig. 4 indicates the presence of a surface-resonance which has not yet been reported inside or near this gap: The dispersion measured at 62.5 eV gives only an indication for this since it comprises degenerate

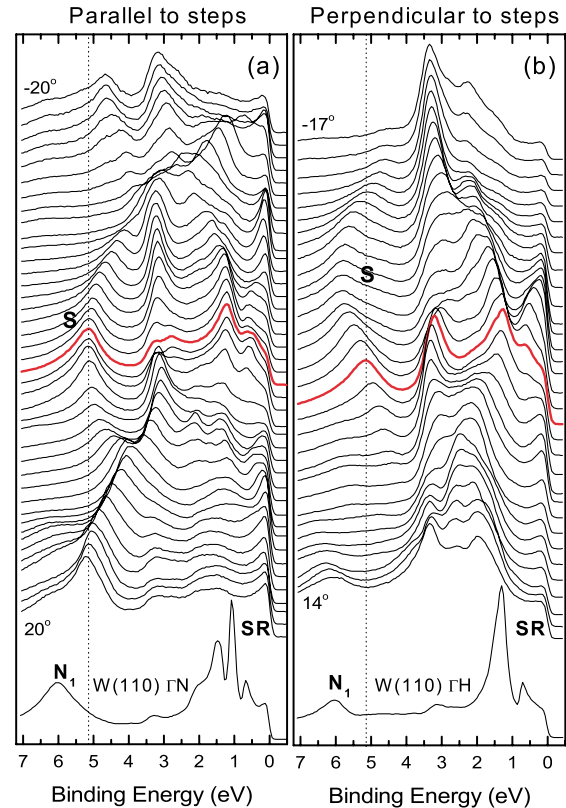


FIG. 2 (color online). Angle-dependent photoemission spectra of W(331) parallel (a) and perpendicular (b) to the step direction for 62.5 eV photon energy. The bottom of the band labeled S appears 6° away from the microsurface normal.

bulk and surface bands. At 110 eV photon energy, however, the Γ point is reached and the bulk-derived emission corresponds to the band bottom at 9 eV. No other emission from W bulk states is expected in normal-emission in the whole energy range from 9 eV up to the border of the band gap at 3.3 eV. Nevertheless, a second dispersion has remained at 5.8 eV and is identified with surface emission. Its dispersion with \mathbf{k}_{\parallel} follows closely the shape of the bulk band gap according to the surface projection of the bulk bands (solid line) calculated in Ref. [20].

Returning to Fig. 2, we note that in the direction perpendicular to the steps, the 5.2 eV peak disperses downwards and assumes a minimum energy of 6 eV up the stairs at about 6° off normal, i. e., at this angle the same energy is reached as for normal-emission on flat W(110). Figure 3 allows for a better judgement of this behavior: Figs. 3(a)–3(c) are a color-scale representation of photoemission spectra at 50, 62.5, and 125 eV photon energy for different polar emission angles perpendicular to the steps. When changing the photon energy, we move in terms of the W bulk band structure along the [110]- or Σ -direction away from the N point (~ 63 eV) towards Γ [19]. At 62.5 eV photon energy, we observe one branch S with binding energy between 4 and 6 eV, shifted away from the microsurface normal. At 50 eV, we observe addi-

tionally a second branch at positive emission angles, S^* . At 125 eV, both branches S and S^* are equally pronounced and shifted approximately symmetrically with respect to the microsurface normal.

Figure 4 allows us to determine the shift between the two dispersions as 0.66 \AA^{-1} . For W(551) we observe even more than two branches with a period of 0.40 \AA^{-1} . These values correspond exactly to the periods of the superlattice Brillouin zones of the two surfaces or, following a simple reasoning, to the distance from $\bar{\Gamma}$ to $\bar{\Gamma}'$ along [001] for W (4.0 \AA^{-1}) divided by the six-fold and ten-fold surface periodicities measured by LEED. In the Brillouin zone picture, the electron is assumed to hop across the steps and form Bloch waves along the macrosurface. This is the simplest interpretation in which the repetition of the band dispersion is due to band periodicity in the repeated zone scheme of the step superlattice. Such behavior would very well be compatible with our identification of the feature S as surface-resonance. This requires the wave function to be oriented parallel to the macrosurface [6,8], which means that in order to be an initial-state effect, the repeated $E(\mathbf{k}_{\parallel})$ dispersions for various photon energies must coincide when \mathbf{k}_{\parallel} is related to the macrosurface (i. e., $\mathbf{k}_{\parallel} = 0$ corresponds to the macrosurface normal) and deviate when \mathbf{k}_{\parallel} is related to the microsurface ($\mathbf{k}_{\parallel} = 0$ at the microsurface normal). Because of the large angles between macro- and microsurface of 13° for W(331) and 8° for W(551) the present experiment can unambiguously distinguish between the two cases. Both cases can be compared in a single figure [see the W(331) data in Fig. 4(b)]: Good agreement is reached for \mathbf{k}_{\parallel} related to the microsurface. That a plot relative to the macrosurface fails can be seen from the macrosurface normals for photon energies of 50, 62.5, and 105 eV which were inserted into Fig. 4 and are clearly separated. The one for 125 eV would appear outside of the figure frame. This shows that in its initial-state the electron occupying S remains localized at the one-dimensional microsurface and that the repetition of band S is not due to an initial-state effect.

In the LEED picture, the electron undergoes scattering in the final-state of the photoemission process. As this concept gives the same periodicity as the initial-state concept, we seek for further support for a final-state interpretation. This is found in the intensities of the two bands which vary strongly with photon energy so that at 62.5 eV the S^* branch even vanishes (Fig. 2). We have recorded LEED patterns *in situ* for comparable primary electron energies and display them in Fig. 3(d)–3(f) *vis-à-vis* the measured dispersions. The LEED spots (dispersions) are split for 44 eV (50 eV) and 125 eV (125 eV), and for 62.5 eV (62.5 eV) almost all of the intensity is concentrated in a single spot (band).

We want to discuss which model can appropriately describe this effect. The present experiment allows us to

relate the measured dispersions to the direction of the [110] microsurface normal given by the bulk-derived Σ_1 band in Fig. 3(c) and in Fig. 4. This is also very clearly seen in the original data of Fig. 2(b) where the peak at $\sim 1.5 \text{ eV}$ disperses around the microsurface normal. On the basis of a description by umklapp scattering at the step superlattice we expect a process according to $\mathbf{k}_{\parallel, \text{vac}} = \mathbf{k}_{\parallel, \text{crystal}} + \mathbf{G}$ with $\mathbf{G}_{331} = 0.66 \text{ \AA}^{-1}$ for W(331) and $\mathbf{G}_{551} = 0.40 \text{ \AA}^{-1}$ for W(551). Instead, if we identify the dispersion of band S on flat W(110) with $\mathbf{k}_{\parallel, \text{crystal}}$ and compare it with the dispersions on W(331) and W(551), we observe $\mathbf{k}_{\parallel, \text{vac}} = \mathbf{k}_{\parallel, \text{crystal}} \pm \mathbf{G}/2$ with the dispersion for $\mathbf{k}_{\parallel} = 0$ completely missing.

More appropriate is the description given for LEED from stepped surfaces [21]. Figure 3(b) of Ref. [21] shows how a single LEED spots splits up into two when the \mathbf{k} vector moves from the in-phase to the antiphase condition: The reciprocal lattice rods for scattering from a stepped surface are perpendicular to the macrosurface and therefore tilted with respect to the microsurface. Because they pass through the Γ point of W , scattering conditions remain unchanged there, but they separate at the N point (antiphase). This explains why in our experiment the dispersion S , which is located at the N point, appears split and the band bottom at 9 eV, which is located at the Γ point, remains single. As the photoemission transition determines the primary beam for electron scattering, it restricts the dispersions which appear repeated to those at the N point. This applies to bulk and surface bands but surface bands dominate the emission from the N point in the present case. We believe that the location at the N point in momentum space is the main cause of the

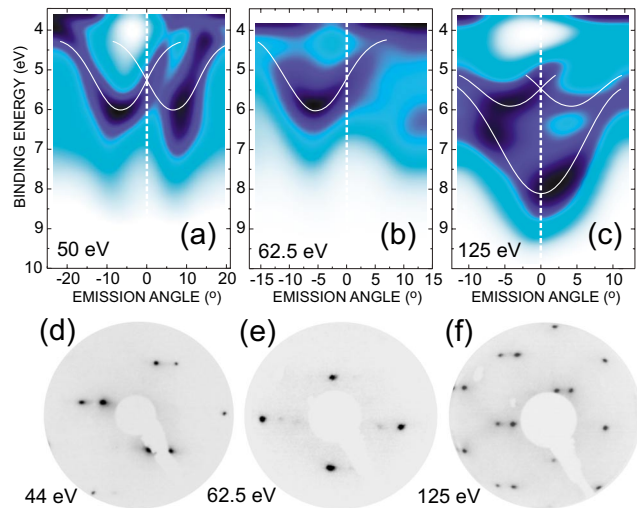


FIG. 3 (color online). Extraction of dispersions from photoemission spectra for W(331) (a–c) together with LEED patterns of similar intensity behavior (d–f). The emission angle is given with respect to the [110] microsurface normal.

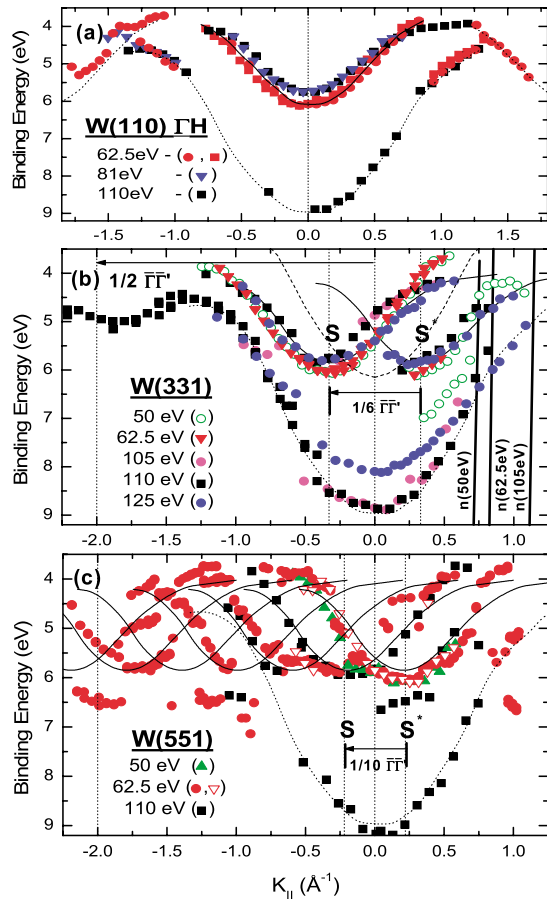


FIG. 4 (color online). Dispersion for \mathbf{k}_{\parallel} -vectors along 001 for W(110) (a) and for W(331) (b) and W(551) (c) i. e., perpendicular to the steps. \mathbf{k}_{\parallel} is given relative to the [110] microsurface normal. The macrosurface normal $n(h\nu)$ shifts strongly between 50 and 105 eV (125 eV outside of the frame) and is therefore not a reference for the repeated surface band S.

repetition of the band structure and that the surface localization is of secondary importance.

In conclusion, we identify a surface-localized feature on W(110) and stepped W(331) and W(551) that shows diffraction effects on a large intensity, energy, and momentum scale in agreement with the lateral superlattice translation vector. The data do not reconcile with an initial-state bandstructure effect of the superlattice but can be explained on the basis of electron scattering from stepped surfaces taking into account where in \mathbf{k} space the photoemission transition takes place. The result that

the repetition is a final-state effect and that the electron wave function is localized at the microsurface is an important prerequisite for tailoring electronic properties in one-dimensional nanostructures grown on stepped W substrates.

This work was supported through DFG (RA 1041/1-1 and 436RUS113/735/0-1), common DFG-RFFI Project No. 03-02-04-024, and the program "Surface and Atomic Structures" (Russia).

*Corresponding author. Electronic address: rader@bessy.de

- [1] R. Notzel *et al.*, Nature (London) **392**, 56 (1998).
- [2] J. Hauschild, U. Gradmann, and H.-J. Elmers, Appl. Phys. Lett. **72**, 3211 (1998).
- [3] O. Pietzsch *et al.*, Phys. Rev. Lett. **84**, 5212 (2000).
- [4] F. J. Himpsel *et al.*, Adv. Phys. **47**, 511 (1998).
- [5] *Angle-Resolved Photoemission*, edited by S. D. Kevan (Elsevier, Amsterdam, 1992).
- [6] A. P. Shapiro, T. Miller, and T.-C. Chiang, Phys. Rev. B **38**, 1779 (1988).
- [7] X. Y. Wang, X. J. Shen, and R. M. Osgood, Jr., Phys. Rev. B **56**, 7665 (1997).
- [8] J. E. Ortega *et al.*, Phys. Rev. Lett. **84**, 6110 (2000).
- [9] A. Mugarza *et al.*, Phys. Rev. Lett. **87**, 107601 (2001).
- [10] F. Baumberger, T. Greber, and J. Osterwalder, Phys. Rev. B **64**, 195411 (2001); F. Baumberger *et al.*, Phys. Rev. Lett. **92**, 16803 (2004).
- [11] K. Ogawa, K. Nakanishi, and H. Namba, Solid State Commun. **125**, 517 (2003).
- [12] A. M. Shikin *et al.*, Phys. Rev. Lett. **90**, 256803 (2003).
- [13] A. Mugarza *et al.*, Phys. Rev. B **66**, 245419 (2002).
- [14] E. O. Kane, Phys. Rev. Lett. **12**, 97 (1964); J. Anderson and G. J. Lapeyre, Phys. Rev. Lett. **36**, 376 (1976); D. Westphal and A. Goldmann, Surf. Sci. **126**, 253 (1983).
- [15] N. E. Christensen and B. Feuerbacher, Phys. Rev. B **10**, 2349 (1974).
- [16] Wei Xu, J. B. Adams, and T. L. Einstein, Phys. Rev. B **54**, 2910 (1996).
- [17] A. M. Shikin *et al.*, Phys. Rev. B **65**, 075403 (2002).
- [18] R. Follath, F. Senf, and W. Gudat, J. Synchrotron Radiat. **5**, 769 (1998); M. R. Weiss *et al.*, Nucl. Instrum. Methods Phys. Res., Sect. A **467-468**, 449 (2001).
- [19] R. H. Gaylord and S. D. Kevan, Phys. Rev. B **36**, 9337 (1987); J. Feydt *et al.*, Phys. Rev. B **58**, 14007 (1998).
- [20] K. W. Kwak, M. Y. Chou, and N. Troullier, Phys. Rev. B **53**, 13734 (1996).
- [21] M. Henzler, Appl. Phys. **9**, 11 (1976).

Electronic states and magnetism of monatomic Co and Cu wires

A. Dallmeyer, C. Carbone,* and W. Eberhardt

Institut für Festkörperforschung, Forschungszentrum Jülich, D-52425 Jülich, Germany

C. Pampuch, O. Rader, and W. Gudat

BESSY, Albert-Einstein-Straße 15, D-12489 Berlin, Germany

P. Gambardella and K. Kern

Institut de Physique Expérimentale, EPF-Lausanne, CH-1015 Lausanne, Switzerland

(Received 13 September 1999; revised manuscript received 29 November 1999)

The electronic structure of monatomic Cu and Co wires grown by step decoration of the vicinal Pt(997) surface has been investigated by angle-resolved photoemission with synchrotron radiation. Sensitivity to the small amount (≈ 0.1 monolayer) of deposited material that forms the one-dimensional wires could be achieved at photon energies close to the Pt 5*d* Cooper minimum, where the photoemission cross section of the substrate valence band is strongly reduced. A single photoemission feature is associated with the 3*d* emission from the Cu monatomic wire. A double-peaked 3*d* structure is instead observed for Co wires, suggesting the presence of a one-dimensional exchange-split band and of local magnetic moments.

The electronic structure and magnetic behavior of a material can be significantly modified by reducing its dimensions along one or more directions in space. Quantum-size effects give rise to electronic and magnetic properties for low-dimensional systems that have no counterpart in the bulk. The physical realization of these systems opens up the possibility of designing new kinds of materials (“atomic engineering of materials”). Nearly two-dimensional (2D) magnetic systems, such as ultrathin films and superlattices, have recently been the aim of intensive investigations.^{1,2} However, very little is known so far about the electronic and magnetic structure of systems with still lower dimensionality because of difficulties in their preparation and characterization.

The manipulation of single atoms and their displacement on surfaces has been demonstrated by scanning tunneling microscopy (STM). However, this technique does not permit the preparation of nanostructured large-area samples, which are required by standard methods for band structure determination, such as angle-resolved photoemission. Large-area samples with a structuring on a nanometer scale, in particular samples with monatomic chains, can be obtained by molecular beam epitaxy exploiting self-organization mechanisms of adatoms on suitable substrates.³ Examples of one-dimensional systems grown by self-organization include Cu, Pd, and Fe chains on Pd(110),^{3,4} and Gd on W(110).^{5,6} During the growth of Au on Ni(110), the development of a Au dimer-trimer chain structure has been observed.⁷ In this system the one-dimensionality of the Au-induced states could also directly be derived from their dispersion behavior.⁸ However, no information about the magnetic properties of 1D systems can be deduced in this case.

1D nanostructures can also be prepared by molecular beam epitaxy on stepped single-crystal surfaces that serve as a template for growing nanowires exploiting step decoration.^{9,10} Submonolayer amounts of Fe on a W(110) surface with irregular atomic steps were found to be ferro-

magnetic down to an Fe coverage of 0.05 ML.¹¹ Smooth and coherent Fe stripes on W(110) still exhibited ferromagnetism at a coverage of 0.5 ML with an average monolayer stripe width of 20 atomic rows.¹² On a vicinal Cu(111) substrate, Fe stripes of 5–15 atom width and 1–2 atom height, with a corresponding coverage of 0.3 ML, were found to exhibit a time dependent remanent magnetization.¹³ Concerning the electronic structure of 1D systems, a pioneering inverse photoemission experiment has already been performed for Cu on W(331),¹⁴ where the authors report on an electronic state which has been interpreted as a “single-row-state.”

Here we present, to the best of our knowledge the first measurements on the electronic and the magnetic properties of a 1D system that approaches the *monatomic* limit. The ideal system for the investigation of 1D electronic and magnetic properties with valence band photoemission is a set of parallel, equidistant, straight monatomic chains consisting of a magnetic element on a nonmagnetic substrate. The distance between the chains has to be large enough to allow mostly intrachain and only weak interchain interaction, but also small enough to ensure a sufficiently large contribution from the chains to the photoemission spectra. In these respects, the vicinal Pt(997) surface represents an excellent substrate. It supports the 1D growth of various elements, in particular the growth of monatomic Co and Cu wires,¹⁵ which are arranged in an array of high regularity with a distance of 8 ± 1 atomic rows. As will be demonstrated here, the step density is high enough to observe chain-induced electronic states in the angle-resolved photoemission experiment.

The characterization of single and multiple monatomic chain growth of Co and Cu on Pt(997) has been extensively carried out at EPF-Lausanne by means of thermal energy helium atom scattering (TEAS) and STM.¹⁵ Pt(997) is a vicinal surface cut 6.5° off normal with respect to the (111) atomic plane. The angle miscut determines the average step separation which is 20.1 Å. Repulsive interactions between adjacent steps suppress step meandering, resulting in steps that run parallel to each other (see Fig. 1). In order to obtain samples with a regular step distribution, repeated cycles of

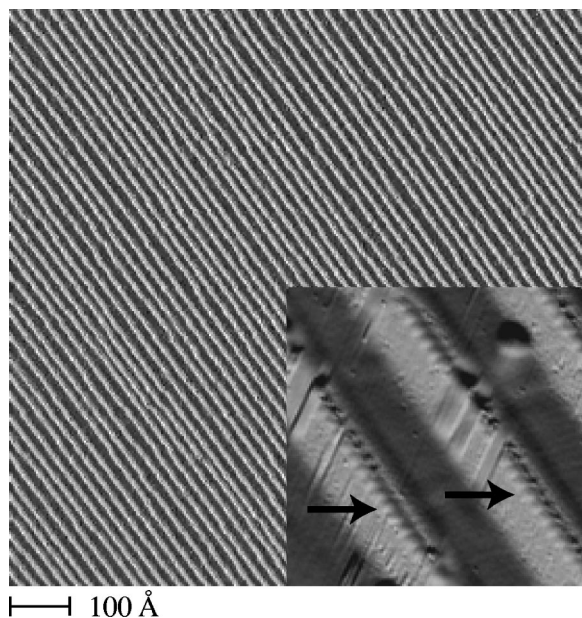


FIG. 1. STM topograph (dz/dx mode) of the clean Pt(997) surface. The terrace width distribution follows a Gaussian law with an average spacing of 20.1 Å [standard deviation $\sigma=2.9$ Å (Ref. 27)]. The step edges appear as white lines. Step down direction is from the upper right to the lower left. The inset shows the decoration of the Pt steps by single monatomic Co chains (indicated by the arrows).

sputtering and annealing to 850 K are performed in a UHV environment (base pressure 1×10^{-10} mbar), followed by a few minutes exposure to 1×10^{-7} mbar oxygen and by a flash to $T > 1000$ K to remove residual contaminants. Cooling the sample to the deposition temperature has to be done at a slow rate (< 40 K/min) to prevent step bunching effects. The quality of the periodic pattern can be routinely checked by taking TEAS diffraction spectra or by low energy electron diffraction (LEED) measurements.

The growth of Co and Cu monatomic chains along the Pt step edges can be followed in real time by TEAS measurements in grazing incidence conditions.^{10,15} TEAS results show that smooth monatomic row growth takes place above 250 K and 150 K for Co and Cu, respectively. The deposition of 0.12 ML in the allowed range of temperatures results in the decoration of each step by a single monatomic row. The inset in Fig. 1 shows Co monatomic chains decorating Pt steps after deposition at 250 K. Chains wider than one atomic row can be obtained by increasing the coverage up to 1 ML.

The angle-resolved photoemission measurements were performed at the undulator beamline TGM-5 at BESSY. The energy analysis of the photoemitted electrons was performed with a 90°-spherical electron energy analyzer with an energy and angle resolution of 250 meV and $\pm 1^\circ$, respectively. Unless specifically mentioned, all measurements have been performed at room temperature. After repeated cycles of Ne-ion sputtering and annealing, a very good LEED pattern with sharp diffraction spots and a low background intensity confirmed a high degree of structural order in the topmost surface layers. In addition to the $p(1 \times 1)$ spots we found extra spots that were induced by the step edges and stressed the high surface quality of the sample used in the photoemission

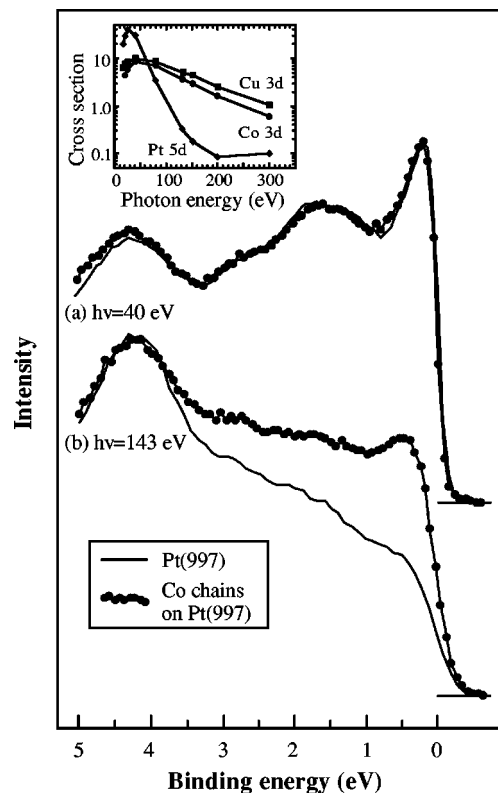


FIG. 2. Photoemission spectra of clean Pt(997) and after the deposition of 0.12 ML Co taken at photon energies of (a) 40 eV and (b) 143 eV. The inset shows the atomic photoionization cross sections for 5d transition metals (e.g., Pt) and 3d transition metals (e.g., Cu and Co) as a function of photon energy (Ref. 16).

experiment. The base pressure of 1×10^{-10} mbar rose to 4×10^{-10} mbar as Co and Cu were deposited by electron beam evaporation. The thickness calibration was done by means of a quartz crystal microbalance. A cross check with Auger spectroscopy enabled us to make a direct comparison of the absolute amounts of deposited material between the samples prepared at BESSY and the ones studied at EPF-Lausanne.

A serious problem for the determination of the electronic states of 1D monatomic chains by angle-resolved valence band photoemission is the small amount of deposited material (≈ 0.1 ML) and its weak contribution to the photoemission spectra which makes the identification of chain-induced states very difficult. It is therefore crucial to find experimental conditions that offer a high spectroscopical sensitivity for the chain-induced states. In fact, for an arbitrary choice of photon energy, nearly no changes in the photoemission spectra could be found after the preparation of Cu or Co wires. This is demonstrated in Fig. 2(a), which shows photoemission spectra of the clean Pt(997) substrate and of 0.12 ML Co on Pt(997), taken at a photon energy of 40 eV. The sensitivity for the small amount of deposited Co can be strongly enhanced, taking advantage of the Pt 5d Cooper minimum. The atomic photoionization cross sections for 3d and 5d transition metals are shown in the inset of Fig. 2. The corresponding cross section ratios in the solid state were found to be of similar magnitude.¹⁷ Photoemission spectra of the clean Pt substrate and with a coverage of 0.12 ML Co show indeed strong changes at a photon energy of 143 eV [Fig. 2(b)].

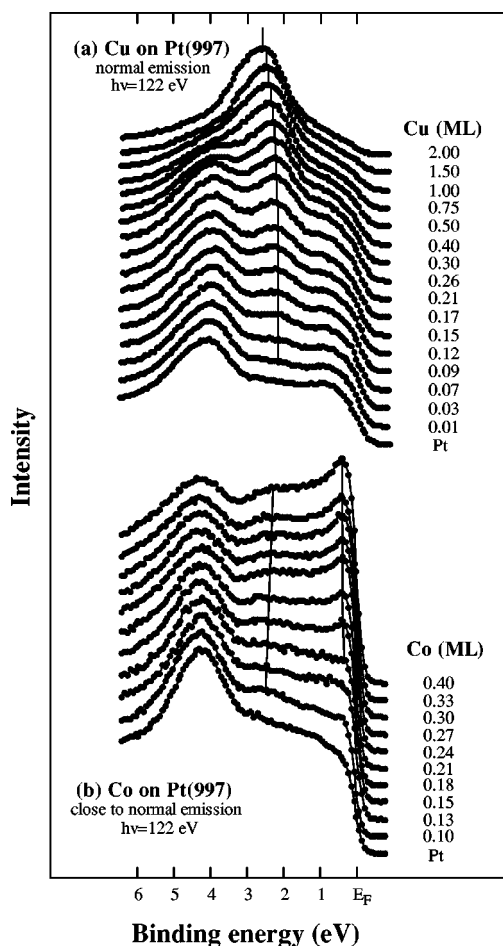


FIG. 3. (a) Photoemission spectra taken at a photon energy of 122 eV displaying the development of Cu states on Pt(997) with increasing coverage. (b) Photoemission spectra taken at a photon energy of 122 eV displaying the development of Co states on Pt(997) after deposition of up to 0.40 ML Co.

In Fig. 3(a), the changes of the electronic states with increasing Cu thickness are displayed. At coverages below 0.1 ML, the development of a single Cu $3d$ state at a binding energy of 2.3 eV already can be observed. No Cu-derived electronic states can be found close to the Fermi level because the Cu $3d$ shell is filled and the photoemission cross sections for s states are very small in this photon energy range. Above a coverage of 0.17 ML, the Cu $3d$ states shift to higher binding energy, and at 2.0 ML they have reached a value of 2.7 eV. These changes in the electronic structure are likely to reflect the changes in the dimensionality of the system. The development from a 1D to a 2D system, as it is realized for the growth of Cu and Co on Pt(997), will result in different electronic configurations, that should lead to observable changes in the electronic structure. At a coverage of 0.17 ML, where the wires are already completely formed and the growth starts to become two-dimensional,¹⁵ the shift of the Cu $3d$ states to higher binding energy begins to take place. For systems with 2D island or 3D cluster nucleation instead, almost no changes in the electronic structure can typically be observed with increasing coverage in the submonolayer regime,^{18,19} because for low coverages the average atomic coordination is already quite similar to the coordination in the monolayer or in the bulk, respectively.

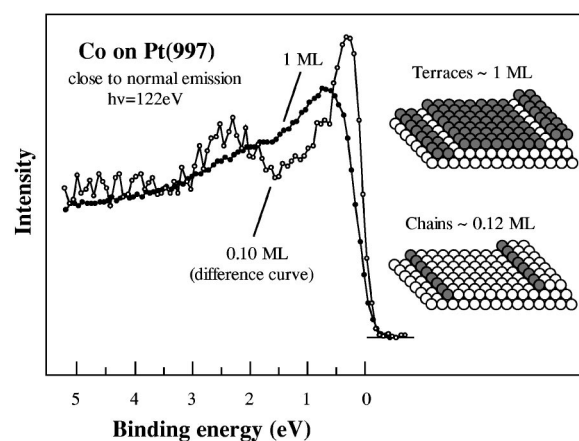


FIG. 4. Difference spectrum showing the Co chain-induced states in comparison with a photoemission spectrum of a Co monolayer (not a difference spectrum) and schematic pictures of Co chains and a Co monolayer on Pt(997).

For Co the development of the electronic states with increasing coverage also has been studied. The sequence of spectra in Fig. 3(b) was taken at a photon energy of 122 eV and close to normal emission (4° off normal). It shows that in the low-coverage region up to 0.4 ML, the changes of the electronic states related to the Co deposition clearly differ from the changes observed in the case of Cu. Here, close to the Fermi level and at a binding energy of approximately 2.4 eV, new electronic states appear in the photoemission spectra. With increasing Co deposition these structures become prominent in the spectra and their separation slightly decreases (see also Fig. 4).

In order to make the chain-induced states more clearly visible, a difference spectrum between the spectrum at 0.10 ML Co and the Pt spectrum has been formed. The normalization of the spectra has been done by equalizing the amplitude of the Pt peak at a binding energy of approximately 4 eV. The resulting spectrum is shown in Fig. 4 in comparison with a spectrum of a Co monolayer. In contrast to the single feature found for the Cu chains, we find two peaks for the Co chains located at binding energies of 0.3 eV and 2.4 eV.

We shall now discuss the presence of a single peak for the Cu chains and of two peaks for the Co chains. One could assume that one of the two Co peaks represents a Co-Pt interface state or a 1D modified surface state. Since for the same geometric arrangement, the electronic structure of Co and Cu is very similar and differs mainly in the energetic position of the bands, we could expect to observe Cu-Pt interface states or 1D Cu states, as well. This is not the case and therefore the double peak structure found for the Co chains is likely to have a *magnetic* origin. In contrast to Cu, that has a completely filled $3d$ shell, Co has a magnetic moment because its $3d$ shell is partially unoccupied. In the electronic structure, this results in an exchange splitting of the Co $3d$ bands that probably leads to the photoemission features close to the Fermi level and at a binding energy of 2.4 eV shown in Fig. 4. So the observation of a double-peaked structure for the Co wires and of a single feature for the Cu wires strongly suggests the presence of a 1D exchange-split Co band and of local magnetic moments.

The comparison of the Co chain spectrum with the Co monolayer spectrum displayed in Fig. 4 shows obvious differences for these two systems. In particular, the magnitude of the exchange splitting seems to be larger for the Co chains than for the Co monolayer, although the exchange splitting of the Co monolayer cannot be safely determined without spin analysis. The broad feature close to the Fermi level could consist of overlapping contributions from states of different spin character and symmetry. However, the positions of the Co-induced states in Fig. 4 indicate that the exchange splitting of the monatomic Co chains is large (~ 2.1 eV). This value can be compared with typical values for thin Co films (1.4–1.9 eV),^{20,21} and for bulk Co (≈ 1.4 eV).^{20,22} This large number for the Co chains suggests that the corresponding local magnetic moments also have a considerable magnitude compared to Co films and to bulk Co. This is in line with recently performed self-consistent calculations for monatomic Co chains.²³

An enhancement of the exchange splitting can be explained in terms of the lowered dimensionality of the Co system. For a magnetic system it is well known that a reduction of its dimensionality from 3D to 2D causes an enhancement of its magnetic moments. This effect is essentially a consequence of the band narrowing due to the reduced atomic coordination in the 2D system. In the electronic structure, this results in a larger exchange splitting compared to the bulk. With the same argument, even larger magnetic moments and a larger exchange splitting can be expected for a 1D system, and this is probably what we observe in the photoemission spectra of the Co wires.

No in-plane spin polarization of the chain-induced electronic states, neither parallel nor perpendicular to the chains, could be found with a high-energy Mott detector down to sample temperatures of 100 K. The absence of long-range ferromagnetic order for a 1D system is at this temperature not surprising. From the theoretical point of view, a spontaneous magnetization with a nonvanishing net moment at $T > 0$ K is not allowed for an Ising chain with nearest neighbor exchange interaction.²⁴ Even if the array of Co chains on Pt(997) behaved unlike an Ising system and showed a long-

range ferromagnetic order, its Curie temperature would possibly be lower than 100 K, because the reduction of the dimensionality of a magnetic system is followed by a reduction of its ordering temperature. It is also possible that the easy magnetization direction of the Co stripes on Pt(997) is not the in-plane direction, as in the case of Fe on stepped W(110),¹² but the out-of-plane direction, which was not accessible in our experimental setup. For submonolayer amounts of Co on a flat Pt(111) surface, the easy magnetization direction was found to be out-of-plane,²⁵ and theoretical investigations predict a change of the easy magnetization axis from in-line to out-of-plane, as a freestanding Co chain is deposited on a Pd(110) surface.²⁶ Also, Fe on a vicinal Cu(111) surface exhibits an anisotropy perpendicular to the surface plane.¹³ This system also showed a time-dependent remanent magnetization, which indicates a superparamagnetic behavior of the Fe stripes, where thermal fluctuations are strong enough to destroy a remanent magnetization. Depending on various parameters, i.e., coverage, anisotropy, and sample temperature,¹³ the time scale for this demagnetization process can change strongly. But even if the array of Co chains on Pt(997) behaved like a superparamagnet, the sample temperature of 100 K would possibly be too high to keep up a remanent magnetization for at least 10^2 – 10^3 seconds to perform the spin analysis of the photoemitted electrons.

In summary, a highly regular array of monatomic Cu and Co wires has been prepared by step-edge decoration of a vicinal Pt(997) surface. The electronic structure of these 1D systems has been investigated by angle-resolved photoemission with synchrotron radiation. A sufficiently high sensitivity for the small amounts of deposited material (≈ 0.1 ML) could be achieved by taking advantage of the Pt *5d* Cooper minimum in the photoionization cross section. While a single photoemission feature is associated with the *3d* emission of the monatomic Cu wires, a *3d* double-peak structure is instead observed for the Co wires. This finding indicates the presence of a 1D exchange-split band and of local magnetic moments.

*Author to whom correspondence should be addressed.

¹F. J. Himpsel, J. E. Ortega, G. J. Mankey, and R. F. Willis, *Adv. Phys.* **47**, 511 (1998).

²C. Carbone *et al.*, *Phys. Rev. Lett.* **71**, 2805 (1993); C. Carbone *et al.*, *Solid State Commun.* **100**, 749 (1996); R. Kläsger *et al.*, *Phys. Rev. B* **57**, R696 (1998).

³H. Röder *et al.*, *Nature (London)* **366**, 141 (1993).

⁴Yinggang Li *et al.*, *Phys. Rev. B* **56**, 12 539 (1997).

⁵R. Pascal, C. Zarnitz, M. Bode, and R. Wiesendanger, *Phys. Rev. B* **56**, 3636 (1997).

⁶J. Kołaczkiwicz and E. Bauer, *Surf. Sci.* **175**, 487 (1986).

⁷L. Pleth Nielsen *et al.*, *Phys. Rev. Lett.* **74**, 1159 (1995).

⁸C. Pampuch *et al.*, *Phys. Rev. Lett.* (to be published).

⁹M. Mundschau, E. Bauer, and W. Świąch, *J. Appl. Phys.* **65**, 581 (1989).

¹⁰V. Marsico, M. Blanc, K. Kuhnke, and K. Kern, *Phys. Rev. Lett.* **78**, 94 (1997).

¹¹H. J. Elmers *et al.*, *Phys. Rev. Lett.* **73**, 898 (1994).

¹²J. Hauschild, H. J. Elmers, and U. Gradmann, *Phys. Rev. B* **57**, R677 (1998).

¹³J. Shen *et al.*, *Phys. Rev. B* **56**, 2340 (1997).

¹⁴F. J. Himpsel and J. E. Ortega, *Phys. Rev. B* **50**, 4992 (1994).

¹⁵P. Gambardella *et al.*, *Phys. Rev. B* **61**, 2254 (2000); P. Gambardella *et al.*, *Surf. Sci.* (to be published).

¹⁶J. J. Yeh and I. Lindau, *At. Data Nucl. Data Tables* **32**, 1 (1985).

¹⁷J. F. van Acker *et al.*, *Phys. Rev. B* **43**, 8903 (1991).

¹⁸H. Knoppe and E. Bauer, *Phys. Rev. B* **48**, 1794 (1993).

¹⁹E. Vescovo, C. Carbone, and O. Rader, *Solid State Commun.* **94**, 751 (1995).

²⁰W. Clemens *et al.*, *Solid State Commun.* **81**, 739 (1992).

²¹C. M. Schneider *et al.*, *J. Electron Spectrosc. Relat. Phenom.* **51**, 263 (1990).

²²U. Alkemper *et al.*, *Phys. Rev. B* **50**, 17 496 (1994).

²³G. Bihlmayer, X. Nie, and S. Blügel (unpublished).

²⁴E. Ising, *Z. Phys.* **31**, 253 (1925).

²⁵C. S. Shern *et al.*, *Surf. Sci. Lett.* **429**, L497 (1999).

²⁶J. Dorantes-Dávila and G. M. Pastor, *Phys. Rev. Lett.* **81**, 208 (1998).

²⁷E. Hahn *et al.*, *Phys. Rev. Lett.* **72**, 3378 (1994).

Paper VI

Electronic Structure of Carbon Nanostripes

A. M. Shikin,^{1,2} S. A. Gorovikov,^{3,2} V. K. Adamchuk,² W. Gudat,^{1,4} and O. Rader^{1,*}

¹BESSY, Albert-Einstein-Strasse 15, D-12489 Berlin, Germany

²Institute of Physics, St. Petersburg State University, St. Petersburg, 198904 Russia

³MAXLAB, Lund University, P.O. Box 118, S-221 00 Lund, Sweden

⁴Institut für Physik, Universität Potsdam, P.O. Box 601553, D-14415 Potsdam, Germany

(Received 12 May 2002; published 26 June 2003)

Carbon nanostripes of graphene structure prepared on the stepped Ni(771) surface have been studied by angle-resolved photoemission. The electronic structure is anisotropic: parallel to the stripe direction, a graphite-type dispersion is measured, whereas the perpendicular direction displays two entangled band structures shifted in energy with respect to each other. These are experimentally identified as the microsurface-centered band structure and its umklapp scattered image caused by the superlattice.

DOI: 10.1103/PhysRevLett.90.256803

PACS numbers: 73.22.-f, 79.60.Dp

For a long time, surface science has dealt with the production of ideal surfaces and the behavior of electrons localized within the two dimensions given by the interface between solid and vacuum. The idea to place obstructions on a surface that are capable of reflecting electrons and can lead to their confinement has received increased attention since a remarkable visualization of these effects has been achieved by scanning tunneling spectroscopy (STS) [1,2]. STS is able to select atoms near a single step, and as it measures the local density of states, it can detect the presence of standing electron waves. In order to study the electronic interaction, the wave-vector-resolving methods of direct or inverse photoemission are required. Only with the help of these methods can one obtain answers to the question how an electron interacts with the step when it is moving parallel to it or when it moves towards it or away from it. Angle-resolved direct and inverse photoemission measure the global electronic structure and in order to obtain a sizable signal require a large number of identical and equally oriented steps. Experiments have shown that the presence of single or periodically repeated steps can cause in addition to the step-localized standing waves [1,2] certain superlattice effects [3–5] and a quantization [6] of the electronic spectrum. The experimental literature reports four different types of dispersion for surface states in the direction perpendicular to such step lattice: (i) a single parabola centered around the normal of the microsurface (terrace) [7], (ii) a single parabola, but arranged relative to the macrosurface normal [3,7], (iii) a repeated band dispersion related to the step periodicity [4,5], and (iv) quantum-well states with no dispersion [6].

It is astonishing that in spite of the principal difference between STS on the one hand and direct, two-photon, and inverse photoemission on the other hand, the states used so far to study steps at clean crystal surfaces are basically the same: Typically, the experiment picks a crystal-induced or image-potential induced surface state in order to probe the laterally structured surface. However, the

L-centered Shockley surface state, which has been used in all photoemission work to date, extends from E_F down to only 0.4 eV binding energy on Cu and Au. Our aim is to overcome this constraint and try to *impose the lateral superstructure of a stepped substrate onto the whole valence band of a monoatomic overlayer*. Therefore, we have prepared nanostripes of graphene (i.e., monolayer graphite), a material which has a truly two-dimensional electronic structure and allows us to probe a much larger *k*-space range and an energy range by almost 2 orders of magnitude wider than in previous photoemission work.

The graphene stripes were formed *in situ* on stepped Ni(771) by cracking of propylene at a partial pressure of 1×10^{-6} mbar and $T = 500^\circ\text{C}$ sample temperature using a procedure elaborated previously for graphene on Ni(111) [8,9]. Propylene cracking is a self-limited reaction: as soon as the Ni surface is covered with a full graphene sheet, the reaction stops because it can take place only at a pure Ni surface. After additional annealing at $450\text{--}500^\circ\text{C}$ in ultrahigh vacuum the system consists of graphene stripes along the Ni terraces with finite width in the perpendicular direction due to the limited size of the terraces. As shown by scanning tunneling microscopy [10], the Ni(771) surface is characterized by monoatomic steps with a height of 1.24 Å and Ni(110)-oriented terraces with a width of ≈ 12.3 Å which are conserved after graphitization. Low-energy electron diffraction (LEED) patterns measured *in situ* for the pure Ni(771) surface [Fig. 1(a)] and after graphene stripe preparation [Figs. 1(b) and 1(c)] display a well ordered structure. Besides the step-derived (7×1) superstructure, the LEED pattern from graphene/Ni(771) shows graphite rings [Fig. 1(c)] surrounding all principal spots of the Ni(110) structure. This is characteristic of graphene on top of surfaces with a nonhexagonal surface structure such as Ni(100) and Ni(110) [11]. Base pressure during experiment was in the upper 10^{-11} mbar range.

Angle-resolved photoemission spectra have been measured at the undulator beam lines I311 at MAXlab and

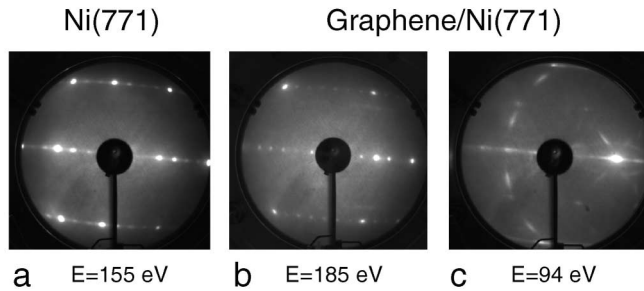


FIG. 1. Low-energy electron diffraction. The (7×1) superstructure of the clean Ni(771) (a) is preserved after preparation of graphene nanostructures (b), which appear as circle sections (c). The steps and stripes run along $[1\bar{1}0]$ which is close to the vertical direction in the figure.

U125/1-PGM at BESSY with linearly polarized light of 50 eV photon energy. Dispersions, i.e., polar angle scans of photoemission spectra, parallel and perpendicular to the step direction $[1\bar{1}0]$, have successively been measured from the same sample after azimuthal rotation by 90° .

Figures 2(a) and 2(b) show a typical series of photoemission spectra for graphene/Ni(771) where the electron emission angle is varied in the direction parallel (a) and perpendicular (b) to the graphene nanostructures. Spectra of clean Ni(771) (not shown) prove that practically all structures in the region 2 to 22 eV binding energy are graphene derived. The dispersions with the macrosurface-projected wave vector \mathbf{k}_{\parallel} corresponding to Fig. 2 are presented in Figs. 3 and 4, separately for π , $\sigma_{2,3}$, and σ_1 states. Figures 3 and 4 summarize data from four different preparations. Features with weak intensity are marked by crosses. The dispersions measured in the direction parallel to the nanostructures [Figs. 2(a) and 3] resemble almost fully the ones obtained from graphene on flat Ni(111) and can be assigned according to Refs. [9,12]. (The $\sigma_{2,3}$ states near $\bar{\Gamma}$ are too weak to be observed for present symmetry conditions.) Compared to monocrystalline bulk graphite, the π and σ branches are shifted towards higher binding energies due to strong $C\pi$ -Ni d interaction of the graphene sheet with the Ni substrate (similar to graphene/Ni(111) in Refs. [9,12]). Figure 3 shows a critical point appearing at about $\mathbf{k}_{\parallel} = 1.55 \text{ \AA}^{-1}$, a value which lies between the ones for M (1.4 \AA^{-1}) and K (1.7 \AA^{-1}) of graphite, indicating that the orientation of graphene hexagons relative to the steps is rotated in agreement with the LEED pattern of Fig. 1(c).

The dispersions observed perpendicular to the stripes, shown in Figs. 2(b) and 4, are very different. (i) *Two instead of one* graphene-type band structure can be recognized for π and σ states. Both band structures lead to photoemission peaks of high intensity with the left-hand one (in Fig. 4) somewhat more intense [see Fig. 2(b)]. The left-hand branches of π and σ states are shifted relative to the macrosurface normal $[771]$ by -6° . This value (which has been determined *in situ* from the parallel dispersion with the help of the azimuthal rotation) is identical to the miscut angle between the Ni(771) macro-

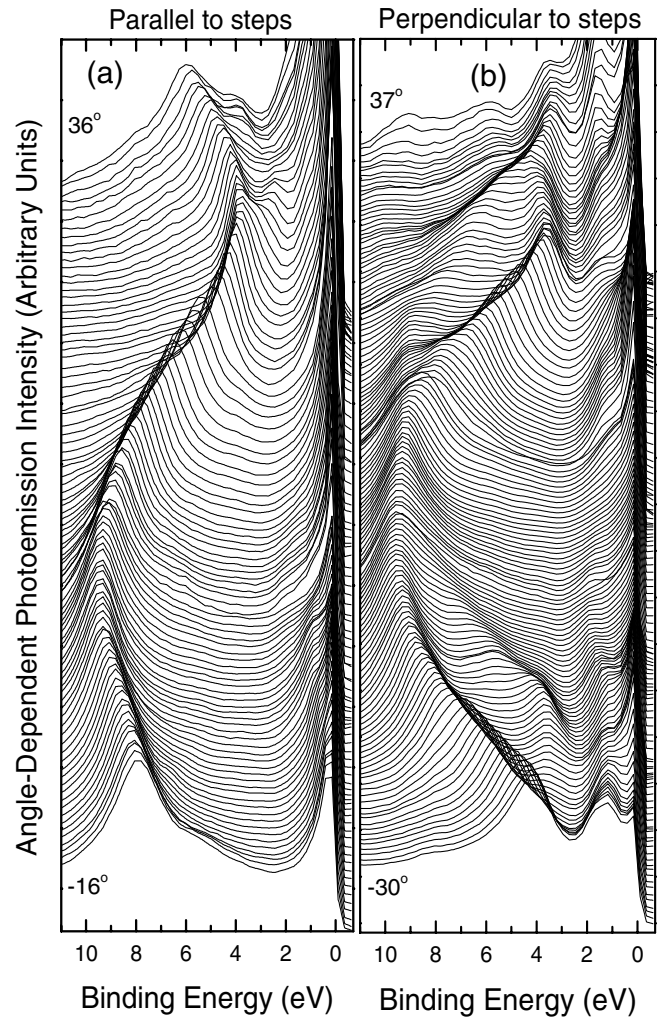


FIG. 2. Photoemission spectra at $h\nu = 50 \text{ eV}$ for \mathbf{k}_{\parallel} parallel (a) and perpendicular (b) to the nanostructure direction.

surface and the Ni(110) terraces [10] and allows us to ascribe the left-hand branches to (110) -microsurface-centered states. Moreover, (ii) the right-hand band structure shows *pronounced gaps* for the π , σ_2 , and σ_1 states, which have no counterpart in the parallel dispersion data [Figs. 2(a) and 3] or for graphene on flat Ni(111) or bulk graphite [9,12]. The most pronounced gap in our data appears at $\mathbf{k}_{\parallel} \approx 1.0 \text{ \AA}^{-1}$ in Fig. 4. (iii) Our data are compatible with further gaps appearing at $\mathbf{k}_{\parallel} = 0$ (flat band at 9.2 eV binding energy), $\approx 1.5 \text{ \AA}^{-1}$ (between 4.3 and 5 eV), and $\approx 2.05 \text{ \AA}^{-1}$ (between 8.1 and 8.8 eV). (iv) A weak band between about 5 and 8 eV binding energy appears periodic characteristic of back-folding into the repeated Brillouin zone scheme of the superlattice which could possibly be described by a one-dimensional Kronig-Penney model for electrons on a stepped surface [13].

The appearance of two band structures is an astonishing, unprecedented observation. The assumption of a second phase due to artifacts such as sputtering defects or faceting is at variance with the STM characterization [10]. It should be kept in mind that, in view of the

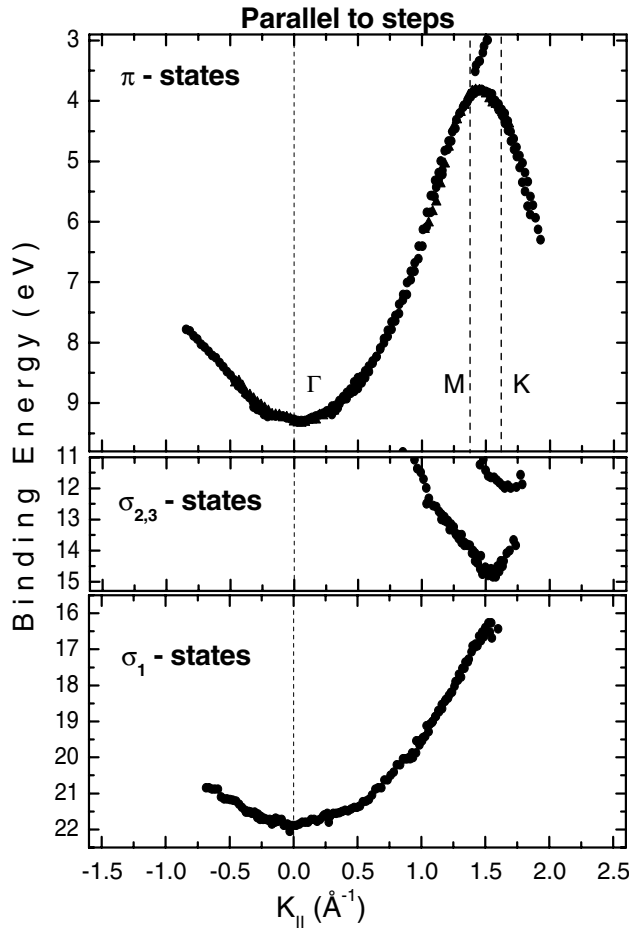


FIG. 3. E vs k_{\parallel} dispersion for the macrosurface-projected wave vector k_{\parallel} parallel to the nanostripe direction.

comparable photoemission intensity of the two branches, any such artifact would have to involve a large portion of the sample surface which does not reconcile with the characterization of the macrosurface as (771) [14]. We consider the two bands and additional parallel branches an intrinsic property of the photoemission from a single phase of graphene nanostripes.

In order to assign the band structures, we varied the photon energy and plotted the dependence on the angle [Fig. 5(a)] and the parallel wave vector relative to the microsurface normal [Fig. 5(b)]. The coincidence of the left-hand branch for all photon energies confirms the assignment as microsurface-centered branch. The right-hand branches also coincide and together with a third branch (see $h\nu = 90$ eV) are shifted by a constant value of \mathbf{G} and $2\mathbf{G}$, respectively, where $\mathbf{G} = 2\pi/L$ and $L = 12.3$ Å is the terrace width. For each band structure shifted by \mathbf{G} we are dealing with the first Brillouin zone branch only since graphite suppresses second-Brillouin-zone emission [15]. In a superlattice as well as in a simple lattice geometry, distinction of a periodic band dispersion from umklapp effects during excitation is usually difficult. The present data, however, give two reasons why the right-hand branch cannot be assigned to

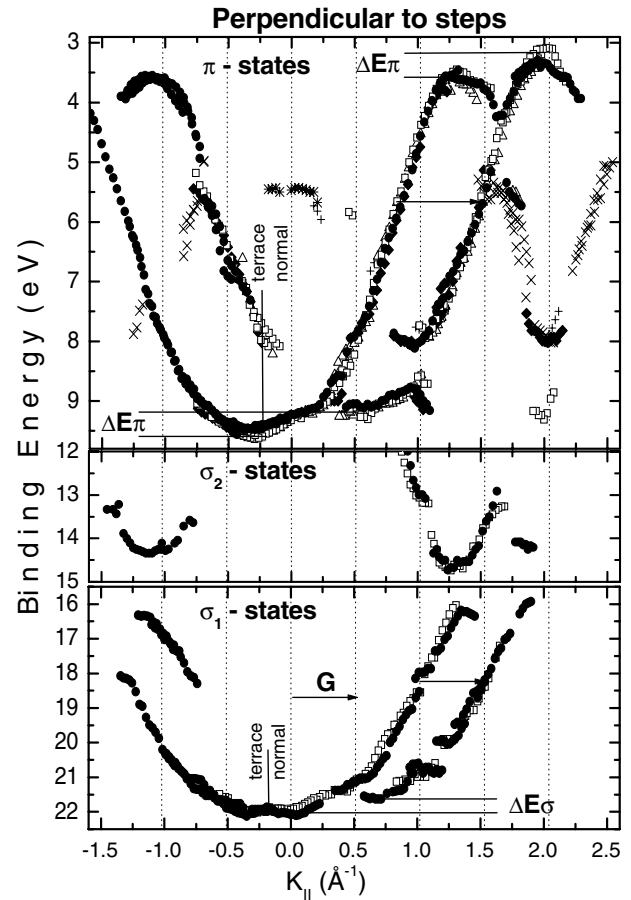


FIG. 4. Same as Fig. 3 but for k_{\parallel} perpendicular to the nanostripe direction. k_{\parallel} is again defined relative to the macrosurface normal. Each symbol represents a new nanostripe preparation. Note that gaps are more or less pronounced depending on the sample preparation (temperature and duration of propylene cracking). Vertical lines mark multiples of the wave vector \mathbf{G} corresponding to the step periodicity.

an initial-state superlattice effect: First is the obvious shift to lower binding energy by 0.4–0.5 eV and 0.3–0.4 eV for π and σ_1 branches, respectively. Second is the fact that the band gap (we refer to ≈ 1.0 Å⁻¹ in Fig. 4) is not a property of the initial-state band structure of the superlattice since it does not appear at constant k_{\parallel} as seen from Fig. 5(b). The right-hand branch must therefore be due to umklapp scattering with wave-vector transfer of $\Delta\mathbf{k} = 2\pi/L$ characteristic of the superlattice structure. Umklapp scattering depends on the availability of final states and this likely introduces the photon-energy dependence of the band gap. For bulk graphite, umklapp scattering contributes substantially to photoemission and its dependence on photon energy has been measured [16]. During umklapp scattering the wave-vector difference is transferred to collective excitations, usually phonons. It is interesting to note in this context that the phonon dispersion of graphite nanostripes on Ni(771) as measured by electron energy loss spectroscopy has indeed displayed strong superlattice effects in the first study of its kind [8]. We caution, however, that a

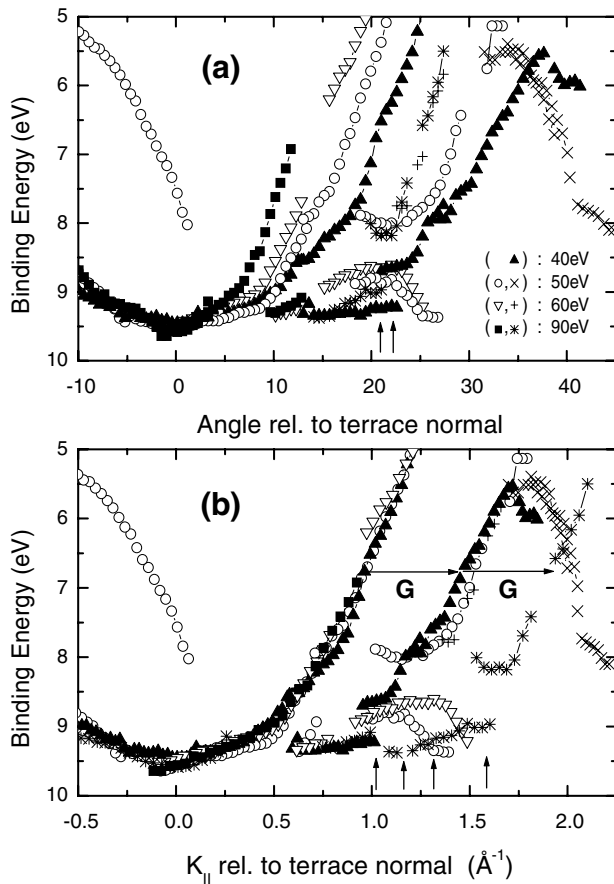


FIG. 5. Photon-energy dependence perpendicular to the stripe direction versus electron emission angle (a) and k_{\parallel} relative to the microsurface normal (b). **G** indicates a reciprocal superlattice vector, and vertical arrows mark band gap positions for various photon energies.

simple identification of phonon excitation with the energy shift measured in this work fails due to the different energy scale and that further research efforts need to be undertaken in this new and exciting field.

In summary, we prepared a regular array of carbon nanostripes and observe an anisotropic dispersion with two band structures in the direction perpendicular to the stripes: a gapped and a microsurface-centered one. We showed that umklapp scattering in the excited state caused by the superlattice instead of a conventional superlattice effect of the ground state is the origin of this behavior.

We are indebted to Professor K.-H. Rieder for helpful discussions. This work was supported by DFG (RA 1041/1-1). Part of this work was performed in the framework of the programme "Fullerenes and Atomic Clusters." S. A. G. was supported by The Swedish Foundation for International Cooperation in Research and Higher Education.

*Corresponding author.

Electronic address: rader@bessy.de

- [1] M. F. Crommie, C. P. Lutz, and D. M. Eigler, *Nature (London)* **363**, 524 (1993).
- [2] P. Avouris and I.-W. Lyo, *Science* **264**, 942 (1994); P. Avouris *et al.*, *J. Vac. Sci. Technol. B* **12**, 1447 (1994).
- [3] A. P. Shapiro, T. Miller, and T.-C. Chiang, *Phys. Rev. B* **38**, 1779 (1988).
- [4] X. Y. Wang, X. J. Shen, R. M. Osgood, Jr., R. Haight, and F. J. Himpsel, *Phys. Rev. B* **53**, 15 738 (1996).
- [5] X. Y. Wang, X. J. Shen, and R. M. Osgood, Jr., *Phys. Rev. B* **56**, 7665 (1997).
- [6] A. Mugarza, A. Mascaraque, V. Perez-Dieste, V. Repain, S. Rousset, F. J. Garcia de Abajo, and J. E. Ortega, *Phys. Rev. Lett.* **87**, 107601 (2001).
- [7] J. E. Ortega, S. Speller, A. R. Bachmann, A. Mascaraque, E. G. Michel, A. Nürmann, A. Mugarza, A. Rubio, and F. J. Himpsel, *Phys. Rev. Lett.* **84**, 6110 (2000); J. E. Ortega *et al.*, *Surf. Sci.* **482–485**, 764 (2001).
- [8] W.-H. Soe, A. M. Shikin, F. Moresco, V. K. Adamchuk, and K.-H. Rieder, *Phys. Rev. B* **64**, 235404 (2001); A. M. Shikin, G. V. Prudnikova, V. K. Adamchuk, W. H. Soe, K. H. Rieder, S. L. Molodtsov, and C. Laubschat, *Phys. Solid State* **44**, 652 (2002).
- [9] A. M. Shikin, G. V. Prudnikova, V. K. Adamchuk, F. Moresco, and K.-H. Rieder, *Phys. Rev. B* **62**, 13 202 (2000); A. M. Shikin, M. V. Poygin, Yu. S. Dedkov, S. L. Molodtsov, and V. K. Adamchuk, *Phys. Solid State* **42**, 173 (2000).
- [10] R. Koch, O. Haase, M. Borbonus, and K.-H. Rieder, *Phys. Rev. B* **45**, 1525 (1992); R. Koch *et al.*, *Ultramicroscopy* **42–44**, 541 (1992).
- [11] T. Aizawa, R. Souda, Y. Ishizawa, H. Hirano, T. Yamada, K. Tanaka, and C. Oshima, *Surf. Sci.* **237**, 194 (1990); G. Ertl, *Molecular Processes on Solid Surfaces* (McGraw-Hill, New York, 1969).
- [12] A. Nagashima, N. Tejima, and C. Oshima, *Phys. Rev. B* **50**, 17 487 (1994).
- [13] L. C. Davis, M. P. Everson, R. C. Jaklevic, and W. Shen, *Phys. Rev. B* **43**, 3821 (1991).
- [14] That the measured band structure is not a simple superposition of two phases can also be seen from details: The upper turning point of the right-hand branch at 2\AA^{-1} ($\approx 3.2 \text{ eV}$) is not at the same energy as for -1.1\AA^{-1} ($\approx 3.6 \text{ eV}$) which, in turn, agrees with the one of the left-hand branch at 1.25\AA^{-1} . This observation indicates that the two branches are not independent of each other and, in particular, are unlikely due to two distinct phases.
- [15] H. Daimon, S. Imada, H. Nishimoto, and S. Suga, *J. Electron Spectrosc. Relat. Phenom.* **76**, 487 (1995).
- [16] F. Matsui, Y. Hori, H. Miyata, N. Suga, H. Daimon, H. Totsuka, K. Ogawa, T. Furukubo, and H. Namba, *Appl. Phys. Lett.* **81**, 2556 (2002); F. Matsui *et al.* (unpublished).

Paper VII

One-Dimensional Spin-Polarized Quantum-Wire States in Au on Ni(110)

C. Pampuch, O. Rader,* T. Kachel, and W. Gudat

BESSY, Albert-Einstein-Strasse 15, D-12489 Berlin, Germany

C. Carbone, R. Kläsger, G. Bihlmayer, S. Blügel, and W. Eberhardt

Institut für Festkörperforschung, Forschungszentrum Jülich, D-52425 Jülich, Germany

(Received 17 November 1999; revised manuscript received 27 April 2000)

Au chain structures have been prepared on Ni(110). Au6s, *p*-derived features in photoemission spectra are identified as quantum-wire states due to their strong dispersion along the chains and absence of dispersion perpendicular to the chains in agreement with our *ab initio* calculation of the electronic structure. Spin analysis reveals that the states have minority-spin character showing that the confinement of electrons in the chain structure depends on the electron spin.

PACS numbers: 73.20.Dx, 79.60.Dp

Research on quantum confinement in metallic heterostructures has intensified very much since the link was found between long-range oscillatory magnetic coupling phenomena in magnetic-nonmagnetic multilayers [1] on the one hand and the periodic appearance of structures in photoemission and inverse photoemission spectra on the other hand [2]. The so-called “quantum-well model of oscillatory magnetic coupling” is based on the confinement of electrons in a metallic layer brought about by spin-dependent band gaps in the neighboring layers. These metallic quantum wells are similar to the ones known in semiconductor structures; however, due to larger offsets of the relative band gaps (several eV) a spatially narrower confinement of electrons can be achieved. The model has been supported by a number of subsequent experiments on bilayers and trilayers revealing the layer-thickness dependence, dispersion parallel to the film plane, spin character, and a second, small period of the appearance of quantum-well states [2–9].

As in these experiments confinement occurs only in the direction perpendicular to the metal-metal interfaces giving rise to two-dimensional quantum-well states, it appears challenging to attempt confinement also within the plane with the aim of producing a *quantum wire* of atomic dimensions. Research interest has been concentrating on steps as natural one-dimensional structures at clean metal surfaces, and these have therefore been studied first by photoelectron spectroscopy. In this way, the one-dimensional equivalent of surface states, i.e., step states, has been identified in photoemission spectra [10,11]. A one-dimensional dispersion could be shown for image-potential states [12].

Deposited metals adsorb preferentially at steps. Taking advantage of this, a growth method termed “step decoration” has been used to grow quasi-one-dimensional structures. For Cu/W(110), a binding-energy shift in Cu3*d* photoemission has been attributed to the formation of Cu stripes [13]. Although much progress has been made concerning the quality of such stripes, e.g., using scanning tunneling microscopy (STM) [14], a one-dimensional

anisotropy of their electronic structure has never been shown. The developments up to this point have been documented in more detail in Ref. [15].

We report in this Letter on a surface alloy that has long-range one-dimensional geometry. By the so-called “dealloying” phase separation during the growth of Au on Ni(110), chains of impressive coherence and a narrow interchain distance (a few surface lattice constants) are observed by STM [16]. The structural characterization of Ref. [16] reveals, in brief, that surface alloying of Au occurs up to a coverage of 0.4 monolayers (ML). Above 0.4 ML, 42% of the Au atoms form dimer-trimer chains out of a Au-Ni surface alloy as a result of a first-order phase transition. These chains are oriented along the [001] direction as seen from our model in Fig. 1. For increasing coverage, the interchain distance decreases until 0.93 ML are deposited [16]. We show below with photoemission that Au/Ni(110) is the first example of a metal-on-metal system where one dimensionality of the chains can be seen from the measured angle dispersion. The characteristic dispersion (strong parallel to the chain orientation and absent perpendicular) is observed for Au5*d* and Au6s, *p* states. Analogous to the case of spin-polarized quantum-well states in multilayer structures, electrons of different spin character are confined to a different degree.

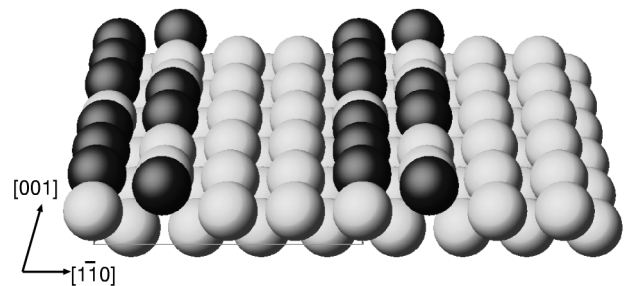


FIG. 1. Geometry of Au/Ni(110) used for the *ab initio* band structure calculation according to the structural model of Ref. [16]. Au atoms (black) for dimer-trimer chains along [001] on top of the Ni substrate atoms (white).

Angle-resolved photoelectron spectra have been measured with a VG Escalab photoemission chamber at 1×10^{-10} mbar with a combined energy resolution of 150 meV and an angle resolution of 2° using linearly polarized synchrotron light from the 3m NIM-1 monochromator at BESSY I. Spin-resolved photoemission at 300 meV and 2° resolution has been done at the TGM-1 monochromator. In both setups, light incidence angle was about 30° with respect to the fixed analyzer direction leading to mixed ($s + p$) polarization in normal emission. Sample preparation was performed *in situ* according to Ref. [16] using a quartz microbalance to adjust the Au evaporation rate (0.1 ML/min) and, in addition, low-energy electron diffraction. We conducted *ab initio* calculations of the electronic structure for a dimer-trimer chain on a $p(3 \times 4)$ Ni(110) surface as shown in Fig. 1 (for clarity, four unit cells are displayed). This structural model has been given by Nielsen *et al.* It does not include those Au atoms (58%) that do not join the chain structure and instead are alloyed into the Ni surface layer since their position is not observed by STM [16] and therefore unknown. We employed the full-potential linearized augmented plane wave method for thin film geometry [17] in the local spin density approximation including spin orbit coupling inside the atomic spheres with the spin direction in the Ni plane. We used approximately 100 augmented plane waves per atom and eight k points in the irreducible part of the Brillouin zone for self-consistency.

Figure 2 shows photoemission spectra of the valence band for clean Ni(110) and Au coverages between 0.1 and 2 ML. The spectra permit a clear distinction of different coverage regions as labeled in the figure: In region I, two peaks at high binding energy (5.7 and 4.2 eV) are seen. These peaks are characteristic of the surface-alloy-formation stage. In region II, an extra structure appears at 3.0 eV, which becomes narrow and sharp at 0.6 ML. In addition, another peak occurs at lower binding energy (1.9 eV). Below we focus on this thickness and spectrum and show that they are characteristic of the one-dimensional Au chain. Towards 0.9 ML, the structures in the spectra become broader and are believed to be due to the formation of a two-dimensional Au film.

Figure 3a shows for 0.6 ML the angle dependence in the $[1\bar{1}0]$ azimuth; i.e., \mathbf{k} is varied perpendicular to the chains. (Here, \mathbf{k} denotes the electron-wave-vector component in the surface plane.) We concentrate on the lower binding-energy region since we observe only here a peak that is not present for lower and for higher Au coverage. This structure remains at constant binding energy of 1.9 eV. For angles along the $[001]$ azimuth, i.e., \mathbf{k} variation parallel to the chains as displayed in Fig. 3b, the structure disperses by almost 1 eV. This can be explained by a confinement of Au electrons perpendicular to the chains and no confinement along the chains as expected for a quantum wire.

In addition, we have performed spin analysis of the spectrum at -8° emission angle in Fig. 3b. The result is

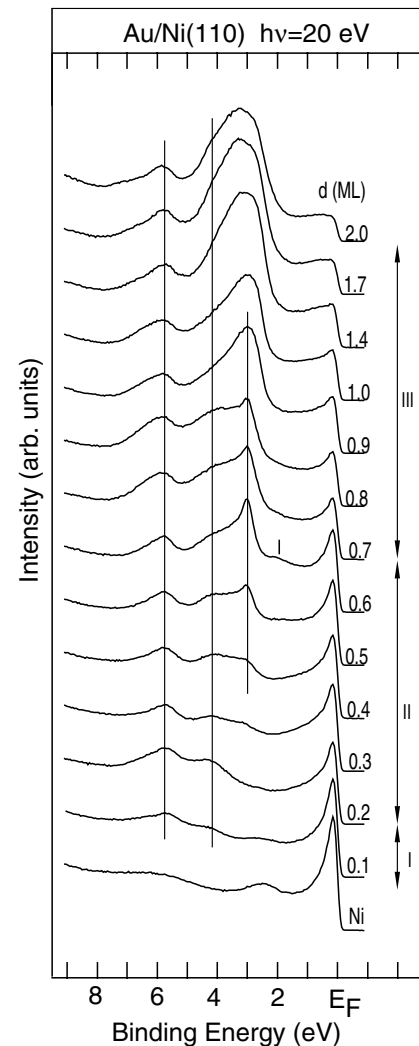


FIG. 2. Thickness-dependent photoemission spectra of Au/Ni(110) at 20-eV photon energy and normal emission. The characteristic chain structure occurs for $d = 0.6$ ML.

displayed in Fig. 4 as comparison of the spin-polarization spectrum between the Ni substrate before and after preparation of the Au chains. Its large and negative spin polarization shows that the quantum-wire state is of minority spin.

The large dispersion and the low binding energy of the quantum-wire peaks suggest that they are derived from Au $6s, p$ states. That Au $6s, p$ states have a highly anisotropic dispersion and must therefore be confined to the one-dimensional structure is surprising in view of the band structures of Au and Ni. The d states of Au and Ni are clearly separated in energy whereas s, p states are overlapping. This fact is easily seen from the calculated partial densities of states on Au and Ni atoms in Fig. 5b. The densities of states, dominated by d states, are for Ni high above and for Au below an energy position of about -3 eV. The s, p states are, however, generally extended over the whole energy range, and in order to assign them we use the band dispersion displayed for states

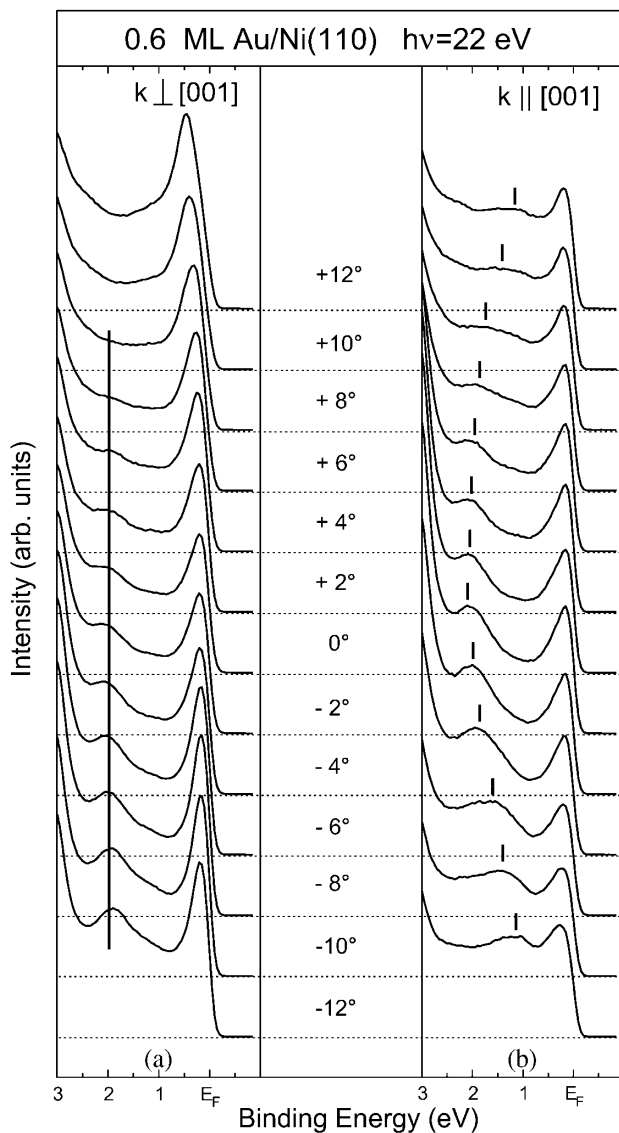


FIG. 3. Angle-resolved photoemission spectra of 0.6 ML Au/Ni(110) taken at 22-eV photon energy. (a) The electron emission angle Θ is varied perpendicular to the chains leaving the quantum-wire peak at fixed binding energy. (b) For angle variation parallel to the chains a finite dispersion is observed.

with substantial charge density on Au atoms ($>15\%$ in Fig. 5a). Although at somewhat lower energy than in the experiment, a band originating at -2.7 eV at $\bar{\Gamma}$ is easily identified and shows a considerable dispersion of about 0.6 eV along the chains and negligible dispersion perpendicular [18]. The experimental dispersion in Fig. 3b also amounts to about 0.5 eV between 0° and the zone boundary at 8° . Moreover, we can analyze this dispersing band further and find, e.g., at \bar{X} with 48% s, p character within Au muffin-tin spheres, a distribution that is typical for s, p states in this energy range [19].

In this way, the calculated results confirm also that (i) the chain-substrate interaction is small enough and (ii) the chain-chain interaction is sufficiently reduced in the pres-

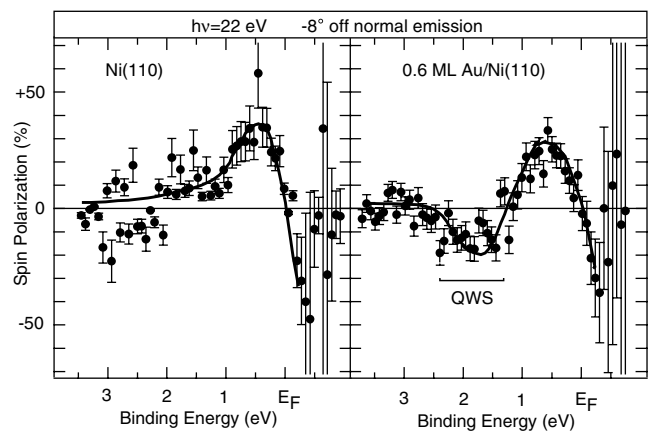


FIG. 4. Spin-polarization spectra show that the quantum-wire state is of minority spin.

ent system and in the model (chain-chain separation of 10.0 Å) in order to cause a one-dimensional band dispersion. We investigated the influence of the height (h) of the chain above the Ni surface and found that above 0.5 Å the dispersion of the bands is constant within 0.01 eV. Closer to the surface the bands parallel to the [001] direction had 0.05 – 0.1 eV less dispersion and were still almost flat perpendicular to [001]. Aware of the fact that the apparent height of an STM image can be quite different from the true atomic positions, we have chosen the structural model of Ref. [16] in Fig. 5 since a small change in dispersion does not affect our interpretation.

We want to discuss the peak broadening seen in Fig. 3b at -8° and 1.5 eV. The periodicity of the zigzag structure (3 Ni lattice constants) leads to Bragg reflection gaps expected at $\pm 8.3^\circ$ and 1.5 eV. Although our calculation does not predict the size of this gap precisely enough, this is the most likely explanation for this broadening [20].

The minority-spin character shows that the confinement of the electrons to the Au chain depends on their spin. Spin-dependent hybridization of electronic states can lead to a stronger chain-substrate interaction for one spin direction and a weaker chain-substrate interaction for the other one, here minority spin, which is confined more strongly to the Au chain. Analysis of the spin character in the calculation shows that the dispersing band in Fig. 5a is of minority spin. Figure 5b shows already that this band is located near a 0.5 -eV wide minority-spin bulk band gap extending around -3 eV. However, two Ni layers as substrate are too thin to observe Ni bulk band gaps in a \mathbf{k} -resolved manner. Comparison to a 13-layer ferromagnetic Ni(110) band structure [21] shows that away from normal emission the measured energy positions of the quantum-wire state lie in a bulk band gap of even symmetry and minority spin. Keeping in mind that in the case of two-dimensional multilayers the spin character of quantum-well states is understood as a result of spin-dependent bulk band gaps in the magnetic material [2–9], this result indicates that also in the present system the confinement in one dimension may

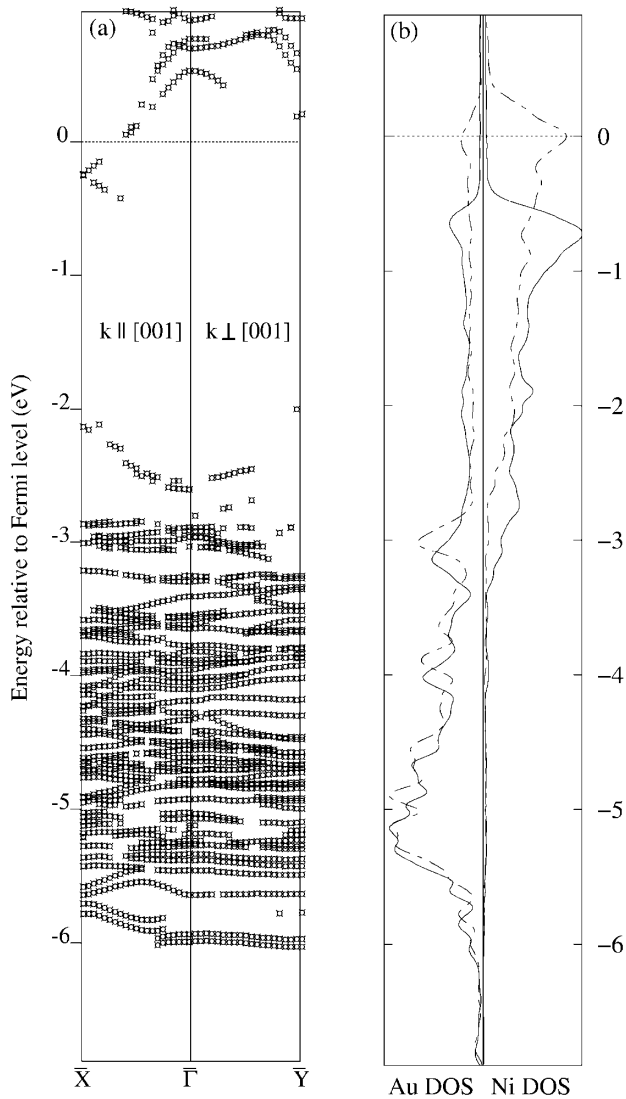


FIG. 5. Results from the *ab initio* calculation. (a) E vs k band dispersions for states with substantial charge density on Au atoms. A strongly anisotropic dispersion is observed. [\bar{X} and \bar{Y} refer to the $p(3 \times 4)$ structure.] (b) Partial densities of states for Au (left) and Ni (right). Solid lines are for majority spin and dashed lines for minority spin.

be imposed by spin-dependent bulk band gaps which lead to the different degree of confinement for the two spin directions.

We thank X. Nie, G. Reichardt, and Ch. Jung for their helpful contributions to the calculation and the experiment, respectively, and J. Redinger for unpublished band structures. This work has been supported by BMBF under Project No. 21.12D.

*Corresponding author.

Electronic address: rader@bessy.de

- [1] P. Grünberg *et al.*, Phys. Rev. Lett. **57**, 2442 (1986); A. Cebollada *et al.*, Phys. Rev. B **39**, 9726 (1989); M. T.

Johnson *et al.*, Phys. Rev. Lett. **68**, 2688 (1992); S. S. P. Parkin, Phys. Rev. Lett. **67**, 3598 (1991).

- [2] J. E. Ortega and F. J. Himpsel, Phys. Rev. Lett. **69**, 844 (1992).
 [3] K. Garrison, Y. Chang, and P. D. Johnson, Phys. Rev. Lett. **71**, 2801 (1993).
 [4] C. Carbone, E. Vescovo, O. Rader, W. Gudat, and W. Eberhardt, Phys. Rev. Lett. **71**, 2805 (1993).
 [5] C. Carbone, E. Vescovo, R. Kläsches, D. D. Sarma, and W. Eberhardt, Solid State Commun. **100**, 749 (1996).
 [6] P. D. Johnson, K. Garrison, Q. Dong, N. V. Smith, D. Li, J. E. Mattson, J. Pearson, and S. D. Bader, Phys. Rev. B **50**, 8954 (1994).
 [7] F. J. Himpsel and O. Rader, Appl. Phys. Lett. **67**, 1151 (1995).
 [8] P. Segovia, E. G. Michel, and J. E. Ortega, Phys. Rev. Lett. **77**, 3455 (1996).
 [9] R. Kläsches, D. Schmitz, C. Carbone, W. Eberhardt, P. Lang, R. Zeller, and P. H. Dederichs, Phys. Rev. B **57**, R696 (1998).
 [10] J. F. van der Veen, D. E. Eastman, A. M. Bradshaw, and S. Holloway, Solid State Commun. **39**, 1301 (1981).
 [11] H. Namba, N. Nakanishi, T. Yamaguchi, and H. Kuroda, Phys. Rev. Lett. **71**, 4027 (1993).
 [12] J. E. Ortega, F. J. Himpsel, R. Haight, and D. R. Peale, Phys. Rev. B **49**, 13859 (1994).
 [13] F. J. Himpsel and J. E. Ortega, Phys. Rev. B **50**, 4992 (1994).
 [14] T. Jung, Y. W. Mo, and F. J. Himpsel, Phys. Rev. Lett. **74**, 1641 (1995).
 [15] F. J. Himpsel, J. E. Ortega, G. J. Mankey, and R. F. Willis, Adv. Phys. **47**, 511 (1998).
 [16] L. P. Nielsen, F. Besenbacher, I. Stensgaard, E. Lægsgaard, C. Engdahl, P. Stoltze, and J. K. Nørskov, Phys. Rev. Lett. **74**, 1159 (1995).
 [17] See, e.g., M. Weinert and S. Blügel, in *Magnetic Multilayers*, edited by L. H. Bennett and R. H. Watson (World Scientific, Singapore, 1993).
 [18] The position of alloyed Au atoms beneath the chains cannot be specified by STM and has been neglected in our model. Note also that our Au chain is embedded in only two layers of Ni and that this might affect energy positions of the Au states.
 [19] For bulk Au the density of states has, e.g., at E_F , 36% s , p character within muffin tins according to D. A. Papaconstantopoulos, *Handbook of the Band Structure of Elemental Solids* (Plenum, New York, 1986).
 [20] Truly one-dimensional metals show Tomonaga-Luttinger-liquid behavior [F. D. Haldane, J. Phys. C **14**, 2585 (1981)], in particular, a power-law behavior of the intensity at the Fermi energy and spin-charge separation in the spectral function. Whether in the present system chain-substrate interaction is sufficiently weak and intrachain Coulomb interaction sufficiently high to lead to observable effects, is at present unclear and might be an interesting matter for follow-up studies. With our method, Au states at the Fermi energy are experimentally not accessible due to dominating Ni-substrate emission, and the various peak broadenings or splittings observed far from the Fermi energy can well be explained on the basis of Bragg scattering.
 [21] J. Redinger (unpublished).

Paper VIII

An Elastic “Sieve” to Probe Momentum Space: Gd Chains on W(110)

O. Rader¹ and A. M. Shikin^{1,2}

¹BESSY, Albert-Einstein-Strasse 15, D-12489 Berlin, Germany

²Institute of Physics, St. Petersburg State University, St. Petersburg 198904, Russia

(Received 29 May 2004; published 13 December 2004)

Electron scattering conditions of one-dimensional nanostructures are explored in angle-resolved photoelectron spectroscopy. Tiny increments of the Gd submonolayer coverage on W(110) lead to strong modifications in the spectra. It is shown that the Gd overlayer represents an elastic superlattice of chains which performs a systematic mapping of the electronic band dispersion of the W substrate through a quasicontinuous series of umklapp wave vectors. Conversely, a single valence-band spectrum contains essential and precise structural information readily accessible by comparison to the band dispersion.

DOI: 10.1103/PhysRevLett.93.256802

PACS numbers: 73.21.Fg, 71.20.Eh, 79.60.-i

Our knowledge of the electronic structure of solids is largely based on measurements by angle-resolved photoelectron spectroscopy since it is the only method to deliver $E(\mathbf{k})$ band dispersions of the valence electrons [1]. These band dispersions determine many fundamental properties like electrical conductivity, magnetism, optical properties, and mechanical properties along the various crystallographic directions, and numerous data have meanwhile been measured and compiled [2]. In order to perform a band mapping experiment on a crystal, it has been necessary to either exploit the conservation of the electron momentum parallel to the surface \mathbf{k}_{\parallel} by measuring different emission angles of the photoelectron or change the wavelength of the exciting photon source to vary the perpendicular wave vector \mathbf{k}_{\perp} along a high symmetry direction of the crystal [1].

With the exploration of the properties of ultrathin films as two-dimensional quantum-well structures, another method to determine $E(\mathbf{k})$ has been devised [3]. It was realized that the interface between the film and the crystalline substrate on which it is grown can serve as a sufficient scatterer for electrons to lead to electron confinement similar as with light waves in an optical Fabry-Perot interferometer. This allows a most precise mapping of the band dispersion by just varying the film thickness layer by layer in an angle-resolved photoelectron spectroscopy experiment [4].

The recent quest for lateral electron confinement in one-dimensional nanostructures has led to impressive interference effects of electron waves when atomic barriers are artificially constructed with the tip of a scanning tunneling microscope (STM) [5] or at the step edges at miscut crystal surfaces as natural scatterers [6]. We therefore pose the question whether lateral nanostructures can offer yet another way to experimentally obtain a band dispersion by photoelectron spectroscopy. To this end, a superlattice of scatterers needs to be constructed with the possibility to tune its lattice constant d over a considerable range. This superlattice could act like a “sieve” selecting the electron momentum k according to $k = 2\pi/d$. It appears promising to utilize self-organization

tendencies among adatoms with repulsive interactions and to break the symmetry by a substrate with a rectangular unit cell in order to force the atoms into chains. Au atoms on Ni(110) form such repulsive chains with a perfect one-dimensional electronic structure but the system has a complicated geometry since the Au is partially immersed in the Ni surface layer [7].

Enhanced versatility is expected turning to adsorbates with stronger repulsive interactions. Adsorbed rare-earth atoms on W(110) experience charge transfer which results in the formation of a strong atomic dipole perpendicular to the surface. The repulsive dipole-dipole interaction among the rare-earth atoms stabilizes a series of superstructures at room temperature [8,9]. Figure 1 displays the structures realized below 0.7 monatomic layers (ML) Gd/W(110) following the characterization by low-energy electron diffraction (LEED) and STM in Refs. [8,9]: Although the 10×2 structure at lowest coverage is a rectangular surface lattice, it is better described as chains running along the $[1\bar{1}0]$ direction of the W(110) substrate.

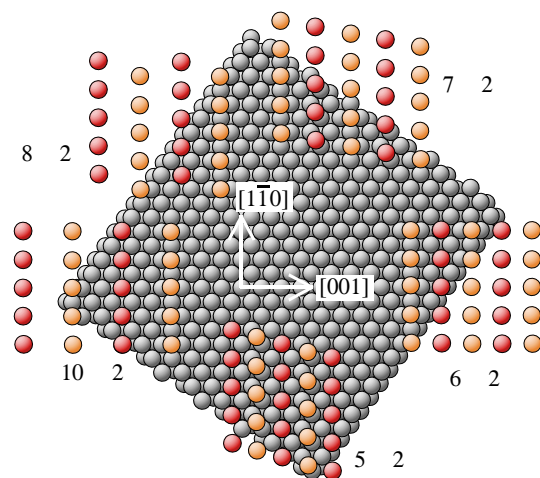


FIG. 1 (color online). Structure of Gd on W(110). Chains along $[1\bar{1}0]$ are formed which approach each other for increased Gd deposition. Colors mark Gd atoms with relatively higher (red) and lower (orange) positions according to Ref. [9].

With increasing coverage, more Gd atoms need to be squeezed in and are accommodated in new oblique lattices in which the chains successively approach each other along [001]. The interatomic distance along the chains is thereby conserved.

The experiment has been performed using a hemispherical photoelectron analyzer with 1° angle resolution and linearly polarized synchrotron light from undulator beam lines U125/1 PGM and UE56/1 PGM at BESSY [10]. Preparation of the W(110) sample and deposition of Gd have been done as described in Ref. [11] for thicker Gd/W(110).

Figure 2 shows at the bottom the clean W(110) spectrum characterized by W 6s states at -6.3 eV and intense emission from a W 5d surface resonance around -1.2 eV (0 eV corresponds to the Fermi energy E_F) [12]. Along the [110] surface normal, W(110) displays an even-symmetry bulk band gap extending from -2 to -6.3 eV [12]. For a photon energy of 62.5 eV, direct transitions from the lower boundary of this gap (-6.3 eV at the N point of the Brillouin zone) dominate the spectrum. Gd was deposited onto the W(110) substrate at room temperature, and after each deposition step the sample was annealed to $\sim 250^\circ\text{C}$ for 2 min. The first indication of Gd adsorption is from the unresolved multiplet of Gd 4f emission ($4f^6$ final state) at -8.3 eV and 0.28 ML coverage. While the W surface resonance and the W 6s peak have lost intensity, new

shoulders appear at -5.4 and -2.3 eV for 0.28 ML. At 0.39 ML, one shoulder has moved to -4.7 eV, and with each further Gd deposition step, the spectral shape changes continuously and becomes dominated by the new features. This behavior, unprecedented in submonolayer growth, continues until the spectral shape saturates with the completion of the first Gd monolayer indicated most clearly by a shift of the Gd 4f levels from -8.3 to -8.05 eV.

Before connecting the observed behavior to the series of superstructures shown in Fig. 1, we perform a test on the origin of the new photoemission structures. As direct photoemission transitions from W are symmetry forbidden in the energy range -2 to -6.3 eV (the small shoulder at -3.3 eV is a so-called high density-of-states peak), emission from Gd 5d states is a possible cause for the new features. Resonant photoemission at the Gd 4d excitation threshold (maximum at ~ 149 eV photon energy) can unambiguously distinguish Gd- from W-derived valence-band states. The resonance process enhances very strongly the Gd 4f emission via $4d^{10}4f^7 + h\nu \rightarrow 4d^9 4f^8 \rightarrow 4d^{10}4f^6 + e^-$ but at the same time also the Gd 5d emission via $4d^{10}4f^7 5d^n + h\nu \rightarrow 4d^9 4f^8 5d^n \rightarrow 4d^{10}4f^7 5d^{n-1} + e^-$. In Fig. 3, the Gd deposition was repeated without annealing and besides 62 eV two vicinal photon energies, 145 and 147 eV, were used. Between these energies the resonant photoemission intensity rises steeply so that the area enclosed between 147 and 145 eV spectra can be taken as a good approximation of the Gd 5d density of states. Interestingly, on this basis none of the peaks in the forbidden gap can be assigned to Gd which rather appears in the energy range between -2 eV and E_F . All new structures marked in Fig. 2 are therefore derived from W.

The behavior of the spectra in Fig. 2 bears a certain similarity to $E(\mathbf{k})$ band dispersions but with k replaced by the Gd coverage. The connection to the superstructures of Gd chains is explained in Fig. 4(a) which shows a cross section through the $(1\bar{1}0)$ plane of the crystal in reciprocal space. It is identical to the Ewald construction for LEED but taking the photoelectron as the primary wave. $\bar{\Gamma}$ is the center of the first surface Brillouin zone of W(110), identified with normal electron emission, and represented by a rod perpendicular to the surface plane. $\bar{\Gamma}'$ is the center of the second surface Brillouin zone of W(110), separated by 4.0 \AA^{-1} along [001]. In addition, reciprocal lattice rods (dashed) from an arbitrary superstructure are shown. All these rods correspond to centers of the superlattice Brillouin zone and one point on a rod away from $\bar{\Gamma}$ is chosen. Figure 4(a) indicates how this point, $\mathbf{k}_{i,1}$, can nevertheless contribute to normal electron emission ($\bar{\Gamma}$) through a single scattering event at the superlattice or surface reconstruction. This is represented by the diffraction vector \mathbf{G}_1 on the Ewald sphere. In angle-resolved photoelectron spectroscopy, this is a non-direct transition known as the umklapp process [13]: \mathbf{k}_{\parallel} is

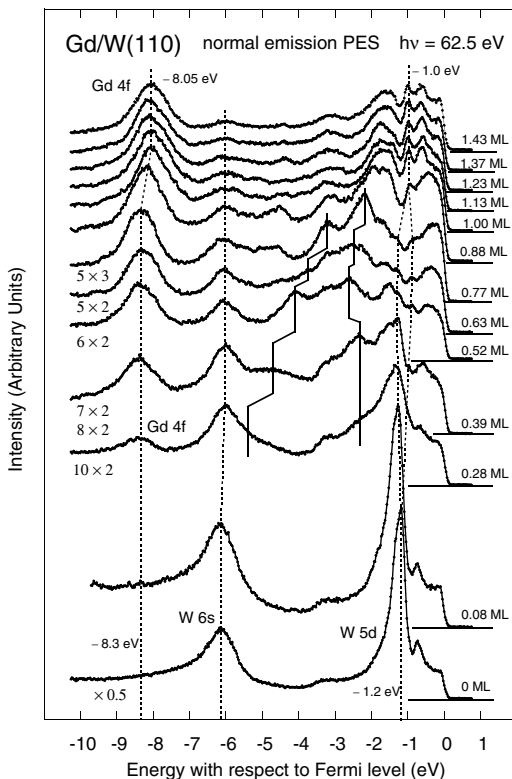


FIG. 2. Photoemission spectra of the valence band for various Gd coverages on W(110). In the range of the forbidden gap of W (-2.0 to -6.3 eV) strong changes occur.

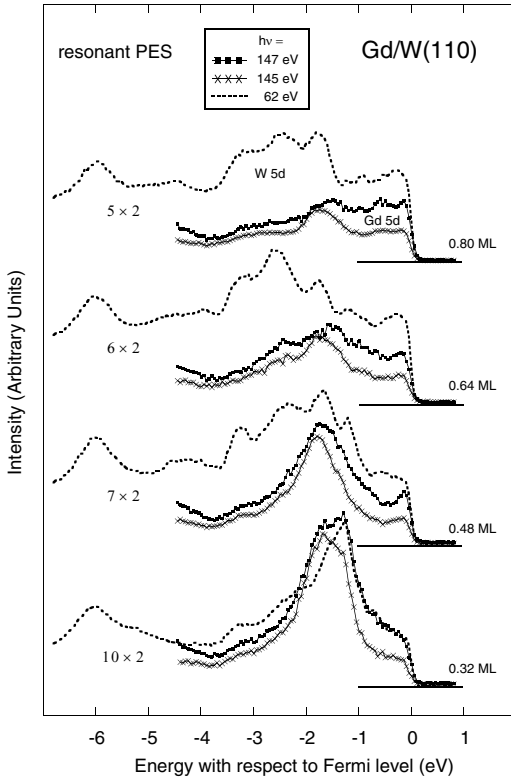


FIG. 3. Photoemission spectra at 62 eV photon energy as compared to resonant photoemission spectra. The difference between resonant photoemission spectra at 147 and 145 eV corresponds to the Gd 5d density-of-states. All characteristic features seen at 62 eV are derived from W.

conserved when the electron passes through the surface according to $\mathbf{k}_{\parallel}^{\text{ext}} = \mathbf{k}_{\parallel}^{\text{int}} + \mathbf{G}_{\parallel}$ where \mathbf{G}_{\parallel} represents any reciprocal lattice vector in the surface plane. This relationship has been used to assign unexpected features in photoemission spectra but never systematically or without varying \mathbf{k}_{\perp} [13]. For the present experiment, this means that the 10×2 structure corresponds to $\mathbf{k}_{\parallel} = -\mathbf{G}_{\parallel} = \frac{1}{10}\overline{\Gamma}\Gamma'$ or 0.40 \AA^{-1} . Figure 4(b) shows how \mathbf{k}_{\parallel} increases with increasing Gd coverage as the $n \times 2$ series continues with 0.50 \AA^{-1} (8×2), 0.57 \AA^{-1} (7×2), 0.66 \AA^{-1} (6×2), and 0.80 \AA^{-1} (5×2) along [001]. The umklapp vector \mathbf{k}_{\parallel} although given by the Gd probes momentum space of the W.

The validity of this interpretation can directly be checked in the experiment. The basis is the observation that angle-dependent photoemission is governed by the same relationships as the umklapp effect: In angle-dependent photoemission, Figs. 4(c) and 4(d), the sample is tilted off normal against the detector by an angle α giving the electron wave vector that is probed a parallel component $|\mathbf{k}_{\parallel}| = (\sqrt{2mE_{\text{kin,vac}}}/\hbar)\sin\alpha$. The Ewald spheres in Fig. 4 indicate further that any identity $\mathbf{G}_1 = \mathbf{k}_{\parallel,1}$ determines that also the respective perpendicular components \mathbf{k}_{\perp} are equal (neglecting changes of the work function); i.e., the same point of the bulk

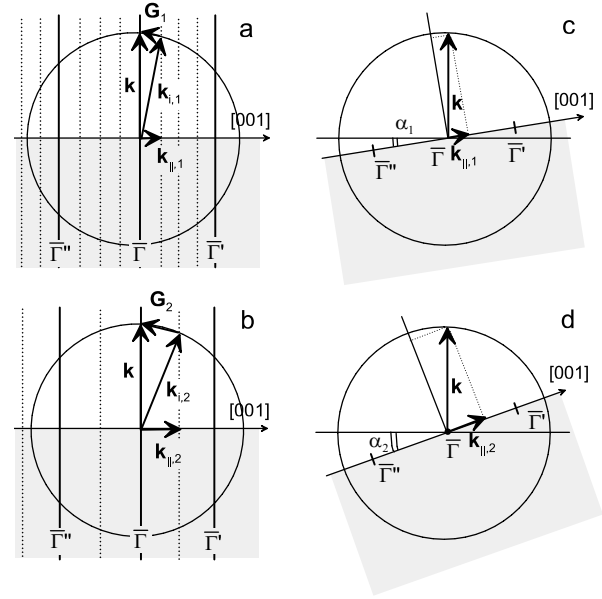


FIG. 4. Proposed model. Reciprocal lattice rods for the W(110) surface (solid vertical lines) and for a Gd superlattice (dotted lines) (a). W bulk states away from $\overline{\Gamma}$ can contribute to normal-emission spectra via a diffraction vector \mathbf{G}_1 . For the given system, the parallel component $\mathbf{G}_{\parallel} = -\mathbf{k}_{\parallel}$ increases in proportion with the adsorbate coverage (b). For comparison, angle-dependent photoemission obeys the same relationships between \mathbf{k} and \mathbf{k}_{\parallel} when the emission angle α is varied thus probing the same initial states in the bulk Brillouin zone of W (c),(d).

Brillouin zone is sampled in 4(a) and 4(c) and in 4(b) and 4(d), respectively.

As a demonstration, we show in Fig. 5(a) a Gd coverage dependence measured under the same conditions as in Figs. 2 and 3 but at room temperature and smaller coverage steps of ~ 0.03 ML and displayed in a color representation *vis à vis* the angle dependence for clean W(110) along [001]. For a Gd coverage from 0 up to ~ 0.7 ML, where the intrachain distance remains constant, an impressive similarity between the two cases is observed in the energy range of the gap (-2.0 to -6.3 eV). The fact that the \mathbf{k}_{\parallel} vector does not change continuously but in discrete steps can be seen from the strongly dispersing band in Fig. 5(a). Energies jump rather abruptly from -4.1 , -4.6 , to -5.4 eV in a range where the Gd coverage is varied in 10 steps at least.

A few remarks should be made concerning the implications of these results. The results emphasize the importance of electron scattering and demonstrate that it will seriously complicate the interpretation of electron spectroscopy of nanostructures assembled on flat, prepatterned, or stepped substrates. The effect occurs more strongly the better the nanostructures are ordered. The present results represent, on the other hand, only the starting point of a more systematic exploitation of the structural information contained in the umklapp emis-

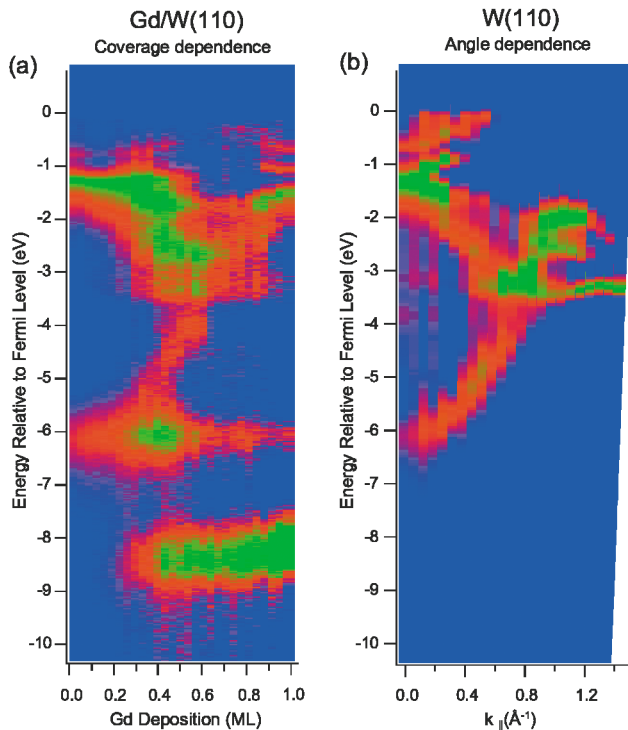


FIG. 5 (color). Coverage dependence in normal emission of Gd/W(110) (a) versus emission angle dependence of clean W(110) along [001] (b). The Gd overlayer provides for a quasicontinuous series of umklapp vectors \mathbf{G}_{\parallel} in proportion to the Gd coverage to sample the W bulk band structure. Up to ~ 0.8 ML, all transitions inside of the gap (-2 to -6.3 eV) are of the umklapp type. Note the direct transitions at -6.3 eV (N-point of W) and -8.3 eV (Gd 4f).

sion. The structural information contained in the umklapp-induced peaks can indeed serve as the basis of a coverage calibration of unprecedented precision and can be used to assign the initial-state effects simultaneously present in the spectra. We want to briefly return to Fig. 2 to point out the behavior of the W surface resonance at -1.2 eV. It was found that this surface resonance directly connects to the two-dimensional Fermi surface of W(110) [14]. The changes of the surface resonance observed in Fig. 2 indicate that Gd acts on the Fermi surface. The dipole interaction between Gd atoms is basically isotropic, but using the structural information contained in the umklapp part of an individual valence-band spectrum together with electronic properties from the direct transitions, it will be possible to identify the modifications of the Fermi surface which force the Gd atoms into chains and in this way put the geometry down to the electronic structure.

In summary, we have shown how a coherent array of Gd nanostructures, stable at room temperature on W(110), can be used to probe the electronic structure of

the W substrate through a series of nondirect photoemission transitions. This emphasizes in an impressive way the importance of scattering when studying electronic properties, and some resulting problems and perspectives for nanostructure research have been addressed.

We acknowledge participation of C. Pampuch, G.V. Prudnikova, and A. Varykhalov in parts of the experiment and thank R. Follath for expert support with the U125 beam line. This work was supported by DFG (RA 1041/1-1 and 436RUS113/735/0-1), the common DFG-RFFI project (03-02-04-024), and the Russian program "Surface and Atomic Structures."

-
- [1] *Angle Resolved Photoemission*, edited by S. D. Kevan (Elsevier, Amsterdam, 1992); S. Hüfner, *Photoelectron Spectroscopy* (Springer, Berlin, 1995).
 - [2] *Electronic Structure of Solids: Photoemission Spectra and Related Data*, edited by A. Goldmann, Landolt-Börnstein, New Series, Group III, Vol. 23 (Springer, Berlin, 1999).
 - [3] R. C. Jaklevic and J. Lambe, *Phys. Rev. Lett.* **26**, 88 (1971); P. D. Loly and J. B. Pendry, *J. Phys. C* **16**, 423 (1983).
 - [4] J. J. Paggel, T. Miller, and T. C. Chiang, *Science* **283**, 1709 (1999); T. C. Chiang, *Surf. Sci. Rep.* **39**, 181 (2000).
 - [5] M. F. Crommie, C. P. Lutz, and D. M. Eigler, *Science* **262**, 218 (1993).
 - [6] P. Avouris and I. W. Lyo, *Science* **264**, 942 (1994); L. Burgi, O. Jeandupeux, A. Hirstein, H. Brune, and K. Kern, *Phys. Rev. Lett.* **81**, 5370 (1998); A. Mugarza, A. Mascaraque, V. Perez-Dieste, V. Repain, S. Rousset, F. J. Garcia de Abajo, and J. E. Ortega, *Phys. Rev. Lett.* **87**, 107601 (2001).
 - [7] C. Pampuch, O. Rader, T. Kachel, W. Gudat, C. Carbone, R. Kläsches, G. Bihlmayer, S. Blügel, and W. Eberhardt, *Phys. Rev. Lett.* **85**, 2561 (2000).
 - [8] J. Kołaczkiwicz and E. Bauer, *Surf. Sci.* **175**, 487 (1986).
 - [9] R. Pascal, Ch. Zarnitz, M. Bode, and R. Wiesendanger, *Phys. Rev. B* **56**, 3636 (1997).
 - [10] R. Follath, F. Senf, and W. Gudat, *J. Synchrotron Radiat.* **5**, 769 (1998); M. R. Weiss *et al.*, *Nucl. Instrum. Methods Phys. Res., Sect. A* **467–468**, 449 (2001).
 - [11] O. Rader and A. M. Shikin, *Phys. Rev. B* **64**, 201406(R) (2001).
 - [12] R. H. Gaylord and S. D. Kevan, *Phys. Rev. B* **36**, R9337 (1987); J. Feydt, A. Elbe, H. Engelhard, G. Meister, Ch. Jung, and A. Goldmann, *Phys. Rev. B* **58**, 14 007 (1998).
 - [13] E. O. Kane, *Phys. Rev. Lett.* **12**, 97 (1964); J. Anderson and G. J. Lapeyre, *Phys. Rev. Lett.* **36**, 376 (1976); D. Westphal and A. Goldmann, *Surf. Sci.* **126**, 253 (1983); G. Paolucci, K. C. Prince, B. E. Hayden, P. J. Davie, and A. M. Bradshaw, *Solid State Commun.* **52**, 937 (1984).
 - [14] R. H. Gaylord, K. H. Jeong, and S. D. Kevan, *Phys. Rev. Lett.* **62**, 2036 (1989).

Paper IX

Structure and electron correlation of Mn on Ni(110)

O. Rader,* T. Mizokawa,[†] and A. Fujimori

Department of Physics, University of Tokyo, 7-3-1 Hongo, Bunkyo-ku, Tokyo 113-0033, Japan

A. Kimura

Department of Physical Sciences, Graduate School of Science, Hiroshima University, 1-3-1 Kagamiyama, Higashi-Hiroshima 739-8526, Japan

(Received 23 May 2001; published 8 October 2001)

We have deposited Mn on the (110) surface of Ni and discover ordering into a $c(2\times 2)$ superstructure for coverages of 0.35–0.5 monolayer Mn. Mn $2p$ photoemission spectra show distinct satellite structures which disappear for higher Mn coverage. Calculations using configuration-interaction theory including multiplet effects on a model cluster representing the local geometry of a surface alloy identify the features as correlation satellites and give model parameters as follows: charge-transfer energy $\Delta=1$ eV, Coulomb energy $U=3$ eV, and transfer integral $T=1.2$ eV. A detailed comparison to the case of $c(2\times 2)$ Mn/Cu(100) leads to the conclusion that $c(2\times 2)$ Mn/Ni(110) is a new magnetic surface alloy.

DOI: 10.1103/PhysRevB.64.165414

PACS number(s): 79.60.Dp, 73.20.Hb

I. INTRODUCTION

A new material class termed *ordered magnetic surface alloys* has recently been characterized by Wuttig, Gauthier, and Blügel.^{1,2} Materials pertaining to this class consist of a metallic crystal surface on top of which atoms that bear a magnetic moment arrange in a certain superstructure. This structure differs not only laterally from a simple $p(1\times 1)$ -type overlayer: Experimental and theoretical structure determinations revealed that the adsorbate occupies sites of the surface atomic layer of the substrate, however at a comparatively large outward relaxation. For the first ordered magnetic surface alloy that has fully been characterized, the system $c(2\times 2)$ Mn/Cu(100) formed by deposition of the mass equivalent of 0.5 monolayer (ML) Mn, this outward relaxation amounts to 14% of the Cu(100) interlayer distance.¹ Subsequent to the characterization of this system, another manganese surface alloy has been identified: $c(2\times 2)$ Mn/Ni(100).³ In addition to these surface alloys at nominal half-monolayer Mn coverage, more complicated structures have been identified for deposited amounts beyond 0.5 ML like the $p2mg(4\times 2)$ Mn/Cu(100) structure.⁴ The stability of these systems has been studied by *ab initio* total-energy calculations with the result that they are stabilized by the presence of the magnetic moment; i.e., the structures would not form for a paramagnetic Mn atom.^{1,2}

Interesting magnetic properties have been predicted. The Mn-Mn distance in the $c(2\times 2)$ Mn/Cu(100) system is by a factor of $\sqrt{2}$ larger than in bulk fcc metals like Cu. This increased distance is expected to revert the magnetic coupling between Mn moments from antiparallel to parallel causing long-range ferromagnetic order.¹ Experimentally, however, neither magnetic circular x-ray dichroism at room temperature⁵ nor spin-resolved photoemission at liquid-nitrogen temperature⁶ have yet been able to confirm this interesting prediction for $c(2\times 2)$ Mn/Cu(100). On the other hand, the surface-alloy system $c(2\times 2)$ Mn/Ni(100) orders ferromagnetically with parallel coupling of the Mn moments to the magnetization of the Ni substrate as seen from mag-

netic circular x-ray dichroism measurements.^{5,7} Temperature-dependent studies show that ferromagnetic order is caused by the ferromagnetism of the Ni substrate and that the Mn follows the magnetization of the Ni surface atomic layer.⁷

In a complete study of the occupied and unoccupied electronic structure of $c(2\times 2)$ Mn on Cu(100) it has been observed that the exchange splitting of Mn $3d$ is almost twice as large in photoemission and inverse photoemission than from first-principles calculations.⁶ For $c(2\times 2)$ Mn/Ni(100) the experimental value exceeds the theoretical one still by a factor of 1.5.⁶ In addition, the angle dispersion of Mn $3d$ minority-spin states has been found to be very small (110 meV) for $c(2\times 2)$ Mn/Cu(100).⁶ Both observations indicate strong correlation of $3d$ electrons in the $c(2\times 2)$ structure. This has been verified by the observation of a valence-band satellite structure for $c(2\times 2)$ Mn/Cu(100) with prominent peaks at 8 eV and 9.6 eV binding energy.⁸ In order to distinguish the Mn-derived valence-band satellite from the well-known Cu-derived satellite peaks at 11.8 eV and 14.6 eV, the assignment of the Mn-derived satellite has been done on the basis of resonant photoemission at the Mn $3p$ excitation threshold. Interestingly, Mn $2p$ core-level photoemission spectra also show intense satellite structures for $c(2\times 2)$ Mn/Cu(100), and this fact renders identification of correlation effects in an element-selective manner particularly convenient.⁸ For this system, the positions of Mn $3d$ states in photoemission and inverse photoemission, of the valence-band satellite, and of the Mn $2p$ core-level satellite have been used in Ref. 8 to consistently describe the system with a simple configuration-interaction cluster model and to derive model parameters.

It is interesting to ask whether the class of ordered magnetic surface alloys is limited to Mn on (100) surfaces of Cu and Ni or whether further members can be identified. In fact, 0.5 ML $c(2\times 2)$ Mn/Cu(110) has been characterized as surface alloy.⁹ On the other hand, the $c(2\times 2)$ superstructure of Mn/Ag(100) has been identified as a double-layer surface alloy involving 1.5 ML Mn.¹⁰ On fcc Co(100), Mn has been found to grow as $p(1\times 1)$ overlayer;¹¹ however, weak $c(2\times 2)$ low-energy electron diffraction (LEED) spots

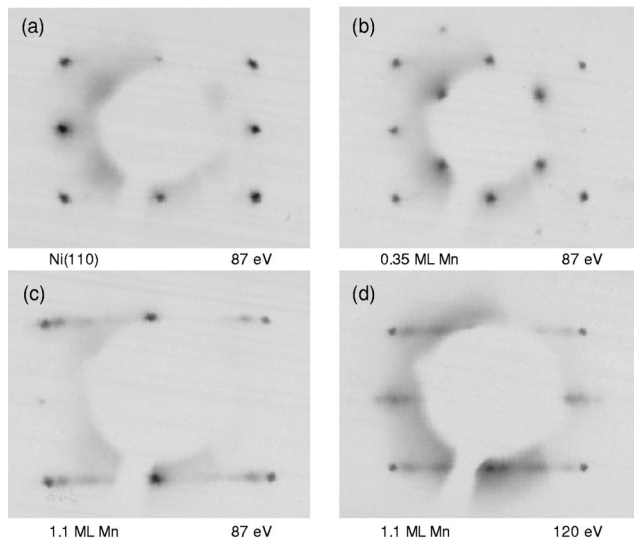


FIG. 1. LEED patterns of (a) clean Ni (110) and (b) 0.35 ML $c(2 \times 2)$ Mn/Ni(110) taken at 87 eV and of 1.1 ML (7×1) Mn/Ni(110) taken at 87 eV (c) and at 120 eV (d). (c) is a closeup.

have recently been reported for 0.3–0.8 ML coverage and considered as indication for surface alloy formation.¹² On Fe(100) and Fe(110), on the other hand, only $p(1 \times 1)$ Mn superstructures have been observed and interpreted as layer growth without interdiffusion.^{13,14} Interestingly, a weak $c(2 \times 2)$ superstructure has also been found for 1 ML Co/Cu(100) after annealing.¹⁵

In the present work, Mn is deposited on Ni(110), and a $c(2 \times 2)$ structure appears around half-monolayer coverage. We study electron correlation effects on the electronic structure. Ni as substrate poses a similar problem to the assignment of valence-band features as the one mentioned above for Cu: countless satellite lines have been distinguished between 6 eV and 35 eV binding energy for pure Ni.¹⁶ Therefore, we use Mn $2p$ x-ray photoelectron spectroscopy. We observe a distinct satellite which disappears together with the $c(2 \times 2)$ superstructure for higher Mn coverage. The satellite is similar to but weaker than the one observed for $c(2 \times 2)$ Mn/Cu(100) in agreement with the expectation of somewhat larger hybridization between Mn and Ni as compared to the case of Mn and Cu. We used the experience gained in previous analyses⁸ of Mn-based surface alloys and analyze the spectra using a corresponding configuration-interaction cluster model.

II. EXPERIMENTS

Experiments were done in a vacuum chamber equipped with standard tools for surface preparation and characterization like LEED as well as a spherical electrostatic analyzer (VG CLAM) for x-ray photoelectron spectroscopy. We used Mg $K\alpha$ radiation for Mn $2p$ spectra. No correction for x-ray satellite lines has been done. Preparation of the Ni(110) single crystal has been performed *in situ* by Ne⁺ ion bombardment and heating cycles until a sharp and intense $p(1 \times 1)$ LEED pattern was visible [Fig. 1(a)]. The

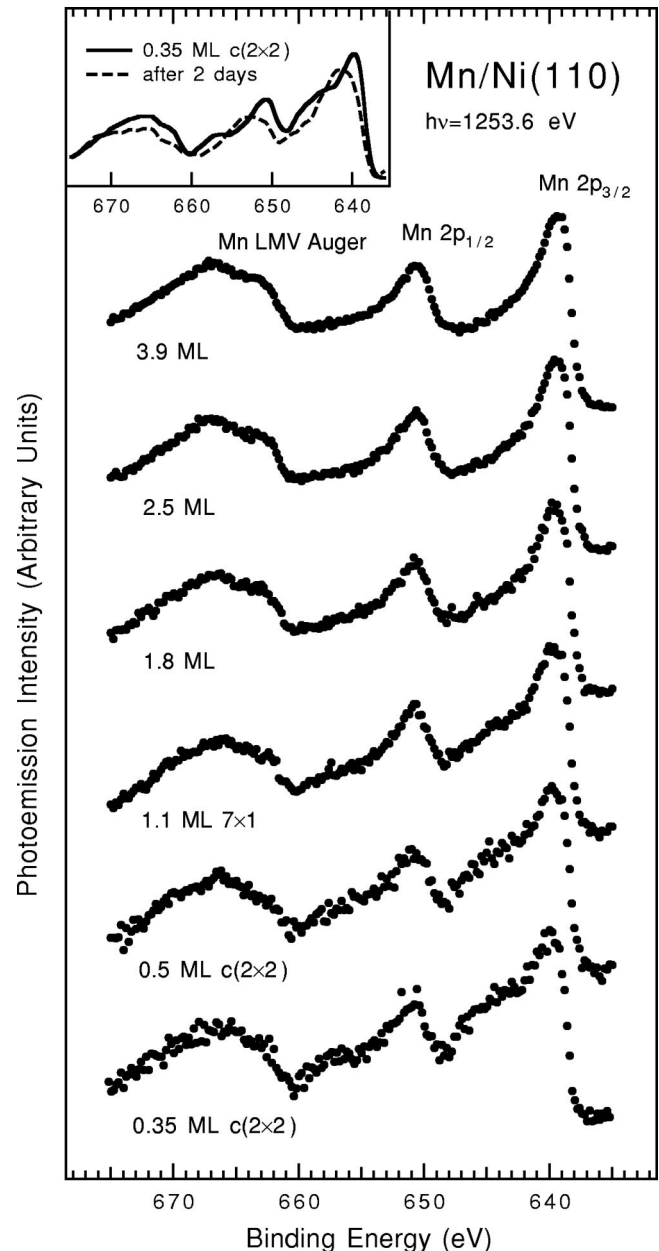


FIG. 2. Mn $2p$ core-level photoelectron spectra for various coverages of Mn on Ni(110). No background correction was done for all but the lowest two coverages, where a linear slope caused by the Ni substrate has been subtracted. Intense satellites about 5 eV below the main peaks appear in particular for the $c(2 \times 2)$ structure.

base pressure was in the upper 10^{-11} Torr range; e.g., when measuring the 0.35-ML spectrum shown in Fig. 2 the base pressure was 6.5×10^{-11} Torr and rose to 9.5×10^{-11} Torr during operation of the x-ray source. Mn has been evaporated from high-purity pieces by electron-beam heating enclosed in a water-cooled jacket. The deposition rate (0.7 ML/min) has been calibrated with an oscillating quartz and kept constant during *in situ* deposition by measuring the Mn ion current. This was particularly useful since spectra from different measurements had to be added. To keep sample contamination at a small level, we completed data acquisition for each sample in less than 2 h time, after which it was repre-

pared and the measurement reiterated. Moreover, we used a pass energy of 50 eV ensuring a high count rate. Spectra were taken with the sample at room temperature.

Figure 1(a) shows the $p(1 \times 1)$ LEED pattern of the clean Ni(110) substrate. For 0.35-ML [Fig. 1(b)] and 0.5-ML Mn coverage an intense $c(2 \times 2)$ superstructure is observed. The substrate temperature was kept at 70 °C during Mn deposition. This temperature has been found favorable for the growth of $c(2 \times 2)$ Mn on the (100) surface of Ni,³ and in fact the present superstructure is as intense as the ones observed previously for $c(2 \times 2)$ Mn on (100) surfaces of Cu and Ni bulk crystals. Around the full monolayer coverage a 7×1 pattern is observed in Figs. 1(c) and 1(d). This structure could be a relaxed full Mn monolayer similar to the one obtained by deposition of 1 ML Mn on Cu(100) at low temperature (<270 K) which results in an 8×2 structure.¹⁷ The thickest coverage deposited in the present work (3.9 ML) leads to a diffuse LEED pattern.

The Ni surface is reactive; this holds even more after Mn deposition. It should be noted in this context that oxygen does not generate a $c(2 \times 2)$ superstructure on Ni(110).¹⁸ Rather, on the contrary, it has for Cu(110) been shown that the addition of oxygen destroys the Mn-induced $c(2 \times 2)$ superstructure.⁹ The actual amount of contamination has in the present work been estimated from the ratio of O 1s versus Mn $2p_{3/2}$ photoemission intensities using tabulated sensitivity factors.¹⁹ Clean surfaces are crucial in this experiment, and the sample with the lowest Mn coverage is most sensitive to a deterioration of the Mn $2p$ spectrum. For the lowest Mn coverage in Fig. 2 (0.35 ML), an oxygen coverage of not more than 0.05 ML results from our estimate. We have also measured the Mn $2p$ spectrum of a 0.35-ML-Mn sample after 2-day exposure to the residual gas and display it in the inset of Fig. 2. This spectrum shows that oxidation leads to a peak at a binding energy between the Mn main peak and the satellite peak (to be discussed below) of the Mn-induced $c(2 \times 2)$ structure. Moreover, the spectrum in the inset of Fig. 2 resembles the MnO₂ spectrum from Ref. 19.

Figure 2 shows the thickness dependence of Mn $2p$ core-level spectra. For the $c(2 \times 2)$ structure, we observe a broad and intense satellite about 5 eV below the $2p_{3/2}$ and $2p_{1/2}$ main peaks which has almost equal intensity for 0.35 and 0.5 ML. For 1.1 ML, the satellite already loses intensity, and for 1.8 ML the spectral shape approaches the one of bulk Mn metal without extra structures.

We will argue in the following section that the reduced Mn-Mn coordination in the $c(2 \times 2)$ structure, where ideally no Mn-Mn next-neighbor pairs exist, results in enhanced electron correlation giving rise to the satellite structures. This holds to a lesser extent also for the the 1.1-ML overlayer where Mn-Mn interaction is reduced due to the vacuum interface and due to missing subsurface Mn neighbors.

III. MODEL CALCULATIONS

For the $c(2 \times 2)$ structure, the Mn $2p$ excitation spectrum can be described by a simple configuration-interaction model on a Mn-Ni cluster. Previously, we have successfully em-

ployed a simpler model for the case of $c(2 \times 2)$ Mn/Cu(100).⁸ In analogy to the cases of Mn on Cu(100), Cu(110), and Ni(100) we tentatively assign the behavior of LEED and photoemission to the formation of a surface alloy. As with these three similar surface alloys, which are structurally very similar to each other, a substantial outward relaxation can be expected. Interestingly, it has been argued that the intense superstructure LEED reflexes are not expected to occur for systems without such a substantial relaxation because of the proximity of the atomic numbers of Mn on the one hand and of Ni or Cu on the other hand.² We use for the present model the same Mn relaxation of $0.06a$ (where a is the substrate lattice constant) as obtained from the quantitative analysis for $c(2 \times 2)$ Mn/Cu(110), keeping in mind that the relaxations for $c(2 \times 2)$ Mn on Cu(100) and Ni(100) have been found to be very similar to each other.

The present data analysis method has widely been applied in studies on transition-metal compounds, and the reader may find basic aspects of the configuration-interaction cluster model in the review literature.²⁰ Core-level photoemission with its element sensitivity is particularly useful when combined with configuration-interaction calculations which include the multiplet effect and charge-transfer effect.^{21–23} In particular, transition-metal $2p$ photoemission, which can efficiently be excited by conventional Mg and Al $K\alpha$ radiation, has been analyzed by configuration-interaction theory in a systematic way.^{24,25} In the configuration-interaction calculation on the cluster-type model, while the multiplet effect is derived from the Coulomb interaction term between the transition-metal $2p$ core hole and transition-metal $3d$ electrons, the charge-transfer effect is due to the hybridization term between the transition-metal $3d$ orbitals and ligand orbitals. It has been found that the charge-transfer effect is more important than the multiplet effect to explain transition-metal $2p$ photoemission line shape observed in many transition-metal compounds.²⁴ (On the other hand, the multiplet effect is much more important than the charge-transfer one in transition-metal $2p$ x-ray absorption, x-ray emission, and electron-energy loss spectra.) Therefore, we used a version of the configuration-interaction cluster model in which the Coulomb interaction term is included in a simplified way²⁴ and, instead, the hybridization term between the Mn $3d$ and ligand orbitals in the Mn-Ni cluster is considered in an exact way.

Figure 3 shows the structural model used in the present work. It is more complex than the one used previously⁸ due to the twofold symmetry of the fcc (110) surface. Two Ni atoms in the surface (S) layer (type 1, Mn-Ni distance $0.710a$ with a being the Ni lattice constant), four in the S-1 layer (type 2, $0.739a$), and one in the S-2 layer (type 3, $0.767a$) are considered; the two remaining atoms in the S layer are too far ($1.003a$) and therefore have been cut off. The ground state of the cluster considers three configurations, i.e.,

$$\psi_g = a_0 |d^5\rangle + a_1 |d^6 \underline{L}\rangle + a_2 |d^7 \underline{L}^2\rangle.$$

Here, \underline{L} denotes a ligand hole, which corresponds to the transfer of an electron from a Ni d orbital to a Mn d orbital.

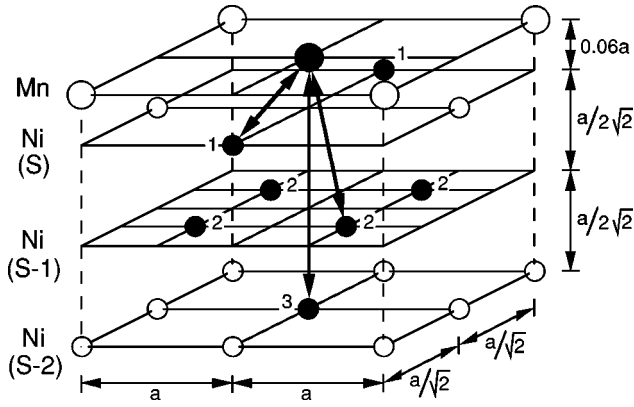


FIG. 3. Structural model employed in the configuration-interaction calculation for the $c(2 \times 2)$ superstructure. Positions of Mn (large circles) and Ni atoms (small circles). Hybridization between atoms marked by solid circles has been included in the model. For clarity, vertical distances appear expanded.

The energy associated with this charge transfer is $\Delta = E(d^6\bar{L}) - E(d^5)$. The Mn $3d$ -Mn $3d$ Coulomb interaction energy is $U = E(d^6) + E(d^4) - 2E(d^5)$, where the energy $E(d^n\bar{L}^m)$ is the center of gravity of the multiplet corresponding to the $d^n\bar{L}^m$ configuration. The transfer integrals describing the hybridization between Mn $3d$ and Ni $3d$ are expressed in terms of Slater-Koster parameters ($dd\pi$) and ($dd\sigma$). Expressions for their anisotropy and distance dependence have been taken from Ref. 26. The final state of Mn $2p$ photoemission is given by

$$\psi_f = b_0|c\bar{d}^5\rangle + b_1|c\bar{d}^6\bar{L}\rangle + b_2|c\bar{d}^7\bar{L}^2\rangle,$$

where c represents a Mn $2p$ core hole. The Mn $2p$ -Mn $3d$ Coulomb interaction energy Q has been tied to U by the typical assumption $U/Q = 0.8$. The Mn $2p$ photoemission intensity is given by

$$I_f \propto |a_0b_0 + a_1b_1 + a_2b_2|^2$$

in the sudden approximation.

IV. ANALYSIS

The remaining parameters to be determined from the comparison to the experiment are Δ , U , and $T = (dd\sigma)$. Out of the two similar experimental spectra representing $c(2 \times 2)$ Mn, the 0.35-ML spectrum has been chosen for comparison to theory. The reason is that the Mn local geometry will not change if a few $c(2 \times 2)$ sites are left empty; however, excess Mn atoms will likely form Mn-Mn dimers which would change the $2p$ spectrum. As usual, Lorentzian and Gaussian broadenings and an integrated background have been applied to the theoretical spectrum. Figure 4 shows the best fit reached for $\Delta = 1$ eV, $U = 3$ eV, and $T = 1.2$ eV. For comparison to the case of $c(2 \times 2)$ Mn/Cu(100) we have repeated the calculation for the MnCu₈ cluster in the geometry described in Ref. 8 with the present model, i.e., including multiplet effects. We obtain $\Delta = 1.5$ eV, $U = 3$ eV, and $T = 1.0$ eV for the Cu-based system and an agreement with experiment sub-

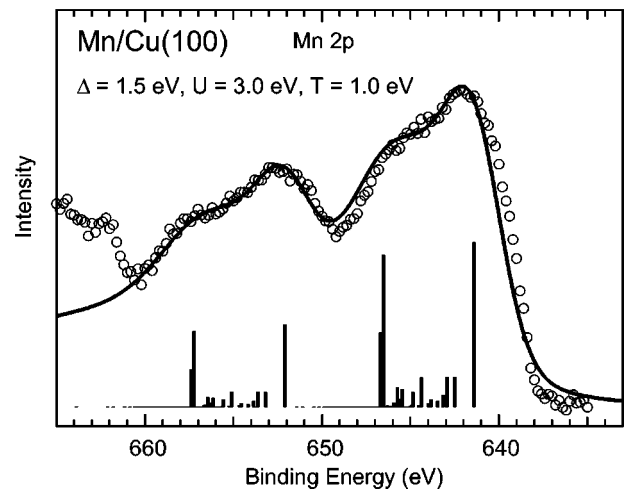
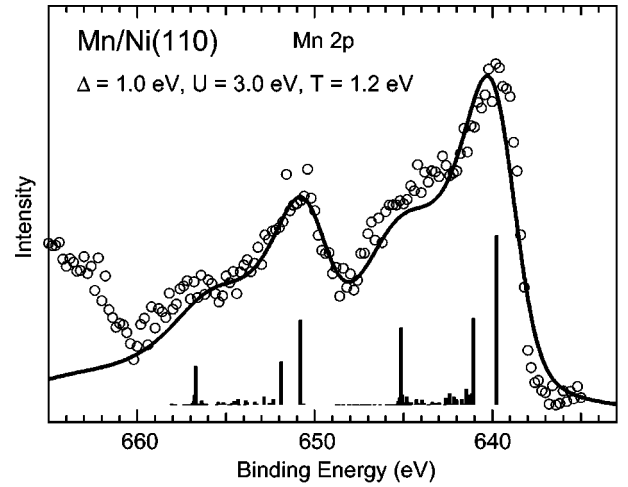


FIG. 4. Configuration-interaction cluster-model theory for $c(2 \times 2)$ Mn/Ni(110) compared to the measured spectrum of 0.35 ML (top). The case of the well-characterized surface alloy 0.5 ML $c(2 \times 2)$ Mn/Cu(100) is shown for comparison (bottom).

stantially improved with respect to Ref. 8—almost perfect matching between model and experiment is now reached in Fig. 4. The inclusion of multiplet splittings leads to slightly altered parameters²³ like a reduction of Q (or U) ($\Delta = 0$ eV, $U = 4$ eV, and $T = 0.7$ eV were obtained in Ref. 8). Similarly, inclusion of multiplets has a comparatively strong effect on Δ for the d^5 configuration.²⁰ Comparison of the two systems of Fig. 4 confirms the expectation that Δ and T , but not U , vary slightly with the chemical environment (Ni and Cu, respectively) of the Mn atom. The small but finite values for the charge-transfer energy Δ are realistic in view of the range obtained for three-dimensional Mn compounds (from $\Delta = 6.5$ eV for MnO to 1.5 eV for MnTe, Ref. 20). The present analysis corroborates $\Delta < U$, which means that in Mn $2p$ photoemission spectra the main peak at lower binding energy is rather dominated by $c\bar{d}^6\bar{L}$ and the satellite at higher binding energy by $c\bar{d}^5$ configurations. From $\Delta < U$ also results that $c(2 \times 2)$ Mn/Ni(110) and $c(2 \times 2)$ Mn/Cu(100) can be characterized as charge-transfer compounds, where in practice metallic conductivity of the systems will be provided by the Ni and Cu substrates.

V. CONCLUSION

It is concluded that geometrical and electronic structure of 0.5 ML Mn on Ni(110) can consistently be described by configuration-interaction theory on a local MnNi₇ cluster. It is demonstrated in this way that electronic properties can be used to conclude to some extent on the local geometrical structure of a metal-on-metal adsorbate system. The cluster-model analysis corroborates the view that the local structural arrangement leads to a strong electron correlation effect on the Mn, and together with our LEED study this indicates that

an ordered surface alloy $c(2 \times 2)$ Mn/Ni(110) has been identified in this work.

ACKNOWLEDGMENTS

We thank A. Harasawa for help with the experimental setup. O.R. was supported by the Japan Society for the Promotion of Science and by Alexander von Humboldt-Stiftung and thanks Professor A. Kakizaki for hospitality at Institute for Solid State Physics-SRL.

-
- *Present address: BESSY, Albert-Einstein-Str. 15, D-12489 Berlin, Germany. Electronic address: rader@bessy.de
- †Also at Department of Complexity Science and Engineering.
- ¹M. Wuttig, Y. Gauthier, and S. Blügel, Phys. Rev. Lett. **70**, 3619 (1993).
- ²See also the review articles by S. Blügel, Appl. Phys. A: Mater. Sci. Process. **63**, 595 (1996); M. Wuttig and B. Feldmann, Surf. Rev. Lett. **3**, 1473 (1996).
- ³M. Wuttig, T. Flores, and C.C. Knight, Phys. Rev. B **48**, 12 082 (1993).
- ⁴M. Wuttig, C.C. Knight, T. Flores, and Y. Gauthier, Surf. Sci. **292**, 189 (1993); M. Wuttig, B. Feldmann, and T. Flores, *ibid.* **331–333**, 659 (1995).
- ⁵W.L. O'Brien, J. Zhang, and B.P. Tonner, J. Phys.: Condens. Matter **5**, L515 (1993); W.L. O'Brien and B.P. Tonner, Phys. Rev. B **51**, 617 (1995).
- ⁶O. Rader, W. Gudat, C. Carbone, E. Vescovo, S. Blügel, R. Kläs-ges, W. Eberhardt, M. Wuttig, J. Redinger, and F.J. Himpsel, Phys. Rev. B **55**, 5404 (1997).
- ⁷D. Schmitz, O. Rader, C. Carbone, and W. Eberhardt, Phys. Rev. B **54**, 15 352 (1996).
- ⁸O. Rader, E. Vescovo, M. Wuttig, D.D. Sarma, S. Blügel, F.J. Himpsel, A. Kimura, K.S. An, T. Mizokawa, A. Fujimori, and C. Carbone, Europhys. Lett. **39**, 429 (1997).
- ⁹Ch. Ross, B. Schirmer, M. Wuttig, Y. Gauthier, G. Bihlmayer, and S. Blügel, Phys. Rev. B **57**, 2607 (1998).
- ¹⁰P. Schieffer, M.C. Hanf, C. Krembel, and G. Gewinner, Surf. Sci. **446**, 175 (2000).
- ¹¹W.L. O'Brien and B.P. Tonner, Phys. Rev. B **50**, 2963 (1994).
- ¹²B.C. Choi, P.J. Bode, and J.A.C. Bland, Phys. Rev. B **59**, 7029 (1999).
- ¹³T.G. Walker and H. Hopster, Phys. Rev. B **48**, 3563 (1993).
- ¹⁴O. Rader, C. Pampuch, W. Gudat, A. Dallmeyer, C. Carbone, and W. Eberhardt, Europhys. Lett. **46**, 231 (1999).
- ¹⁵F. Nouvertne, U. May, A. Rampe, M. Gruyters, U. Korte, R. Berndt, and G. Güntherodt, Surf. Sci. **436**, L653 (1999).
- ¹⁶W. Eberhardt and E.W. Plummer, Phys. Rev. B **21**, 3245 (1980); N. Mårtensson, R. Nyholm, and B. Johansson, *ibid.* **30**, 2245 (1984).
- ¹⁷Y. Gauthier, M. Poensgen, and M. Wuttig, Surf. Sci. **303**, 36 (1994).
- ¹⁸C.R. Brundle and J. Broughton, in *The Chemical Physics of Solid Surfaces and Heterogeneous Catalysis*, edited by D.A. King and D.P. Woodruff (Elsevier, New York, 1985).
- ¹⁹*Handbook on X-ray Photoelectron Spectroscopy*, edited by G.E. Muilenberg (Perkin-Elmer, Eden Prairie, Minnesota, 1979).
- ²⁰For a review see M. Imada, A. Fujimori, and Y. Tokura, Rev. Mod. Phys. **70**, 1039 (1998).
- ²¹G. van der Laan, C. Westra, C. Haas, and G.A. Sawatzky, Phys. Rev. B **23**, 4369 (1981).
- ²²J. Zaanen, C. Westra, and G.A. Sawatzky, Phys. Rev. B **33**, 8060 (1986).
- ²³K. Okada and A. Kotani, J. Phys. Soc. Jpn. **60**, 772 (1991); **61**, 4619 (1992).
- ²⁴A.E. Bocquet, T. Mizokawa, T. Saitoh, H. Namatame, and A. Fujimori, Phys. Rev. B **46**, 3771 (1992); A.E. Bocquet, T. Mizokawa, A. Fujimori, M. Matoba, and S. Anzai, *ibid.* **52**, 13 838 (1995).
- ²⁵A.E. Bocquet and A. Fujimori, J. Electron Spectrosc. Relat. Phenom. **82**, 87 (1996).
- ²⁶W. A. Harrison, *Electronic Structure and the Properties of Solids* (Dover, New York, 1989).

Parallel, antiparallel and no magnetic coupling in submonolayer Mn on Fe(110)

O. RADER¹(*), C. PAMPUCH¹, W. GUDAT¹, A. DALLMEYER²
C. CARBONE² and W. EBERHARDT²

¹ *Berliner Elektronenspeicherring-Gesellschaft für Synchrotronstrahlung (BESSY)
Lentzeallee 100, D-14195 Berlin, Germany*

² *Institut für Festkörperforschung, Forschungszentrum Jülich - D-52425 Jülich, Germany*

(received 7 August 1998; accepted in final form 1 February 1999)

PACS. 73.20Hb – Impurity and defect levels; energy states of adsorbed species.

PACS. 75.30Pd – Surface magnetism.

Abstract. – An unusual sequence of magnetic couplings in the epitaxial-growth system Mn/Fe(110) is revealed using the element-selective magnetic circular X-ray dichroism (MCXD) method. Clean Mn shows an unprecedented vanishing magnetization up to 0.3 monolayers (ML). At 0.4 ML a parallel Mn-Fe coupling sets in with relatively small net Mn moment ($1.0 \pm 0.2\mu_B$ for 0.4–2 ML). Successive adsorption of oxygen changes the Mn-Fe coupling from parallel to zero to antiparallel and eventually to zero again.

There are a number of phenomena in magnetic storage technology in the stage of application or close to it that are based on properties of antiferromagnet-ferromagnet interfaces. These effects comprise long-range oscillatory magnetic coupling through Cr and Mn, giant magnetoresistance, and exchange biasing and are at present poorly understood [1]. Prerequisite for progress in comprehension is the knowledge of the actual magnetic structure at the antiferromagnet-ferromagnet interface. In the past years, the monolayer Mn on Fe(100) has emerged as model system studied by many researchers. Its magnetic structure is basically the result of competing interactions: The Mn monolayer itself prefers antiferromagnetism [2], so that the question is whether the interaction with the substrate is strong enough to impose ferromagnetic order on the Mn overlayer. After initially a whole range of different magnetic configurations had been obtained as ground state, the consideration of more complex magnetic structures and permission of lattice relaxation effects has led to agreement between theorists on antiferromagnetism or ferrimagnetic order of Mn as ground state with very small net moments ($< 0.1\mu_B$) and large local moments (about $3\mu_B$) [3-5].

The experimental view, on the other hand, is still controversial: MCXD measurements find antiparallel Mn-Fe coupling for submonolayers and vanishing coupling for 1 ML Mn/Fe(100) grown on Pd [6] and Ag [7]. Surprisingly, subsequent MCXD experiments [8] show parallel

(*) E-mail: rader@bessy.de

coupling, raising the question whether samples grown on MgO are a better representation of the Fe(100) surface. This was denied by the results of a recent study of Mn on an Fe(100) crystal, where antiparallel coupling, vanishing for 1 ML, was observed [9]. It should be noted that for each of these substrates not all of the conditions order, cleanliness, and magnetization are easy to optimize, and that there are therefore good reasons for the use of each of them. Very recently, there are also indications that perfect Mn/Fe(100) growth and absence of Mn-Fe interdiffusion cannot be achieved at the same time [10]. This argument would hold for any of the substrates.

These findings call for a better experimental system. The densest surface of bcc Fe is (110). Growth of Fe(110) on W(110) has been well characterized in the past. Note also that Fe/W(110) is a very well established system where a monolayer is ferromagnetic [11]. Moreover, Mn has a tendency of dealloying on Fe(110) [12]. First work has already been reported for Mn/Fe/Cu(110), where antiparallel Mn-Fe coupling was observed [13].

In this letter, we report on three intriguing coupling effects occurring in the same system and sample: i) absence of coupling in the low-coverage limit, which has never been reported before, ii) parallel coupling from 0.4 to 2 ML, contrasting our findings on the (100) surface of antiparallel coupling vanishing at 1 ML, and iii) a surprising reversal to antiparallel coupling by oxygen dosage. We will discuss explanations for the first two in detail, the oxygen effect, however, remains much less understood.

The measurements were performed at the BESSY synchrotron light source using the PM3 monochromator for circularly-polarized soft X-rays [14]. We prepared clean Fe(110) surfaces by epitaxial growth of 15 ML Fe onto a W(110) crystal and subsequent annealing to 400 °C. By pulses along the in-plane $[1\bar{1}0]$ direction, the sample is magnetized remanently. Mn was deposited with the sample at room temperature at rates of 0.2 ML/min after repeated calibrations with a quartz microbalance. Thicknesses were cross-checked using Mn L_3 peak heights in absorption spectra in order to verify the stability of the evaporation rate. We estimate the accuracy of thicknesses given here to be around 30%. Low-energy electron diffraction reveals sharp $p(1 \times 1)$ patterns and no superstructure for clean Fe and all Mn coverages studied here. In addition, core-level X-ray photoemission was measured to verify cleanliness and to monitor oxygen dosage. Base pressure was 1.0×10^{-10} mbar and rose to 2×10^{-10} mbar and 3.5×10^{-10} mbar during evaporation of Fe and Mn, respectively.

MCXD in absorption is a powerful method to study the magnetic order in an element-selective manner [15]. In the present experiment, we kept the photon spin constant and switched the sample magnetization. MCXD spectra were obtained using a total-electron-yield channeltron with an entrance grid electrically grounded. The angle between light and magnetization directions was 25°. This, together with the incomplete light polarization of about 80% at 0.6 mrad off the storage-ring plane [14], reduces the MCXD effect by a factor of 0.725, which the spectra were corrected for.

Figure 1 displays at the top typical Fe $L_{2,3}$ MCXD spectra serving here merely as reference for size and direction of the Mn dichroism effect. The individual spectra are for sample magnetization directed parallel (R) and antiparallel (L) to the spin of the incident photons and for the difference between the two. Below that, Mn spectra are shown for selected coverages. At 0.3 ML a dichroism effect is absent as seen from the flat magnified MCXD difference. A clear but small dichroism signal appears at 0.42 ML and at 2.0 ML. The sign of the coupling is always parallel to the Fe substrate. For 4.6 ML the dichroism has vanished again. To further explore the thickness dependence, the maximum MCXD asymmetry $(R - L)/(R + L)$ is plotted in fig. 2a. In particular, there are data points with zero asymmetry for 0.1, 0.2, and 0.3 ML before ferromagnetic order sets in. Note that different symbols are used to distinguish series of subsequent Mn deposition (upper two and lower two measurements in fig. 1 can be

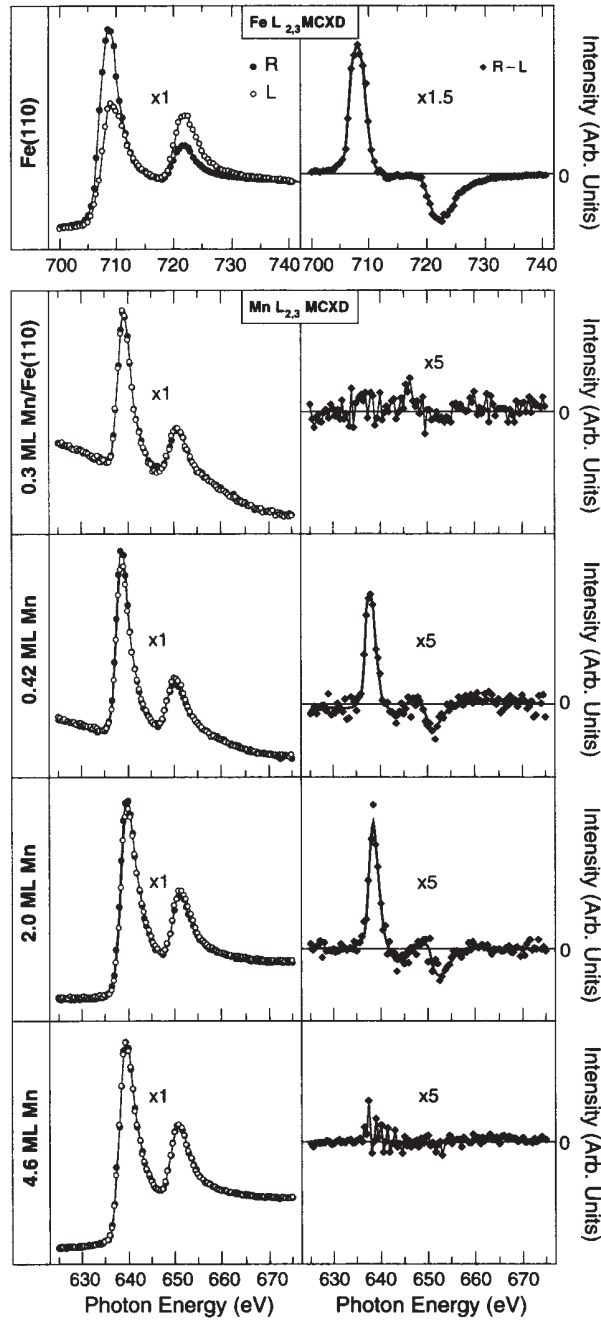


Fig. 1. - Mn and Fe MCXD spectra for various Mn coverages on Fe(110). Spectra are shown for magnetization and photon spin parallel (R) and antiparallel (L) as well as the difference between the two. With increasing coverage the magnetic coupling is absent, parallel, and absent again.

retrieved in fig. 2 as open and full squares, respectively). At larger thicknesses, the asymmetry has to decrease again because bulk Mn is antiferromagnetic and the measurement averages over several surface layers. Because of the comparatively small $2p$ spin-orbit splitting of Mn,

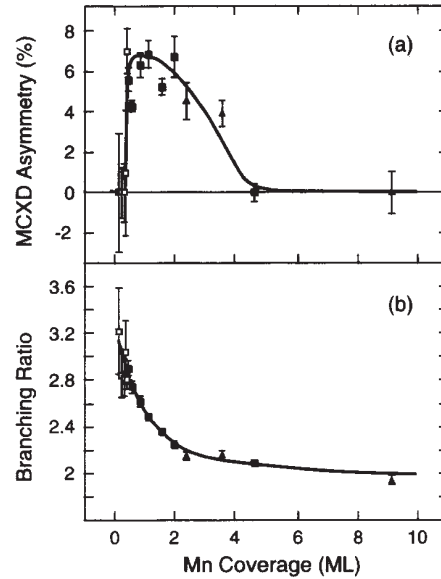


Fig. 2. – Thickness dependence of the maximum Mn MCD asymmetry (a), corresponding to the Mn net magnetic moment, and of the Mn branching ratio (b), characterizing the Mn electronic structure.

the spin magnetic moment should not be determined using the Thole sum rules [16]. We extract the net magnetic moment from the MCD spectra on the basis of calculated spectra as pointed out before [6] and obtain a value of $1.0 \pm 0.2 \mu_B$ at 0.42 ML. In fig. 2b the Mn branching ratio $[R(L_3) + L(L_3)]/[R(L_2) + L(L_2)]$ is plotted. Its increase below 2 ML shows that the Mn electronic structure is atomiclike for lowest coverages. The large branching ratio indicates large local moments like for Mn/Fe(100) which has been found to be in the d^5 configuration [6, 7]. The small net moment of $1.0 \pm 0.2 \mu_B$ here is therefore nothing more than the result of cancelling contributions and indicates that there exists rather a ferri- than a ferro-magnetic alignment within the Mn.

The sign of the coupling is opposite to the one found for Mn/Fe/Cu(110) [13], the structure of which is not established yet. It also contrasts results on the (100) surface by ourselves [6] and other groups [7, 9] of antiparallel coupling below and vanishing coupling at 1 ML. Parallel coupling for 1 ML Mn/Fe(100) has been reported in ref. [8] and for 1 ML Mn/Co(100) in ref. [17]. As long as calculations for the (110) surface are missing, it can only be argued that theory finds for 1 ML Mn/Fe(100) antiparallel coupling least likely, *i.e.*, in order of increasing energy, *ab initio* calculations obtain a net moment close to zero, parallel, and antiparallel coupling [3, 4].

For the surprising finding of an onset of Mn magnetization above 0.3 ML, we will discuss three possible explanations: i) The Mn local moment increases with coverage. ii) The interaction of Mn neighboring atoms brings about a change in the net Mn-Fe coupling. iii) Different coupling orientations are caused by different Mn-Fe distances.

Beginning with thesis i) we argue that an increase of the coordination number generally *decreases* the local magnetic moment from the atomic value ($5 \mu_B$ for Mn). Especially the atomic d^5 configuration is extremely stable, as can be seen from the term scheme [18], from photoemission studies on related systems [19], and from the fact that all calculations cited here give Mn moments between 3 and $4 \mu_B$, regardless of the magnetic configuration. Furthermore,

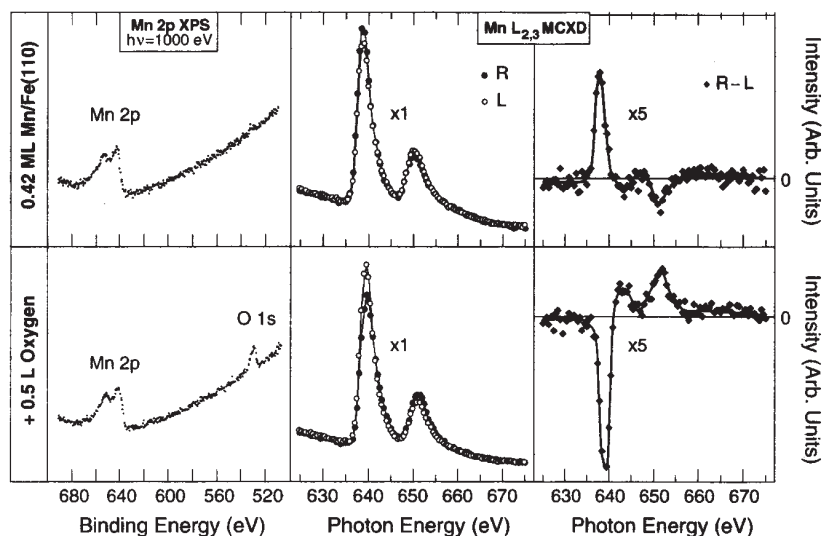


Fig. 3. – Comparison of 0.42 ML Mn/Fe(110) before and after dosage of 0.5 L oxygen through X-ray photoemission overview spectra (left), MCXD spectra, and MCXD difference spectra (right). The magnetic coupling of Mn to Fe reverses its sign.

the decrease of the branching ratio in fig. 2b supports rather a local moment decreasing with coverage, not even with a sudden change when ferromagnetic coupling sets in. Turning to thesis ii) we note that Mn-Mn interaction is antiferromagnetic and strong, especially in a close-packed (110)-layer. An increasing number of Mn neighbors with more antiparallel couplings necessarily

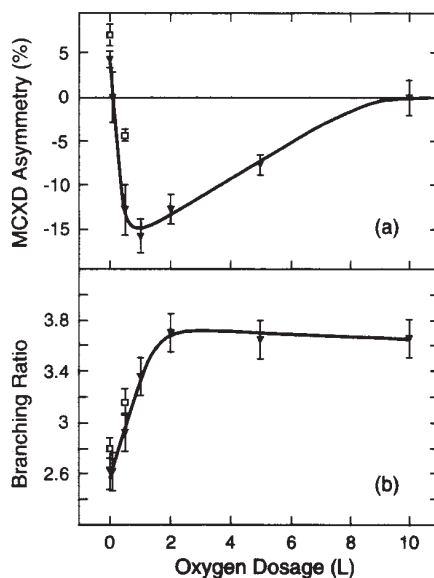


Fig. 4. – Oxygen coverage dependence of the maximum Mn MCD asymmetry (a) and of the Mn branching ratio (b). Symbols distinguish the 0.42-ML-Mn sample of figs. 1-3 (open squares) and a 0.8-ML-Mn sample (downward triangles). The Mn-Fe coupling changes from parallel to zero to antiparallel while the Mn electronic structure becomes increasingly more localized.

reduces the Mn *net* moment. Mn neighbors should, nevertheless, have an effect on the Mn-Fe distance, leading us to thesis iii): In the early stages of overlayer growth the Mn-Fe distance likely increases. It is, *e.g.*, known that an adatom pair resides farther above the surface than a single adatom because the formation of the interaction bond weakens the adatom-surface bond [20]. On the other hand, there are indications that the sign of the coupling of a Mn atom reverses when it is moved closer to the Fe surface: The calculated Mn-Fe distance of 1 ML Mn/Fe(100) is smaller for antiparallel than for parallel Mn-Fe coupling [3,4]. In ref. [21] a Mn adatom is predicted to couple parallel to Fe(100), whereas immersed in the Fe surface layer it favours antiparallel coupling. Note, however, that ref. [21] neglects relaxation effects, *i.e.*, the adatom is assumed to occupy an ideal lattice position. The real position will be closer, so that the coupling may fall instead into a transition region, where parallel and antiparallel orientations are energetically degenerate, leading to a zero net moment. As a final comment, it is not unlikely to have at 0.3 ML still many small Mn units (adatoms, dimers etc.), where these relaxation effects are strong. The reason is the repulsive nature of Mn-Mn interactions, which is crucial for the structure of $c(2 \times 2)$ Mn/Cu(100) [22], but also strong for Mn/Fe(100) [23].

We have also tried to modify the adsorption of Mn to Fe by deposition at low temperature, additional Fe deposition, and oxygen dosage. The most striking effect occurs for oxygen (fig. 3). With increasing oxygen dosage, the coupling of 0.42 ML Mn reverses its sign. The effect is seen in more detail in fig. 4, where the resulting MCXD effect becomes larger than for the clean Mn. It is difficult to give an explanation without detailed knowledge of the oxygen adsorption geometry. MnO and FeO are both antiferromagnets. Thus, oxygen could mediate a superexchange-type coupling between Mn and Fe. This would imply that oxygen changes drastically the Mn electronic structure. As a matter of fact, the branching ratio (fig. 4b) strongly increases with oxygen, but the magnetic coupling reverses before the branching ratio saturates, *i.e.*, it occurs just when oxygen bonding begins. Therefore it is possible that oxygen, at least for small dosage, just influences the geometry of Mn adsorption and thus the sign of the coupling. Recently, the strong influence that oxygen has on structure and stability of Co/Fe(100), even though it remains on the surface, has been revealed [24].

In conclusion, we observe transitions between three different kinds of magnetic coupling in submonolayer Mn/Fe(110), contrasting previous studied where Mn-Fe coupling was either parallel or antiparallel and never absent. We suggest that the results can be understood as sensitive dependence of the sign of the Mn-Fe coupling on the Mn-Fe distance, which should be verified by appropriate calculations including relaxation effects. Moreover, the comparison of clean and oxygen-covered samples places contamination beneath interdiffusion as second possible cause of antiparallel Mn-Fe coupling.

We thank CH. JUNG and H. GUNDLACH for their support with the experiment and D. SCHMITZ for helpful discussions.

REFERENCES

- [1] See, *e.g.*, BLAND J. A. C. and HEINRICH B. (Editors), *Ultrathin Magnetic Structures* (Springer, Berlin) 1994 and the volume *J. Magn. & Magn. Mater.*, **165** (1997).
- [2] BLÜGEL S. and DEDERICHS P. H., *Europhys. Lett.*, **9** (1989) 597.
- [3] RUQIAN WU and FREEMAN A. J., *Phys. Rev. B*, **51** (1995) 17131.
- [4] HANDSCHUH S. and BLÜGEL S., *Solid State Commun.*, **105** (1998) 633.
- [5] ELMOUHSSINE O., MORAITIS G., DEMANGEAT C. and PARLEBAS J. C., *Phys. Rev. B*, **55** (1997) R7410.

- [6] RADER O., GUDAT W., SCHMITZ D., CARBONE C. and EBERHARDT W., *Phys. Rev. B*, **56** (1997) 5053.
- [7] DRESSELHAUS J., SPANKE D., HILLEBRECHT F. U., KISKER E., VAN DER LAAN G., GOEDKOOP J. B. and BROOKES N. B., *Phys. Rev. B*, **56** (1997) 5461; ROTH CH., KLEEMANN TH., HILLEBRECHT F. U. and KISKER E., *Phys. Rev. B*, **52** (1995) R15691.
- [8] ANDRIEU S., FINAZZI M., YUBERO F., FISCHER H., ARCADE P., CHEVRIER F., HENNET L., HRICOVINI H., KRILL G. and PIECUCH M., *Europhys. Lett.*, **38** (1997) 459.
- [9] IGEL T., PFANDZELTER R. and WINTER H., *Phys. Rev. B*, **58** (1998) 2430.
- [10] IGEL T., PFANDZELTER R. and WINTER H., *Surf. Sci.*, **405** (1998) 182.
- [11] See ELMERS H. J., HAUSCHILD J., FRITZSCHE H., LIU G., GRADMANN U. and KÖHLER U., *Phys. Rev. Lett.*, **75** (1995) 2031 and references therein.
- [12] CHRISTENSEN A., RUBAN A. V., STOLTZE P., JACOBSON K. W., SKRIVER H. L., NØRSKOV J. K. and BESENBACHER F., *Phys. Rev. B*, **56** (1997) 5822.
- [13] DÜRR H. A., VAN DER LAAN G., SPANKE D., HILLEBRECHT F. U. and BROOKES N. B., *Europhys. Lett.*, **40** (1997) 171.
- [14] PETERSEN H., WILLMANN M., SCHÄFERS F. and GUDAT W., *Nucl. Instrum. Methods Phys. Res. A*, **333** (1993) 594.
- [15] SCHÜTZ G. *et al.*, *Phys. Rev. Lett.*, **58** (1987) 737; CHEN C. T. *et al.*, *Phys. Rev. B*, **42** (1990) 7262; KOIDE T. *et al.*, *Phys. Rev. B*, **44** (1991) 4697.
- [16] TERAMURA Y., TANAKA A. and JO T., *J. Phys. Soc. Jpn.*, **65** (1996) 1053.
- [17] O'BRIEN W. L. and TONNER B. P., *Phys. Rev. B*, **50** (1994) 2963.
- [18] VAN DER MAREL D., WESTRA C., SAWATZKY G. A. and HILLEBRECHT F. U., *Phys. Rev. B*, **31** (1985) 1936.
- [19] RADER O. *et al.*, *Phys. Rev. B*, **55** (1997) 5404; *Europhys. Lett.*, **39** (1997) 429.
- [20] FEIBELMAN P. J., *Phys. Rev. Lett.*, **58** (1987) 2766.
- [21] NONAS B., WILDBERGER K., ZELLER R. and DEDERICHS P. H., *J. Magn. & Magn. Mater.*, **165** (1997) 137.
- [22] FLORES T., JUNGHANS S. and WUTTIG M., *Surf. Sci.*, **371** (1997) 1 and references therein.
- [23] BLÜGEL S., unpublished.
- [24] KIM S. K., PETERSEN C., JONA F. and MARCUS P. M., *Phys. Rev. B*, **54** (1996) 2184.

Exchange splittings of Mn- and Sb-derived states by spin-resolved valence-band photoemission of MnSb

Oliver Rader*

Department of Physics, University of Tokyo, 7-3-1 Hongo, Bunkyo-ku, Tokyo 113, Japan

Akio Kimura, Nozomu Kamakura, Ki-Seok An, and Akito Kakizaki

Institute for Solid State Physics (ISSP), University of Tokyo, 7-22-1 Roppongi, Minato-ku, Tokyo 106, Japan

Shintaro Miyanishi and Hiroyuki Akinaga

Joint Research Center for Atom Technology, National Institute for Advanced Interdisciplinary Research (JRCAT-NAIR), 1-1-4 Higashi, Tsukuba, Ibaraki 305, Japan

Masafumi Shirai

Department of Physical Science, Graduate School of Engineering Science, Osaka University, 1-3 Machikaneyama-cho, Toyonaka 560, Japan

Kenya Shimada and Atsushi Fujimori

Department of Physics, University of Tokyo, 7-3-1 Hongo, Bunkyo-ku, Tokyo 113, Japan

(Received 8 October 1997)

We have grown epitaxial (0001)-oriented films of the ferromagnetic intermetallic compound MnSb on GaAs(111) substrates. The *ex situ* grown samples can be reprepared in such a way that clean, ordered, and magnetically saturated surfaces are obtained. Using spin-resolved photoemission, Sb5*p*- and Mn3*d*-derived spectral features are identified, and large exchange splittings (1.4 and 1.7 eV for Mn-Sb bonding states and about 3.0 eV for Mn nonbonding states) are measured. Our *ab initio* band-structure calculation agrees rather well with the experiment, reproducing the exchange splittings of Mn-Sb states but slightly underestimating that of Mn states. [S0163-1829(98)50802-8]

Progress in various research areas has in the past years rendered the ferromagnetic manganese monopnictides MnAs, MnSb, and MnBi prime candidates for materials of novel electronic devices: Large Kerr rotation angles, needed in magneto-optical recording, have been measured for MnBi (Ref. 1) and MnSb5%Pt.² Both MnSb and MnBi have a large magnetic moment and a Curie temperature well above room temperature (e.g., MnSb: $\mu = 3.5\mu_B$ and $T_C = 585$ K; see Ref. 3). The hexagonal crystal structure [NiAs type, Fig. 1(b)] is favorable for obtaining uniaxial magnetocrystalline anisotropies, and it has already been achieved to induce perpendicular magnetic anisotropy, which is desired in recording devices, in films of MnSb_{1-x}Bi_x.² MnSb has been studied by magnetic circular x-ray dichroism, and a substantial orbital magnetic moment was found.⁴ Very recently, epitaxial growth of MnAs (Ref. 5) and MnSb (Ref. 6) films on GaAs crystals has become possible, thus enabling the integration of ferromagnetic storage into semiconductor devices.

The various theoretical approaches to the electronic structure of MnSb have been reviewed in Ref. 3. In brief, ionic-like models and alloylike models for different degrees of hybridization between Mn and Sb electronic states have been proposed. Recently, several calculations employing a band-structure model were conducted.^{3,7} However, these predictions have never been tested by angle-resolved photoemission, and comparison to experimental data was limited to magnetic-moment and specific-heat measurements. Valence band x-ray photoemission⁸ was only of limited benefit as it

was found to be in agreement both with a simple superposition of spectra of pure Mn and Sb in Ref. 8 and with a band calculation predicting a large Mn moment and strong Mn3*d*-Sb5*p* hybridization in Ref. 3.

Using spin- and angle-resolved photoemission, we want to verify experimentally which model of the electronic structure is appropriate. The experiment on MnSb is particularly challenging from the preparative point of view because of the limited probing depth of the experiment (a few atomic layers) and the possibility of losing the large Mn magnetic moment and the ferromagnetic coupling of these moments in the probed surface area if that should deviate from the ideal MnSb crystal structure. It will be seen that it is possible to obtain well-ordered and magnetically saturated surfaces and that analysis of the spin is indeed essential in order to assign spectral features and to verify in this way the complicated electronic structure of MnSb.

MnSb(0001) films in the μm thickness range were grown onto GaAs(111) in a molecular beam epitaxy chamber at JRCAT. Characterization during the growth was done using reflection high-energy electron diffraction and Auger electron spectroscopy. Growth parameters were similar to the ones published in Ref. 6. The samples were capped with Sb and exposed to air during transport to the beamline. Sample surfaces were reprepared by Ne⁺ ion bombardment and annealing cycles until an intense and sharp hexagonal low-energy electron diffraction pattern became visible indicating a well-ordered surface. It was verified by Auger spectroscopy

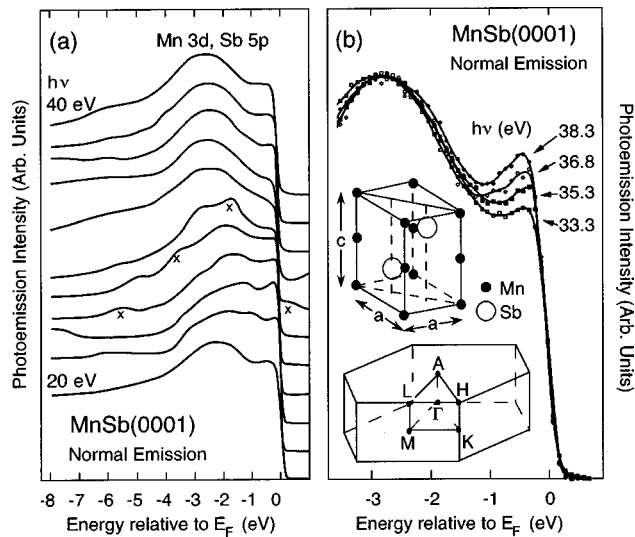


FIG. 1. (a) Angle-resolved photoemission spectra between 20 eV and 40 eV photon energy in steps of 2 eV. Light polarization is mixed $s + p$. Intensity induced by second-order light is marked. (b) Selected spectra for mainly s -polarized light near Γ . The spectra are consistent with a minority-spin band crossing E_F on the way from A to Γ . Crystal structure (NiAs type) of MnSb and bulk Brillouin zone are also given.

copy and photoemission at low photon energies that carbon and oxygen contaminations had completely been removed. Samples were remanently magnetized by applying a magnetic pulse in the film plane. We verified with magneto-optical Kerr effect that the remanent magnetization was almost 100% of the saturation magnetization. Spin- and angle-resolved photoemission measurements have been performed using linearly polarized light from the revolver undulator beamline⁹ 19A of ISSP at Photon Factory, Tsukuba, for excitation and a 100-keV Mott detector¹⁰ for spin analysis. The light was predominantly s polarized (18° off-normal incidence). Angle-resolved photoemission spectra were also taken at beamline 18A with mixed (s and p) polarization (45° incidence). The vacuum was between 1 and 2×10^{-10} Torr, and the sample was cooled to LN_2 temperature during spin-resolved measurements.

The appropriate photon energies for probing the electronic structure of MnSb lie below the $3p$ - $3d$ resonant excitation threshold of Mn (50 eV). We measured angle-resolved photoemission spectra between $h\nu = 20$ eV and 40 eV [Fig. 1(a)]. Emission was found to extend from E_F down to about 6 eV, assigned to Sb $5p$ and Mn $3d$ states and 10–11 eV assigned to Sb $5s$ states (not shown). However, a clear separation of Mn $3d$ - and Sb $5p$ -derived spectral features appears difficult, possibly due to substantial hybridization between these orbitals.

Figure 2 shows spin-resolved photoelectron spectra. For 25.8 eV and 38.2 eV photon energies we expect to probe bulk initial states near the A and Γ points, respectively [see the Brillouin zone in Fig. 1(b)].¹¹ The spectrum at the bottom, measured at 25.8 eV photon energy, displays large differences between the majority- (upward triangles) and the minority-spin channel (downward triangles), proving ferromagnetic order in the surface region of the sample. In detail, there appears a single peak in the minority spectrum at -2.0

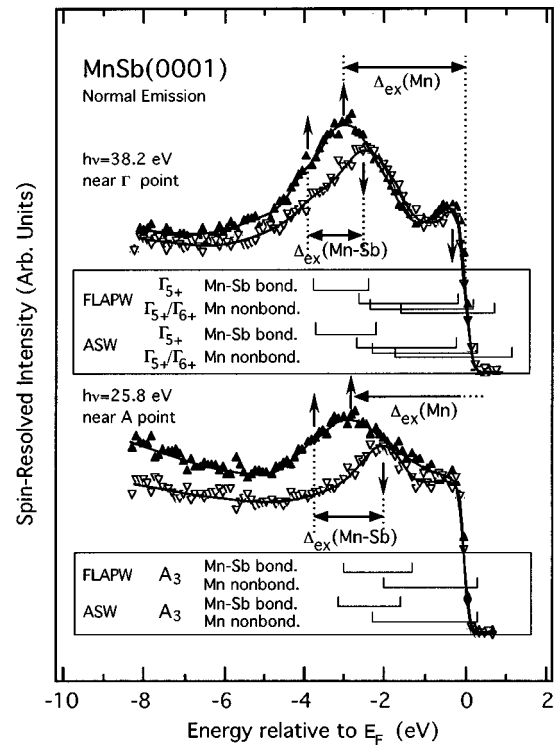


FIG. 2. Spin- and angle-resolved photoemission spectra of MnSb(0001). Upward triangles denote majority spin, downward triangles minority spin. Spectral features corresponding to exchange-split pairs of states are indicated. In addition, predictions for energy positions of exchange split states from this work (FLAPW) and Ref. 3 (ASW) are given.

eV and a broader peak (≈ -2.8 eV) with a low-energy shoulder (≈ -3.7 eV) in the majority spectrum. We expect Sb-derived emission to be less intense than Mn emission because the photoionization cross section favors Mn $3d$ over Sb $5p$ at this photon energy.¹² The structures in each spin channel with lowest energy, i.e., the majority-spin shoulder at -3.7 eV and the minority-spin peak at -2.0 eV, are of comparable intensity and smaller than the main majority-spin peak. Their energy separation, 1.7 eV, is incompatible with pure Mn $3d$ states in view of the large measured Mn moment of $3.5\mu_B$, and they are for this reason assigned as exchange-split states with substantial Sb $5p$ character. The maximum of the intense peak centered around -2.8 eV is, on the other hand, assigned to Mn $3d$. As a second intense minority spin peak is absent, the spectrum suggests that the Mn exchange splitting is very large (>2.8 eV), so that the corresponding minority-spin state is unoccupied.¹³

This interpretation is corroborated by our electronic structure calculations from first principles using the full-potential linearized augmented plane wave (FLAPW) method:¹⁴ In Fig. 3 we have highlighted Mn-Sb bonding states (dashed) and Mn nonbonding states (solid). For symmetry reasons¹⁵ we expect in the present setup along $[0001]$ (Γ - A - A direction) emission from Λ_5 and Λ_6 initial states. The band structure shows that the A point is fortunate for determining the exchange splitting since Λ_5 and Λ_6 states are degenerate here and, for minority spin, emission from only one initial state (A_3 symmetry) is expected.

Towards Γ , the Λ_5 bands disperse to lower energies. This

- *Electronic address: rader@exp.bessy.de
- ¹K. Egashira and T. Yamada, *J. Appl. Phys.* **45**, 3643 (1974).
- ²M. Takahashi, H. Shoji, Y. Hozumi, and T. Wakiyama, *J. Magn. Magn. Mater.* **131**, 67 (1994).
- ³R. Coehoorn, C. Haas, and R. A. de Groot, *Phys. Rev. B* **31**, 1990 (1985). Eigenvalues quoted here were taken from Fig. 4.
- ⁴A. Kimura, S. Suga, S. Imada, T. Muro, T. Shishidou, S. Y. Park, T. Miyahara, T. Kaneko, and T. Kanomata, *J. Electron Spectrosc. Relat. Phenom.* **78**, 287 (1996); *Phys. Rev. B* **56**, 6021 (1997).
- ⁵M. Tanaka, J. P. Harbison, M. C. Park, Y. S. Park, T. Shin, and G. M. Rothberg, *Appl. Phys. Lett.* **65**, 1964 (1994).
- ⁶H. Akinaga, Y. Suzuki, K. Tanaka, K. Ando, and T. Katayama, *Appl. Phys. Lett.* **67**, 141 (1995); H. Akinaga, K. Tanaka, K. Ando, and T. Katayama, *J. Cryst. Growth* **150**, 1144 (1995).
- ⁷K. Motizuki, *J. Magn. Magn. Mater.* **70**, 1 (1987).
- ⁸K. S. Liang and T. Chen, *Solid State Commun.* **23**, 975 (1977).
- ⁹A. Kakizaki, H. Ohkuma, T. Kinoshita, A. Harasawa, and T. Ishii, *Rev. Sci. Instrum.* **63**, 367 (1992).
- ¹⁰J. Fujii, T. Kinoshita, K. Shimada, T. Ikoma, A. Kakizaki, T. Ishii, H. Fukutani, A. Fujimori, K. Soda, H. Sugawara, in *Proceedings of the International Symposium on High Energy Spin Physics*, edited by T. Hasegawa, N. Horikawa, A. Masaïke, and S. Sawada (Universal Academy Press, Tokyo, 1992), p. 885.
- ¹¹Critical-point energies could not ambiguously be extracted from angle-resolved photoemission spectra. Therefore, \mathbf{k}_{\perp} was estimated with free-electron parabolas assuming an inner potential of -10 eV and a work function of 4.5 eV. For initial states of -3 eV, A and Γ points are predicted at 25.6 eV and 37.9 eV photon energy, respectively.
- ¹²Photoionization cross sections vary strongly in the photon energy range studied here. Ratios, calculated for the atom, of $Mn3d$ vs $Sb5p$ cross sections are 5.12 at 25.8 eV and 22.70 at 38.2 eV [J.-J. Yeh, *Atomic Calculation of Photoionization Cross-Sections and Asymmetry Parameters* (Gordon and Breach, New York, 1993)].
- ¹³There is also some intensity closer to the Fermi level (around -1 eV for majority spin and around E_F for minority spin). This intensity was found to depend on annealing conditions and is therefore not thought of as representative of stoichiometric bulk MnSb.
- ¹⁴For details of the calculations, see M. Shirai and Y. Tokioka, *J. Electron Spectrosc. Relat. Phenom.* (to be published).
- ¹⁵F. J. Himpsel and D. E. Eastman, *Phys. Rev. B* **21**, 3207 (1980).
- ¹⁶A. Santoni and F. J. Himpsel, *Phys. Rev. B* **43**, 1305 (1991).
- ¹⁷K. Mimura, H. Sato, S. Senba, H. Namatame, and M. Taniguchi, *Physica B* **237-238**, 392 (1997).
- ¹⁸O. Rader, W. Gudat, C. Carbone, E. Vescovo, S. Blügel, R. Kläs-ges, W. Eberhardt, M. Wuttig, J. Redinger, and F. J. Himpsel, *Phys. Rev. B* **55**, 5405 (1997).
- ¹⁹R. A. de Groot, F. M. Mueller, P. G. van Engen, and K. H. J. Buschow, *Phys. Rev. Lett.* **50**, 2024 (1983).

Signs of strong electron correlation in the band dispersion of bcc

Mn

O. Rader, C. Pampuch, W. Gudat

BESSY

Albert-Einstein-Str. 15, D-12489 Berlin, Germany

A. Dallmeyer, C. Carbone, W. Eberhardt

Institut für Festkörperforschung, Forschungszentrum Jülich

D-52425 Jülich, Germany

Abstract

The system Mn/W(110) has been characterized by low-energy electron diffraction and angle-resolved photoemission. Epitaxy of thick $p(1 \times 1)$ films is achieved by annealing. Photoemission spectra are dominated by intense peaks near E_F and at -2.6 eV. While the low-binding-energy feature shows substantial dispersions, the higher-binding-energy feature remains fixed in energy for variation of electron wave vectors perpendicular and parallel to the film plane. This result does not reconcile with published spin-polarized band structure calculations for bcc Mn bulk and (110) surface. Strong electron correlation in bulk bcc Mn is suggested as reason for this.

PACS 79.60.Bm, 71.20.Be

Typeset using REVTeX

The electronic structure of the magnetic transition metals has intensively been studied in past years. Angle-resolved photoemission and inverse photoemission have successfully been applied, notably the only experimental methods to directly probe the electron-wave-vector dependence of electronic states [1]. Using synchrotron radiation for excitation, it has been possible to obtain experimentally almost complete occupied band structures by angle-resolved photoemission of antiferromagnetic Cr and ferromagnetic Fe, Co, and Ni. On the other hand, no data is available for antiferromagnetic Mn [2]. The complicated crystal structure of α -Mn may be thought of as reason for this lack of data, though it remains astonishing in view of the fact that epitaxial growth of Mn overlayers would be a possible way to obtain crystalline samples and promising growth modes have occasionally been reported in the literature [3–6].

During the course of a recent study of the magnetic behavior of thin Mn on Fe(110), grown epitaxially on a W(110) substrate, we noticed that for all Mn coverages studied [0 - 4 monolayers (ML)], a clear $p(1 \times 1)$ low-energy electron diffraction (LEED) pattern occurs [7]. We have explored Mn epitaxy further and find that the $p(1 \times 1)$ structure can be produced also without the Fe interlayer and for large Mn thicknesses (30 ML) by annealing. The large thickness is important for valence-band photoemission since it ensures that bulk properties of Mn are studied and, secondly, that any contributions from the W substrate to valence-band photoemission are suppressed even at low kinetic energies with the enhanced probing depth of several atomic layers. The assignment of the thick $p(1 \times 1)$ Mn/W(110) to a bcc Mn(110) surface is supported by the small misfit of only 2.5% between the lattice constants of W (3.16Å) and of the high-temperature bcc phase δ -Mn (3.08Å at 1133 °C). Epitaxy of Mn/W(110) has also been characterized up to 4 ML by LEED and scanning tunneling microscopy in Ref. [8]. The present study deals with bcc Mn(110), a separate study on the electronic structure of fcc Mn(100) films will be published elsewhere [9].

Photoemission experiments have been performed in a vacuum chamber equipped with a spherical electrostatic analyzer of 150 mm radius. Monochromatized, linearly polarized synchrotron light of mixed (s+p) polarization has been used for excitation. For simplicity,

the temperature of the W sample during annealing of Mn films has been calibrated after the experiment by a Ni-NiCr thermocouple fixed at the sample site as 675 K. Photoemission spectra have been taken at room temperature. The W(110) single crystal has been prepared *in situ* as usual by oxygen treatment at 5×10^{-8} mbar and 1200°C and flashing to 2000–2200°C by resistive heating. Mn was evaporated from ultrapure pieces by electron bombardment. The deposition rate (0.5 - 1 ML/min) has repeatedly been calibrated using an oscillating-quartz microbalance. The base pressure was 1×10^{-10} mbar and rose during evaporation of Mn to 3×10^{-10} mbar.

After flashing, the W(110) substrate crystal shows a sharp $p(1 \times 1)$ LEED pattern. The first monolayers of Mn cover W(110) at room temperature in a layer mode as seen from STM [8] and from the intensity behavior of the W $4f_{7/2}$ core level [10]. An equally sensitive indicator of Mn growth is the behavior of the valence band spectrum due to the sharp features of W(110), e. g., at 62.5 eV photon energy [11], which are still visible at 5 ML Mn/W(110) [10]. Films are very rough around this coverage as evidenced by STM [8] and for further deposition (> 9 ML according to [8]) we observe that the LEED pattern is eliminated. Deviating from the conclusions in Ref. [8], we recover an intense $p(1 \times 1)$ LEED pattern by annealing 15–30 ML Mn to 675 K for 2 min (see pattern at 186 eV in Fig. 1a). The pattern is less sharp than the one of clean W(110) and shows a diffuse background contribution comparable to the one for room-temperature deposition of 2.3 ML Mn (see pattern at 160 eV in Ref. [8]) and less than for 4.1 ML Mn [8]. Surface roughness is intrinsic of the growth of bcc(110) around room temperature and has been studied for Fe/Fe(110) [12]. The roughness increases with the square root of the deposition but can completely be eliminated by postannealing [12]. In heteroepitaxy, however, the annealing temperature needed to reach the sharpest LEED pattern may cause the film to break up into crystallites and expose the substrate signal in electron spectroscopy. Such has been observed for Cr/W(110) [13], and the present case of Mn/W(110) is similar. The sharp photoemission features of the W(110) valence band [11] are easily detectable on top of the broad Mn-derived features and are absent in our data as is emission from W core levels.

Figures 1b and c show results of the angle-resolved photoemission study. Mn surfaces are very reactive. The absence of features around -6 eV for low photon energies shows the cleanliness of the present sample [18]. In Fig. 1c, spectra in normal-emission geometry are shown for photon energies ranging from 6 to 160 eV. Because of the crystallinity of the film (Fig. 1a), the varying photon energy varies the electron wave vector perpendicular to the film plane. Each spectrum shows two peaks: one close to the Fermi level (E_F) and one at -2.6 eV. Near E_F a small dispersion is marked that amounts to 400 meV. The straight vertical line highlights the constant binding energy of the higher-binding-energy feature. This peak is strongly broadened and the broadening amounts to at least the one found for Fe [FWHM $\sim 0.6(E - E_F)$] [19]. Due to this, we can exclude the presence of a dispersion only on an energy scale of > 0.3 eV.

Turning to Fig. 1b, we see the emission-angle dependence for a photon energy of 15 eV. Also here, where the electron wave vector is varied along the in-plane [001]-direction, there appears a peak at fixed energy of -2.6 ± 0.1 eV and a second one near E_F . The dispersion near E_F is rather large (~ 0.7 eV) marking even more clearly the difference between the peaks near E_F and the one at -2.6 eV.

We have tried to map the band dispersion marked in Fig. 1c using free electron parabolas as approximation to the final state [1]. Good agreement between dispersions in the 2nd and 4th Brillouin zone is obtained for Γ -N = 1.50 \AA^{-1} and an inner potential V_0 of 10 eV leading to final state energies E_f of 25 eV (Γ), 68 eV (N), and 138 eV (Γ). The result is shown in Fig. 1d. It proves that the crystalline structure of the film evidenced by LEED is sufficient for measuring the dispersion of E vs. wave vectors \mathbf{k}_{\parallel} as well as \mathbf{k}_{\perp} . We recall that the behavior seen in Fig. 1d marks a clear difference between Mn on the one hand and Fe, Co, Ni, and, in particular, Cr with the same atomic $3d^5$ configuration on the other hand, since in all of these metals substantial dispersions of $3d$ bulk states have been measured in angle-resolved photoemission [2]. For the bcc structure and emission along [110], the following evidence for dispersions exists: For Fe(110), a dispersion of the Σ_1^{\uparrow} band by more than 1 eV from Γ_{25}^{\uparrow} at -2.7 eV towards E_F is observed [14]. For antiferromagnetic Cr(110) the Γ'_{25} point appears

at -1.0 eV and its dispersion has been traced up to -0.3 eV [15].

A number of band structure calculations has been published for the various crystal structures of Mn. If we neglect paramagnetic calculations because they generally do not lead to densities of states that extend far enough below E_F to explain the current spectra, there are ferromagnetic calculations using the local density approximation of bcc Mn for various lattice constants by Fuster *et al.* [20]. Fuster *et al.* obtain a low-spin-to-high-spin transition for lattice constants between 5.90 and 6.025 a. u. This prediction was fully confirmed recently on the basis of the generalized gradient approximation [16]. The ground state, however, differs mainly due to typically different equilibrium volumes in local density and generalized gradient approximations [17] (antiferromagnetic in Ref. [16] and nonmagnetic in Ref. [20]).

We want to compare the results with experiment: (i) The dispersion predicted by Ref. [20] (for $a_{\text{Mn}} = 5.95$ a. u.) along [110] amounts to 1.1 eV up to the N_1 -point (Σ_1), thus much larger than the upper limit in the present experiment of 0.3 eV. (ii) Calculated energies are summarized in Fig. 2 for Γ_{25}^{\uparrow} which is the deepest point of the d band observable (emission from the Σ_2 band is forbidden in normal emission for any light polarization [21]). On the left hand side of Fig. 2 we see how the energy positions below and above E_F change and the exchange splitting increases as the lattice constant is enlarged. Lattice constants shown in Fig. 2 are larger than 5.90 a. u. and therefore on the high-spin side of the phase transition [20]. Although it follows that bcc Mn is high spin, we also see that the states at the center of the Brillouin zone (Γ) do not nearly reach an energy of -2.6 eV as measured in experiment. They are rather predicted at ~ -1.7 eV for the lattice constant of the W substrate (see arrow in Fig. 2). Only for unrealistically large lattice constant (8 a. u.) and magnetic moment ($4.9 \mu_B$) a binding energy corresponding to our experiment is reached at the right hand side of Fig. 2. It is clear that in this case the minority-spin states (open symbols) are completely unoccupied and no explanation for the strong peak seen near the Fermi level in Fig. 1 would remain.

The calculation by Fuster *et al.* provides band structures for the bulk only. At the

surface, however, enhanced moments can occur due to the reduced electronic interaction with neighboring atomic sites. For bcc Mn, there exists a magnetic calculation for the (110) surface [22]. For an antiferromagnetic surface atomic layer, magnetic moments of $+2.95$ and $-2.95\mu_B$ are obtained, whereas in the layers below it the moments are only about $2\mu_B$ in magnitude [22]. If we assume roughly 1 eV exchange splitting per $1\mu_B$ magnetic moment, this magnetic moment could explain the present peak at -2.6 eV. The enhanced magnetic moment is, however, predicted only for the topmost surface layer. At low photon energies and thus low kinetic energies the probing depth is much larger than 1 ML. In case of a surface effect, at least some signature of bulk band dispersion at lower binding energy than 2.6 eV should be visible. Moreover, oxygen adsorption studies do not indicate a large surface effect [10].

This observation of a nondispersing peak near -2.6 eV and a dispersing one near E_F is similar to the one obtained from γ -Mn(100) [9] which can be stabilized on Cu_3Au [6]. One difference is, however, is that γ -Mn is, due to its fcc structure, a strongly frustrated antiferromagnet and this can enhance electron localization whereas for δ -Mn with bcc structure a simple sc lattice can describe the antiferromagnetism like in simple models describing bcc Cr. We have systematically studied the electronic structure of metallic Mn systems in past years. The exchange splittings from photoemission and inverse photoemission of the surface alloys $c(2 \times 2)$ Mn on Cu(100) and Ni(100) are larger than predicted by local density theory by factors of 2 and 1.5, respectively [23]. Substantial transfer of spectral weight into photoemission satellites was observed for the valence band [24] and for Mn core levels [25]. Electron correlation can be strongly enhanced in the d^5 configuration of Mn but it is not clear whether the Hund rule occupation for Mn in the $c(2 \times 2)$ structure is preserved for higher coordinated Mn. The photoemission satellites, at least, disappear when the Mn thickness is increased beyond 1 ML [25]. The full majority spin polarization of the -2.8 eV peak in bulk MnSb is a hint for Hund rule occupation although deviations of the energy position from band theory (-2.2 eV) are not extremely large [26].

The large Coulomb correlation energy of Mn ($U = 3$ eV [24,25]) rather independently of

the chemical environment) is expected to lead to strong effects on photoemission spectra because its value is comparable to the width W of the occupied d band. This effect is missed in local density calculations also of Mn metal. It has been shown in Ref. [18] that previous attempts to establish strong electron correlation in Mn through a valence band satellite were without basis. The new experimental effort with a crystalline film of bcc Mn permits us to attack this problem again. We have experimentally excluded problems of crystallinity (by LEED, by angle dependent photoemission), uncertainty about \mathbf{k}_\perp (by the photon energy dependence), the surface (varying the probing depth and by adsorption). Beyond any reasonable doubt our data shows that bcc Mn cannot be understood in the framework of the standard local density approximation (because of wrong binding energies) or a standard quasiparticle picture (because of the missing dispersion). The data indicate, instead, spectral weight transfer from the coherent and dispersive part to a broad incoherent part of the spectrum and that an appropriate description of the electronic structure cannot be gained without inclusion of electron correlation. On the basis of the present data, it will be possible to establish Mn as the second strongly correlated transition metal besides Ni [2]. In view of the strong effects observed, the difference between various bulk crystal structures of Mn will be negligible as shown for fcc and bcc Ni [27].

REFERENCES

- [1] *Angle-Resolved Photoemission*, edited by S. D. Kevan (Elsevier, Amsterdam, 1992).
- [2] O. Rader and W. Gudat, Landolt-Börnstein, New Series III, Vol. 23c2 (ed. A. Goldmann), Springer, Berlin (1999).
- [3] S. T. Purcell, M. T. Johnson, N. W. E. McGee, R. Coehoorn, and W. Hoving, Phys. Rev. B **45**, 13064 (1992).
- [4] T. G. Walker and H. Hopster, Phys. Rev. B **48**, 3563 (1993).
- [5] X. Jin, M. Zhang, G. S. Dong, Y. Chen, M. Xu, X. G. Zhu, Xun Wang, E. D. Lu, H. B. Pan, P. S. Xu, X. Y. Zhang, and C. Y. Fan, Phys. Rev. B **50**, 9585 (1994).
- [6] B. Schirmer, B. Feldmann, A. Sokoll, Y. Gauthier, and M. Wuttig, Phys. Rev. B **60**, 5895 (1999).
- [7] O. Rader, C. Pampuch, W. Gudat, A. Dallmeyer, C. Carbone, and W. Eberhardt, Europhys. Lett. **46**, 231 (1999).
- [8] M. Bode, M. Hennefarth, D. Haude, M. Getzlaff, and R. Wiesendanger, Surf. Sci. **432**, 8 (1999).
- [9] S. Biermann, A. Dallmeyer, C. Carbone, W. Eberhardt, C. Pampuch, O. Rader, M. I. Katsnelson, and A. I. Lichtenstein, unpublished.
- [10] O. Rader *et al.*, unpublished.
- [11] See the clean W(110) spectrum in O. Rader and A. M. Shikin, Phys. Rev. B **64**, 201406 (2001).
- [12] M. Albrecht, H. Fritzsche, and U. Gradmann, Surf. Sci. **194**, 1 (1993)
- [13] J. Zukrowski, G. Liu, H. Fritzsche, and U. Gradmann, J. Magn. Magn. Mat. **145**, 57 (1995).

- [14] Y. Sakisaka, T. Maruyama, H. Kato, Y. Aiura, and H. Yanashima, Phys. Rev. B **41**, 11865 (1990).
- [15] Y. Sakisaka, T. Komeda, M. Onchi, H. Kato, S. Suzuki, K. Edamoto, Y. Aiura, Phys. Rev. B **38**, 1131 (1988).
- [16] M. Eder, J. Hafner, and E. G. Moroni, Phys. Rev. B **61**, 11492 (2000).
- [17] T. Asada and S. Blügel, Physica B **237**, 359 (1997).
- [18] S. Raaen and V. Murgai, Phys. Rev. B **36**, 887 (1987)
- [19] A. Santoni and F. J. Himpsel, Phys. Rev. B **43**, 1305 (1991).
- [20] G. Fuster, N. E. Brener, J. Callaway, J. L. Fry, Y. Z. Zhao, and D. A. Papaconstantopoulos, Phys. Rev. B **38**, 423 (1988).
- [21] J. Hermanson, Solid State Commun. **22**, 9 (1977).
- [22] M. Aldén, H. L. Skriver, S. Mirbt, and B. Johansson, Surf. Science **315**, 157 (1994).
- [23] O. Rader, W. Gudat, C. Carbone, E. Vescovo, S. Blügel, R. Kläsges, W. Eberhardt, M. Wuttig, J. Redinger, and F. J. Himpsel Phys. Rev. B **55**, 5404 (1997).
- [24] O. Rader, E. Vescovo, M. Wuttig, D. D. Sarma, S. Blügel, F. J. Himpsel, A. Kimura, K. S. An, T. Mizokawa, A. Fujimori, and C. Carbone Europhys. Lett. **39**, 429 (1997).
- [25] O. Rader, T. Mizokawa, A. Fujimori, and A. Kimura, Phys. Rev. B **64**, 165414 (2001).
- [26] O. Rader, A. Kimura, N. Kamakura, K.-S. An, A. Kakizaki, S. Miyanishi, H. Akinaga, M. Shirai, K. Shimada, and A. Fujimori, Phys. Rev. B **57**, R689 (1998).
- [27] N. B. Brookes, A. Clarke, and P. D. Johnson, Phys. Rev. B **46**, 237 (1992).

Figure captions:

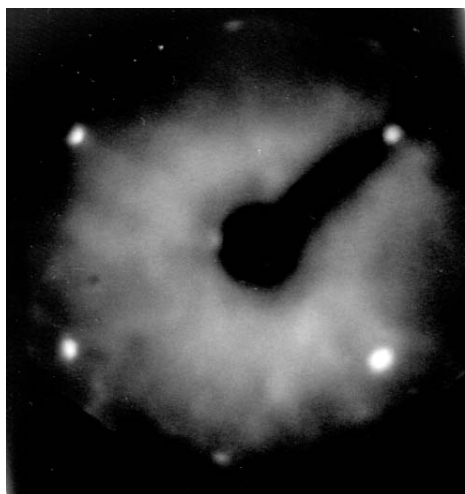
Fig 1. (a) $p(1 \times 1)$ LEED pattern of 15 ML Mn on W(110). Angle-resolved photoemission spectra at 15-eV photon energy for various emission angles (b) and for various photon

energies in normal emission (c). The higher-binding-energy structure stays fixed at -2.6 eV. The structure near E_F moves somewhat. Band dispersion determined from the data in (c) using a free electron parabola to approximate the final state (d).

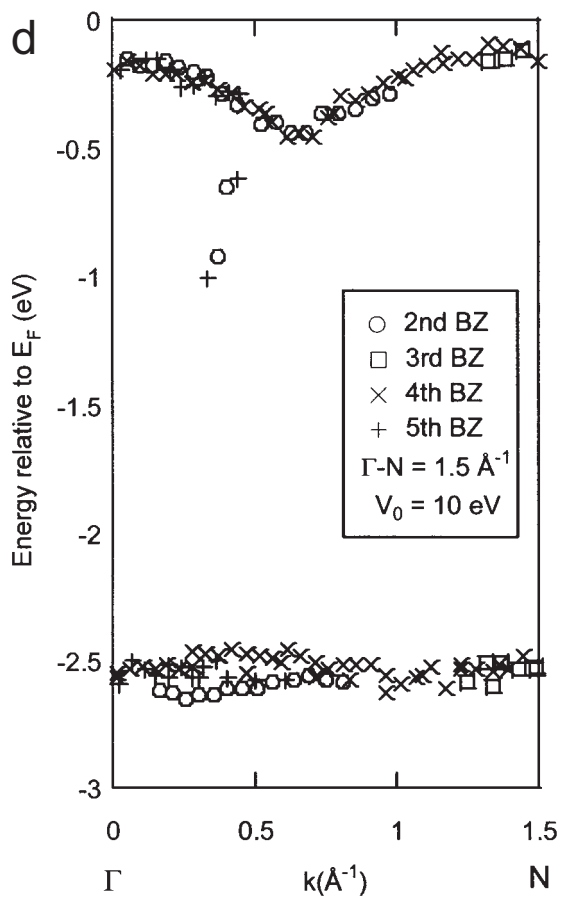
Fig. 2. Calculated critical point energies from Fuster et al. (Ref. [20]) for various lattice constants of ferromagnetic bulk bcc Mn. The arrow marks the lattice constant of the W substrate used in the experiment.

bcc Mn(110)/W(110)

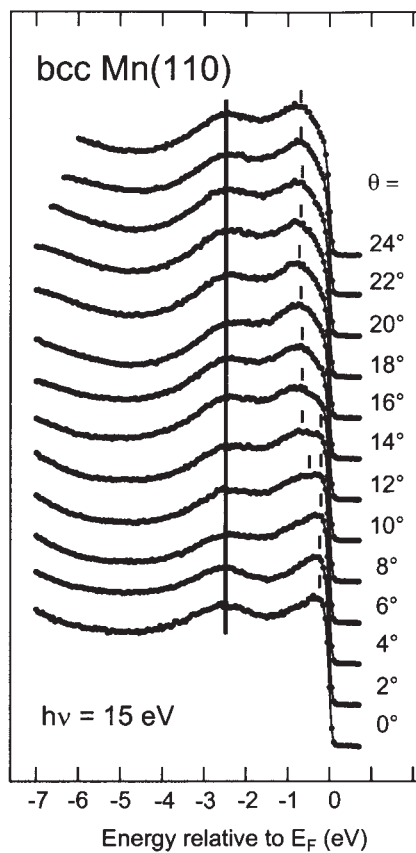
a



E = 186 eV



b



c

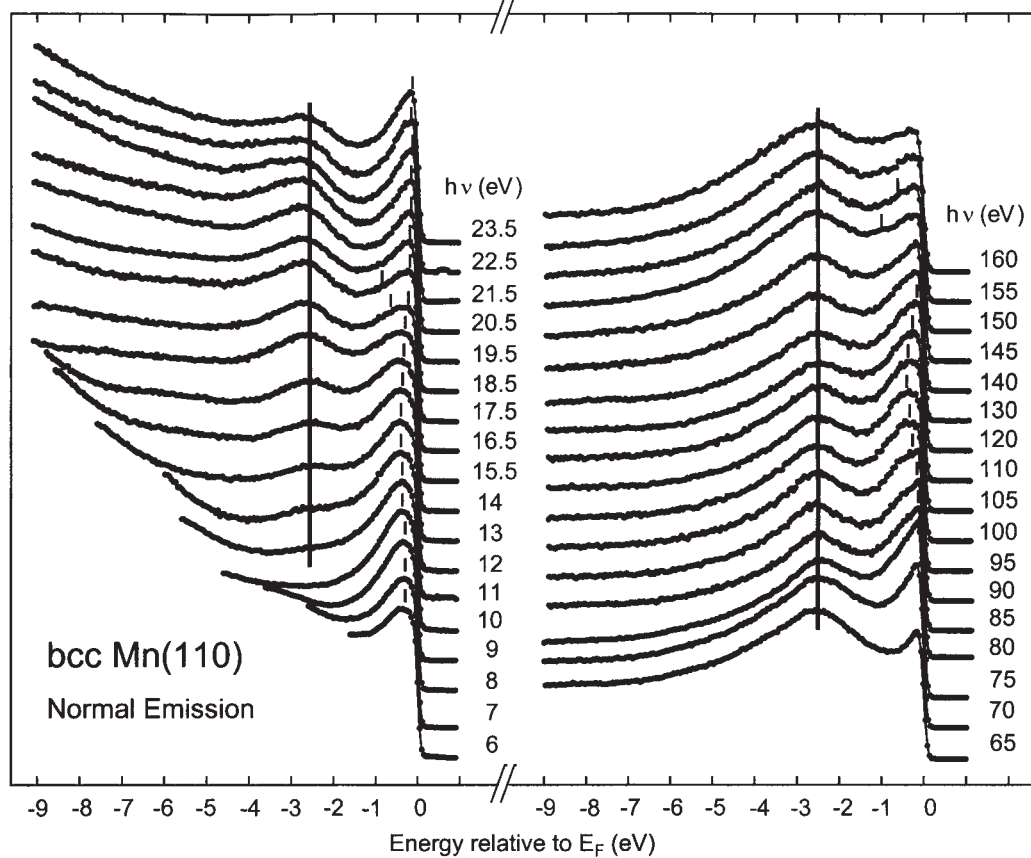


Fig. 1

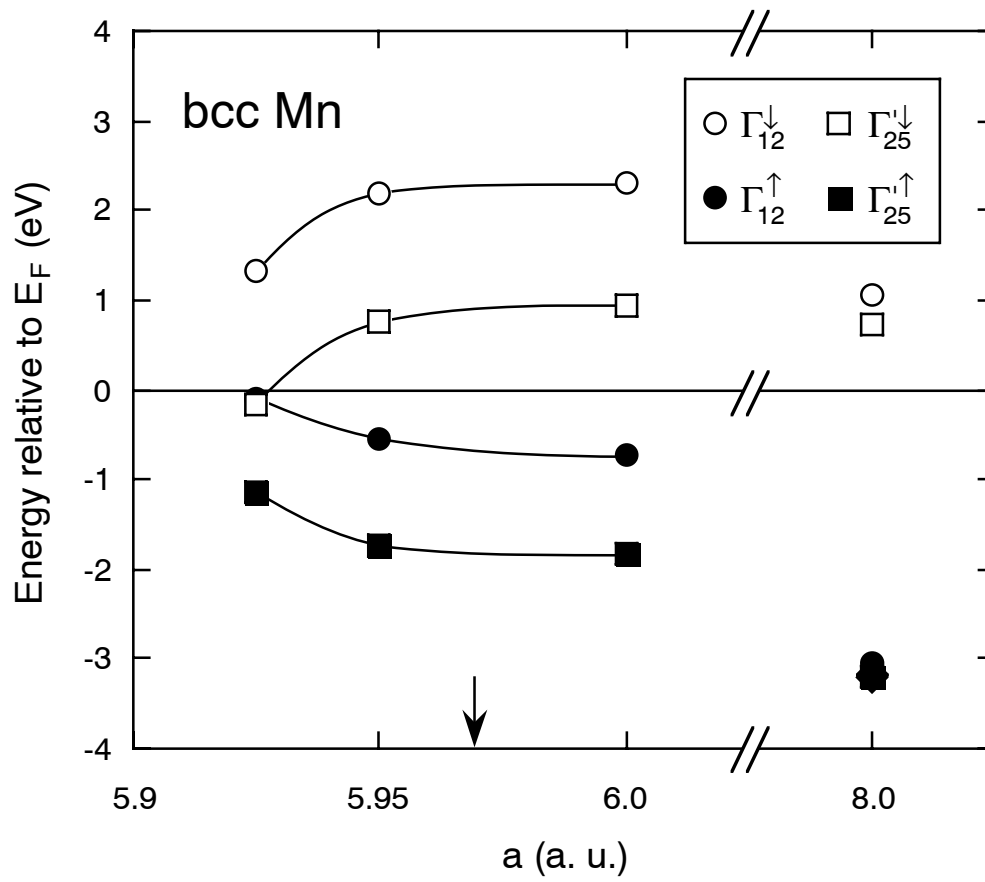


Fig. 2